INFORMATION TO USERS

This manuscript has been reproduced from the microfilm master. UMI films the text directly from the original or copy submitted. Thus, some thesis and dissertation copies are in typewriter face, while others may be from any type of computer printer.

The quality of this reproduction is dependent upon the quality of the copy submitted. Broken or indistinct print, colored or poor quality illustrations and photographs, print bleedthrough, substandard margins, and improper alignment can adversely affect reproduction.

In the unlikely event that the author did not send UMI a complete manuscript and there are missing pages, these will be noted. Also, if unauthorized copyright material had to be removed, a note will indicate the deletion.

Oversize materials (e.g., maps, drawings, charts) are reproduced by sectioning the original, beginning at the upper left-hand corner and continuing from left to right in equal sections with small overlaps.

ProQuest Information and Learning
300 North Zeeb Road, Ann Arbor, MI 48106-1346 USA
800-521-0600

UMI®

Reproduced with permission of the copyright owner. Further reproduction prohibited without permission.

Reproduced with permission of the copyright owner. Further reproduction prohibited without permission.

THE UNIVERSITY OF ALBERTA

STUDY OF ELECTRONS IN MAGNETRON SPUTTERING SYSTEMS FOR NOVEL THIN FILM APPLICATIONS.

By

DAVID JAMES FIELD

A THESIS SUBMITTED TO THE FACULTY OF GRADUATE STUDIES

AND RESEARCH IN PARTIAL FULFILMENT OF THE REQUIREMENTS

FOR THE DEGREE OF DOCTOR OF PHILOSOPHY

DEPARTMENT OF ELECTRICAL AND COMPUTER ENGINEERING

EDMONTON, ALBERTA

Spring, 2005

Reproduced with permission of the copyright owner. Further reproduction prohibited without permission.

Library and Archives Canada

Published Heritage Branch

395 Wellington Street
Ottawa ON K1A 0N4
Canada

Bibliothèque et Archives Canada

Direction du Patrimoine de l'édition

395, rue Wellington
Ottawa ON K1A 0N4
Canada

0-494-08233-X

Your file Votre référence
ISBN:
Our file Notre reference
ISBN:

NOTICE:
The author has granted a non-exclusive license allowing Library and Archives Canada to reproduce, publish, archive, preserve, conserve, communicate to the public by telecommunication or on the Internet, loan, distribute and sell theses worldwide, for commercial or non-commercial purposes, in microform, paper, electronic and/or any other formats.

AVIS:
L'auteur a accordé une licence non exclusive permettant à la Bibliothèque et Archives Canada de reproduire, publier, archiver, sauvegarder, conserver, transmettre au public par télécommunication ou par l'Internet, prêter, distribuer et vendre des thèses partout dans le monde, à des fins commerciales ou autres, sur support microforme, papier, électronique et/ou autres formats.

The author retains copyright ownership and moral rights in this thesis. Neither the thesis nor substantial extracts from it may be printed or otherwise reproduced without the author's permission.

L'auteur conserve la propriété du droit d'auteur et des droits moraux qui protège cette thèse. Ni la thèse ni des extraits substantiels de celle-ci ne doivent être imprimés ou autrement reproduits sans son autorisation.

In compliance with the Canadian Privacy Act some supporting forms may have been removed from this thesis.

Conformément à la loi canadienne sur la protection de la vie privée, quelques formulaires secondaires ont été enlevés de cette thèse.

While these forms may be included in the document page count, their removal does not represent any loss of content from the thesis.

Bien que ces formulaires aient inclus dans la pagination, il n'y aura aucun contenu manquant.

Reproduced with permission of the copyright owner. Further reproduction prohibited without permission.

Abstract

Understanding the structure and dynamics of the plasma within magnetron sputtering systems is important to the continued and extended exploitation of this deposition technique for the production of novel and industrially valuable thin films. To achieve this goal, it is necessary to understand how electrons, as a critical constituent of the plasma, respond, in terms of spatial densities and temperatures, to process conditions such as pressure, gas mixture, and cathode current.

In this investigation, a combination of experimental and simulation techniques are utilized. An electrostatic or Langmuir probe is used to observe basic plasma parameters including electron density (up to 6×10^{16} cm^{-3}), plasma electrical potential (typically 1 to 3 volts), floating potential (down to below -12 volts), and electron temperature (typically 0.5 to 5 eV), as functions of process conditions. The results indicate that electron transport throughout the magnetron reactor is not due to a simple or obvious mechanism. The electron density and temperature spatial profiles are strongly dependant on the magnetic field and the neutral gas species type and density profile. A Monte-Carlo simulation technique has also been used to study those dependencies. Such a technique involves following the three dimensional trajectories of electrons and accounts for an-isotropic and inelastic or elastic collisions with neutral gas atoms. The simulations demonstrate that the magnetic field and density of neutral gas species are important to the evolution of electron densities and temperatures. Additionally, the sputtered atom density (Ag in this case) seems to play a role in electron temperature profiles because of the lower ionization threshold for Ag. It also appeared that cathode voltage was not a major factor in the spatial

Reproduced with permission of the copyright owner. Further reproduction prohibited without permission.

electron temperature distribution. Finally, it appears that the presence of a group of hot electrons detected with the Langmuir probe, which are not in equilibrium with the bulk group of electrons, may result as the evolution of electrons originating from the cathode or within the cathode sheath.

Reproduced with permission of the copyright owner. Further reproduction prohibited without permission.

Acknowledgements

Creating the 'Magnetronus Electronica' was interesting and challenging. Much to my relief and delight, when I was in *le creux de l'enfer*, I also found myself amongst great individuals, who were always supportive and encouraging.

I am, of course, greatly indebted to the guidance and patience of Dr. Steven K. Dew whose insights and enthusiasm, for anything scientific, I always found admirable. Dr. Jim Stiles, *inventor extraordinaire*, who displayed remarkable passion for science and always had time for me, though probably had something better to do. Dr. Ying Tsui for his ceaseless support, kindness and continued interest in what I was doing. Patricia Beatty (Neo) for time and again kindly helping me with some insufferable bug. Mr. Francisco Javier Jimenez for his help, infectious enthusiasm and computer expertise. Mrs. Kimberley Svitich who generously donated her valuable time. Mr. Paul Dews and Dr. Anthony Naylor for ensuring I had a work environment, for the entire duration of my studies, which supported and respected my choice to pursue graduate studies. I should also thank Dr. Robert E. Burrell for encouraging me to pursue graduate studies.

To all of these people I am extremely indebted, much more than can be expressed on one simple page, much less within the confines of this thesis.

Reproduced with permission of the copyright owner. Further reproduction prohibited without permission.

Table of Contents

Chapter		Page
1.	**Introduction and Background.**	1
1.1	Outline and Justification	1
1.2	Glow Discharges	6
1.3	Magnetrons	8
1.4	Experimental Program	15
1.4.1	Langmuir Probe	15
1.4.2	Simulation.	18
1.4.2.1	SPUDII Simulation Overview	22
1.4.2.2	Collaborative Development of the SPUDII project	30
2.	**Experimental Equipment**	31
2.1	The ARGO	31
2.2	Langmuir Probe	35
2.2.1	Mechanical Description	35
2.2.2	Instrumentation	36
3.	**Langmuir Probe Investigation**	38
3.1	Introduction	38
3.2	Theory and Operation.	39
3.3	Data and Discussion	50
3.3.1	Spatial Surveys in Pure Argon	50

Reproduced with permission of the copyright owner. Further reproduction prohibited without permission.

3.3.2 Spatial Surveys with Oxygen Component . . 66

3.3.3 Oxygen Surveys for Three Select Locations within the Reactor 75

3.3.4 Pressure Surveys for Three Select Locations within the Reactor 80

3.3.5 Cathode Current Surveys for Three Select Locations within the Reactor 85

3.4 Summary and Conclusions 91

4. **Simulation** 99

4.1 Plaspud1: General Operational Details, Boundary Conditions, and Initial Conditions 99

4.1.1 Numerical solution to the equations of motion for charged particles in electric and magnetic fields. . . . 100

4.1.2 Collision with obstructions such as walls and targets . 101

4.1.3 Gas phase collisions. 103

4.1.4 Boundary Conditions 107

4.1.5 Initial Conditions 108

4.1.5a Pressure or neutral gas density . . . 108

4.1.5b Plasma Density 109

4.1.5c Sheath Thickness 109

4.1.5d Potential and Electric Field. . . . 111

4.1.5e Secondary Electron Emission Coefficient . . 113

Reproduced with permission of the copyright owner. Further reproduction prohibited without permission.

4.1.5f Electron Reflection Coefficient . . . 114
4.1.5g Cathode Ion Flux 114
4.1.5h Magnetic Field 115
4.2 Plaspud1 Functional Algorithm 117
4.2.1 General Description of Algorithm . . . 117
4.3 Extracting Meaningful Data from the Simulation . . 120
4.3.1 Fast Electron Density 120
4.3.2 Ion and Electron Creation Rates 121
4.3.3 EEDFs 122
4.4 Practical Details 123
4.5 Results and Discussion 125
4.5.1 Simulations at 5 mTorr. 125
4.5.1.1 Uniform Argon Pressure 125
4.5.1.2 Effect of Various Levels of Sputtered Ag in Gas Phase 142
4.5.1.3 Effect of Cathode Voltage 146
4.5.1.4 Effect of Metastable Argon Gas . . . 149
4.5.1.5 Effect of Secondary Electron Emission Coefficient (γ_p) and Electron Reflection Coefficient (ERC) . 153
4.5.1.6 Effect of Gas Rarefaction at 5 mTorr . . 156
4.5.1.7 Effect of Cathode Sheath Thickness . . 160
4.5.2 Simulations at 40 mTorr 164
4.6 Simulation Summary and Conclusions . . . 169

Reproduced with permission of the copyright owner. Further reproduction prohibited without permission.

5. **Summary** 174

5.1 Summary and Conclusions 174

5.2 Recommended Future Studies 178

Appendix 1: Experimental Run Conditions and Cathode Voltage. . . 180

Appendix 2: Spatial map of locations where Langmuir Probe data has been obtained. 182

References 183

Reproduced with permission of the copyright owner. Further reproduction prohibited without permission.

List of Tables:

Table		Page
4.1	Electron-argon and electron-silver collision processes and respective inelastic energy of that process. . . .	106
4.2	Response of creation rates, fast electron density, n_e^M, and T_e to various tested simulation parameters. . . .	173

Reproduced with permission of the copyright owner. Further reproduction prohibited without permission.

List of Figures

Figure	Description	Page
1.1	Depiction of simple sputtering process	2
1.2	Thornton's Structure Zone model	3
1.3	Log reduction of viable MRSA bacteria on exposure to silver	4
1.4	General architecture of a glow discharge	7
1.5	Planar magnetron magnetic field and electron drift path	10
1.6	Basic magnetron sputtering system	11
1.7	A classic Langmuir probe characteristic	17
1.8	Modular composition of SPUDII software project	23
2.1	The ARGO sputtering chamber	32
2.2	The ARGO magnet assembly	34
2.3	The ARGO magnetic field 2-D vector plot	34
2.4	Detail of Langmuir probe assembly	35
2.5	Schematic of Langmuir probe intrumentation	36
3.0	Typical Langmuir probe I-V semi-log plots	43
3.1 a	Electron density for lateral surveys with pure argon	51
3.1 b,c	Plasma potential (V_p) and floating potential (V_f) for lateral surveys in pure argon	52
3.1 d,e	Electron temperature (T_e), and hot and cold electron group temperatures (T_e^{hot} and T_e^{cold}) for lateral surveys in pure argon	53
3.2 a	Electron density for normal surveys with pure argon	54
3.2 b,c	Plasma potential (V_p) and floating potential (V_f) for normal surveys in pure argon	55
3.2 d,e	Electron temperature (T_e), and hot and cold electron group temperatures (T_e^{hot} and T_e^{cold}) for normal surveys in pure argon	56
3.3	Semi-log plot of probe current versus voltage for various distances above cathode demonstrating progression from Maxwellian to bi-Maxwellian nature	62

Reproduced with permission of the copyright owner. Further reproduction prohibited without permission.

3.4	Energy Dependant elastic and super-elastic electron collision cross sections for argon	64
3.5 a,b	Electron density and plasma potential (V_p) for lateral surveys in oxygen	68
3.5 c,d	Floating potential (V_f) and electron temperature (T_e) for lateral surveys in oxygen	69
3.5 e	Hot and cold electron group temperatures (T_e^{hot} and T_e^{cold}) for lateral surveys in oxygen	70
3.6 a,b	Electron density and plasma potential (V_p) for normal surveys in oxygen	71
3.6 c,d	Floating potential (V_f) and electron temperature (T_e) for normal surveys in oxygen	72
3.6 e	Hot and cold electron group temperatures (T_e^{hot} and T_e^{cold}) for normal surveys in oxygen	73
3.7 a	Electron density for surveys with oxygen	76
3.7 b,c	Plasma potential (V_p), floating potential (V_f), for surveys in oxygen.	77
3.7 d,e	Electron temperature (T_e) and hot and cold electron group temperatures (T_e^{hot} and T_e^{cold}) for surveys with oxygen	78
3.8 a,b	Electron density and plasma potential (V_p) for surveys in pressure	82
3.8 c,d	Floating potential (V_f) and electron temperature (T_e) for surveys in pressure	83
3.8 e	Hot and cold electron group temperatures (T_e^{hot} and T_e^{cold}) for surveys in pressure	84
3.9 a,b	Electron density and plasma potential (V_p) for surveys in cathode current	87
3.9 c,d	Floating potential (V_f) and electron temperature (T_e) for surveys in cathode current	88
3.9 e	Hot and cold electron group temperatures (T_e^{hot} and T_e^{cold}) for surveys in cathode current	89
3.10	2-D spatial map of electron density for 40 and 5 mTorr of pure argon gas.	92

Reproduced with permission of the copyright owner. Further reproduction prohibited without permission.

3.11	2-D spatial map of electron temperature for 40 and 5 mTorr of pure argon gas.	92
3.12	2-D spatial map of electron density for 4% and 16% O_2 at 40 mTorr.	93
3.13	2-D spatial map of electron temperature for 4% and 16% O_2 at 40 mTorr.	93
3.14	Average electron density (n_e) and temperature (T_e) versus pressure in pure argon.	96
3.15	Average hot and cold electron temperatures (T_e^{hot} and T_e^{cold}) versus pressure in pure argon.	96
3.16	Average electron density (n_e) and temperature (T_e) versus cathode current in pure argon.	97
3.17	Average hot and cold electron temperatures (T_e^{hot} and T_e^{cold}) versus cathode current in pure argon.	97
4.1	Energy dependant normalized scattering angle probability for electron-argon collisions	105
4.2	Collision cross sections for electron-argon and electron-silver collisions	107
4.3	Electric potential with simulation cathode sheath for various sheath widths	112
4.4	Target erosion profile versus magnetic field profile.	116
4.5	Flow chart for operation of Plaspud 1 simulation module	119
4.6	Electron and ion creation rates for 5mTorr simulation with uniform argon density	126
4.6	Fast electron density for 5mTorr simulation with uniform argon density	127
4.8	Demonstration of effective trapping of low energy electron deep within magnetic trap	128
4.9	Fast electron density along chord above etch region for 5mTorr simulation with uniform argon density	129
4.10	Fast electron density in sheath for 5mTorr simulation with uniform argon density	129
4.11	Maxwellian and Rundle distribution fits to EEDF's generated by simulation 4cm above etch track with uniform argon density	131

Reproduced with permission of the copyright owner. Further reproduction prohibited without permission.

4.12 a	EEDF's at 3 and 4 cm above etch region and Maxwellian fits for 5 mTorr uniform gas density simulation	134
4.12 b,c	EEDF's at 5, 6, 8 and 10 cm above etch region and Maxwellian fits for 5 mTorr uniform gas density simulation	135
4.13	Maxwellian electron temperatures derived from EEDF's generated by simulation with uniform 5mTorr gas density	136
4.14	Maxwellian electron densities derived from EEDF's generated by simulation with uniform 5mTorr gas density	137
4.15	EEDF's obtained above 'well' region for simulations with 5 mTorr uniform gas density	18
4.16	EEDF's obtained laterally across cathode at 5 cm distance for simulations with 5 mTorr uniform gas density	139
4.17	EEDF and Maxwellian fit taken at 2 mm outside sheath above etch region for simulations at 5 mTorr uniform gas density	140
4.18	High energy portion of EEDF taken at 2 mm outside sheath above etch region for simulations at 5 mTorr uniform gas density	141
4.19	Normalized density profile used in runs incorporating Ag gas atoms	142
4.20	Fast electron density along chord above etch region for 5mTorr simulation using Ag gas profile	144
4.21	EEDF's 5 cm above etch region for simulations with and without Ag gas density. Maxwellian fits included	144
4.22	Maxwellian electron temperatures derived from EEDF's generated by simulation with various Ag gas densities	145
4.23	Maxwellian electron densities derived from EEDF's generated by simulation with various Ag gas densities	146
4.24	EEDF's 4 cm above etch region for simulations with two different cathode voltages	147
4.25	Fast electron density along chord above etch region for 5mTorr with two cathode voltages	147
4.26	Electron and ion creation rates along chord above etch region with two different cathode voltages	148

Reproduced with permission of the copyright owner. Further reproduction prohibited without permission.

4.27 Electron creation rates along chord above etch region for various densities and allowed processes invloving metastable argon 150

4.28 Ion creation rates along chord above etch region for various densities and allowed processes invloving metastable argon 150

4.29 Fast electron densities along chord above etch region for various densities and allowed processes involving metastable argon 151

4.30 Maxwellian electron densities derived from EEDF's generated by simulation with various metastable argon densities and allowed processes 152

4.31 Maxwellian electron temperatures derived from EEDF's generated by simulation with various metastable argon densities and allowed processes 153

4.32 Electron creation rates along chord above etch region for various values of γ_p and ERC coefficients 154

4.33 Ion creation rates along chord above etch region for various values of γ_p and ERC coefficients 155

4.34 Fast electron densities along chord above etch region for various values of γ_p and ERC coefficients 155

4.35 Normalized gas density profile used in 5 mTorr simulation involving rarefied gas density 156

4.36 2-D electron creation rates for rarefied and un-rarefied gas densities 157

4.37 2-D fast electron densities for rarefied and un-rarefied gas densities 157

4.38 Maxwellian electron densities derived from EEDF's generated by simulation with rarefied and unrarefied gas densities 158

4.39 Maxwellian electron temperatures derived from EEDF's generated by simulation with rarefied and unrarefied gas densities 159

4.40 2-D electron creation rates for two cathode sheath thicknesses 161

4.41 1-D electron creation rate along chord above etch region for two cathode sheath thicknesses 161

4.42 2-D fast electron density profile for thick sheath simulation 163

4.43 2-D fast electron density profile for thin sheath simulation 163

Reproduced with permission of the copyright owner. Further reproduction prohibited without permission.

4.44	Various rarefied gas density profiles used in simulations at 40 mTorr	164
4.45	Maxwellian electron temperatures above etch region derived from EEDF's generated by simulation with rarefied and unrarefied gas densities at 40 mTorr	165
4.46	Maxwellian electron densities above etch region derived from EEDF's generated by simulation with rarefied and unrarefied gas densities at 40 mTorr	166
4.47	Maxwellian electron temperatures above well region derived from EEDF's generated by simulation with rarefied and unrarefied gas densities	167
4.48	Maxwellian electron densities above well region derived from EEDF's generated by simulation with rarefied and unrarefied gas densities	168

Reproduced with permission of the copyright owner. Further reproduction prohibited without permission.

List of Variables

k	Boltzman constant (1.380658×10^{-23} J/K)
e	electron charge (1.602177×10^{-19} C)
m_e	electron mass (9.109389×10^{-31} kg)
m_i	ion mass
m_n	neutral mass
n_e	electron density
n_e^M	electron density obtained from Maxwellian distribution fit to simulated data
n_i	ion density (positive)
T_e	electron temperature
T_{eff}	effective electron temperature (non-Maxwellian groups)
T_e^{hot}	hot electron group temperature
T_e^{cold}	cold electron group temperature
V_p	plasma electrical potential
V_f	plasma floating electrical potential
d_s	plasma sheath thickness
R_p	Langmuir probe radius
V_B	Langmuir probe electrical bias
A_{coll}	collection area of Langmuir probe
I_e^{*hot}	Langmuir probe saturation current due to hot electrons
I_e^{*cold}	Langmuir probe saturation current due to cold electrons
L_r	Larmor radius

Reproduced with permission of the copyright owner. Further reproduction prohibited without permission.

B	Magnetic field vector
E	Electric field vector
λ_m	particle mean free path (mfp)
H	Hall parameter (λ_m/ L_r)

Reproduced with permission of the copyright owner. Further reproduction prohibited without permission.

Chapter 1: Introduction and Background

1.1 Outline and Justification

Thin films are an important component of numerous industrially relevant technologies, and are exploited for many reasons, including their electrical, magnetic, optical, tribological, and catalytic properties. They have found extensive application in forming microelectronic circuitry as conductors, insulators, semiconductors and diffusion barriers. They are used as antimicrobial, tribological, and biocompatible coatings on medical devices, anti-reflective coatings on eyeglasses and windows, hardness coatings on tools, magnetic coatings on data storage media, and as decorative coatings on everything from clothes to automobiles. These functions, and the plethora of other applications, have allowed thin films to become an important and regular component in everyday life.

Given the infiltration of thin films into such a wide range of technologies, they must have a diverse range of physical characteristics and properties to function as required. The desirable characteristics that these films demonstrate are, of course, dependent on film composition, but also are often extremely sensitive to the microstructure of the film. For example, metallization of conductor lines in microchips should exhibit good coverage and uniformity over topographical features with large grains and oriented and smooth surfaces. On the other hand, catalytic films may need to address a different set of criteria, where maximizing the film surface area, potentially by increasing voids and defects in the film, may be desired.

As the characteristics of the film depends on the film structure, so too, does the film structure depend on the process whereby the film is created. Often these films are formed by a process commonly referred to as sputter deposition, or 'sputtering'. Sputtering is, in general, a process whereby a free ion energetically bombards a solid surface (called a target), and ejects atoms of target material by virtue of the nature of that collision (see figure 1.1). If this is done in a sufficiently low gas pressure environment, the ejected atoms may eventually encounter the substrate. By condensing there, they contribute to the formation of a thin film.

Reproduced with permission of the copyright owner. Further reproduction prohibited without permission.

Depending on the gas pressure in the system, the sputtered target atoms may arrive at the substrate rectilinearly, if they have no collisions with gas atoms on the way, or by diffusion, if they have several collisions with gas atoms on the way.

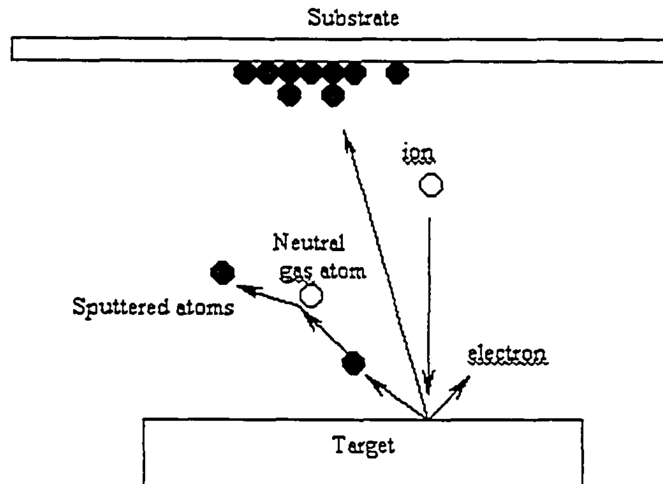

Figure 1.1: Depiction of the simple sputtering process.

Typically, the film microstructures produced by such methods can be viewed with respect to 'structure zone models' such as that produced by Thornton[1] (see figure 1.2). This model is based on substrate temperature relative to the melting temperature of the film, and gas pressure in the sputter system. Substrate temperature is, in itself, sufficient to explain three of the four film structure zones. Low temperature, Zone 1 structures are characterized by columnar tapered units well defined by voided growth boundaries. Such structures are understood as resulting from depositing atoms that condense and do not significantly diffuse over the surface of the film or substrate (i.e., low adatom mobility)[1]. Atoms that deposit from an oblique direction are effectively prevented from reaching the bottom of the voids, and deposit near the top of the tapered structures, building them higher. This is often referred to as atomic shadowing. Columnar grains with metallurgical grain boundaries characterize Zone 2 structures, where the grains increase in width at higher temperatures. This is understood as resulting from increased surface diffusion rates such that depositing atoms can diffuse over the film structure's surface, filling voids and forming the metallurgical boundaries[1]. Zone 3 structures consist of large

Reproduced with permission of the copyright owner. Further reproduction prohibited without permission.

equiaxed grains, which increase in size with temperature. These are understood as resulting from atomic diffusion through the bulk of the film[1]. A fourth zone, identified as Zone T, is typified by a dense array of poorly defined fibrous grains and is believed to be a transition region between zones 1 and 2. Zone T structures are felt to be a consequence of the bombarding effect of energetic ions which have been neutralized and reflected from the cathode surface. These particles subsequently impinge on the substrate with high energy[1]. At higher pressures, these energetic 'reflected neutrals' collide with more gas atoms before encountering the substrate and thus arrive there with less energy and at a more oblique angle. Thus, a dependence on gas pressure is part of the zone model. The mechanism by which reflected neutrals influence grain structure is not well understood[1]. Since, for Zone T structures, the substrate temperature is low, surface and bulk diffusion processes do not dominate and Zone 2 or 3 structures are not observed.

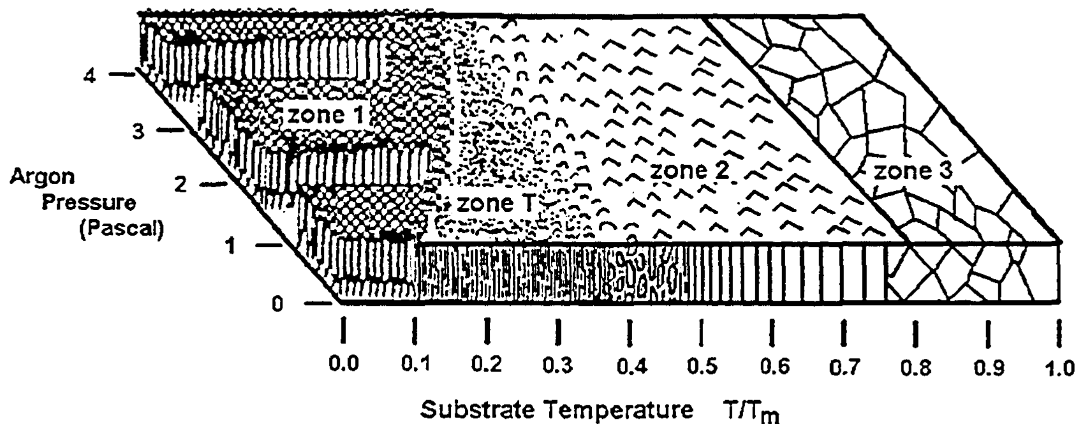

Figure 1.2: Thornton's Structure Zone Model. Graphic after Tait[2]

As the industrial and scientific world matures, new materials with advanced characteristics are continuously being developed. In particular, the last few years have witnessed vastly increased interest in nano-technology. Of specific interest here are nano-crystalline films, which are an aggregate of many crystals with dimensions of a few nano-meters across, typically 1 to 10 nm but sometimes up to 100 nm [3]. The unique atomic arrangement of these structures, where a large proportion of the atoms in each crystal resides on the surface rather than within the bulk, imbues unique qualities to the materials comprised of them[3]. For example, nanocrystalline silver-

Reproduced with permission of the copyright owner. Further reproduction prohibited without permission.

based films are being used as antimicrobial agents in treating infection in burn victims. These films are far more efficacious than conventional silver technologies such as silver sulfadiazine and silver nitrate. Figure 1.3 shows how this product (produced by Nucryst Pharmaceuticals, 10102-114 St., Fort Saskatchewan Alberta, and sold under the tradename Acticoat©) kills methecillin resistant *Staphlococcus aureus* (MRSA). This antibiotic resistant bacteria is a so called 'superbug' since it is difficult ot control and has serious and sometimes fatal effects on patients. The Acticoat© product reduces the population of this bacteria by a factor of 100,000 in half of an hour, far better than other silver treatments. Since this material is so promising, it is highly desireable to optimize the film characteristics responsible for its efficacy.

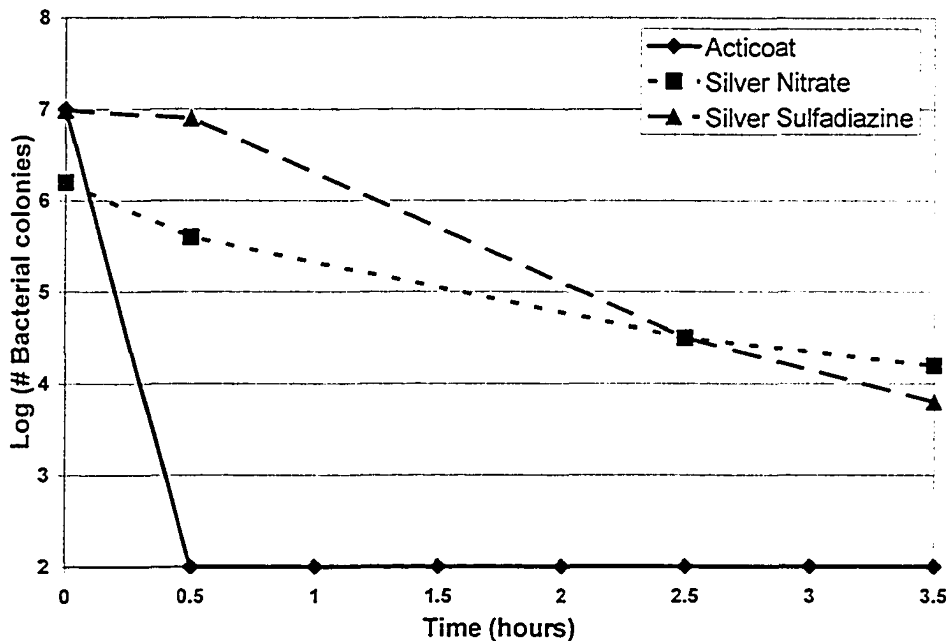

Figure 1.3 Log reduction of viable MRSA bacteria within a broth solution for Acticoat© and convential silver based treatments versus time.

There have been examples of other such materials being produced by magnetron sputtering[4,5,6,7] (which generates and utilizes a magnetically confined plasma to produce the ions which liberate atomic particles from a cathode) though it is poorly understood what, within the process, the relevant mechanisms are that lead to their formation[8]. For example, in addition to liberating material from the cathode

Reproduced with permission of the copyright owner. Further reproduction prohibited without permission.

that deposits on the substrate, the magnetron plasma can also generate a wide variety of charged, excited, energetic, or reactive particles, all of which may bombard the growing thin film. This then, can lead to a wide variety of physical and chemical processes at the growing film's surface, which in turn are relevant in establishing the morphological and chemical structure of the deposited material[9]. Models such as Thornton's do not account for these processes, and so a deeper understanding of such systems is necessary. As noted by Ivanov *et al*[10], there is a widespread belief that film growth kinetics can be strongly linked to the characteristics of the quasi-neutral plasma region within a magnetron. Therefore, to understand how this process results in the formation of unique films, the structure of the plasma must be understood first. The issue at hand was most eloquently put by Vlcek *et al*[11]:

> "The large scale application of non-equilibrium low-temperature plasma in various branches of science and technology requires complex experimental and theoretical study of physical and chemical processes occurring in plasmas. Thus, further development and improvement of experimental methods and diagnostics along with creation of new, realistic theoretical models are necessary to elucidate the phenomenon observed under various conditions in different types of plasmas.
>
> For purposes of practical application it is of key importance to understand the correlation between external process parameters (such as gas flow rates, gas composition, pressure, electrical power and frequency, magnitude direction and shape of external magnetic fields, substrate temperature and reactor geometry) and local plasma parameters (such as energies, densities, and fluxes of electrons and ions, neutral atoms and molecules) which actually govern the plasma processes and plasma-surface interactions."

To achieve this Vlcek[12] indicated the necessity of obtaining

> "...detailed information of internal plasma parameters, such as ion density, electron temperature and plasma and floating potentials...".

and Sheridan *et al*[13] commented:

> "Understanding electron transport in the sputtering magnetron is essential to understanding the operation of these devices."

Thus, research into the detailed dynamics within magnetron sputtering systems is a natural and requisite consequence resulting from the desire to create new advanced, effective materials. As a better understanding of plasma dynamics becomes available, advanced simulations can be developed, taking simulation from

Reproduced with permission of the copyright owner. Further reproduction prohibited without permission.

predominantly being a research tool to an engineering tool as well. For example, Bogearts *et al* developed a simulation of an analytical cell glow discharge[14], which was used to optimize the cell geometry, yielding better analytical sensitivity and performance. It is noted that simulations of such entities are just now becoming useful in engineering actual systems.

Magnetron sputtering, which is a specific implementation of the general sputtering process, has long been a workhorse in many industries for the deposition of thin films. It is a process that is relatively easy to use, which, coupled with its versatility, is why it enjoys the popularity that it does. For these reasons, and its apparent ability to produce unique films, magnetron sputtering is an excellent candidate for exploitation to that end. The goal, then, of this research, is to investigate the structure of the plasma within a magnetron sputtering system and to determine how that structure changes in response to process parameters such as pressure, gas type or mixture, and electrical current or power to the system.

Before the research at hand is described in detail, it will be necessary to present basic information on glow discharges, of which magnetron plasmas are a subclass. Then, enough detail of a magnetron sputtering system will be presented so that the reader can better appreciate the research undertaken thereafter. Glow discharges are described in §1.2, magnetrons in §1.3, and a forward perspective on the research undertaken in §1.4.

1.2 Glow Discharges

Typically a glowing or light emitting electrical discharge can be sustained between two electrodes provided the gas pressure, electrode geometry, and difference in electrical potential between the electrodes are chosen appropriately. Typical values are pressures of a few Torr (1 mTorr $\approx$ 7.5 Pa) with electrodes separated by a few centimetres with an electrical potential difference of a several hundred volts. When a negative potential is applied to one of the electrodes (cathode), a small population of electrons may be emitted either by thermionic (heating of an electron to higher energy so that it may overcome the potential barrier at the surface) or field emission

Reproduced with permission of the copyright owner. Further reproduction prohibited without permission.

(reduction of the potential barrier by an applied electric field so that electrons may tunnel out more easily) effects. These electrons are accelerated away from the cathode by the electric field and collide with neutrals creating even more electrons and ions through impact ionisation. The ions are accelerated in the electric field and eventually collide with the cathode where additional electrons (known as secondary electrons) are emitted. As a result an increasing number of electrons accelerate away from the cathode generating an increasing number of ions. This in turn results in a current through the cathode that continues to rise independent of voltage until the processes of electron impact ionisation, secondary electron liberation from the cathode, loss of electrons to the anode and loss of ions to the cathode are all in balance. Once this balance is achieved the discharge is known as a self sustaining glow discharge and qualifies as a plasma.

The general architecture of a glow discharge is shown in Fig. 1.4 below. Several distinct regions develop, each with unique luminosity, electrical, and density characteristics.

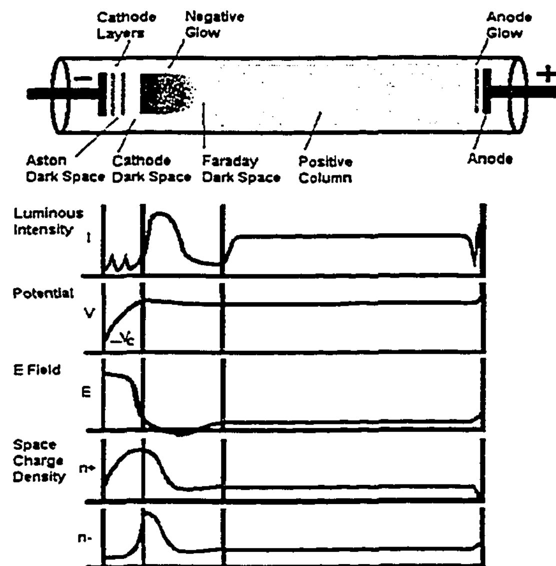

Figure 1.4: General architecture of a glow discharge, after Nasser[15].

Reproduced with permission of the copyright owner. Further reproduction prohibited without permission.

Obviously, the previous discussion does not account for the complexity observed in even a simple glow discharge, so the reader is referred to the abundant literature, Chapman[16], Manos and Flamm[17], and Cuomo and Rossnagel[18] being excellent examples. There are, however, three salient points from Chapman that should be observed:

1) The plasma does not take a potential intermediate between those of the electrodes, as it might be expected, the plasma is the most positive body in the discharge.
2) The electric fields are restricted to the electric sheaths at each of the electrodes. [In the magnetron, most of the applied potential difference is restricted to the cathode dark space.]
3) The sheath fields are such as to repel electrons trying to reach either electrode.

Glow discharges can be maintained in pretty much any gas, gas mixture or vapour, although, if the electrode separation is too small, or the gas pressure too low, then the number of ionisations per secondary electron will be too low to sustain the discharge. Alternately, if the electrode separation is too large, or the gas pressure too high, the ions created in the discharge will be decelerated by collisions or insufficiently accelerated by a weak electric field rendering the ion current to the cathode too low to liberate a sufficient population of secondary electrons from the cathode. It is worthy to note that the entire positive column can be eliminated by sufficiently reducing the electrode spacing, which is a typical arrangement in most magnetron sputtering systems. These systems usually exist with only two distinct regions, the negative glow and the cathode dark space (sheath region). Note that commonly used gases are Ne, Ar, Kr, or Xe, and sometimes He, although Ar is predominantly used in industry due to its low cost, widespread availability and good functional characteristics. Reactive sputtering, where compound films are reactively formed at the substrate, frequently uses oxygen, nitrogen or organic gases in addition to or, in some cases, exclusive of the commonly used noble gases.

1.3 Magnetrons

Magnetrons are simply glow discharges with the addition of a magnetic field. This magnetic field permits the discharge to be sustained at a much lower pressure

Reproduced with permission of the copyright owner. Further reproduction prohibited without permission.

(less than 10^{-3} Torr) than conventional glow discharges. As before, there are two basic processes that permit the discharge to be sustained: liberation of secondary electrons from the cathode and impact ionisation of gas atoms by the energetic secondary electrons. If the electrons do not ionise enough gas atoms, the plasma will not be sustained, so it is optimal if the electron exhausts a majority of its energy through ionising collisions. Ionisation efficiency is detrimentally affected if the electron finds its way to a vacuum chamber wall before exhausting its kinetic energy. Also, if a gas atom is ionised far from the cathode then there is a greater chance of the newly created ion being lost to a chamber wall (or anode) instead of finding its way to the edge of the cathode sheath. Only by reaching the edge of the cathode sheath can an ion be captured by the electric field there and drawn to the target resulting in a sputtering event and ejection of more secondary electrons. It is obviously better if the ionisation events all take place close to the cathode and that the energetic secondary electrons exhaust their energy through ionising collisions in this region. In a regular glow discharge this is accomplished by relatively high gas pressure (low electron mean free path), however, at low pressures this effect can be achieved by the addition of a magnetic field whose flux lines run mostly parallel to the cathode surface. This creates an electron trap, which extends the time an energetic electron spends near the cathode surface enhancing the probability of an ionisation event occurring there.

There are several different common implementations of the magnetic field for these devices, one of the most popular of which is the planar magnetron. In this case the magnetic field is generated by permanent magnets that are mounted behind a planar cathode in a pattern so as to form a magnetic trap for the electrons. (see figs. 1.5 and 1.6) Even though the magnetic field is primarily oriented parallel to the cathode surface, it is configured such that the **E** x **B** drift (see Chen[19] for a detailed description of this phenomenon) of the secondary electrons forms a closed loop. The closed loop prevents the secondary electrons drifting away from the vicinity of the cathode before exhausting the majority of their kinetic energy. This causes the ion density to be highest close to the cathode resulting in a high current, low voltage discharge (typically 500V and a few amps compared to ~2500V and a few hundred milli-amps for a non-magnetised discharge). This increase in current results in an

Reproduced with permission of the copyright owner. Further reproduction prohibited without permission.

increase in sputter rate and consequently an enhanced film deposition rate. This device is popular as a thin film deposition technique for its simplicity, ease of use, and ability to create high quality repeatable results. The plasma localization does cause nonuniform target usage with the creation of a 'racetrack' erosion profile. A simplified schematic of this device is shown in figures 1.5 and 1.6.

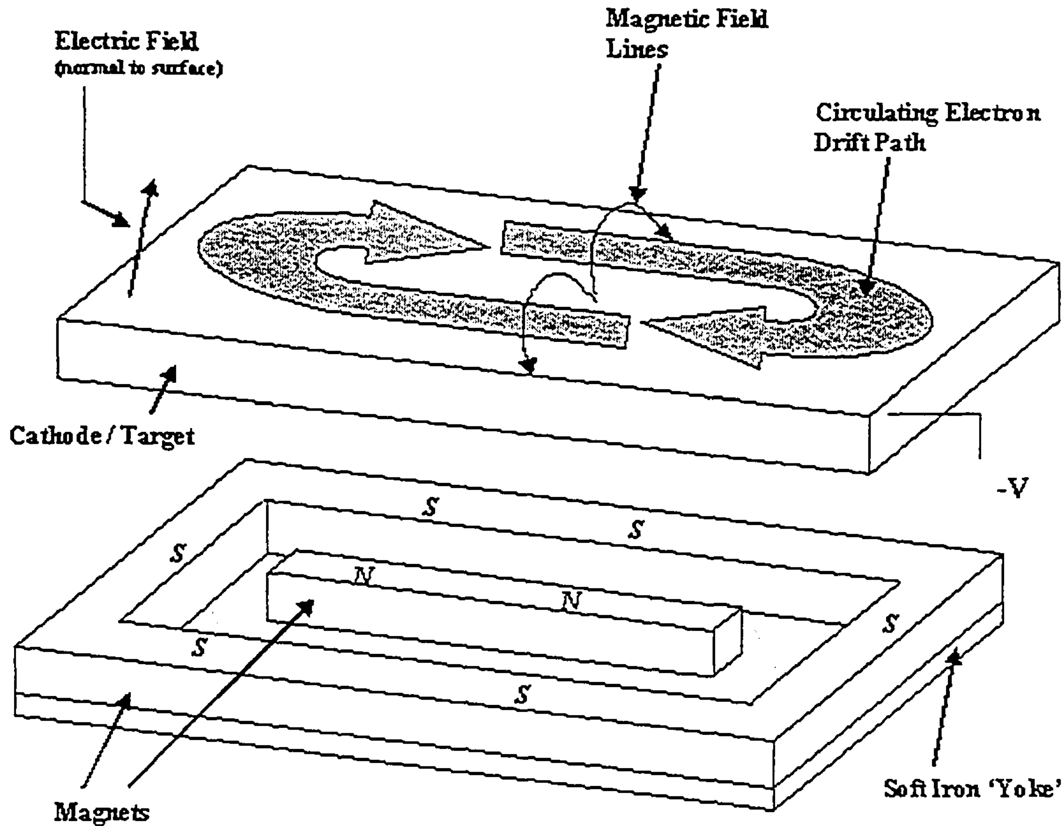

Figure 1.5: Exploded view of planar magnetron magnetic assembly and target. In practice the magnet assembly is placed below but in contact with the target. The electron drift path is indicated (after Mattox[20])

The positive ions that are incident on the cathode surface 'sputter' off a few atoms of cathode (target) material, provided the ion has enough kinetic energy. For a simple glow discharge at high pressure, these sputtered atoms undergo many collisions with gas atoms in a region very close to the cathode due to the small mean free path. This makes it quite likely that the sputtered atom will redeposit on the cathode nullifying any useful effect. At low pressures, such as in the case of a magnetron, the sputtered material will travel much farther between collisions and

Reproduced with permission of the copyright owner. Further reproduction prohibited without permission.

have a much higher probability of finding its way to another surface. So if the goal is to coat a substrate with target material, it is much more efficacious to do so at lower pressure, such as with a magnetron.

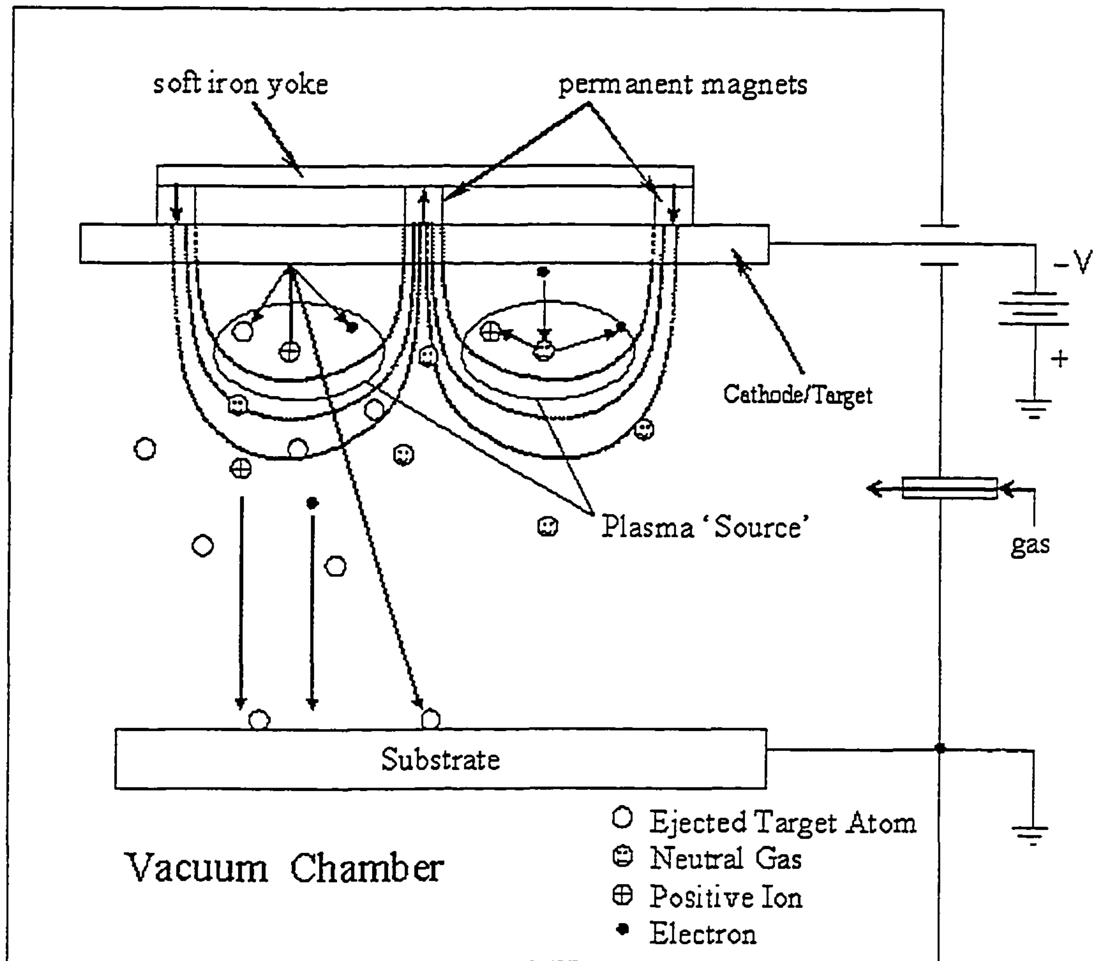

Figure 1.6: Basic magnetron sputtering system

Magnetron sputtering systems seem quite simple and elegant at first glance and while they are elegant in implementation, there appears a whole world of complexity as one probes deeper into their nature. It is appropriate, therefore, to define the context and limitations of the research to be undertaken here. This investigation is focused on plasma structure as it pertains to thin film growth dynamics. For a growing thin film, the important plasma characteristics are the densities and energy distributions of the electronic, ionic, atomic or molecular species

Reproduced with permission of the copyright owner. Further reproduction prohibited without permission.

that impinge on the growing film. Of lesser importance here, though not of insignificant interest, are the dynamic processes within the plasma environment. These dynamic processes are many and the identification of them can be an extremely protracted process, far beyond the scope of this study. Hence, dynamic processes will be dealt with only when it is necessary or appropriate to do so in the context of the forthcoming investigation. The focus, therefore, is on the plasma structure within the reactor and not on the dynamic processes that result in that structure. Having said this, it is still instructive to convey to the reader a brief summary of some of the dynamic processes that may or may not occur within the plasma environment.

The dynamic complexity of the plasma can be divided into two main types of processes', transport processes and collisional processes, which are inextricably linked. 'Collisional processes' refers, of course, to the ionisation and sputter processes, but also to a large number of other events. Aside from ionisation (i) there generally is, for a given atom, the potential for processes such as electron-ion recombination (ii), excitation (iii), de-excitation (iv), electron attachment (v), and electron detachment (vi). Each of these general processes may arise through a variety of means. For example, an ionisation event may be the result of:

Note: X* refers to an atom X in an excited state

a) $A + e \rightarrow A^+ + 2e$	electron impact ionisation
b) $A + e \rightarrow A^* + e \rightarrow \ldots \rightarrow A^+ + 2e$	cumulative ionisation
c) $A + B^* \rightarrow A^+ + B + e$	Penning ionisation
d) $A^* + B^* \rightarrow A^+ + B + e$	excited particle collisions
e) $A + h\nu \rightarrow A^+ + e$	photo-ionisation
f) $A^+ + B \rightarrow A + B^+$	charge transfer

The other general processes can be equally diverse. It is not particularly helpful at this point to detail all of these processes so the reader is encouraged to examine the abundant literature available on the topic, most appropriately Chapman[16].

In the case of molecular species, more types of general processes are possible, including atomic or molecular association to form a new molecule (vii), dissociation

Reproduced with permission of the copyright owner. Further reproduction prohibited without permission.

of a molecule into atoms or sub molecules (viii) and even 'mixture' processes involving (vii) or (viii) and potentially any of (i) through (vi). Additionally, new possibilities arise for excitational states since non-monoatomic gases may be rotationally or vibrationally excited.

It is worth noting that the predominant inelastic process remains electron impact ionisation and excitation. The recombination processes typically have a very low probability since a third body must be present to ensure both energy and momentum are conserved in the process[16]. Thus ionisation is generally common but recombination is not. This means that ions and electrons usually leave the system via the chamber walls, the electrodes, and the substrate. This implies that the substrate may be heavily bombarded by charged particles in addition to neutral materials. Radiative recombination, where a released photon acts as the third body may still be a factor)

The local density and energy distributions of plasma species will, of course, depend on the dynamic balance of the collisional processes but also on the balanced state achieved between these processes and the 'transport processes'. 'Transport processes' refers to the method by which any particle, charge, or energy is transported from one region in the system to another region, such as from the target to the substrate. Neutral particles are not generally subject to any subtle or unexpected transport mechanisms. Depending on which pressure regime they are in, their motion is governed by collisions with other particles (low mean free path (mfp) so fluid dynamics and diffusion dominate) or collisions with the reactor walls (very long mfp so ballistic transport dominates). For charged species such as electrons and atomic or molecular ions in the presence of electric and magnetic fields, the transport processes can be varied and exotic.

When regarded as individual particles charged particles are subject to the influence of the electric and magnetic fields within the plasma. Since the charged particles will gain or lose enrgy from the electric field these charged particles will be prone to varying influences by the magnetic field through the Lorentz force. The magnetic field in itself may possess significant curvature or gradients, which will

Reproduced with permission of the copyright owner. Further reproduction prohibited without permission.

create drifts in particle trajectories. Even in a normal **E** and **B** field there will be a drift velocity in the **E** x **B** direction.

When regarding plasmas as fluidic entities, new drift mechanisms are observed, one example being diamagnetic drift. Here, there is a net drift in a direction perpendicular to a density gradient and the magnetic field even though individual particles do not themselves drift (see Chen[19] page 71). The presence of an electric or magnetic field may also alter the diffusion characteristics of charged particles, although by different mechanisms as each field applies forces to the particle in different ways. Additionally, anomalously enhanced diffusion across magnetic field lines has been observed and is described by the semi-empirically derived Bohm diffusion, which is still poorly understood, although frequently attributed to turbulent transport effects. Ambipolar diffusion results when positive and negative species diffuse together. As the more mobile of the two species leaves behind a charge of the opposite sign, an electric field builds up, enhancing the diffusivity of the slower species and reducing that of the more mobile species. As a result they tend to diffuse together at a rate primarily determined by the slower of the two species[19].

In addition to particle transport processes one may also regard the energy transport aspect of the plasma. Certainly energy is carried by individual particles and part of this investigation is to determine the energy distribution of those particles since this is likely important to growing film characteristics. However, energy can also be transported by other means such as wave phenomena, acoustic waves, electromagnetic waves and waves due to oscillatory charged particle motions. Waves are likely more common in an rf system where they are intentionally introduced, as opposed to a DC system where they are not. Any wave phenomena in a DC plasma reactor would have to be spontaneously created. Wave phenomenon and radiation may have implications for the growth mechanisms of a thin film.

A magnetron plasma is rife with potentially interesting phenomena not immediately obvious by its apparent simplicity. It is invaluable to dissect such a contrivance to understand the inherent structure and predominating collisional and transport processes. Unfortunately, it is unreasonable to expect to do all of this within the context of such an investigation as this. The most immediately useful goal then, is

Reproduced with permission of the copyright owner. Further reproduction prohibited without permission.

to determine the spatial structure in terms of the density and energy distribution of plasma phase species and their response to process conditions such as pressure, cathode current and gas atmosphere. This information will likely give rise to many more questions regarding plasma dynamics, which can be investigated by future research programs. At the same time these results will be useful in studying the formation of advanced thin films. Part of this research will be to develop a simulation package that will be an appropriate tool for investigations into the dynamic plasma processes, the plasma structure, and film formation.

1.4 Experimental Program

For this research, simulation will be used as a tool to complement the experimental findings of an electrostatic or Langmuir probe.

A Langmuir probe (LP) provides absolute plasma (electron and ion) densities, electron energy distributions (temperatures), plasma potential and floating potential, but does not provide relative ion densities or ion temperature. Interpreting LP data is known to be difficult, so computer simulation is a valuable comparison for experimental methods.

The value of simulation goes far beyond this since its very nature is amenable to investigating specific processes within a plasma. For example, within a simulation it is easy to exclude or include excitation collisions between electrons and ground state gas species thereby specifically evaluating the effect of this process on the overall plasma structure. There is no way to do this in an experimental situation.

A basic introduction to each of these techniques is provided here for the readers benefit but the details of theory and operation are left to dedicated chapters.

1.4.1 Langmuir Probe

As a preamble to Langmuir Probes, it will be useful to briefly describe the basic interaction of solid materials and plasmas. In a plasma, the electron density and ion density are roughly equal (quasi-neutrality condition for plasmas) and, if the

Reproduced with permission of the copyright owner. Further reproduction prohibited without permission.

electrons and ions are in thermal equilibrium, the average speed of the electrons will be enormous (~ 270 times) compared to the average speed of the ions due to the discrepancy in mass. If an electrically isolated conducting substrate is suspended in the plasma, it will initially be bombarded by electron and ion fluxes. Since the average electron speed is much higher, the electron flux to the substrate will be higher due to the roughly equal number densities. Thus, the substrate begins to build up a negative charge repelling subsequent electrons and attracting ions. The negative charge will build on the substrate until the electron flux equals the ion flux. The electrical potential on the substrate at this point is known as the *floating potential* and occurs when the net current to the isolated substrate is exactly zero. Since electrons are repelled by the substrate potential, it follows that the substrate will acquire a net positive charge around it. This region, which differs from the undisturbed plasma, is known as the *plasma sheath region* or *sheath*. Outside this region (typically less than 1 mm from the substrate for magnetrons) the plasma is essentially undisturbed.

A Langmuir probe (LP) is a small metal probe that can be held at any desired potential while the current through the probe is monitored. The small size of the probe and the ability to locate it almost anywhere within the plasma gives it fine spatial resolution. Primarily, it will indicate the absolute densities of positive and negative particles but will not distinguish between different types of positive ions or negative ions. There are detailed sources of literature on the theory and practical use of LPs, including Chen[21], Laframboise[22], Swift and Schwarr[23], Herskowitz[24] and many others.

Figure 1.7 shows an illustrative current-voltage response, a *probe characteristic (or characteristic or trace)*, for an LP. There are three distinct regions. The first region (A) is where the probe potential is highly negative and thus repels all electrons. The current in this region is due exclusively to positive ions and is rather small, since, for equal concentration of electrons and ions, the latter have a much smaller velocity and therefore a much lower flux. As the probe voltage is ramped upward, it eventually is not sufficient to repel all of the electrons, and the more energetic ones will reach the probe and contribute to the current (region B). As the potential continues to rise, the current goes from ion dominated to electron dominated

Reproduced with permission of the copyright owner. Further reproduction prohibited without permission.

with the switchover occurring when the current is exactly zero. The corresponding voltage is the previously mentioned floating potential. By further raising the probe potential, more and more electrons are able to impinge on the probe and the current continues to rise. Eventually the probe obtains a potential where the sheath is essentially absent[21]. At this point the potential on the probe represents the *plasma potential*, which is the potential of the undisturbed plasma. Continuing to raise the probe potential (region C) causes an electron sheath to form while the ions are completely repelled. In this region, known as *electron saturation*, all electrons incident on the probe sheath are collected. Increases in current with voltage are due to increases in the sheath size so that electrons are sampled from a greater area.

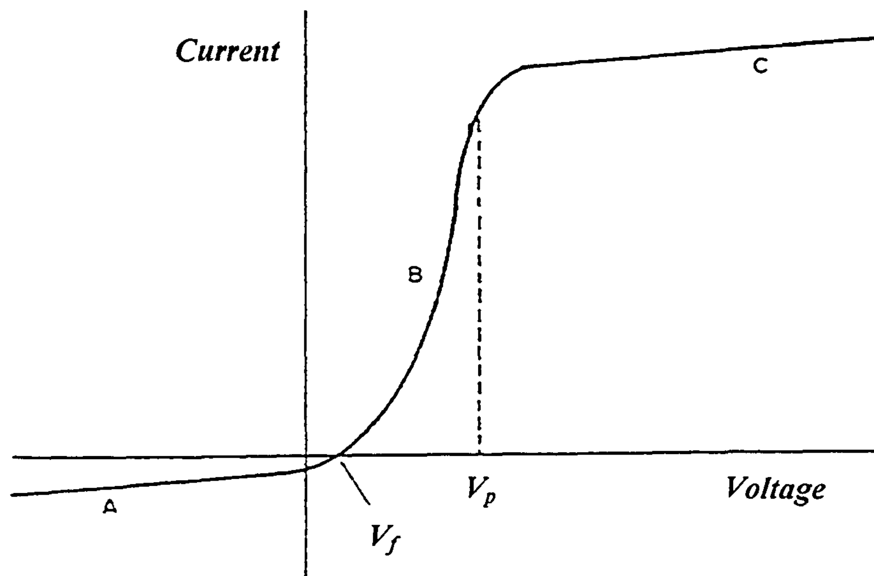

Figure 1.7: A classic probe characteristic.

Unfortunately, LP's are not this simple in reality. To determine how the probe current represents the charged particle densities, it is necessary to fully understand how the charged particles are collected. As it turns out, the collected ions/electrons are approximately those that impinge on the interface between the plasma and the plasma sheath surrounding the probe, so it is necessary to know what the size and shape of this sheath are. This will depend mostly on the plasma density but also on the probe's potential, since the sheath changes size as the potential changes. A further unfortunate condition is that the transition from plasma to sheath is not abrupt; it is, in

Reproduced with permission of the copyright owner. Further reproduction prohibited without permission.

fact, smooth and occurs over some space. Additionally, effects such as particle collisions (for dense plasmas), flowing plasmas and magnetic field effects on the particles must be taken into account when appropriate. These issues will be discussed in more detail in Chapter 3 as deemed necessary. For a more general discussion the reader is again referred to Chen[21], Swift and Schwarr[23], and Herskowitz[24].

1.4.2 Simulation

Recent years have seen increasing reliance on simulation as a means of investigating plasma state devices. Simulations are capable of accurately capturing the salient dynamic processes within plasmas[25,26], are showing potential as engineering tools[27], and can provide data that is otherwise difficult to obtain. For example, by following the life history of a series of energetic particles, one can determine the spatially dependant ionization (or ion creation) rates and average number of ionization events per energetic particle. This is easy to do in a simulation but exceedingly difficult experimentally.

There are several different approaches to modeling plasmas, although there are basically three types of techniques reported in plasma physics literature[25]: fluid models, Monte-Carlo models, and kinetic models.

Fluid models regard the plasma species as continua in equilibrium with the electric field and magnetic field structure. They are modeled using conservation law-based continuity equations and flux equations that consider both diffusion and drift in the electric and magnetic field. Such models cannot account well for non-equilibrium species (such as energetic electrons) which are present in magnetron systems. Since fluid models deal only on the macroscopic level, they tend to produce results quickly but are approximate[25].

Monte Carlo models simulate the behavior of each particle explicitly. Particles are simulated one after another based on Newton's laws and random collision (or other interaction) events. A large number of such particles are tracked providing a statistically meaningful picture of the discharge. The results of MC simulations do not depend on or make assumptions about the energy or state of the species it is

Reproduced with permission of the copyright owner. Further reproduction prohibited without permission.

simulating. Since MC simulations deal on the microscopic level they produce accurate results but are quite slow given the vast number of particles they need to simulate. Thus, MC models are well suited for simulating the non-equilibrium particles that fluid models cannot deal with.

Kinetic or Boltzmann models treat the plasma species as distribution functions in energies and in space. They track a large number of 'macro-particles' (which are representative of the entire discharge) using Newton's laws and usually run iteratively with an electric field solver so that a self-consistent solution emerges. These simulation types do not make assumptions about a particles equilibrium status and thus can simulate both equilibrium and non-equilibrium particle at once. However, they do simulate a large number of particles over many iterative cycles and thus convergence may be difficult to obtain for models of the required complexity[28], requiring a long solution time. To reduce computation time, fewer macro-particles may be simulated or a shorter solution time specified but this often results in 'noisy' output. The Particle-in-Cell (PIC) technique is commonly used as a kinetic simulation model.

Hybrid models are becoming increasingly utilized as researchers attempt to exploit the strengths of the various techniques as well as overcome their weaknesses. A popular hybrid model is the MC-fluid model which attempts to gain the accuracy of the MC model for non-equilibrium particles but solves rapidly for the equilibrium particles using the fluid model.

Historically, several groups have been involved in dc diode and magnetron plasmas. Sheridan[27,29,30] *et al*, and Nanbu[31] *et al* used 3-D MC models to simulate energetic plasma species in a magnetron. Ido[32] *et al* also produced a 3-D MC model in a magnetron system. Other purely MC models included simulations of non-magnetron, dc glow discharges. 1-D models were completed by Carman[33], and 3-D models by Li[34,35] *et al*, Razdan[36] *et al* and Bogaerts[37] *et al*. Other examples include Beouf[38] *et al* and Sun[39] *et al*.

Kinetic models have been used fairly extensively. PIC simulations have been used in magnetron systems by Shon[40,41,42] *et al* (2-D and 3-D models) and by van der

Reproduced with permission of the copyright owner. Further reproduction prohibited without permission.

Straaten[43,44] *et al* (1-D). Nanbu[28,45,46,47,48,49,50,51] *et al* have made extensive use of this technique to investigate magnetrons in both 2 and 3 dimensions.

While purely fluid or continuum models in such systems are not too common, a 2-D diffusion model has been used by van Straaten[52] *et al* in a glow discharge and a 2-D purely fluid model by Bukowski[53] *et al* in an Inductively Coupled Plasma (ICP) system. Costin[54] *et al* used a 2-D fluid model for dc magnetrons.

Finally, one important method for simulation of magnetrons and glow discharges has been the hybrid models, which have gone from very simple models only a dozen years ago to much more sophisticated models recently. Surendra[55] *et al* combined fluid and MC models in a 1-D simulation of a diode glow discharge. Boeuf[56] *et al* also simulated a diode glow discharge but in 2 dimensions. Shidoji[57,58,59,60,61] *et al* recently developed 2-D MC-fluid models for magnetron sputtering systems. One of the larger bodies of work comes from Bogearts *et al* who began with purely MC models[37] but soon coupled 1-D fluid models with 3-D MC models[62,63] and then extended this to a 2-D fluid, 3-D MC model[25,64,65,66,67,68,69]. While Bogaerts focus was on analytical glow discharge cells, as a body of work it is a good reference and demonstrated well the ability of such methods to exploit the strengths of each model in hybrid schemes.

The immediate goal of the simulation work carried out here is to develop a Monte Carlo (MC) simulation module for tracking energetic plasma species. A MC simulator will generally randomly sample physical events based on the most probable outcomes. For example, if an energetic particle collides with an atom, there is a finite probability that atom will be ionized. This probability depends on the species of the two particles and their relative kinetic energy. Within the simulation, any time two such particles collide, ionization events will randomly occur based on that probability. By keeping statistics on where and when such events occur a macroscopic picture of the system can be obtained. Here the MC module will be used to track energetic (or 'fast') electrons (which sustain the plasma) from creation through removal. A fast electron is 'born' by emission from the cathode or through an ionization event within the sheath. In either case, the new electron gains a significant amount of energy from the electric field within the sheath and becomes energetic. It is

Reproduced with permission of the copyright owner. Further reproduction prohibited without permission.

considered lost when it strikes a wall or when its energy falls under an energetic threshold below which it is considered thermalized. By doing this, one can build a statistical spatial model of fast electron density, creation rate of positive ions, creation rate of thermalized electrons, and electron energy distribution functions (EEDF). The fast electron density and EEDF information can be compared to data provided by the LP. While MC models have been implemented in investigating magnetron plasmas before, the model here is unique in that it obtains a portion of the EEDF. It will be used here to investigate parameters not specifically addressed by other simulations, such as the influence of target voltage on fast electron density.

While such a simulation module serves the immediate purpose, it must also serve as a step towards the greater goal of understanding the important overall physics of magnetron systems and film formation and, eventually, serve as a tool to engineer advanced materials. This means the MC plasma code must comprise one portion of a comprehensive 3-D simulation encapsulating all the relevant physics within magnetrons. Such a simulation would enable examination of the effects of reactor variables such as magnetic field, gas pressure, cathode current, reactive gases, substrate biases, etc. on film structures (on all scales from nano to macro), film chemistry and substrate coverage. While various simulation types have been used to investigate glow discharges and magnetron systems, there is not currently a truly comprehensive 3-D magnetron sputtering model. Current simulators tend to focus on individual aspects of the overall complex problem.

As examples, models by Motohiro[70], Turner[71], Dew[72], Kadlec[73], and others[74,75,76] dealt exclusively with neutral particle gas scattering and transport, though neglected gas flow, gas heating from the plasma, and the plasma component in general. In some cases gas heating and density variations were neglected altogether[27,70,71]. As already discussed, several research groups have developed plasma models. However, those models neglected either magnetic fields, neutral gas heating or sputtered particle transport. Given the strong coupling between the plasma, gas density, particle transport and target interactions, and given the strong dependence of film properties on all of these factors, it will be impossible to obtain an accurate film growth model without a complete magnetron sputtering system

Reproduced with permission of the copyright owner. Further reproduction prohibited without permission.

simulator. Provided in the next section, although outside the scope of this report, is a description of the overall design for such a simulation package (called SPUDII) providing greater context for the MC plasma model. The reader may omit this section without loss of continuity.

The remainder of this thesis is arranged in four chapters. Chapter 2 provides a description of the experimental magnetron sputtering chamber and the LP device. Chapter 3 discusses the relevant LP theory and methods used to obtain meaningful experimental data, as well as a discussion of those results. Chapter 4 details the MC simulation algorithm and provides simulation results and discussion. Finally, chapter 5 briefly reviews chapters 3 and 4.

1.4.2.1 SPUDII Simulation Overview

In order to incorporate all of the important effects into a comprehensive model, there will be four basic modules; PLASPUD, TARGSPUD, GROFILMS, and THERMSPUD (shown in figure 1.8). These modules will be capable of running independently, when appropriate, but will realize much greater capabilities when integrated into a whole. PLASPUD (PLASma SPUtter Deposition) is the module responsible for all issues related to the sputtering plasma, including plasma generation, plasma species densities and energy distributions, and plasma species angular distributed fluxes to the target and substrate. It also must calculate local electric potentials and fields. TARGSPUD (TARGet SPUtter Deposition) is the module responsible for providing flux, energy and angular distribution of sputtered particles from the target as well as creation of secondary electrons and energetic neutral particles. Essentially, this module generates particle emissions based on neutral and plasma particle interactions with the target. THERMSPUD (THERMal SPUtter Deposition) is responsible for all neutral gas species and their localized density and energy distributions. As such, it must track neutral gas rarefaction due to heating effects and transport of neutral particles from target to substrate.

Reproduced with permission of the copyright owner. Further reproduction prohibited without permission.

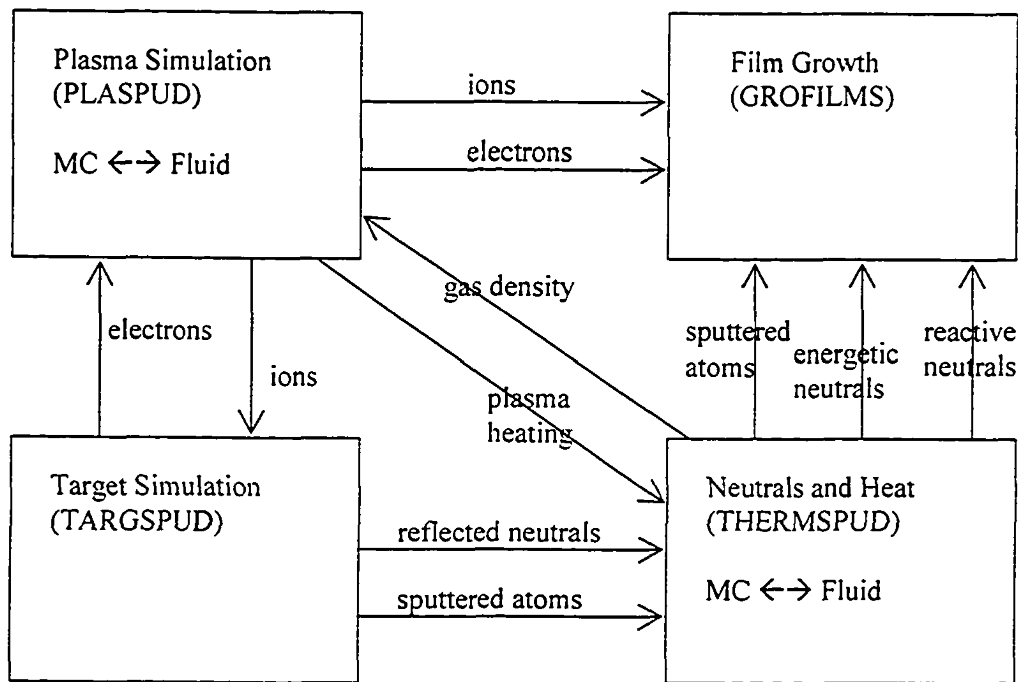

Figure 1.8: Modular composition of SpudII project with interaction of various modules indicated. After Dew[77].

All modules will rely on input from each other. For example, the emitted flux of sputtered particles calculated by TARGSPUD will rely heavily on the flux of ions to the target supplied by PLASPUD. To do this accurately, PLASPUD requires local gas densities provided by THERMSPUD. However, THERMSPUD can only determine local gas density by tracking sputtered particle energy deposition into the background gas. This requires an accurate sputtered particle emission model from TARGSPUD. Obviously, an iterative solution algorithm is needed. These modules will iterate sequentially until convergence and the steady state results will provide the GROFILMS (GRain Oriented FILm Microstructure Simulator) module the densities, fluxes and energy distributions of species bombarding the growing film in order to predict film nano-structure.

Each module is described in more detail below along with a description of required input from other modules and output provided.

Reproduced with permission of the copyright owner. Further reproduction prohibited without permission.

TARGSPUD[77]

An accurate model of the events taking place at the target is necessary for systems such as a magnetron. There are, strictly speaking, analytical models that predict flux, energy and angular distributions of sputtered particles. However, these models are usually only valid for ion energies higher that normally observed in magnetrons and, as a result, deviations from the models can be observed for such systems[78]. One potential approach is a Monte Carlo model similar to that used by Yamamura[78] which has success in accurately predicting sputter yield and emission characteristics as a function of incident ion energy and angle.

The TARGSPUD module uses as input:

- the flux, energy and angular distribution of incident energetic ions and electrons (from PLASPUD), and
- the flux, energy, and angular distribution of energetic neutral particles (from THERMSPUD).

As output it provides:

- the flux, energy, and angular distribution of sputtered atoms,
- the flux, energy, and angular distribution of emitted secondary electrons,
- reflection probability of electrons and ions incident on the target, and
- the flux energy, and angular distribution of reflected energetic neutral particles.

  The output of this module is used by PLASPUD (charge particle output) and THERMSPUD (neutral particle output).

THERMSPUD

The THERMSPUD module will deal with transport of sputtered atoms from the target to the substrate and is primarily designed to deal with effects of collisions with intervening gas atoms or molecules. The density of these gas particles will determine how much of the sputtered atom's energy or momentum is transferred to the gas and how much remains with the atom when it condenses on the substrate.

Reproduced with permission of the copyright owner. Further reproduction prohibited without permission.

Heating of the gas can cause density and temperature inhomogeneities and may significantly alter the energy distributions of particles incident on the substrate as well as affect plasma generation and dynamics. Essentially, THERMSPUD operates in two-stage or hybrid fashion. The first part will track neutral energetic particles such as reflected neutrals and sputtered atoms. Both types of 'primary' particles are tracked from the target surface, and collisions with gas particles are recorded until the primary is incident on a wall or substrate or until it is considered to be in thermal equilibrium with its surroundings. The location and amount of energy transferred to a background gas atom in any collision is recorded and, after many sputtered particles are tracked, a statistically representative spatial distribution of energy deposition into the neutral background gas can be obtained. Particle and net energy deposition onto the substrate will also be tracked. Serikov[46] showed that gas heating by plasma-neutral species interactions can also be significant and is thus also included in a similar manner. The deposited energy onto the background gas is collected by a spatial grid and a second-stage fluid model is used to calculate new temperatures and pressures (and thus densities) in each grid cell for all equilibrium neutral species.

The THERMSPUD module uses as input:

- flux, energy and angular distribution of sputtered atoms and reflected neutrals (from TARGSPUD), and
- spatial distribution of collisional energy transfer from plasma species to neutral species (from PLASPUD).

As output it provides:

- spatial distribution of density and temperature for all thermalized neutral species including sputtered atoms and background gas,
- spatial density distribution of non-thermalized sputtered atoms and other energetic neutrals,
- the flux of thermalized and energetic neutrals to the target and other chamber features,

Reproduced with permission of the copyright owner. Further reproduction prohibited without permission.

- the flux, energy, momentum and angular distribution of all neutral species, including excited or reactive species, incident on the substrate.

PLASPUD

The PLASPUD module deals with the generation, transport, loss, density, energy and flux of all charged particle species. To accomplish this, PLASPUD uses a hybrid approach similar to that used by THERMSPUD, although necessarily more complex due to coupling with the electric and magnetic fields. A MC model is used for energetic (non-equilibrium) plasma particles and a fluid model for thermalized ones. This is similar to the approach used by Bogaerts[65] though includes effects from magnetic fields and eventually gas rarefaction. Gas rarefaction appears to be important but does not seem to have been included in any magnetron plasma models.

Monte Carlo methods track many individual particles and is thus able to build a statistical picture of the discharge. This is accomplished by moving the representative particle according to relevant physical principles and using a set of probability distributions to determine what types of processes the particle undergoes. These probabilities represent the likelihood of collision events occurring with any of the species in the system. Also, the type of collision event (elastic, ionization, excitation, etc.) is considered. When a collision does occur, energy loss of the particle, energy transfer to the struck species, and new species creation events are recorded. This method is quite accurate but also is computationally intensive, involving large solution times to track the large number of particles needed for statistical convergence. The method is not good for tracking low energy particles since they move very slowly about the simulation space, increasing the simulation time immensely. Typically, this method relies on assumed or otherwise provided (for example, from a fluid model) electric potential and electric field distributions. This is because it would be far too computationally intensive to track sufficient numbers of low energy particles to obtain a complete density profile of all the charged species. Thus, MC simulations cannot practically provide electrical potential or field information. What they do provide, quite accurately, is the spatial distribution of

Reproduced with permission of the copyright owner. Further reproduction prohibited without permission.

ionization, excitation and other collisional events. They also supply the density of the tracked energetic species and can be used to obtain energy distribution information.

Fluid models treat the plasma species as individual fluids moving in response to electric and magnetic fields taking into consideration complications such as collisions with neutral species. All of these factors influence the diffusion and drift characteristics of plasma species dictating where and how they move. However, these models assume thermalized electron and ion populations and thus cannot account for the motion, density or unique effects from energetic plasma species such as high energy electrons. It therefore, is very limited in predicting ionization and excitation rates. In the fluid model, the distribution of the electric potential, electric field and of the various species densities is solved simultaneously eventually converging to a steady state. To solve for electric potential (and then electric field) this model also requires densities of all energetic charged species which is provided by a MC model.

Hybridization brings the two complementary models together using a fluid model for low energy, thermalized, particles and a MC model for high energy particles. The MC model will generate a spatial distribution of high energy particles and creation rates of low energy particles (through collisional events etc.) based on assumed electric fields and potentials. Upon convergence, the fluid model will use these distributions and rates to solve and generate a total particle distribution profile and new electric potential and field distributions. The MC model will run again with the new electric field and then the fluid model again. This iterative procedure continues until convergence to a self consistent solution where creation rates of all species, loss rates (diffusion to walls etc.), charged particle density profiles, electric fields, and electric potentials are all in a steady state. For the purpose of the overall proposed simulation, the hybrid method using both MC and fluid models is implemented with the intent of minimizing solution time, retaining accuracy, and providing self–consistency. The particle-fluid method is also compatible with the methodology used in THERMSPUD and is easily extensible in terms of adding new chemical and physical processes and new species types.

For the immediate purpose related to this research, the MC model is used exclusively. This module is referred to as Plaspud1 where Plaspud2 is the fluid

Reproduced with permission of the copyright owner. Further reproduction prohibited without permission.

module and the combination of the two comprises PLASPUD. The development and application of Plaspud1 is a major contribution of this thesis. Chapter 4 will further discuss plasma simulations and detail Plaspud1, providing better context with respect to the overall simulation.

The PLASPUD module uses as input:

- electrical potential boundary conditions on target and chamber walls,
- neutral gas density and temperature distribution (from THERMSPUD), and
- secondary electrons generated from the target (from TARGSPUD).

As output it provides:

- ion flux, energy and angular distribution to all walls, substrates and targets (TARGSPUD),
- electron flux and energy to all walls, substrates and targets,
- transfer rates of energy to neutral gas species from energetic and thermalized plasma species,
- densities of all plasma species,
- densities of energetic plasma species,
- creation rates for ions, electrons, excited atoms, and meta-stable atoms,
- electrical potential and fields,
- some energy distribution functions for energetic electrons, and
- net electrical current to the target.

GROFILMS

The current GROFILMS[79,80,81] module essentially operates by tracking angular fluxes of macro-particles to a substrate surface, allowing them to stick or reflect based on reaction probabilities and once stuck, allowing them to 'relax' into a local low energy state on the surface. The simulator has been very successful in predicting film coverage, microstructure, density, compositional variations and roughness for various processes including sputtering, evaporation, and CVD[77]. While

Reproduced with permission of the copyright owner. Further reproduction prohibited without permission.

it has been successful it does not predict crystallinity, nano-structure, or take into account many features provided by a detailed reactor model. Thus, GROFILMS will need extensions to accommodate the additional information provided by the other modules. This includes modeling effects of energetic neutral and ion bombardment, including angular incidence dependence of reaction probabilities for energetic particles, parallel momentum effects on surface diffusion, a more complete heating model, and effects of reactive or ionic particle deposition on film chemistry and structure.

At energies above ~15 eV, the probability of an incident particle reflecting off a surface is angular dependant[82] where a normally incident particle tends to stick and oblique angle incidents tend to reflect. SPUDII will more carefully determine the angular and energy dependant fluxes of such particles, an effect that can be incorporated into GROFILMS.

The parallel momentum effect refers to a tendency of depositing atoms to diffuse anisotropically along a surface in a direction parallel to the incident momentum as provided by bombarding particles. The heating effect must allow for a time varying temperature when calculating thermally dependant rate (chemical, etc.) factors for film growth. Both of these effects can be accounted for with the more detailed reactor model.

Effects from incident reactive or ionic particles can also be incorporated along with many other processes. The reader is referred to Mattox[9] for an excellent overview of these.

The GROFILMS module will use as input:

- the flux, angular distribution, and energy of all ionic species and electrons incident on the substrate (from PLASPUD)
- the flux, angular distribution, and energy of sputtered atoms, energetic neutrals, and reactive neutrals on the substrate (from THERMSPUD).

As output it provides a detailed prediction of films characteristics including:

- crystallinity,

Reproduced with permission of the copyright owner. Further reproduction prohibited without permission.

- chemical composition,
- compositional variations,
- structure on the nano scale,
- coverage,
- density, and
- compositional variations from nano- to micro- scale.

With the ever increasing capacity in computing power available to researchers, especially affordable power in the form of 'off the shelf' personal computers (PC's), simulations of complex entities such as plasmas is becoming much more practical. The widespread availability of PC's also makes them a desirable platform for simulating plasmas of industrial interest since any business can easily afford one and can take advantage of the simulation tool. As such the entire simulation package, SPUDII, is designed to run on a PC platform.

1.4.2.2 Collaborative Development of the SPUDII project.

The development of the SPUDII project is a collaborative effort with the different parts contributed by various individuals or groups. PLASPUD1, the MC plasma algorithm, was designed, written, and integrated into SPUDII by Field (this author). Only this module is used for simulations within this thesis. PLASPUD2, the plasma fluid module is by to Shao, Li, and Dew, TARGSPUD is by Stepanova and Liu, THERMSPUD is by Jimenez, Leonard, and Dew, and GROFILMS is by Friedrich and Dew. The SPUDII architecture is by Leonard, Beatty, and Dew.

Reproduced with permission of the copyright owner. Further reproduction prohibited without permission.

Chapter 2: Experimental Equipment

2.1 The ARGO

The experimental portion of this research is carried out in a vacuum chamber (figure 2.1) referred to as the ARGO[1] since it was designed to sputter with ARGon and Oxygen. The ARGO is a 304 stainless steel cylindrical shell with a 62.0 cm ID and a 24.1 cm depth, oriented such that the cylinder's axis is horizontal. Through one end of the chamber are fed the Langmuir Probe and process gases inlet tube. The pressure gauges are mounted on this end of the chamber (figure 2.1.b) and there is included a feed-through port for future installation of a Plasma Sampling Mass Spectrometer (PSMS). The other end of the chamber has a 25.4 x 38.1 cm hole cut through it to accommodate a water-cooled aluminum magnetron head (figure 2.1.c). The head is electrically isolated from the chamber by means of an o-ring fitted Teflon spacer which also ensures the integrity of the vacuum. Within the magnetron head (atmosphere side of chamber) is mounted a magnet assembly (figure 2.2) which can be laterally translated up to 9 cm from center in either direction.

The magnet assembly (12.5 cm width x 17.5 cm height) consists of a 4 mm thick soft iron plate on which are mounted a series of thirteen 3.0 x 1.0 x 0.5 cm NeFeB magnets. It is mounted lengthwise vertical. Spatial surveys with the LP are performed in a plane halfway up the assembly's height (at 8.75 cm). The magnetic field generated by this assembly is presented as a vector plot in figure 2.3. This plot was created using data from Gemini 1.01 Electromagnetics Analysis Software from Infolytica Corporation that uses the finite element method to solve the magnetic field equations. The results of simulated magnetic field were compared to extensive measurements made with a Lakeshore 410 Gauss meter. Qualitatively they are in excellent agreement though the software consistently predicted stronger magnetic fields. Since the simulation is only two-dimensional it assumes an infinite array of magnets normal to the solution plane in contrast to the finite array in the real

[1]The ARGO was also the 'vessel of discovery' sailed by Jason and the Argonauts in *The Argonautica* written by Apollonius of Rhodes in the 3rd century B.C.

Reproduced with permission of the copyright owner. Further reproduction prohibited without permission.

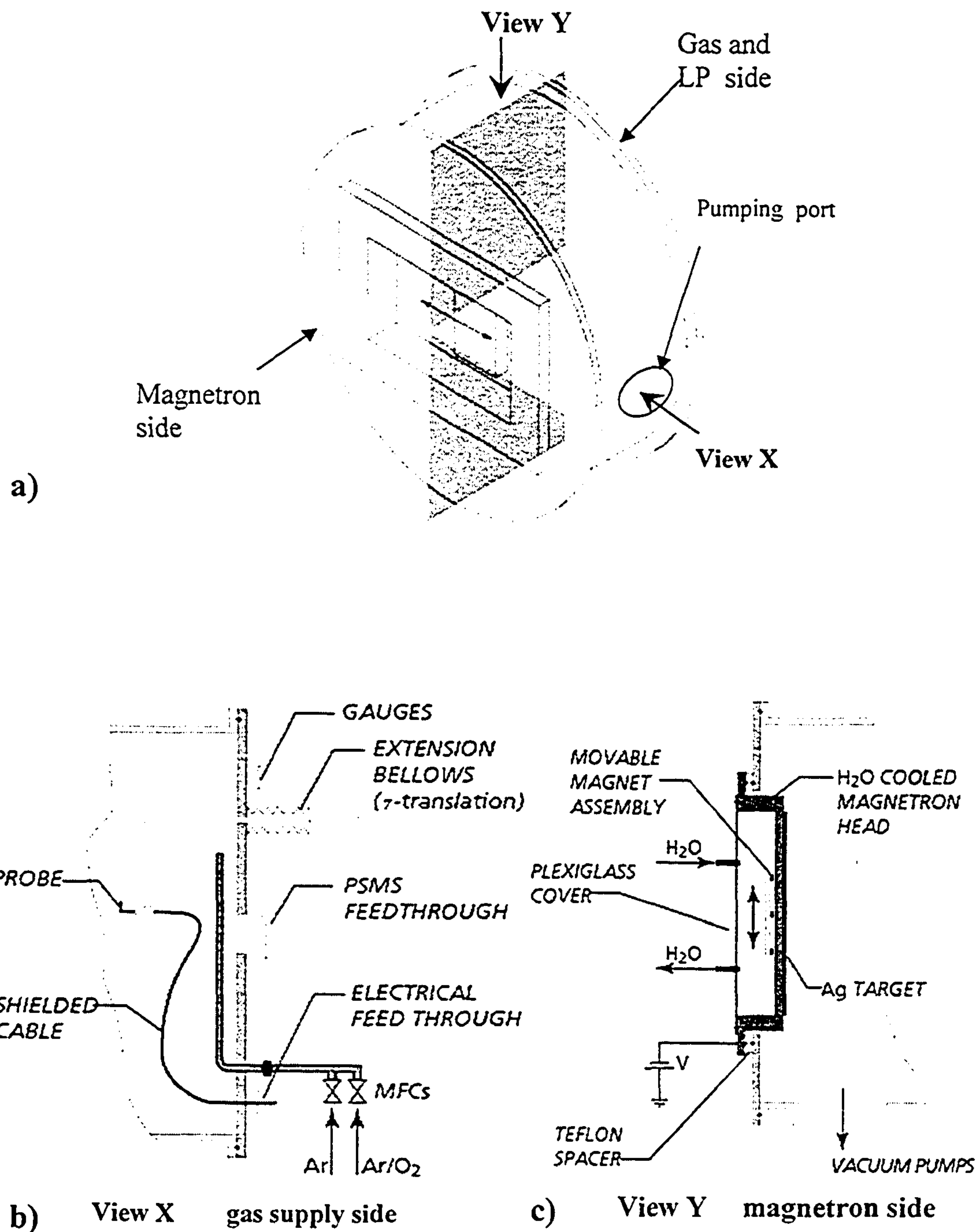

Figure 2.1

a) ARGO chamber. View X is for Gas supply end of chamber (side view of chamber). View Y is for magnetron end of chamber (top view). These different views are presented for clarity.
b) Detail of gas and LP end of ARGO. Viewed from side.
c) Detail of cathode end of ARGO. Viewed from above.

Reproduced with permission of the copyright owner. Further reproduction prohibited without permission.

assembly. This would account for the quantitative discrepancy with the Gauss meter results. The Gauss meter indicated a maximum magnetic field parallel to the target surface to be 214 Gauss at 4 cm from the center of the magnet assembly (taking measurements every cm). This is approximately where the plasma glow is most intense and the target etch track is deepest. The simulation predicted a maximum parallel magnetic field of 285 Gauss at 4.4 cm from the center of the magnetic assembly. Since they are qualitatively so close, the simulated values are taken to represent the shape of the magnetic field.

In figure 2.1.c, the vacuum side of the magnetron head (cathode) has mounted a *20.64 cm high* x *33.34 cm wide* x *0.6 cm thick* pure silver *(99.99%)* target supplied by Johnson-Mathey. The lateral translation of the magnet assembly will effectively move the plasma over the surface of the target providing lateral (x-direction) translation of the plasma with respect to centrally mounted LP (which is axially translatable).

The chamber is pumped by a Edwards CR160/700 diffusion pump and Edwards E2M18 rotary vane pump combination. Base pressures for this chamber were commonly 4.0 x 10^{-7} Torr or better. Base pressures were measured by a MKS 919 hot cathode gauge and operating pressures were monitored by an MKS 626 Baratron (capacitance manometer) gauge. Gas is introduced into the system by means of two Hastings 202 mass flow controllers (MFC's) where one MFC supplies pure argon and the other supplies 20% oxygen in argon (see figure 2.1.b). This way the sputter gas can be adjusted anywhere from 0 to 20% O_2 by adjusting the two flow rates. Typical total flow rates for this system were 50 sccm and were fed into the chamber through a perforated stainless steel tube mounted on the end of the chamber opposite the cathode. For a given gas flow rate, the chamber pressure is adjusted by manipulating a butterfly valve mounted on top of the diffusion pump. Above the butterfly valve is 70 cm of 16 cm diameter pipe that connects to the ARGO at the side of the cylindrical body. Cathode power is provided by an Advanced Energy MDX DC 10K power supply operated in constant current mode. This means the current level is set by the operator and the power supply adjusts the voltage as needed to provide the required current.

Reproduced with permission of the copyright owner. Further reproduction prohibited without permission.

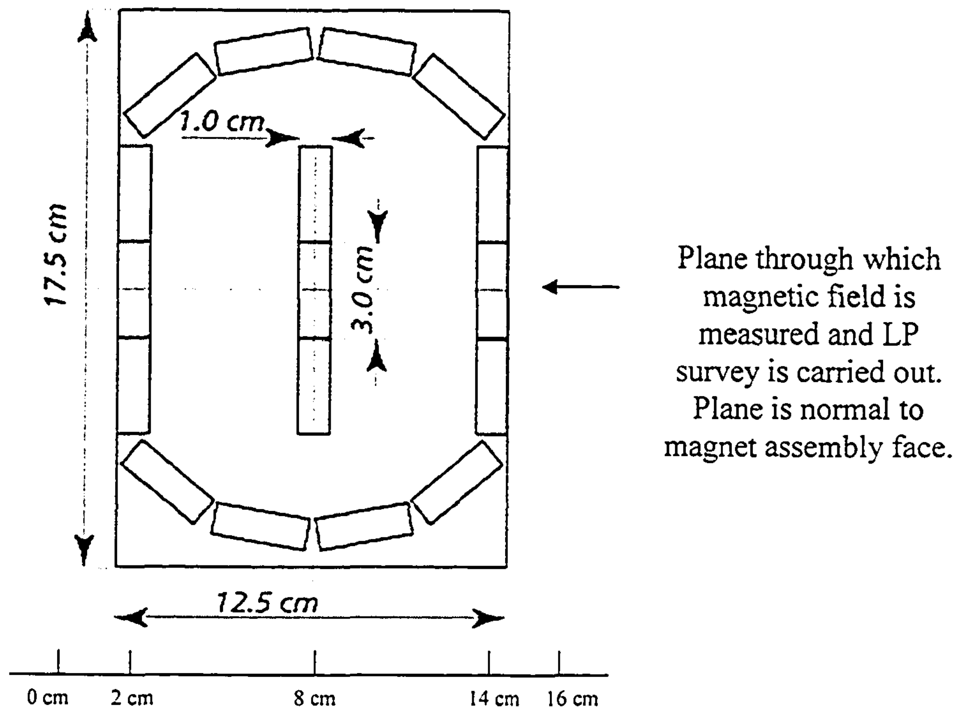

Figure 2.2 NdFeB magnet assembly.

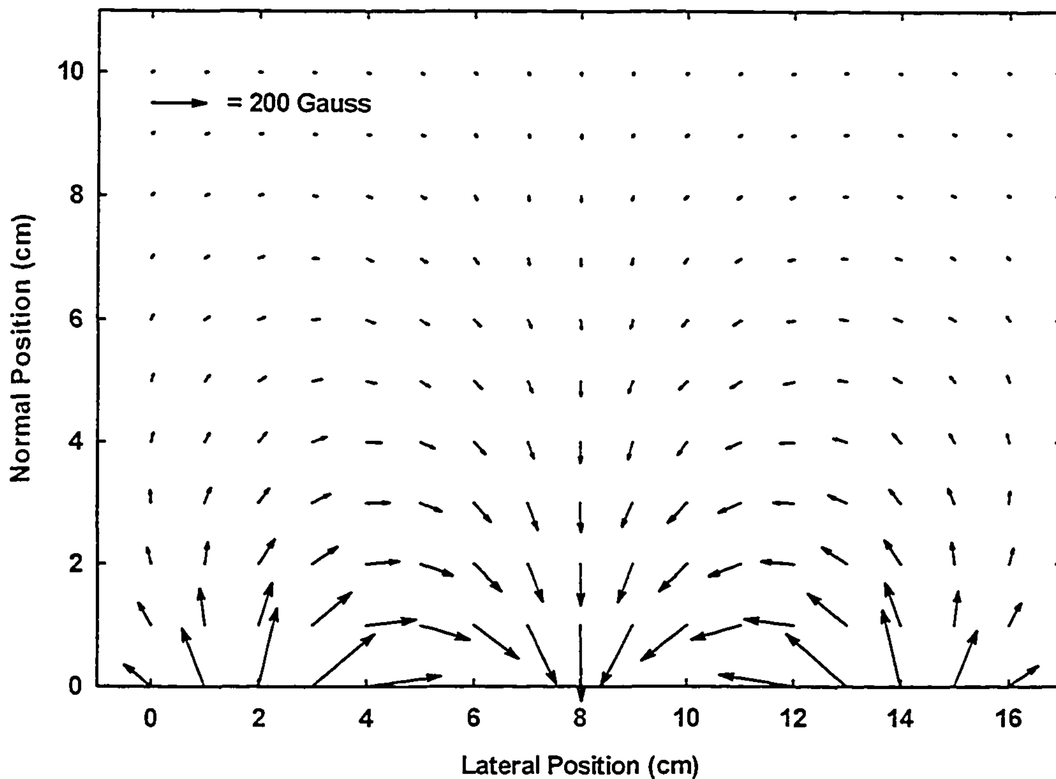

Figure 2.3 Vector plot of magnetic field. B(x,z), for magnet assembly in Figure 2.2.

Reproduced with permission of the copyright owner. Further reproduction prohibited without permission.

2.2 Langmuir Probe

2.2.1 Mechanical Description

A Langmuir probe is a very simple device to construct and immerse into a plasma. It is nothing more than a small piece of metal of some geometrically symmetrical shape. While these devices are simple to construct, the resulting I-V characteristics are notoriously difficult to analyze, although this can be somewhat simplified by the geometric symmetry. These probes are typically planar, spherical or cylindrical. Of these, the simplest to physically build is the cylindrical variety since it can be just a small piece of bare wire. For this investigation a piece of 0.25 mm diameter tungsten wire is used. The wire is fed through a 2.5 mm ID (4.9 mm OD) piece of alumina tubing and bent at 90° so that 4.2 mm of wire is exposed to the plasma (see figures 2.1.b and 2.4). The alumina tube is in turn held by a larger diameter alumina tube to facilitate mounting on the aluminum bar.

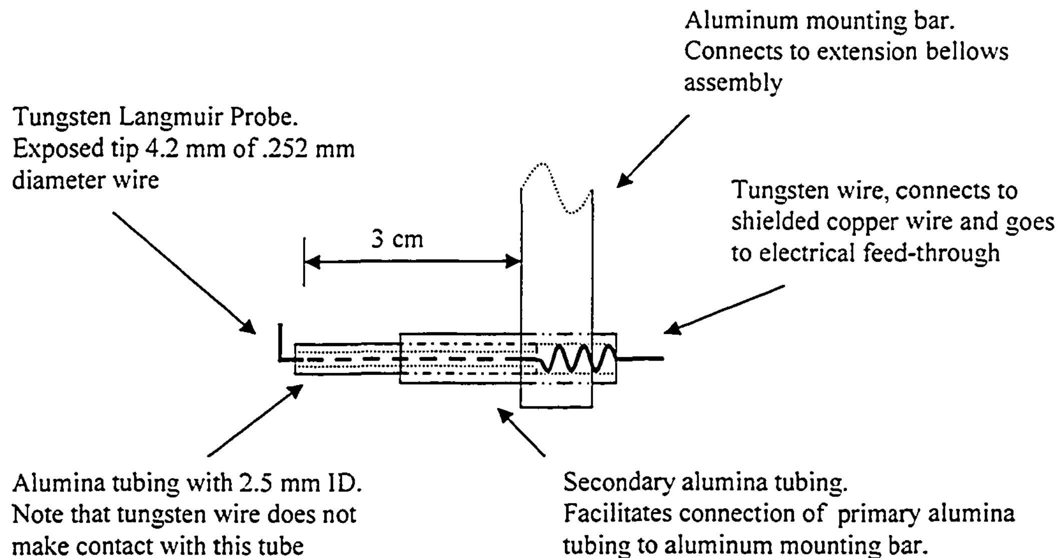

Figure 2.4: Details of Langmuir Probe assembly.

The alumina assembly is mounted at the end of an aluminum bar that in turn is fixed to a stainless steel rod. This rod is mounted on an extension bellows located on the end of the ARGO opposite the cathode. Manipulation of the bellows from the

Reproduced with permission of the copyright owner. Further reproduction prohibited without permission.

outside of the chamber provides translation of the probe in the z or normal direction with respect to the cathode. The setup is such that the probe is situated on the very axis of the vacuum chamber. The 90° bend in the probe means that a majority of the probe length is equidistant from the cathode, which is a more desirable situation than having it simultaneously sample from several distances at the same time. This configuration will be discussed more in the theoretical section. At the back end of the alumina tubing, the tungsten wire is connected to a shielded copper wire which is coupled to an electrical feed-through. The wire shielding is copper braid and is grounded to the ARGO chamber.

2.2.2 Instrumentation

On the outside of the ARGO, the probe connection is immediately fed into a grounded faraday cage in which resides the instrumentation electronics (figure 2.5) for the probe. This system is a variation on systems used by other researchers[83,84,85,86]. Essentially a LP operates by providing a known voltage and recording the resultant current extracted from the plasma. As such, any instrumentation must facilitate these two aspects of operation.

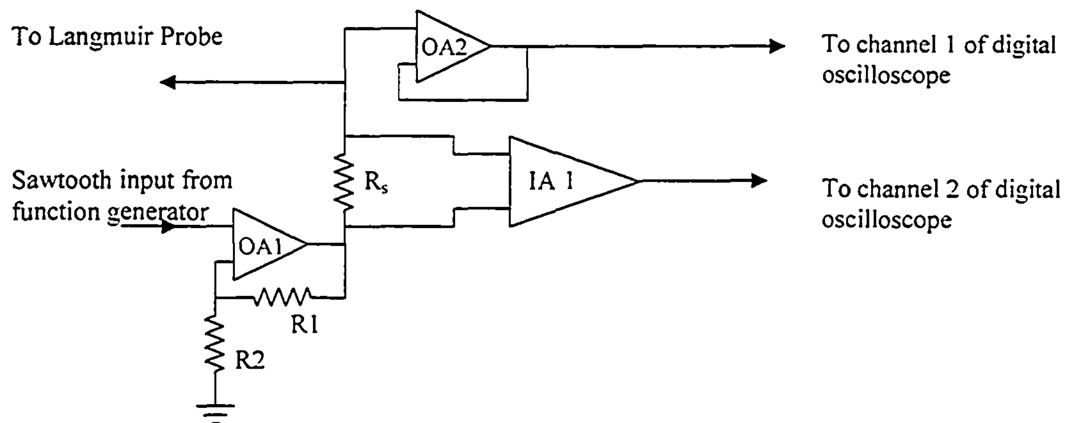

Figure 2.5: Schematic of Langmuir Probe Instrumentation. OA1 is an operational amplifier in a voltage amplification configuration with resistors R1 and R2. It provides voltage to the probe through sampling resistor R_s. OA2 is an operational amplifier in a voltage follower configuration which measures instantaneous probe voltage. IA 1 is an instrumentation amplifier which measures voltage drop across the sampling resistor R_s (~100 Ω)

Reproduced with permission of the copyright owner. Further reproduction prohibited without permission.

Applying a probe voltage and measurement of same.

This circuit functions by providing a sawtooth voltage signal to the probe and directs the collected current through a sampling resistor for measurement. More specifically a function generator (Model HP 8116A) provides a signal to an National Semiconductor LF411 amplifying operational amplifier (OA1 in schematic) which in turn applies the voltage to the probe through a resistor (R_s). The actual probe voltage is measured by an LF411 operational amplifier (OA2) in a voltage follower configuration. The output signal of this operational amplifier is fed into a 520C Tektronix digital oscilloscope. The sawtooth voltage signal to the probe is set at 500 Hz. This frequency is low but sufficient to obtain many repeat voltage sweeps to obtain averaged data for noise reduction purposes. Typically, 10 seconds is used to obtain an averaged probe characteristic.

Recording the probe current.

The voltage applied to the probe extracts charged particles from the plasma which results in a current through the sampling resistor (R_s). This occurs because the only viable current path is through the sampling resistor and resistors R1 and R2 to ground. All other paths lead to very high impedance ($>10^9$ ohms) connections on operational amplifiers or the instrumentation amplifiers. The current through R_s will become a voltage drop across R_s which is sampled by the difference amplifier (Analog Devices AD524 instrumentation amplifier). This signal is also sent to the oscilloscope. The oscilloscope receives two signals, one representing the probe voltage and one representing the probe current. They are recorded simultaneously on two channels and stored to an on-board floppy drive for numerical analysis. The data is further subjected to smoothing by means of the Savitzky-Golay algorithm[87]. This method performs a least squares fit to a small, odd numbered, group of points. The middle point is then given the value of the curve and the group of points is reselected to smooth the next data point.

Reproduced with permission of the copyright owner. Further reproduction prohibited without permission.

Chapter 3: Langmuir Probe Investigation

3.1 Introduction

As indicated in chapter one, understanding key gas phase, plasma, and chemical processes within magnetron plasmas is of great value for industrial coating processes as more and more unique films are being produced with this method[5,88,89,90]. Unfortunately, not much is known about the two or three-dimensional structure of such plasmas. There have been experimental studies using Langmuir (electrostatic) probes[12,26,91,92,93,94,95,96,97,98], optical emission spectroscopy[99,100], and laser induced fluorescence[101,102]. However, the experimental surveys typically investigate a restricted number of spatial locations in the plasma and thus provide limited insight into the overall structure.

A Langmuir Probe (LP) is a common tool used to investigate such entities, since it is a simple technique to employ and returns a substantial amount of data including electron density (n_e), positive ion density (n_i), plasma potential (V_p), floating potential (V_f), and the electron temperature (T_e) (or electron energy distribution function (EEDF) for non-Maxwellian electron groups). Additionally, the LP technique has been a common method of investigation for similar plasmas and, as such, provides a wider basis of comparison for experimental results. The simplicity of application and abundance of data provided by such probes is unfortunately offset by the varied and complicated analytical methods for interpreting raw data. As such, the most straightforward methods are best used where possible.

This chapter deals with LP surveys of the magnetron plasma within the ARGO chamber as well as the response of this plasma to process conditions. Spatial surveys are first presented for pressures of 5 and 40 mTorr in pure argon gas. These represent typical conditions for non-reactive magnetron sputter deposition in industrial situations. The probe is scanned laterally across the plasma at three distances (3, 5, and 10 cm from the cathode) and also is scanned in the normal direction at two locations above the target (one directly above the etch track and one

Reproduced with permission of the copyright owner. Further reproduction prohibited without permission.

above the center of the target between the two etch tracks. See appendix 2.). Spatial surveys are then repeated with oxygen as a component of the sputter gas (both 4% and 16% of O_2 in Ar). Finally, surveys are conducted with respect to oxygen level, total gas pressure and cathode current for 3 select probe locations within the plasma. These locations are chosen as they seem to best typify the various plasma spatial regions.

While a few of these types of surveys have been done in similar systems it is novel to have all this data for a single system. This provides a greater basis on which pre-existing theoretical models can be validated or eliminated, as well as a greater database on which new models can be established. Where previous theories or conclusions exist they will be discussed.

The goal of this chapter's investigation is to determine what conditions exist in the sputtering environment, how those conditions respond to process parameters and to provide guidance for future research projects with respect to the physical mechanisms and phenomena within sputtering plasmas. At the end of this chapter is a review of the salient features from this investigation as well the main conclusions and unresolved issues raised therein. When practical, Chapter 4 on simulations will serve as an investigative medium to confirm, assess and extend some of the more interesting experimental results found herein.

3.2 Theory and Operation

Given the complex dynamics within plasmas there are many different perspectives and theories on the best way to analyze LP data to extract n_e, n_i, T_e, V_p and V_f. Variations in methodology are frequently based on the thickness of the sheath (d_s) around the probe and perhaps more importantly the ratio of d_s to the probe radius (R_p) in the case of a cylindrical probe. This in itself is not straightforward, since the sheath thickness depends on plasma density (which is what one is trying to measure) and also can depend on the probe bias with respect to plasma potential. Corrections for probe geometry can also be used.

Reproduced with permission of the copyright owner. Further reproduction prohibited without permission.

A researcher can spend an exorbitant amount of time finding and verifying the applicability of a specific theoretical method or even several methods if the range of experimental conditions warrants it. Even so, there still may be gaps where experimental conditions fall in a transition regime between one theoretical method and another. A good example of this is the use of Orbital Motion Limited (OML) theories or Radial Motion theories (RM)[21]. OML is used for large d_s/R_p and RM for small d_s/R_p ratios. OML theory is based on the rate and energy of collected particles when it encounters the sheath edge whereas the simpler RM theory only considers that rate at which particles encounter the sheath edge. However, it is not always clear how to treat data when d_s/R_p is ~ 1. Switching techniques in the middle of a data set can show up as a discontinuity and may obscure trends and responses. As the presented data was analyzed, the sheath to probe radius ratio was monitored, and it was found most often the appropriate methods are based in the thin sheath assumption. The d_s/R_p ratio was commonly in the range between 0.15 and 0.3 (for over 70 % of cases) with only a small fraction (< 3.0%) greater than 1, though never greater than 2. In some cases, the d_s/R_p ratio, while not sufficient enough to warrant the use of OML theory, was enough to suggest some corrections for the probes cylindrical geometry[21] as opposed to the case of thin sheaths. Considering the desirability to consistently use simple methods, the thin sheath assumption was used for all data analysis. Use of the simpler, and thus more transparent, thin sheath methods facilitates interpretation when a large amount of data is present and provides data that is more directly comparable to other researchers results. One does recognize that error may increase in the cases of large d_s/R_p, which in turn is dependant on T_e and n_e. (Given the dimensions of the probe used here, the d_s/R_p ratio will be less than 1 if $(T_e/n_e)^{1/2}$ remains below 3.4×10^{-5} where T_e is in eV and n_e in cm^{-3}.) The methods used here have been used, in varying degrees, by several researchers under similar plasma conditions[92,12,13,103,104,105].

Aside from theoretical limitations when using Langmuir probes there are also some practical or physical considerations. These can arise due to the presence of magnetic fields[21,97] or flowing plasmas[26,96,98], both of which can alter the shape of the raw I-V probe trace and obfuscate interpretation. It is therefore important to

Reproduced with permission of the copyright owner. Further reproduction prohibited without permission.

determine which of these aspects are relevant to the plasma of immediate concern to ensure application of appropriate analyses.

Magnetron plasmas have, by definition, a magnetic field as one of their components. The magnetic field serves to 'trap' electrons in a region near the cathode, thereby enhancing the local ionization and thus the sputter rate, leading to a more efficient process. Unfortunately, the magnetic field can complicate the acquisition of Langmuir probe characteristics. This arises because the charged particles (usually electrons since the heavy mass of ions makes them much less susceptible to Lorentz forces) are constrained to gyrate around the magnetic field lines and can only cross them by means of a collision with another particle. Essentially the electron's mean free path across the magnetic field is limited by the Larmor radius. If the Larmor radius of an electron is much smaller than the probe sheath thickness, then transport of electrons to the probe across the magnetic field is collisional in nature which can vary significantly from non-collisional transport across a sheath[21]. Also, since electrons are constrained to gyrate around magnetic field lines, one expects transport of electrons to be much easier along the field lines than across them. This implies electrons moving to the probe along field lines are transported quite differently than those across field lines, which may affect probe current collection characteristics. Passoth *et al*[97] investigated these issues for similar experimental conditions and determined the relative error in electron density is never more than 20%, which is comparable to the estimated error here (estimated error bars are present on all figures). Passoth also found the influence of the magnetic field is minimized when the probe is oriented perpendicular to the magnetic field lines which is the orientation used for all scans in this investigation. The influence of the magnetic field on the probe characteristic is thus considered negligible.

For these experiments, it was found that the probe sheath was always smaller than the Larmor radius of the electrons (calculated using the local electron temperature and magnetic field strength). It is noted that for all survey locations, $|\mathbf{B}|$ is never greater than 60 Gauss (see figure 2.1.3 in Chapter 2). Therefore, the Larmor radius could never be less than ~0.4 mm even if the electron temperature is 0.5 eV. It is further noted that 0.5 eV is a temperature typical of electrons farther out of the magnetic trap

Reproduced with permission of the copyright owner. Further reproduction prohibited without permission.

where the magnetic field is weaker, so 0.4 mm represents an absolute minimum Larmor radius. This is over three times the probe radius and thus larger than d_s which in turn is never more than two times R_p. Since this is the case, the magnetic field is not considered a critical factor affecting probe traces and is thus ignored.

It has been established in some magnetron systems that there is a significant drift velocity of electrons in the **E** x **B** direction[98,106] which is the azimuthal direction with respect to the magnet assembly. Sheridan[98] found that close to the cathode the drift velocity was most significant, whereas farther from the cathode it drops off to nominal values with respect to plasma thermal velocities. It has been shown that this flow of plasma can affect the shape of the obtained characteristic leading to incorrect electron temperatures and plasma potentials[26]. However, the probe only picks up drift velocity components that are perpendicular to the probe surface[96] so that if the drift velocity is along the axis of the probe then the probe will not pick up any signal from it. If, however, the drift velocity is perpendicular to the probe axis then some effect should be observed. This provides a fast method of determining if the drift velocity is of significant magnitude to be of concern. A characteristic is obtained first with the probe oriented parallel to the **E** x **B** drift and then with it oriented perpendicularly. Having done this for several conditions and locations within the plasma, there were no noteworthy differences in the traces and so it can be concluded that the flow velocity of the plasma is not a significant factor. The probe for experimental purposes is already oriented perpendicular to the magnetic field lines which means the probe length is oriented parallel with the direction the plasma might flow.

Complications due to secondary electron emission from the probe was deemed negligible as thermionic emission (using the Richardson-Dushman equation) and field effect emission (using the Fowler-Nordheim equation) both indiacted secondary electron emission currents on the order of a few ten of nanoamps, at least 1000 times lower than the currents recorded herein.

Briefly, when a LP characteristic is obtained the plasma potential (V_p) and floating potential (V_f) are determined first, then the electron temperature (T_e) (or effective temperature, T_{eff}), followed by the ion density (n_i), and finally the electron density (n_e). Specific methodology for obtaining these values follows.

Reproduced with permission of the copyright owner. Further reproduction prohibited without permission.

i.) Plasma and Floating Potentials (V_p and V_f)

The floating potential is perhaps the easiest value to obtain since, by definition, it occurs when the probe current is zero. Simply finding this condition on the probe characteristic yields the value for V_f (see fig. 3.0a).

The plasma potential can be found by two main methods, the two-tangent (TT) method and the derivative method, both of which have been used fairly extensively. The two-tangent method involves taking the semi-log plot of the I-V characteristic (after subtracting the ion contribution from the characteristic, see ii. below) and fitting a straight line through the retardation and electron saturation regions. These lines will meet at the 'knee' of the characteristic and provide V_p. This

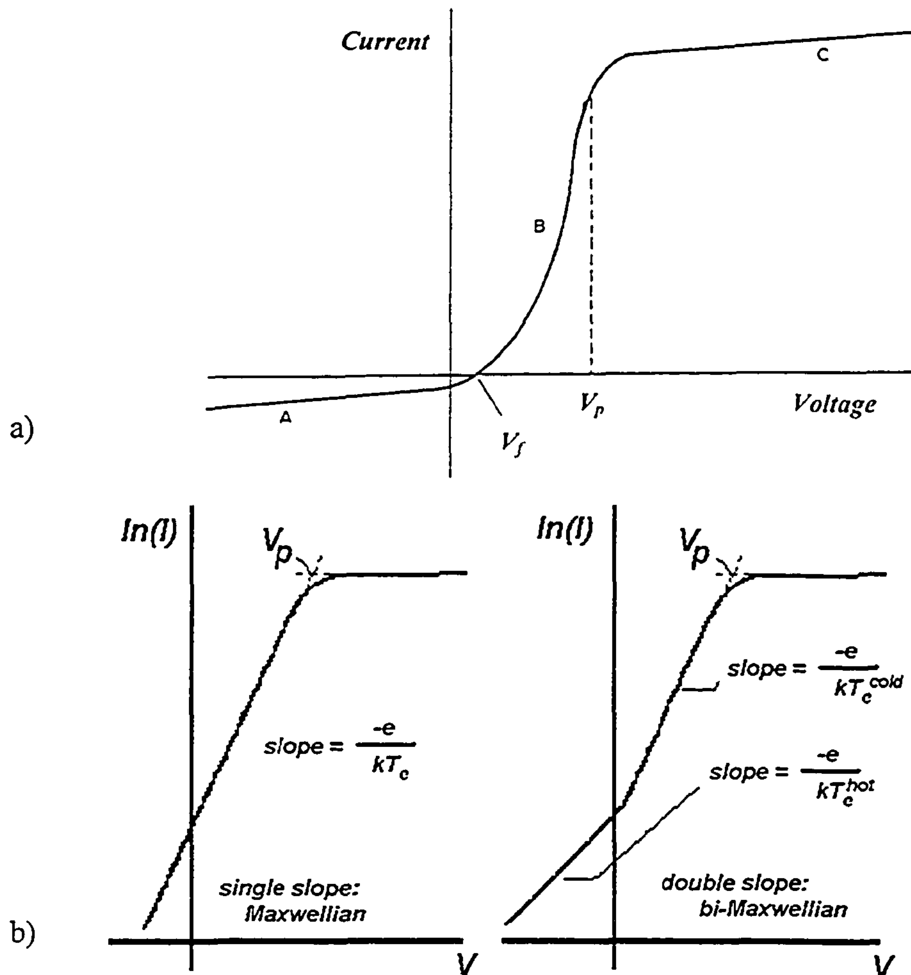

Figure 3.0: a) Typical Langmuir Probe characteristic or trace. b) semi-log plots of Langmuir probe traces, one with a Maxwellian distribution and one with a bi-Maxwellian distribution (see text)

Reproduced with permission of the copyright owner. Further reproduction prohibited without permission.

method is commonly used[107,108] and is a simple, logical, and efficient way to obtain V_p. The derivative method uses the inflection point in the probe characteristic as the indicator of V_p. It has been suggested by Fang and Marcus[109] that the derivative method is more accurate. However, it appears most researchers with similar systems use the TT method so it is used here. The TT method is demonstrated in fig. 3.0b.

ii.) Electron Temperature (T_e)

If the electron energy distribution is Maxwellian in nature, the current to the probe in the electron retardation region will be[16]:

$$I_e = 0.25 e n_e v_e A_{coll} e^{\frac{-e(V_p - V_B)}{kT_e}} \qquad V_B < V_p \tag{1}$$

where V_P is the plasma potential, V_B is the probe bias, A_{coll} is the collection area of the probe and

$$v_e = \sqrt{\frac{8kT_e}{m_e \pi}}$$

The natural log (as in fig. 3.0b) of both sides gives:

$$\ln(I_e) = \frac{-e}{kT_e}(V_p - V_B) + C \tag{2}$$

where C is a constant. Thus the electron temperature is the inverse of the slope of the region where V_B is less than V_p. Since it is only the electron current that is desired for this analysis, the ion contribution to the I-V characteristic must be removed. This is accomplished by fitting a line to the ion saturation current region of the I-V trace and subtracting that from the trace as per Koo, Hershkowitz and

Reproduced with permission of the copyright owner. Further reproduction prohibited without permission.

Sarfaty[108]. The ion current contribution to the total probe current near V_p is minor which implies T_e will be unchanged within error limits by subtracting the ion current contribution.

For the case of bi-Maxwellian electron distributions, where there are two electron groups present, each with a different temperature, two slopes are present below V_p in the ln(I)-V trace[21] (see fig. 3.0b). In this case, the two slopes provide the hot and cold electron temperatures[21] which can be used to generate an effective temperature (T_{eff})[108]. When V_B is less than V_P, bi-Maxwellian electron current to the probe can be written as[12,13].

$$I_e = I_e^{*cold} e^{\frac{-e(V_P - V_B)}{kT_e^{cold}}} + I_e^{*hot} e^{\frac{-e(V_P - V_B)}{kT_e^{hot}}} \tag{3}$$

where I_e^{*cold} and I_e^{*hot} are the electron saturation currents due to cold and hot electron groups. I_e^{*hot} is thus experimentally obtained by extrapolating the line fit through the hot electron group to the plasma potential. When it is subtracted from the net electron current at V_P one gets I_e^{*cold}. With these values, the effective temperature can be estimated from[108]:

$$T_{eff} \cong \left(\frac{I_e^{*hot}}{\left(T_e^{hot}\right)^{1/2}} + \frac{I_e^{*cold}}{\left(T_e^{cold}\right)^{1/2}} \right) * \left(\frac{I_e^{*hot}}{\left(T_e^{hot}\right)^{3/2}} + \frac{I_e^{*cold}}{\left(T_e^{cold}\right)^{3/2}} \right)^{-1} \tag{4}$$

It should be noted that the hot electron group may be represented by a relatively small signal so subtraction of the ion current may be significant in determining T_e^{hot}. When bi-Maxwellian electron distributions exist, the ion current is always subtracted before analyzing the characteristic for T_e^{hot}, T_e^{cold} and T_{eff}.

Reproduced with permission of the copyright owner. Further reproduction prohibited without permission.

iii.) Ion density (n_i)

There are several theoretical methods for extracting the ion density from the ion saturation branch of the probe characteristic. The ion branch is, however, of low magnitude with respect to the electron saturation branch and more prone to error due to noise. It is expected the ion density will have a greater associated error than the electron density and so the electron density is taken to represent the plasma density. This is reasonable since plasmas are quasi-neutral outside of any sheath regions where this survey is conducted.

The method used here for ion density is to fit a straight line to the ion saturation branch and to extrapolate that line up to the plasma potential (as determined by the two-tangent method). At V_p there is theoretically no sheath so it is appropriate to use thermal transport to calculate the ion density[24]. The ion density is given by:

$$n_i = \frac{I_i^*}{0.6e^{3/2}A_{coll}}\sqrt{\frac{e\mu_i}{kT_e}} \qquad (5)$$

where I_i^* is the saturation current due to ions, A_{coll} is the effective collection area of the probe, and μ_i is the effective ion mass[108], accounting for systems with more than one atom or molecular type present.

After fitting a straight line to the ion branch, it is subtracted from the probe characteristic so all that remains is the probe current due to electrons.

Ion density is not reported here as electron density measurement is more accurate and therefore taken to represent the plasma density. Ion density was monitored to ensure qualitative consistency with the electron density.

iv.) Electron density (n_e)[21, 23, 24]

The electron density has, as for just about every other plasma parameter, been determined by more than one method. One common method used, perhaps because of

Reproduced with permission of the copyright owner. Further reproduction prohibited without permission.

its simplicity, is to calculate the density at the plasma potential using the level of current there. At this point the electron current to the probe is much greater than the ion current so can be attributed to electrons only, regardless of whether or not the ion current has been subtracted. One can then use the formula:

$$n_e = \frac{I_{e,V_p}}{eA_{col}} \sqrt{\frac{2\pi m_e}{kT_e}} \quad (6)$$

to calculate the electron density. I_{e,V_p} is the electron current at the plasma potential. This is commonly compared to the theoretical electron current in the retardation region as given by:

$$I_{e,V_B} = I_{e,V_p} e^{\frac{-e(V_p - V_B)}{kT_e}} \quad (7)$$

where V_B is the bias voltage of the probe. Combining (6) and (7) gives the electron density as:

$$n_e = \frac{I_{e,V_B} e^{\frac{e(V_p - V_B)}{kT_e}}}{eA_{col}} \sqrt{\frac{2m_e\pi}{kT_e}} \quad (8)$$

which is equivalent to (1).

In the case where the EEDF is bi-Maxwellian, (3) is substituted for (7). This ensures both groups of electrons are sufficiently accounted for when determining the absolute density. Eqn. (8) becomes:

$$n_e = \frac{I_{e,V_B}^{cold} e^{\frac{e(V_p - V_B)}{kT_e^{cold}}} + I_{e,V_B}^{hot} e^{\frac{e(V_p - V_B)}{kT_e^{hot}}}}{eA_{col}} \sqrt{\frac{2m_e\pi}{kT_{eff}}} \quad (9)$$

Reproduced with permission of the copyright owner. Further reproduction prohibited without permission.

where T_{eff} is the effective electron temperature due to (4).

The error bars present on all graphs are determined by fitting worst-case slopes to the characteristics and extracting values therefrom. When the analytical method requires it these results are subsequently used to continue the analysis, such as when an ion saturation linear fit is subtracted from the characteristic. Thus the error is propagated through the entire analysis. In this way the error bars are estimated. Several traces are analysed in this fashion and the largest error bars are used for all data sets.

v.) Negative Ions

The presence of negative ions in a plasma is expected when electronegative gases, such as oxygen, are incorporated into the sputter gas. This does have implications for analysis of probe characteristics and the interpretation of results derived from those characteristics. The condition of plasma quasi-neutrality remains which means[110]:

$$n_+ = n_e + n_-$$

where n_+ is the positive ion density, n_- the negative ion density and n_e the electron density. The negative ions, unlike the electrons, will be much closer to thermal equilibrium with the neutral gas and/or the positive ions. This is true since negative ions are strongly coupled with positive ions and neutral gas species through collisions because of their similar masses and subsequent efficient momentum transfer. They are not coupled strongly with high energy electrons because of the poor energy transfer in collisions between species with high mass discrepancies.

The potential effects of negative ions on the LP characteristic must be determined (if only theoretically) to ensure the appropriateness of methods used for analysis. In the positive ion saturation branch, no negative particles are collected by definition. In the electron retardation region (potentially this can now be called the negative particle retardation region), negative ions will only be collected when their

Reproduced with permission of the copyright owner. Further reproduction prohibited without permission.

energy is sufficient to penetrate the potential difference between the probe and plasma. Since the negative ions are approximately in thermal equilibrium with the neutral gas atoms their energy should be on the order of 0.03 eV (~350K) which means they will only contribute to the electron retardation region current within 0.03 volts of the plasma potential.

In the electron saturation region, both electrons and negative ions are collected according to their relative densities and energies. However, if the contribution to the probe current from negative ions is small enough, then the entire signal can be attributed to the electrons without introducing significant errors. This also implies the contribution of negative ions in the retardation region can be ignored. The negative ion density must be less than the positive ion density or quasi-neutrality would be lost. This implies that the negative ion current to the probe (in electron saturation region) must be less than the positive ion saturation current (under approximately equivalent conditions). If the magnitude of current in the positive ion saturation region is much less than the current in the electron saturation region then the current in the electron saturation region must be predominantly due to electrons. For the cases studied in this chapter where oxygen is a component of the sputter gas the ratio of electron saturation current to ion saturation current is monitored and found to be such that the electron saturation current can be attributed solely to electrons, disregarding negative ions as a contributing factor. This is also true where negative ions are collected by the probe in the electron retardation region since near the plasma potential the electron signal is large compared to negative ion signal.

In summary, negative ions will exist when oxygen is a component of the sputtering gas. The degree to which they are present is unknown but this is not considered a complicating factor when the goal is to acquire information on the electron population only. Accepting the negative ion current is always lower than the positive ion current, the positive ion current can be regarded as representing the maximum error introduced to the electron saturation current due to negative ions. Since this is a very small error it is unnecessary to account for negative ions.

Reproduced with permission of the copyright owner. Further reproduction prohibited without permission.

3.3 Data and Discussion

3.3.1 Spatial Surveys in Pure Argon[2,3]

A 99.99% pure silver cathode is used with 99.99% pure Ar gas at pressures of 5 and 40 mTorr. The magnetron is operated in constant current mode at 0.6 A, which equates to an average current density of $\approx 46 A/m^2$ over the sputtered area of the target. The target voltages were 409 ± 4 volts at 40 mTorr and 575 ± 20 volts at 5 mTorr (see Appendix 1 for a table of target voltages for all experimental conditions listed by section). Three lateral surveys were completed for each pressure at distances of 3, 5 and 10 cm from the cathode (see Appendix 2 for a map of the spatial locations where data has been taken with respect to the cathode). The lateral surveys were comprised of 9 LP characteristics taken 2 cm apart extending a total of 16 cm with the 8 cm position located directly above the center of the magnet assembly. Two normal surveys were also completed at each pressure. One set at the 4 cm lateral position (above the center of an etch track hereafter referred to as the 'etch' region) and one set at the 8 cm lateral position (directly above the center of the magnet assembly in-between the etch tracks, hereafter referred to as the 'well' region). Each normal scan was comprised of 6 LP characteristics located 3, 4, 5, 6, 8, and 10 cm distance from the cathode.

The results of the lateral surveys are presented in figure 3.1 and those of the normal surveys in figure 3.2. In figure 3.1a, at 3 and 5 cm distance from the cathode, the electron density is highest above the etch region and is at a local minimum above the well region. Above the well region and close to the cathode the magnetic field is relatively strong (see fig. 2.3 for a shcematic of this) and directed predominantly normally in contrast to the etch region where the magnetic field is predominantly tangential to the cathode and slightly weaker. In the well region, this implies electrons will move more easily in the normal direction, but are restricted by the magnetic field

---

[2] D.J. Field, S.K. Dew and R.E. Burrell, J. Vac. Sci. Technol. A 20 (6), Nov/Dec 2002

[3] D.J. Field, S.K. Dew and R.E. Burrell, Proceedings of The International Conference On Plasma Sciences, May (2002).

Reproduced with permission of the copyright owner. Further reproduction prohibited without permission.

from moving in the lateral direction. As a result, electrons will be severely impeded in moving laterally from the etch region into the well region but can be easily transported away from the well region along the field lines normal to the cathode. Hence, the observed reduction in density compared to the etch regions is consistent with basic theory. Further out, the magnetic field is considerably weaker above the well region so electrons may move much more freely in the lateral direction and the difference in density above the two regions should be reduced, as was observed. At 10 cm distance, the magnetic field is so weak electrons should move essentially isotropically. At this distance, the relative spatial distribution of the plasma has changed so that the density maximum is above the well region. Thus, at progressively greater distances from the cathode, the plasma changes from being highly structured to being more spatially distributed. In almost all cases, the effect of lowering the pressure from 40 mTorr to 5 mTorr caused a significant decrease in electron density. The only notable exception to this was for the 3 cm distance at the extreme edges where electron density is comparable or slightly higher at 5 mTorr than at 40 mTorr although there is no difference within experimental error.

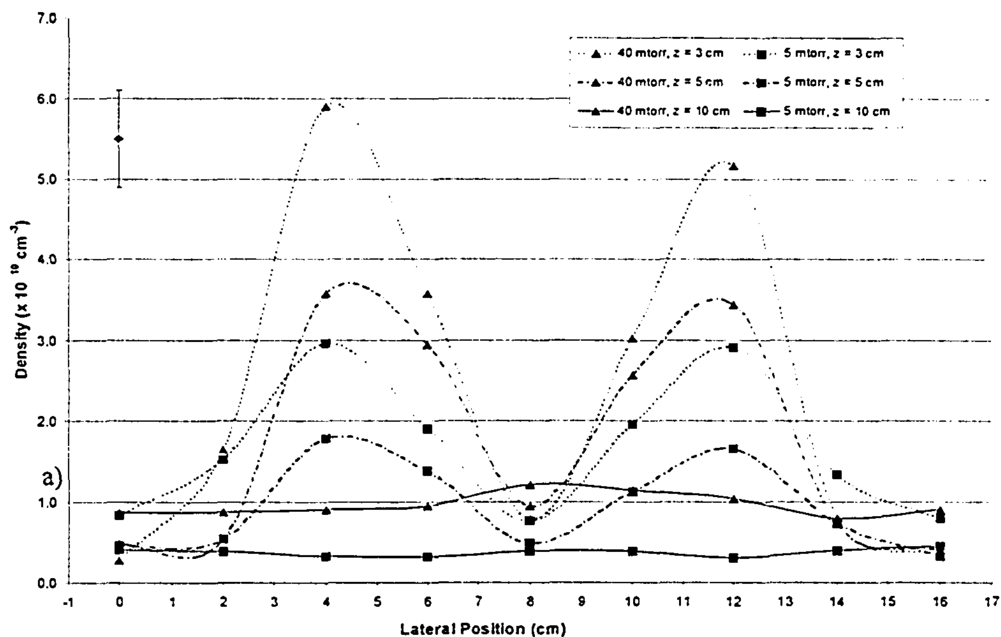

Figure 3.1 a) Electron density for lateral surveys above the cathode. Typical error bars are indicated on each graph.

Reproduced with permission of the copyright owner. Further reproduction prohibited without permission.

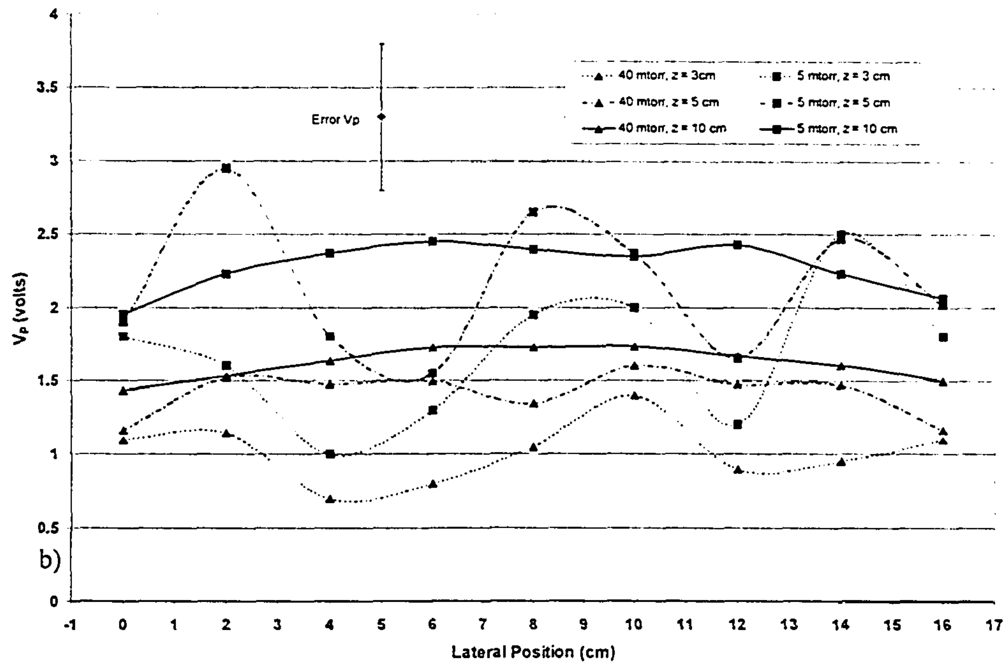

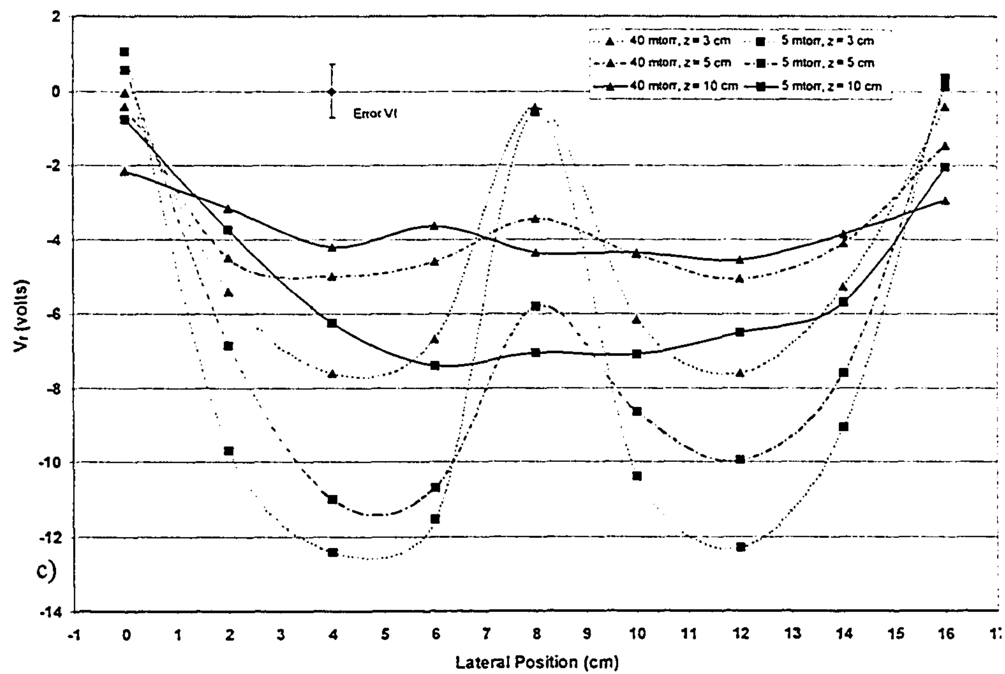

Figure 3.1: b) plasma potential (V_p), c) floating potential (V_f) . Typical error bars are indicated on each graph.

Reproduced with permission of the copyright owner. Further reproduction prohibited without permission.

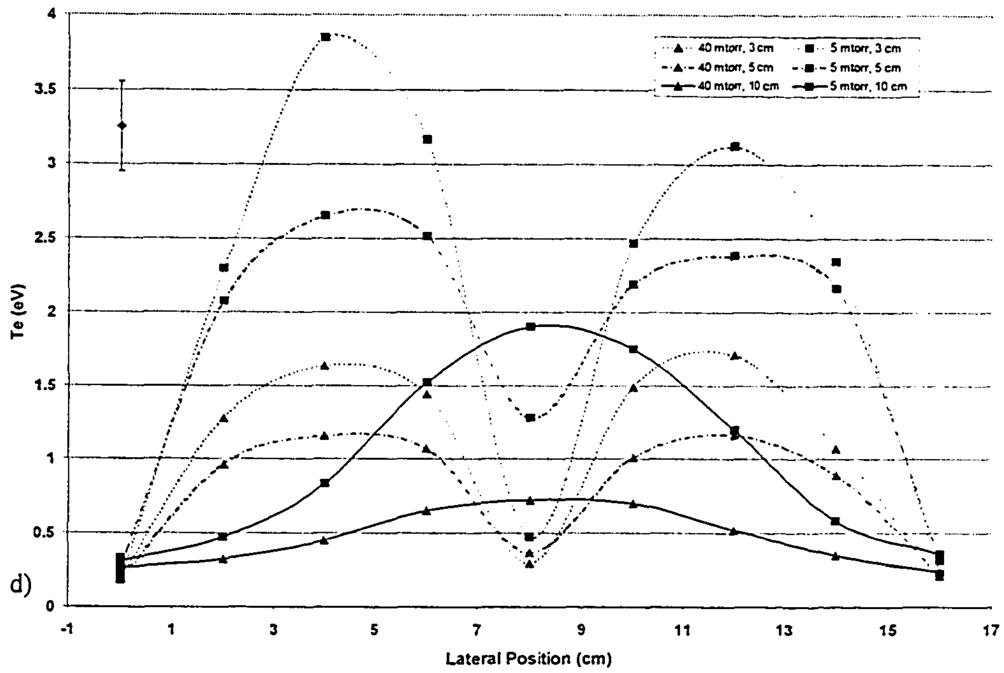

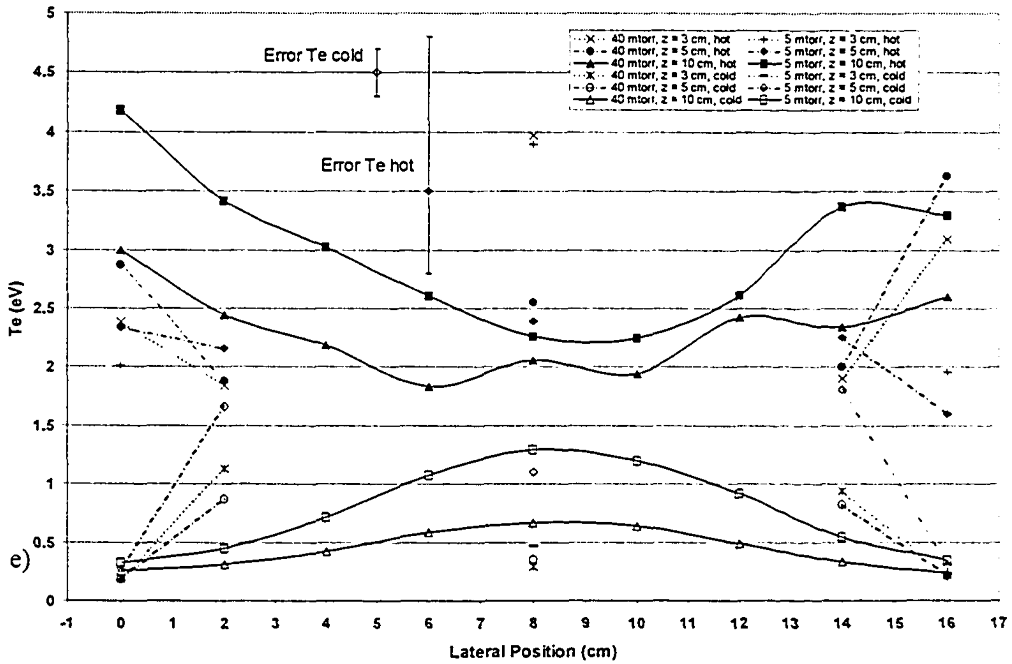

Figure 3.1: d) electron temperatures (T_{eff} where bi-Maxwellian distributions exist). e) hot and cold electron group temperatures where bi-Maxwellian groups exist. Typical error bars are indicated on each graph.

Reproduced with permission of the copyright owner. Further reproduction prohibited without permission.

In figure 3.2a (normal surveys) with the probe located above the etch region (4 cm laterally) there is a steady decrease in the electron density (for both pressures) at progressively greater distances from the cathode. When the probe is positioned at 3 cm distance above the etch track, it is at its closest to the plasma 'source' (inside the magnetic trap). In the well region and at 40 mTorr there appears a slight increase of density at greater distances from the cathode while at 5 mTorr it is flat or slightly decreasing with distance. The magnitude of these changes is significantly smaller than those of the normal scans taken above the etch region. This trend is also observed at the outer edges of the cathode at the 0 and 16 cm lateral positions (see figure 3.1a).

Figure 3.1b shows the plasma potential, 3.1c floating potential and 3.1d shows the electron temperature for the lateral scans. Figure 3.1e shows the hot and cold electron temperatures where bi-Maxwellian electron distributions exist. An absence of data points in 3.1e means the electrons are Maxwellian in nature and are represented by a single temperature in fig. 3.1d. All other points in 3.1d are

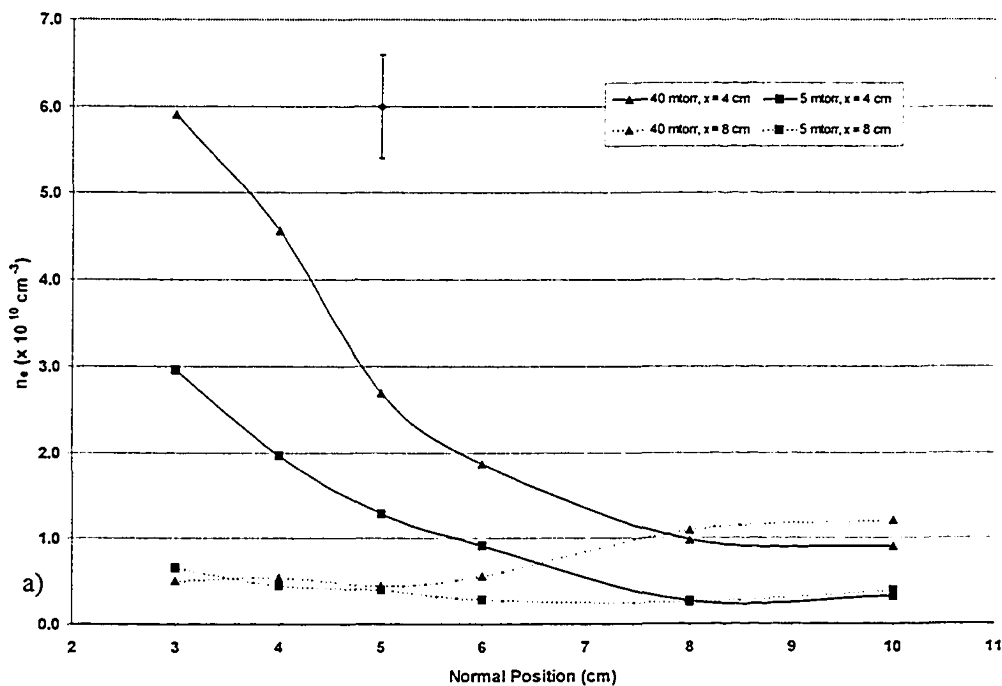

Figure 3.2 a) Electron density for normal surveys above the cathode. Typical error bars are indicated on each graph.

Reproduced with permission of the copyright owner. Further reproduction prohibited without permission.

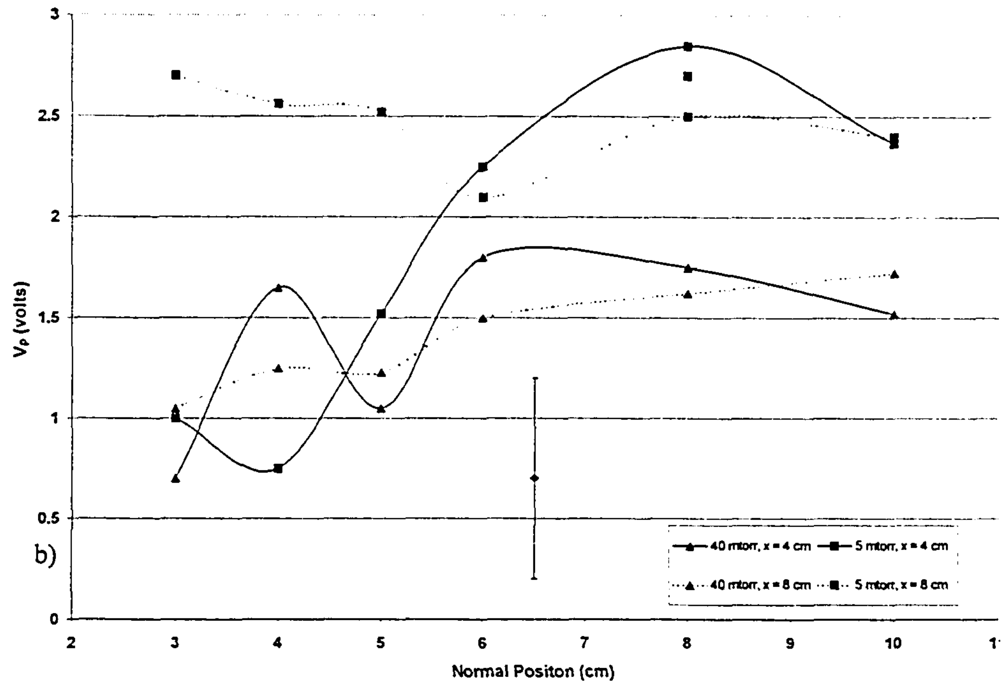

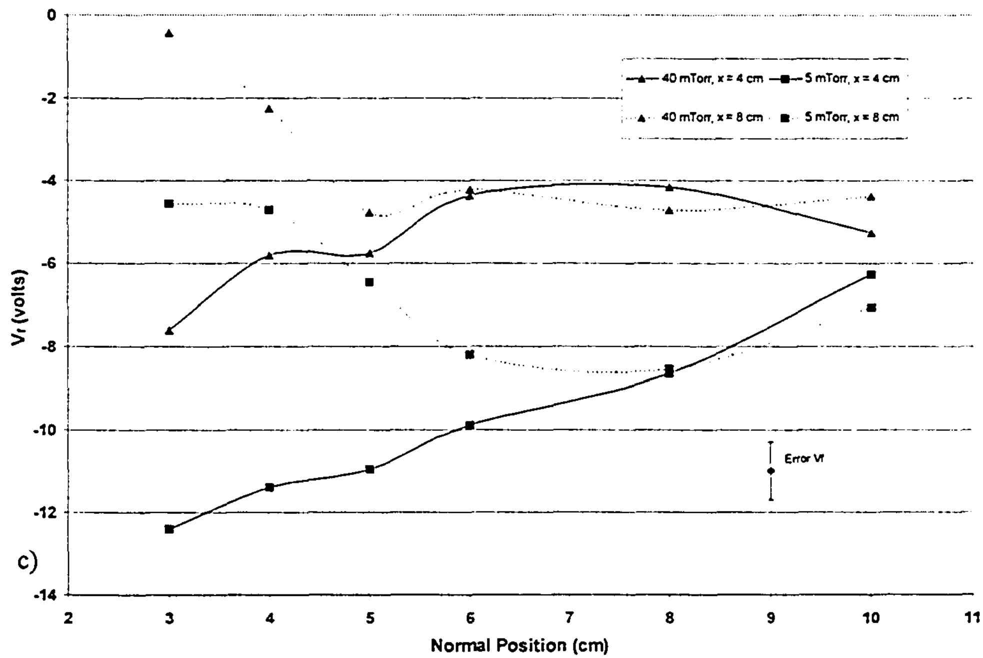

Figure 3.2: b) plasma potential (V_p) c) floating potential (V_f). Typical error bars are indicated on each graph.

Reproduced with permission of the copyright owner. Further reproduction prohibited without permission.

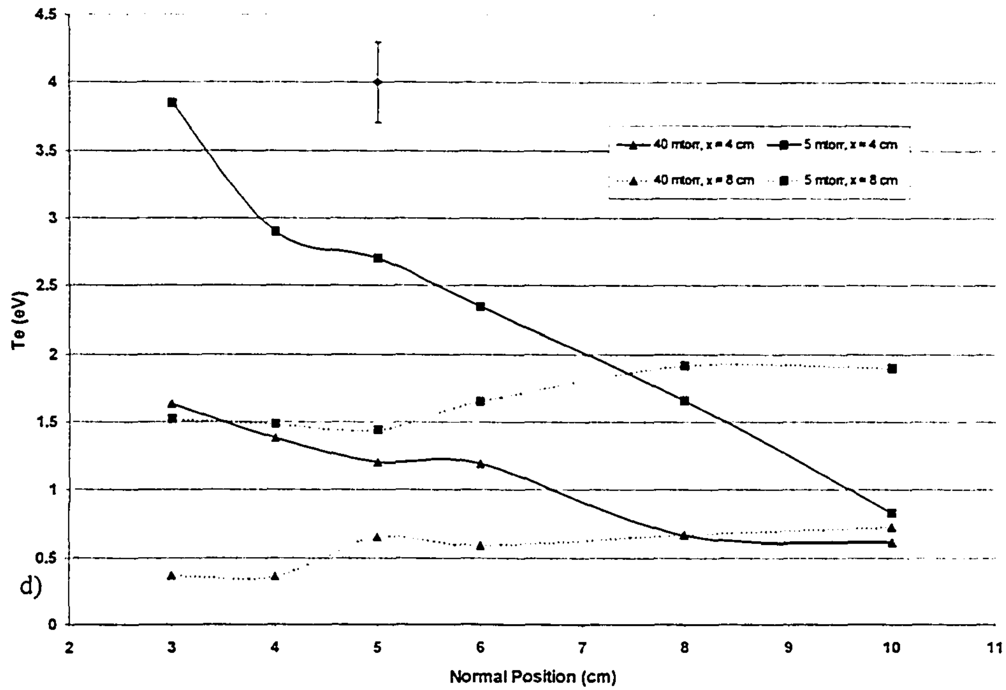

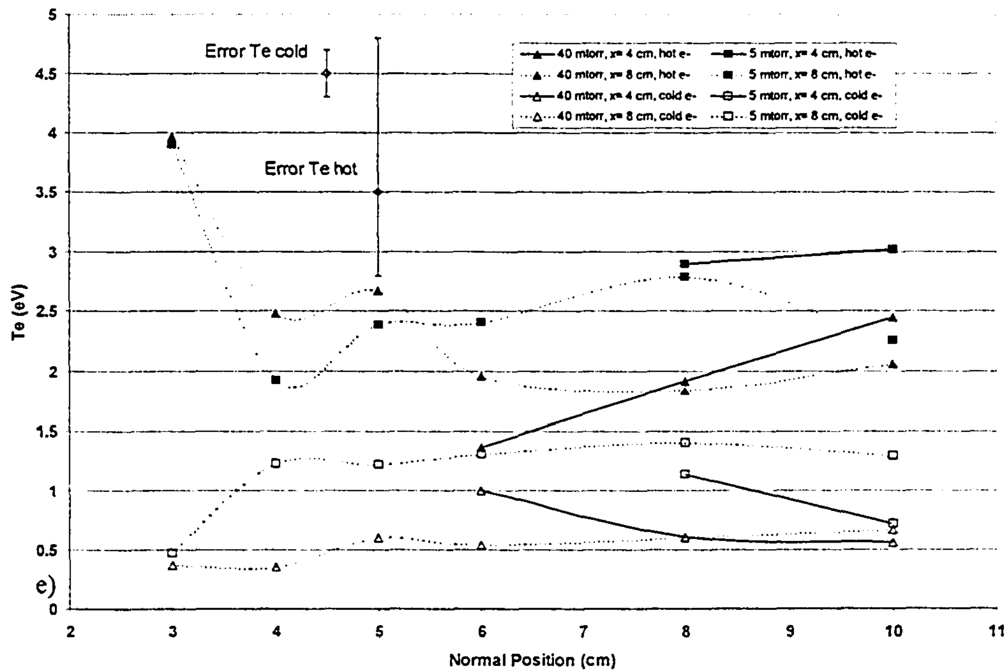

Figure 3.2: d) electron temperatures (T_{eff} where bi-Maxwellian distributions exist), e) Hot and cold electron group temperatures where bi-Maxwellian groups exist for normal surveys above the cathode. Typical error bars are indicated on each graph.

Reproduced with permission of the copyright owner. Further reproduction prohibited without permission.

effective temperatures determined using eqn. (4) and data from 3.1e. A similar convention is used for all electron temperatures henceforth.

For all spatial surveys there appeared only subtle variations in V_p. In each lateral scan there appears spatial variation only at 3 cm from the cathode (at 5 and 40 mTorr) and at 5 cm (only at 5 mTorr) (see fig. 3.1b). This slight variation is also reflected in the normal surveys. Sheridan[26] *et al* found some spatial dependence of V_p in similar devices but had no notable comments on why such variation existed. A more careful survey or alternate experimental method is required to assess more precisely the spatial response of plasma potential. Additionally, it appears from the data that there is some dependency on pressure. Lower pressures appear to have moderately higher V_p, although this is least clear in the region above the etch track (4 and 12 cm lateral) and closer to the cathode (3 and 5 cm). This will be more carefully scrutinized in §3.3.4 where surveys in pressure are conducted.

In contrast to V_p, V_f (fig. 3.1.c) has a strong dependence on pressure and spatial location. At 5 mTorr, the 3 cm distance lateral scan shows the strongest response, where V_f is near 0 volts at the outer edges of the cathode but drops rapidly to ~ -12 volts above the center of the etch tracks only 4 cm away. Proceeding toward the center of the cathode, V_f rises dramatically to almost 0 volts. The floating potential is dependent on the relative flux of electrons and ions to the probe where flux, in turn, depends on the density and energy of the respective species. Since the plasma is regarded as quasi-neutral, any discrepancy in flux will result from energy differences between the electrons and positive ions. Due to the great incongruity in mass, the electrons are much more mobile than the ions[21,24] so the floating potential is expected to depend essentially on the electron's energy. Hence, the dramatic changes in the floating potential should be mirrored by changes to the electron energies or, in this case, the electron temperature (T_e). Figure 3.1d shows just this behavior in T_e. At the outer edges of the cathode T_e is about 0.3 eV but rapidly rises to over 3 eV above the etch tracks and again falls rapidly to about 0.3 eV above the center of the cathode.

At the same distance but at 40 mTorr, the response of V_f is similar to the 5 mTorr result, but to a lesser degree. The T_e also shows a comparable response to that of the lower pressure, but tends to be cooler. Lower T_e at higher pressure has been

Reproduced with permission of the copyright owner. Further reproduction prohibited without permission.

frequently observed[12,91,95] and is typically attributed to the change in collision rate due to neutral species density. A lower collision rate implies a lower rate of energy loss as electrons migrate out of the magnetic trap resulting in higher T_e. Additionally, one observes at 5 mTorr the target voltage is ~40% higher than at 40 mTorr, so the electrons injected into the plasma begin with higher energy. Since the electrons should lose energy at a lower rate for lower pressures, one would expect the energy difference to widen as the electrons are transported out of the trap. At 5 mTorr and 3 cm above the etch region, the T_e is ~200% higher than the 40 mTorr case, indicating the difference in electron energy has widened in the space between this location and the cathode. Unfortunately, this picture is not consistent with the rest of the data. In fig. 3.2d the T_e converges, rather than diverging, for the two pressures as the electrons migrate out of and away from the magnetic trap. This is to say the electrons appear to be losing energy at a higher rate at lower pressures. This is also observed in the pressure surveys presented later.

The model just described assumes that as an electron migrates out of the trap the number of collisions it has with neutral species changes with pressure. Higher pressure implies a higher density of neutrals which means more collisions for the electron. This is, in effect, an application of classical diffusion processes. However, it is worth a brief discussion to determine if classical diffusion is an appropriate model.

Consider an electron orbiting a magnetic field line with Larmor Radius, L_r, where $L_r = (m_e v_n / q\mathbf{B})$. L_r depends on $\mathbf{B}$, the magnetic field strength, and v_n, the electron velocity in the direction normal to $\mathbf{B}$. We can ignore the velocity component parallel to $\mathbf{B}$ since we are only interested in electron transport across field lines (i.e. out of the trap region). Now consider an extremely low pressure of background gas such that the mean free path (λ_m) of the electron at that pressure is very high compared to the L_r ($\lambda_m \gg L_r$), say on the order of 10,000. Since the ratio of λ_m/L_r is known as the Hall Parameter (H), this is the case of a very large H. With a large H an electron will complete, on average, several thousand orbits before a collision takes place. After many collisions, the electron will have undergone a random walk and, on average, have been transported a certain distance out of the trap region. The average step length for this walk is determined by L_r, not λ_m. Collisions are only the impetus

Reproduced with permission of the copyright owner. Further reproduction prohibited without permission.

for a step occurring, the approximate length of the step being determined by L_r. If the background gas pressure is doubled, then the λ_m will be reduced to about 5000 times L_r. The only thing that has changed now is that the electron orbits the field line fewer times before undergoing a collision. The random walk itself remains the same for an average electron. That is to say, the same number of collisions occur for an average electron to migrate a specific distance. The only thing that has changed is the rate of that migration. Thus, a change in pressure does not change the number of collisions, and therefore energy loss, of an electron as it is transported out of the trap region. This picture should be valid at least approximately down to the point where H = 10.

In contrast to this is the case where H is very small ($L_r \gg \lambda_m$), say, for example 0.0001. In this case the electron trajectory is essentially linear between collisions and the step length for a random walk is determined by the λ_m. Decreasing the pressure will increase λ_m and thus the step length for the random walk. As a result, for an electron to migrate a specific spatial length, the number of collision it undergoes, and thus the amount of energy it loses, will depend on pressure. This is the classical diffusion model and should be valid at least up to the point where the H = 0.1.

Between these two regimes lies a transition regime where 0.1 < H < 10 and the mechanics of electron collisions, energy loss and diffusion are not as obvious.

For this investigation, the mean free path for an electron collision in neutral argon is on the order of 2 mm at 40 mTorr and a few cm at 5 mTorr. The maximum Larmor radius (assuming the electron is traveling perpendicularly to the magnetic field and based on measured T_e and magnetic field values) ranges from ~ 1 mm at the 3 cm distance to ~2.5 mm at the 5 cm distance above the etch region. Clearly the Larmor radius and the λ_m are of comparable magnitude and therefore, we are in, or at least very near to, the transition regime. Being in this transition regime results in a more complex system where it is not clear how changes in pressure affect the observed T_e as electrons migrate out of the trap region. Additionally, it is unclear if the collision rate (changes in pressure) conspires with differences in target voltage to produce such responses in T_e.

It is worth noting the λ_m (for a 'significant' collision[21]) for electron-electron (e-e) or electron-ion (e-i) collisions is on the order of 10 cm for our highest recorded

Reproduced with permission of the copyright owner. Further reproduction prohibited without permission.

density (6.0 x 10^{10} cm^{-3}) and a 0.5 eV electron (near our lowest temperature). Since the e-e or e-i or electrostatic mean free paths (λ_m^e) are long compared to the electron-neutral λ_m, it is not considered a dominating factor, though this should not be considered conclusive. The λ_m^e increases with lower density or higher energy electrons, so 10 cm is near the lowest realized λ_m^e for the spatial locations tested.

It remains conceivable that the dominant factor in the T_e – pressure response lies elsewhere. One alternative explanation might be found in Bohm diffusion, where the semi-empirically derived diffusivity is given by:

$$D_{Bohm} \equiv D_{\perp} = \frac{KT_e}{16e\mathbf{B}}$$

where $D_{\perp}$ is diffusivity perpendicular to the magnetic field line. This differs from the theoretically derived, Fick-like diffusion which scales as $1/\mathbf{B}^2$ instead of $1/\mathbf{B}$ (see Chen[19]). The Bohm diffusivity formula was developed as a result of observed anomalously poor magnetic confinement and not until the 1960s was the theoretical $1/\mathbf{B}^2$ dependence experimentally observed. As mentioned, at 5 mTorr the magnetron operates at a ~40% greater voltage, so secondary electrons introduced into the plasma from the target will have more initial energy. Since Bohm diffusion is independent of density but does depend on electron temperature, more energetic electrons will diffuse faster and lose less energy in atomic collisions. As a result a higher electron temperature may be realized everywhere for the lower pressure case. Unfortunately, the precise physical mechanics of Bohm diffusion do not appear to be well understood, so it is difficult to determine the full or partial applicability to magnetron plasmas. More work is needed to investigate these phenomena and their effect on the spatial dependence of T_e.

Finally, the effect of instabilities and fluctuations in electron dynamics may have a role in electron transport across magnetic field lines. Sheridan and Goree[93] observed minimal turbulence in such devices and concluded any fluctuations were not responsible for electron transport. This suggests that DC magnetrons of this type are relatively quiescent, though this too, remains an area worthy of more investigation.

Reproduced with permission of the copyright owner. Further reproduction prohibited without permission.

Returning to the data set and figures 3.1c and d, it is seen that at 5 cm distance the same trends in T_e and V_f are observed for both pressures across the width of the cathode. Again, the higher pressure results in higher n_e, lower V_f and lower T_e. There is, however, an attenuation of the structure observed at 3 cm distance.

At 10 cm from the cathode, profiles in density have become quite flat and higher densities are still observed at 40 mTorr compared to 5 mTorr. The highest density is no longer observed above the etch tracks but is now above the center of the cathode. The electron temperature here is also highest at both pressures, so these electrons likely have their source in a region where the electron temperature is higher such as at 5 cm above the etch region where the magnetic field is weak enough to permit more significant lateral movement of electrons. Above the well region, the electron temperatures actually rise at greater distances from the cathode.

For the normal survey (fig. 3.2) at the 8 cm lateral location (well region), the picture is a complex one. Close to the cathode the electron density is low and comparable for 40 and 5 mTorr. At greater distances, n_e rises for the 40 mTorr case. At 5 mTorr, n_e appears to drop slightly though not more than the estimated error. The electron temperature in this region starts as colder near the cathode and increases at greater distances. At approximately 7 or 8 cm distance the electron temperature for both pressures surpasses the electron temperature at similar distance but above the etch region. This implies that electrons are moving toward the well region from the etch regions when still closer than 7 cm to the cathode. Additionally, electrons may move back toward the cathode in the well region since it is much easier for electrons to move along magnetic field lines than across them. This is to say that electrons may move into the well region not by crossing field lines direct and laterally from the etch region, but actually along field lines from farther out in the well region. To ferret out the details, a spatial scan of finer resolution could be done or even a detailed computer simulation where electron flux is monitored.

At the 4 cm lateral location (etch region) in the normal scans (figure 3.2), the density drops with increasing distance from the cathode, the electron temperature drops and the floating potential increases toward zero. This can be explained simply

Reproduced with permission of the copyright owner. Further reproduction prohibited without permission.

as the flux of electrons in these regions is dominated by transport from the source of the plasma and directed normally away from the cathode.

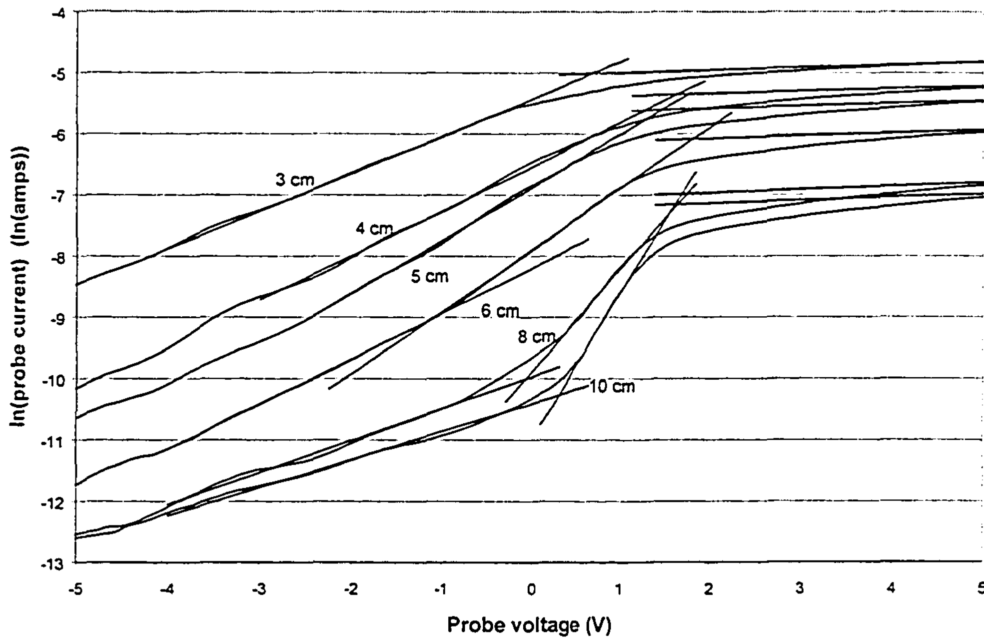

Figure 3.3: Semi-log plot of probe current versus voltage for various distances above the cathode demonstrating progression from Maxwellian EEDF at 3 cm to bi-Maxwellian at 10 cm.

Bi-Maxwellian electron energy distributions have previously been observed in magnetron plasmas[12,13], though there has not been a definitive explanation as to how such distributions arise. In this regard, the most instructive data here generated is the 40 mTorr normal survey centered above the etch track at x = 4 cm. Along this chord, the T_e (or T_{eff}) and n_e steadily decrease at greater distances from the cathode. At about 5 or 6 cm the electron population bifurcates into hot and cold groups. Figure 3.3 shows the ln(I)-V characteristics for this normal survey. The electron groups energy profile progresses from Maxwellian (single slope) at 3 cm to bi-Maxwellian (2 slopes) at 10 cm. There are some suggested explanations as to how these types of distributions arise, though none of them appear to be satisfactory in this case.

One potential explanation relates to the collision cross section of electrons in argon. As the electron population diffuses from the source, it cools by virtue of collisions. The probability of a single electron undergoing a binary collision is dictated by the collision cross section, which is energy dependent. The cross section for Ar is known to have a minimum at an energy where the electron's energy interpreted as a quantum wavelength is approximately the same as the spatial extent

Reproduced with permission of the copyright owner. Further reproduction prohibited without permission.

of the particle with which it collides. This minimum is known as the Ramsauer minimum and for argon occurs at around 0.3 eV (see figure 3.4). So it is expected that electrons in the plasma with an energy at or near this minimum will be less likely to suffer collisions and lose energy. Other electrons may be cooled in a much more efficient manner if their energy is sufficiently far from the cross section minimum. A bifurcation in the Maxwellian distribution will result. However, this is not a very satisfying explanation. In fig. 3.3, the 8 and 10 cm distance characteristics show hot electron groups (represented by the low slope region of the characteristic) comprised of electrons with energies greater than 1 eV (relative to plasma potential). These energies are higher than that at the Ramsauer minimum so it appears the Ramsauer minimum energy does not match the energies inherent in the tenacious hot electron group. In fact, the Ramsauer minimum occurs at an energy represented by electrons within the cold electron group (higher slope region). Therefore, if this effect is real and significant, a resilience to energy loss (and therefore degradation of population) by reduced collision probability should be evident in a portion of the electrons representing the cold electron group. This is to say there is no apparent mechanism for the persistence of the hot electron group, which should move toward thermal equilibrium with the much more abundant cold electrons. Between ~0.3 eV and 1.0 eV, the electron-Argon cross section (fig 3.4) rises by an order of magnitude so, as this energy range is within the cold electron group, one would expect the EEDF to significantly depart from Maxwellian there due to the discrepancy in collision probabilities based on energy. This is not observed. Not only does the Ramsauer minimum not appear to account for the observed electron temperature bifurcation, it, in fact, should give rise to phenomena not observed such as departure from Maxwellian distribution within the cold electron group.

The work of Sheridan *et al*[13] indicated that the Ramsauer minimum was not an acceptable explanation for all bi-Maxwellian electron distributions in magnetrons. They found such distributions existed in He based systems where, as they noted, the minimum in the collision cross section is essentially absent. They went on to suggest that the hot electron component was a group of electrons moving from the cathode

Reproduced with permission of the copyright owner. Further reproduction prohibited without permission.

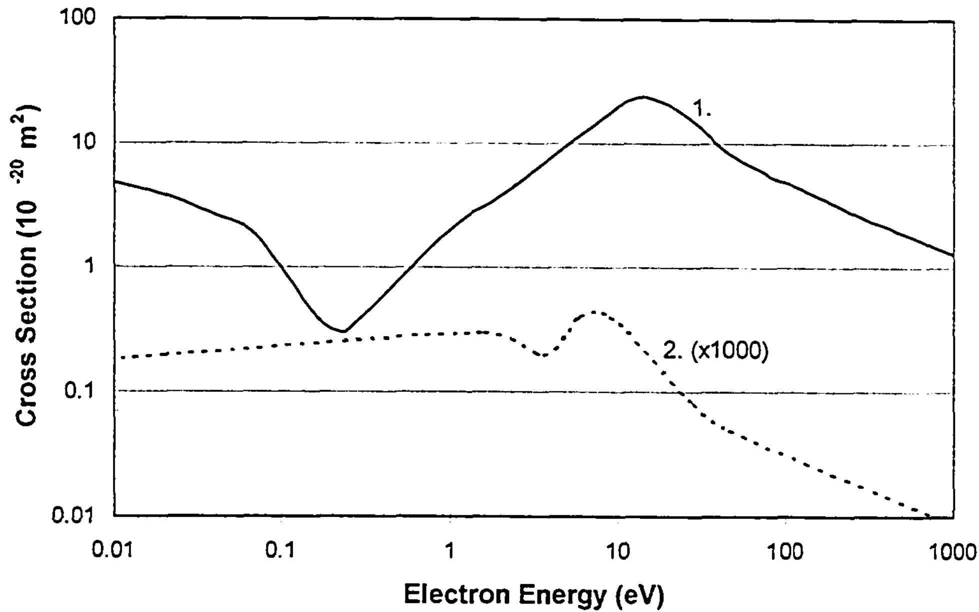

Figure 3.4: Energy dependant electron collision cross sections. 1) elastic collisions with argon, 2) super-elastic collisions with meta-stable argon. (Note super-elastic cross section has been multiplied by a factor of 1000)

and cooling as they approached the anode. The cold electron group was the low energy component of the hot electron group that could not penetrate the anode sheath and were thus reflected back into the plasma bulk forming a background collection of electrons. Additionally, Sheridan found the total electron density did not decrease at increasing distances from the cathode but remained constant. As they noted, this is in contrast to the observations of Rossnagel and Kaufman[91] who, as here, observed an overall decrease in n_e with distance. It may be the Sheridan system is not directly comparable. Sheridan's explanation as to the source of the hot and cold electron groups also does not seem applicable here. In this system, the cold electron group becomes colder (higher slope in fig. 3.3) and total n_e decreases as it approaches the anode (chamber wall) which implies that it is moving toward the anode and is not static or moving away from it. The hot electron group increases in temperature (lower slope in fig. 3.3) as it approaches the anode, although the probe current (and thus the density) due to these hot electrons is reduced.

Finally, one intriguing possibility was suggested by Lee and Lieberman[111] where electrons undergo superelastic collisions with metastable argon atoms:

Reproduced with permission of the copyright owner. Further reproduction prohibited without permission.

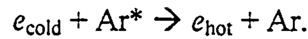

$$e_{cold} + Ar^* \rightarrow e_{hot} + Ar.$$

(See figure 3.4). In this case, the inelastic energy held by the metastable argon atoms is transferred to the cold electron resulting in a hot electron. If this process occurs at a sufficient rate then there would be a non-negligible population of hot electrons. It is also reasonable to expect this group of electrons would appear Maxwellian since the source group of cold electrons is Maxwellian and the energy transferred in the collision is always the same due to the discrete inelastic energy of the excited argon atom.

There does appear to be one consistent trend with respect to the bifurcation of hot and cold electron temperatures. In figure 3.1e (lateral survey), the 10 cm scans show a trend whereby the hot and cold T_e are closest directly above the well region where electron density is highest. As one moves laterally the density drops and the separation in hot and cold T_e widens. This is the same as the trend observed for the normal survey above the etch region and appears to be a consistent trend regardless of pressure. In summary, where bi-Maxwellian distributions exist, the hot and cold electron temperatures are closest where the electron density is highest. As the density drops, further from the plasma source, the cold electron temperature drops and the hot electron temperature rises.

It is noted that electron-electron (e-e) collisions are an important consideration in the thermalization of EEDF's due to the efficient transfer of energy in like-particle collisions. However, our investigation shows little evidence that the two Maxwellian groups comprising the EEDF are moving toward thermal equilibrium or are even significantly coupled. Further, it is noted that the frequency of e-e collisions is much lower than for electron-neutral collisions due to the low ionization fraction (< 0.1%) and differences in mean free paths. Koo, Hershkowitz and Sarfaty[108] indicated that this low ionization fraction meant e-e collisions were not a significant factor for transport of electrons across magnetic field lines. While the dynamics are different for thermalization, it does appear that the effect of e-e collisions may also not be significant enough to relax EEDF's into Maxwellian distributions in magnetron devices of this scale.

Reproduced with permission of the copyright owner. Further reproduction prohibited without permission.

3.3.2 Spatial Surveys with Oxygen Component

Oxygen is commonly used in magnetrons as a reactive gas to form oxidized films. The addition of an electronegative, diatomic gas into the sputter atmosphere greatly increases the complexity of the plasma environment. Previously, with argon gas, there were few important impact processes between electrons and atoms. With oxygen gas several new processes are possible[50,111,112,113] including:

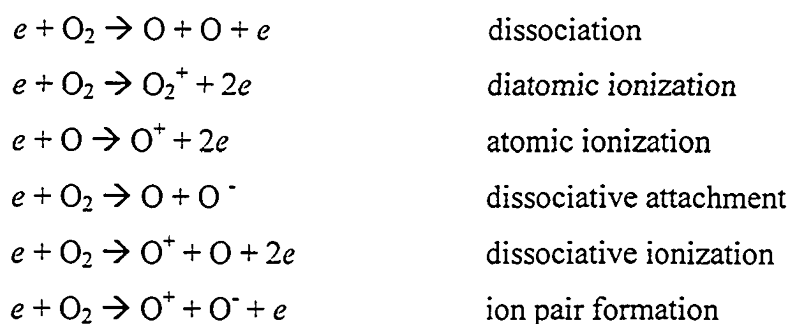

$e + O_2 \rightarrow O + O + e$	dissociation
$e + O_2 \rightarrow O_2^+ + 2e$	diatomic ionization
$e + O \rightarrow O^+ + 2e$	atomic ionization
$e + O_2 \rightarrow O + O^-$	dissociative attachment
$e + O_2 \rightarrow O^+ + O + 2e$	dissociative ionization
$e + O_2 \rightarrow O^+ + O^- + e$	ion pair formation

as well as a fairly vast array of recombination, excitation, charge exchange and other ionization processes. Nanbu[50] used a set of 31 oxygen processes for simulation purposes, noting that processes whereby negative ions are formed have relatively small cross sections. The addition of so many new inelastic processes has some major implications. The energy of primary electrons is now distributed over many more processes, some of which do not result in positive ions used to sustain the discharge, a factor that may be amplified since negative ions are now a component of the plasma environment. Also an important consideration, as Chapman[16] noted, dissociation, attachment and ionization of diatomic gases in glow discharge devices normally results in enhanced chemical activity since the products of such a process are usually more reactive than the parent molecule.

Here lateral and normal surveys are repeated with 4% and 16% O_2 in argon and compared to the pure argon cases. The lateral surveys are done for only half the cathode width since the pure argon lateral surveys demonstrated symmetry about the middle of the cathode. Normal surveys are still done with one above the center of an etch track (4 cm position) and one above the well region (8 cm position). These

Reproduced with permission of the copyright owner. Further reproduction prohibited without permission.

surveys are done at 40 mTorr only. Cathode voltages were 441 ± 5 volts for 4% O_2 and 506 ± 6 volts for 16% O_2 (see Appendix 1).

Results are displayed in figures 3.5 and 3.6 where 3.5 provides the usual complement of data for the lateral surveys (including pure argon results from the previous section) and 3.6 provides this data for the normal surveys.

Figure 3.5a shows the general response to various oxygen atmospheres. At 10 cm from the cathode, the electron density drops considerably for the higher (16%) oxygen environments. There also appears to be a nominally lower density for 4% O_2 over pure argon. At 10 cm the electron density changes little spatially except for a slight increase in density above the well region at the center of the cathode, as seen before. At 5 cm distance the maximum n_e increases and moves to the region above the etch track. The trend where higher electron density levels are consistent with lower oxygen admixture in the sputtering environment remains. At 3 cm distance from the cathode the density increases again and remains over the etch region nearest the plasma 'source'. At this distance it is not clear that there is much difference between the different oxygen levels in terms of profile or density. This is contrasted by the normal surveys (fig. 3.6a) at the 4 cm lateral location which shows higher electron density for lower oxygen admixtures. All three oxygen levels show the same trend along this chord where density is highest near the cathode and drops at greater distances.

The normal survey conducted above the well region shows a small increase in density farther from the cathode though the total span of densities along this chord is not greater than the estimated error for all oxygen compositions.

It is difficult to speculate on the dominant factors that result in lower densities with increased oxygen levels due mostly to the much more complex dynamics involved. There are, however, potential contributing factors of which a couple are mentioned here. It is observed that the cathode voltage increases with higher oxygen levels and so, for a given cathode current, the power input to the gas will be greater, heating the gas. As the ions are generally in thermal equilibrium with the gas, the flux of ions to the cathode sheath edge will be unchanged (for a constant cathode current) only if the density of ions decreases. Also, at higher oxygen levels a greater portion of

Reproduced with permission of the copyright owner. Further reproduction prohibited without permission.

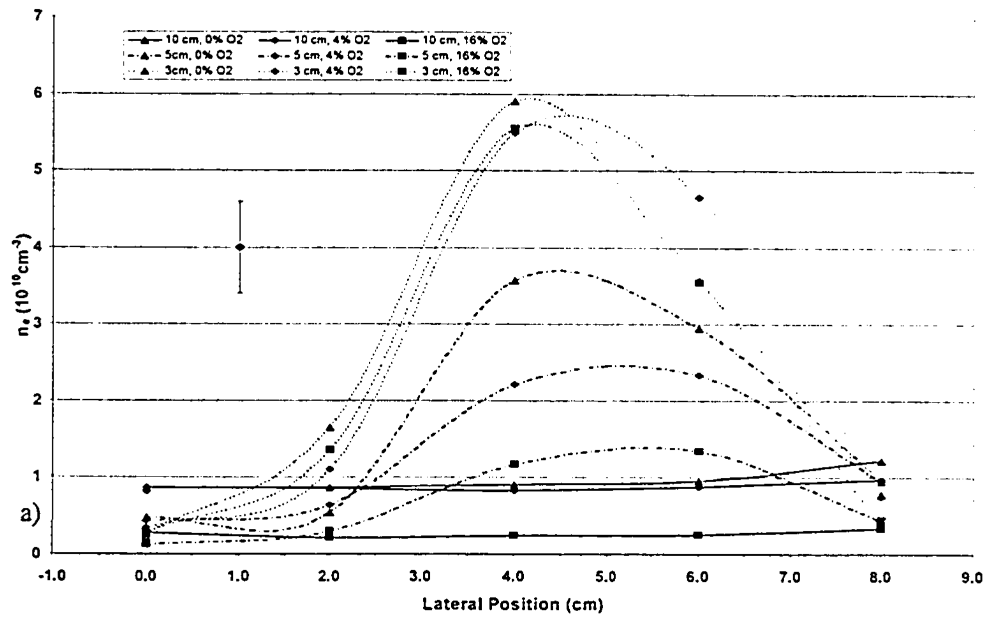

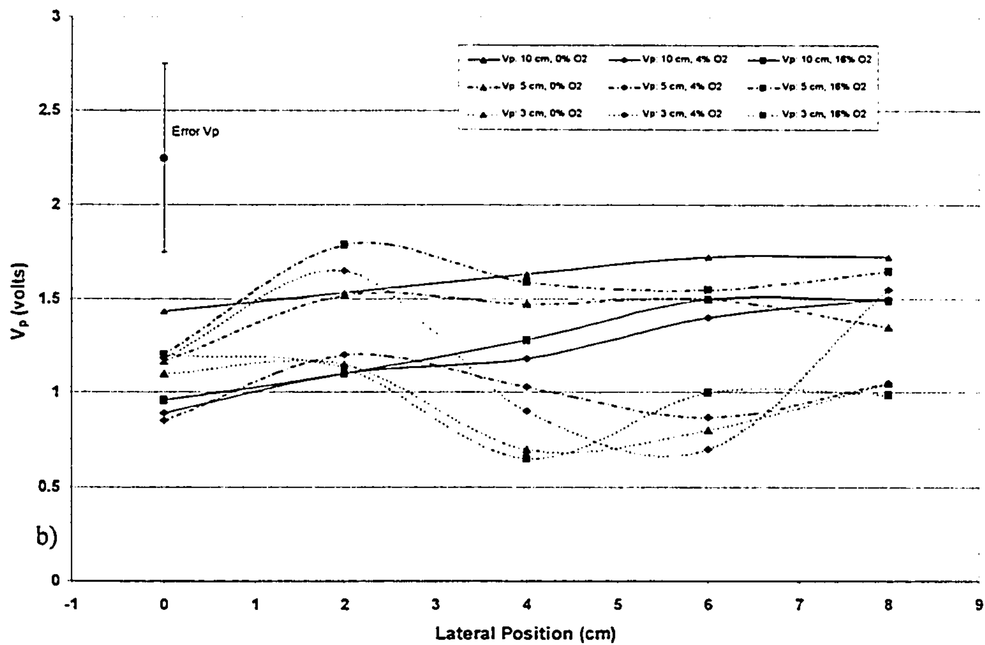

Figure 3.5: a) Electron density for lateral surveys with oxygen at 3 distances from the cathode and at 40 mTorr., b) plasma potential (V_p) Typical error bars are indicated on each graph.

Reproduced with permission of the copyright owner. Further reproduction prohibited without permission.

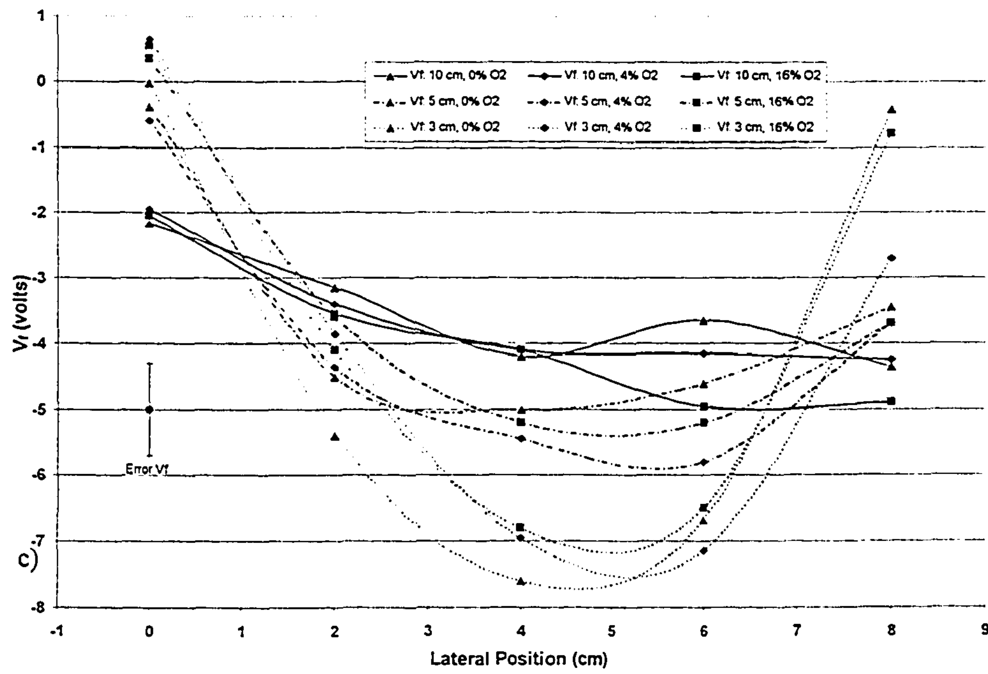

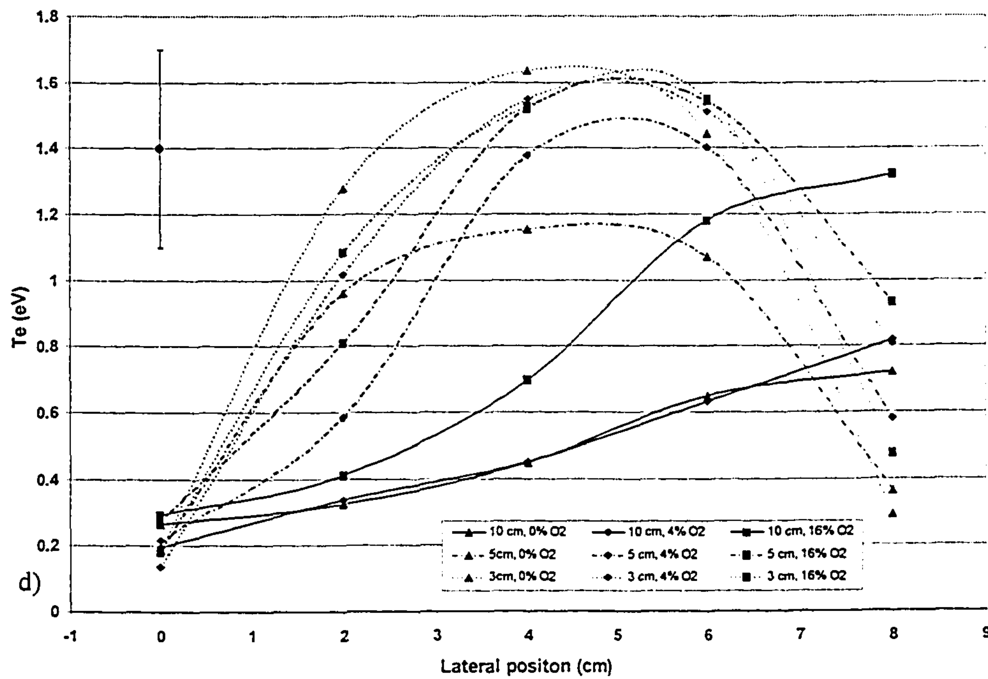

Figure 3.5: c) floating potential (V_f), d) electron temperature (T_e) Typical error bars are indicated on each graph.

Reproduced with permission of the copyright owner. Further reproduction prohibited without permission.

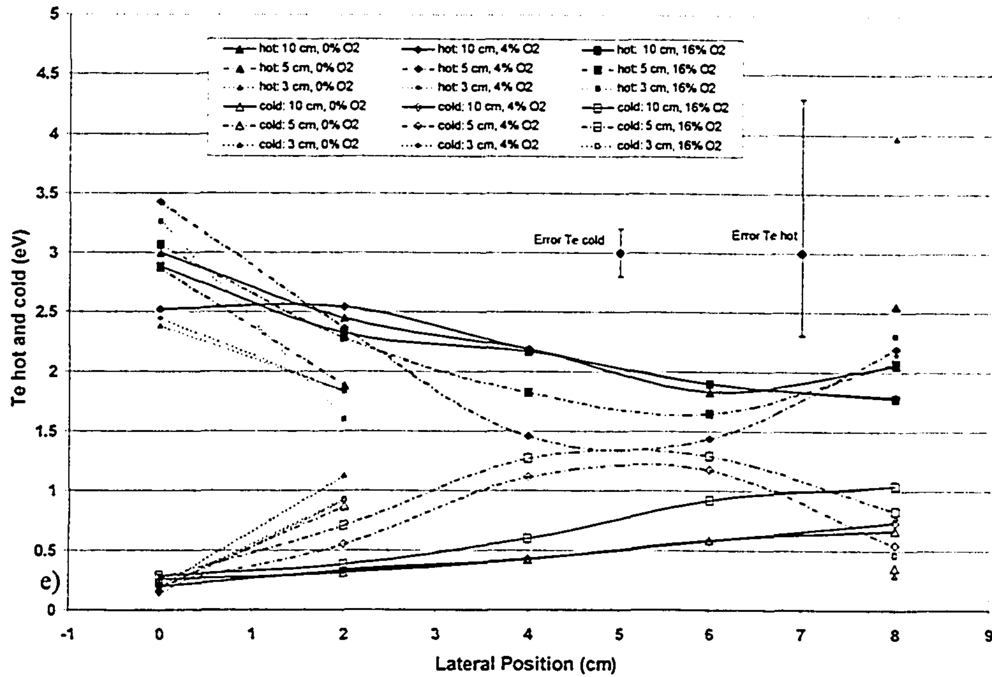

Figure 3.5 e) hot and cold electron group temperatures where bi-Maxwellian groups exist. Typical error bars are indicated on each graph.

an energetic electron's energy goes into dissociative processes which do not result in ion formation. Production of negative ions is also known to increase at higher oxygen levels[114]. These factors are capable of altering the dynamic equilibrium of the plasma. These concepts, as examples of the much more complex plasma environment, make it very difficult to experimentally determine what processes dominate in providing the observed response of electron density to oxygen level. Use of simulation where a researcher can selectively include or exclude specific processes (such as ionic recombination) likely is the most fruitful avenue to investigate these complex plasmas.

The lateral and normal surveys indicate there are some trends in T_e with respect to oxygen. Figure 3.5d shows electron temperature for all lateral surveys and oxygen environments. As with n_e, the 3 cm distance lateral surveys show no distinguishable difference vs. oxygen for T_e. Electron temperatures are highest above the etch region, reach a local minimum above the well region and are lowest at the outer edge of the cathode. At the 5 cm distance, there appears a general trend whereby higher oxygen

Reproduced with permission of the copyright owner. Further reproduction prohibited without permission.

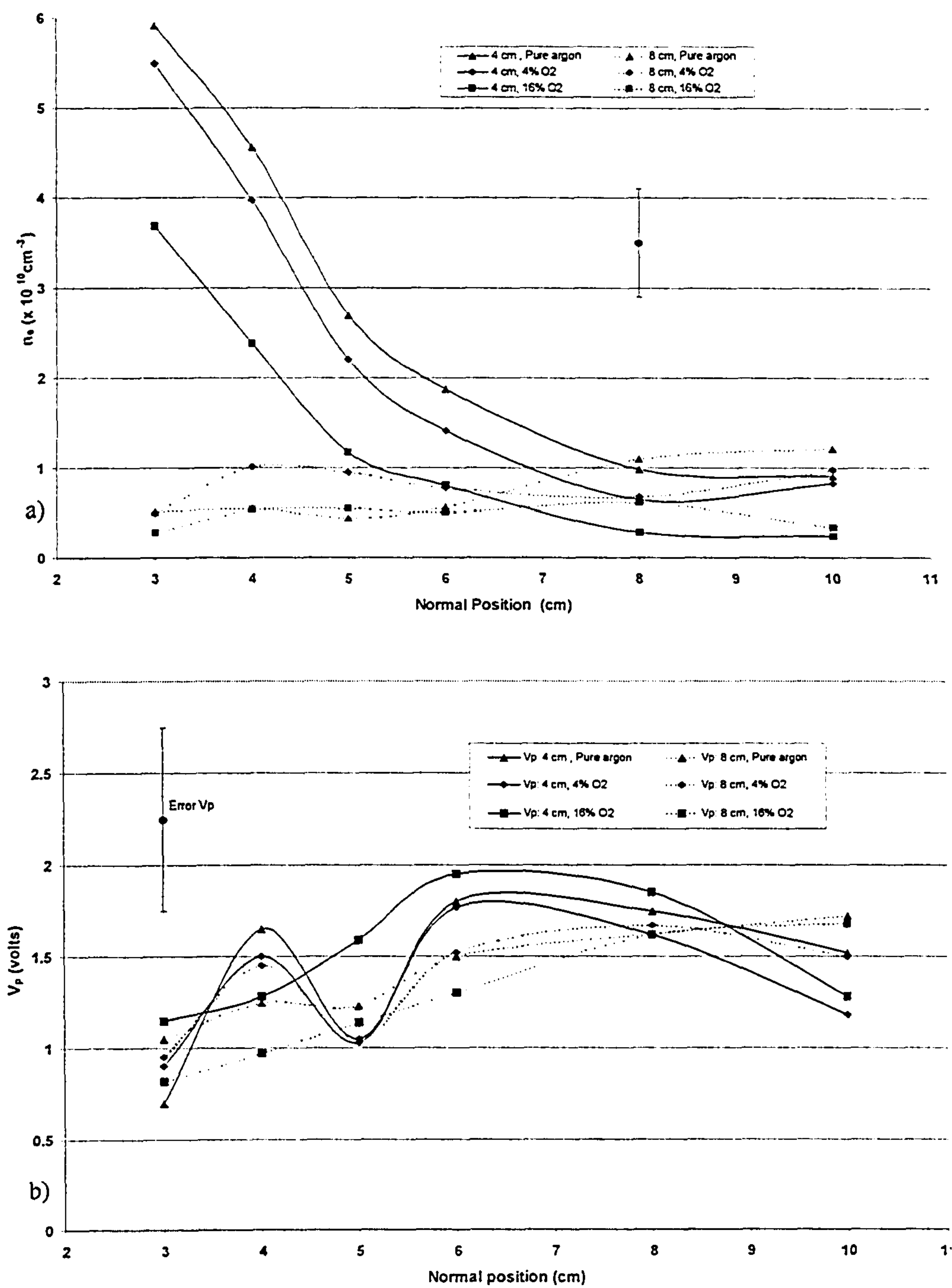

Figure 3.6: a) Electron density for normal surveys with oxygen at 3 distances from the cathode and at 40 mTorr., b) plasma potential (V_p) Typical error bars are indicated on each graph.

Reproduced with permission of the copyright owner. Further reproduction prohibited without permission.

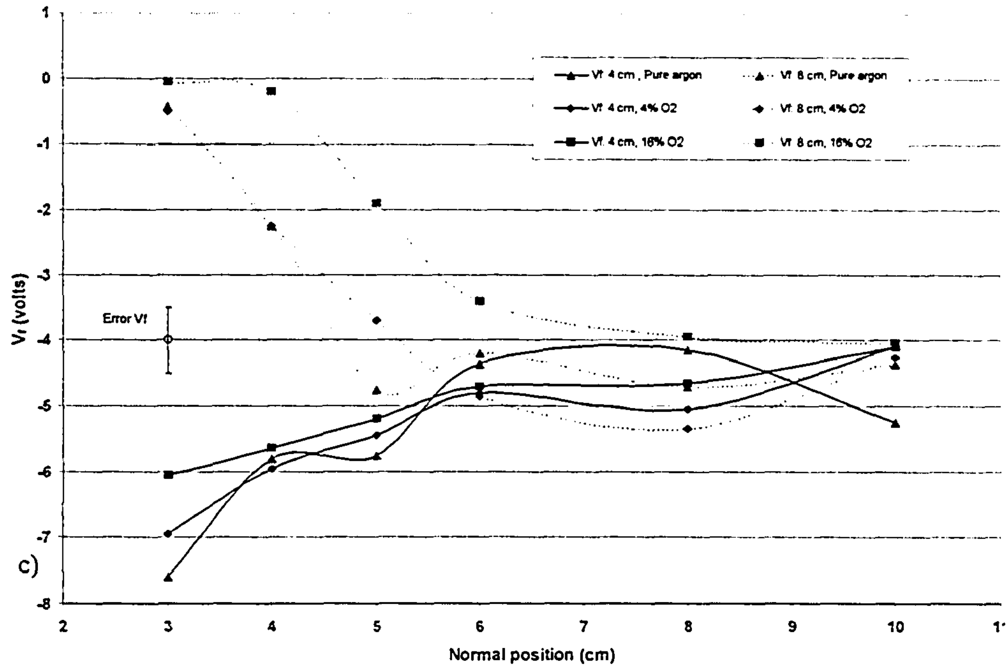

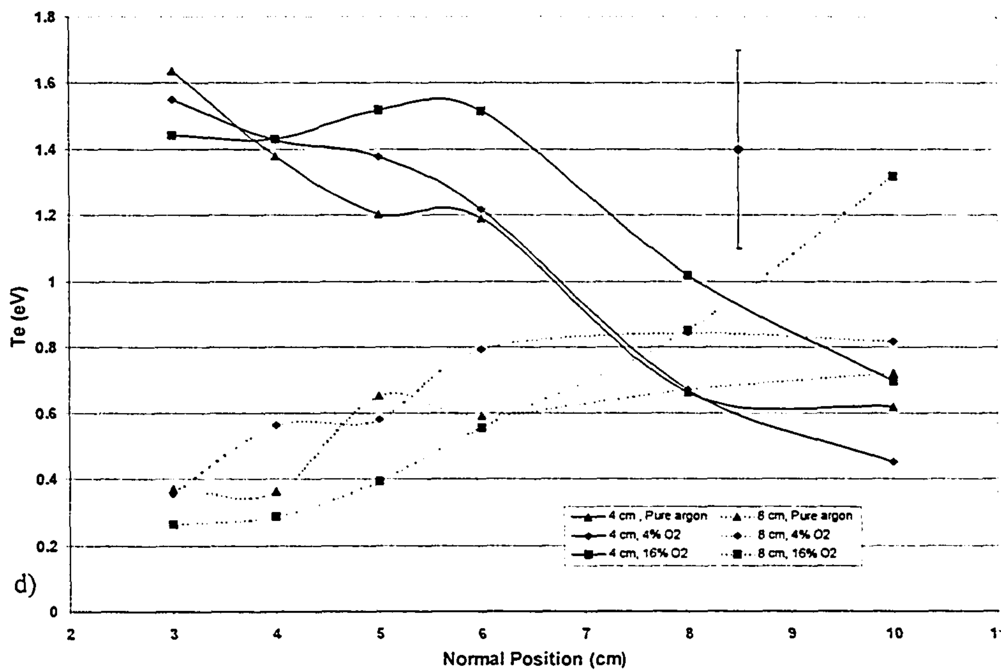

Figure 3.6: Plasma parameters for normal surveys with oxygen. c) floating potential (V_f). d) electron temperature (T_e). Typical error bars are indicated on each graph.

Reproduced with permission of the copyright owner. Further reproduction prohibited without permission.

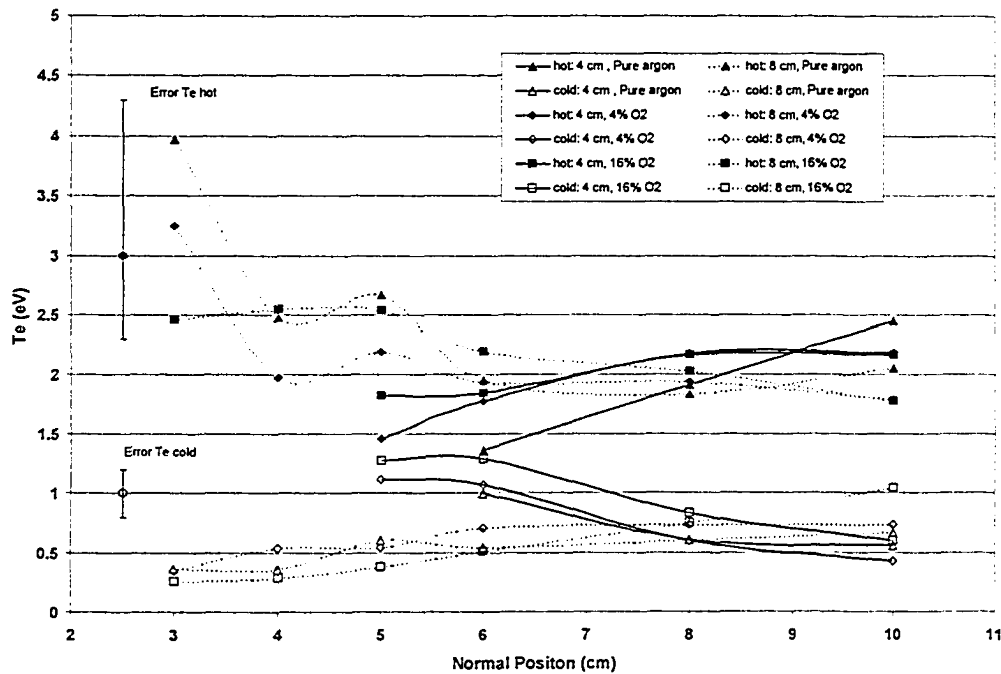

Figure 3.6 e) hot and cold electron group temperatures where bi-Maxwellian groups exist. Typical error bars are indicated on each graph.

levels are associated with higher T_e. At 10 cm distance, this trend seems to also exist where the 16% O_2 case has higher T_e. There is little difference between the 0% and 4% O_2 cases.

The observation of higher T_e with more O_2 is consistent with higher cathode voltages as primary electrons are injected into the plasma bulk with higher energy. The rise in cathode voltage may be due to several factors. As more oxygen is added, more energy is spent by primary electrons in dissociation processes. In this case, primary electron energy has been expended in an event that does not create a new positive ion resulting in a loss of ionization efficiency. The cathode voltage must increase to maintain the required cathode current. Additionally, the voltage will increase if there is significant oxidation of the cathode surface resulting in a thin insulating layer[115] of oxides on the cathode surface reducing the conductivity of the target. In either case, a higher cathode voltage will imply more energy is given to ejected electrons. Since the primary electrons are introduced into the plasma atmosphere with more energy, it is quite reasonable to expect an overall increase in the electron temperature.

Reproduced with permission of the copyright owner. Further reproduction prohibited without permission.

The reality of these trends must be scrutinized after an examination of figure 3.5c which shows no apparent trend in V_f with respect to oxygen for any of the lateral surveys. As previously mentioned, one usually expects a trend in T_e to be mirrored by a trend in V_f which is not the case here. Either the dynamics of the plasma environment have changed or the trends observed in T_e are not real. This interesting situation is also present in the normal surveys above the etch region (figure 3.6d, 4 cm lateral position) which shows higher T_e with more O_2 at all distances greater than 5 cm from the cathode. Closer to the cathode than this, any differences in T_e are obscured. Consistent with the lateral survey, there is no apparent trend in V_f with respect to O_2 except at 10 cm where higher oxygen levels are consistent with higher T_e. The presence of negative ions could account for an unresponsive V_f when T_e changes. Since V_f is a function of the relative fluxes of positive and negative charges to the probe, replacing a portion of the electrons with less mobile negative ions would reduce the flux of negative charges to the probe. This would give rise to a less negative V_f. At the same time, if the electrons are more energetic, then the flux of electrons, relative to their own density, would increase leading to a more negative V_f. If these two effects are of similar magnitude then V_f could conceivably be unresponsive in the face of a significantly different T_e. There has, however, been no evidence that there is a significant population of negative ions (see §3.2.(v)).

To confirm or refute the trends observed for T_e and V_f, it is likely fruitful to use a mass spectrometer to determine the ratio of negative to positive ions and then conduct a more detailed analysis of the LP data. As Kim[116] *et al* indicated, LP diagnostics are 'very difficult' in the presence of negative ions. This suggests the complexity of such environments makes it unwise to speculate on such unusual responses until more information is available.

The V_p appears to have the same small scale response as was observed in the pure argon case (§3.3.1), particularly for the lateral surveys (fig. 3.5b). The normal surveys (fig. 3.6b) do seem to indicate a lower V_p nearest the cathode above the etch track, generally rising at progressively greater distances from the plasma source. This is a weak trend overall and may be real given the consistency from survey to survey though requires confirmation.

Reproduced with permission of the copyright owner. Further reproduction prohibited without permission.

Consistent with previous data are the temperatures of the hot and cold electron groups. The same trends are observed for surveys with oxygen in fig 3.5e (lateral surveys) and 3.6e (normal surveys) that were observed for pure argon cases. Bifurcation in electron groups takes place in approximately the same locations regardless of the oxygen component of the system. The coldest cold electrons are found where the hottest hot electrons are found and visa versa. Where the hot and cold electron temperatures are the closest the electrons density is the highest relative to all locations where bi-Maxwellian distributions exist. Since the cold electrons are the dominant species, the effective temperature essentially follows the same trend as the cold electrons.

These surveys do not, as yet, present a very clear picture of how the plasma environment responds to the presence of oxygen. This is due to the sometimes weak responses with respect to oxygen levels and the sometimes conflicted data. Obtaining more LP characteristics where the oxygen level is adjusted in finer increments at only a few select locations within the plasma may help to confirm the observed trends with respect to oxygen levels. This is done in the next section (§3.3.3). Also, simulations of such scenarios may help to confirm the presence of weak trends that are not easy to experimentally confirm due to the level of error in such techniques. This, however, is an extensive undertaking and thus recommended as future work. The real value of these surveys is likely to become apparent when coupled with surveys using the PSMS or OES techniques. With such spatial information, a much better understanding of the electron-ion relationship can be obtained with the commensurate insights into magnetron plasma dynamics.

3.3.3 Oxygen Surveys for Three Select Locations within the Reactor

Langmuir probe surveys were conducted with respect to changes in the oxygen component of the sputtering gas. Oxygen was varied from 0% to 20% O_2 in argon at both 40 mTorr and 5 mTorr and the cathode current was held constant at 0.6 A. Cathode voltages ranged from 407±2 volts (0% O_2) to 518±4 volts (20%) at 40 mTorr and from 562±6 volts (0% O_2) to 645±14 volts (20% O_2) at 5 mTorr. The

Reproduced with permission of the copyright owner. Further reproduction prohibited without permission.

voltages for all of these data points are given in appendix 1. Surveys were conducted at three different locations within the reactor that typified the different plasma regions. One location was 5 cm directly above the etch region (z = 5 cm, x = 4 cm) which is near to the plasma source. A second location was 10 cm directly above the etch region (z = 10 cm, x = 4 cm) which is a location farthest from the source. It could be argued that this point should be above the well region since the electron density is highest there for the 10 cm distance. However, the difference is small and the chosen location more directly comparable with the location nearest to and above the plasma source. The third location chosen was 5 cm directly above the well region (z = 5 cm, x = 8 cm) since this region represents a unique local minimum. Results from these surveys are given in figure 3.7.

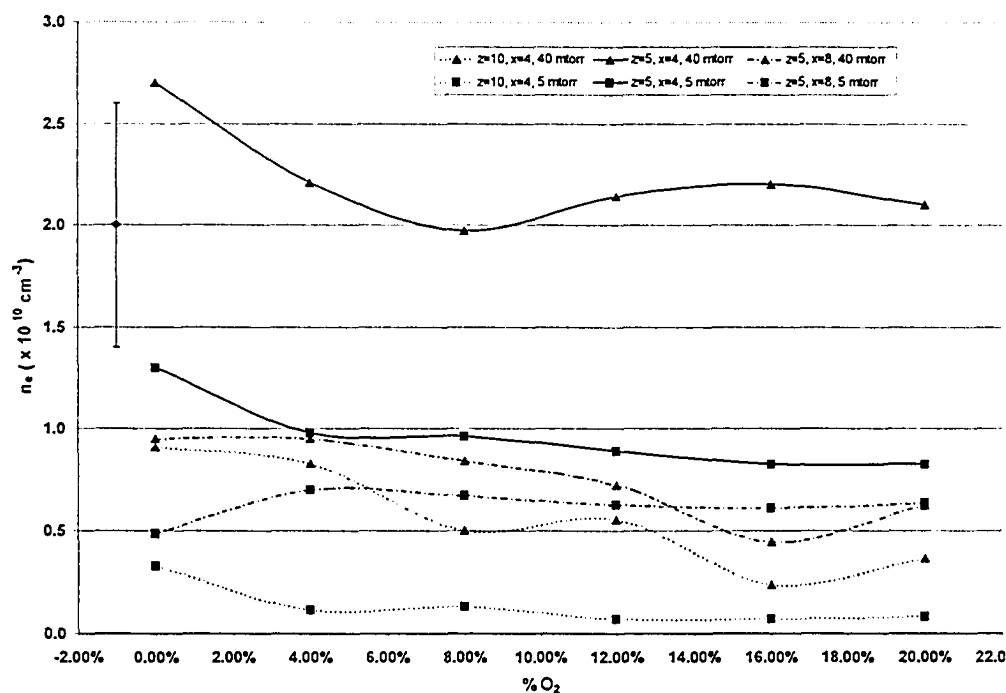

Figure 3.7: a) Electron density for oxygen surveys at 3 locations within the reactor and at 5 and 40 mTorr. Typical error bars are indicated on each graph.

Reproduced with permission of the copyright owner. Further reproduction prohibited without permission.

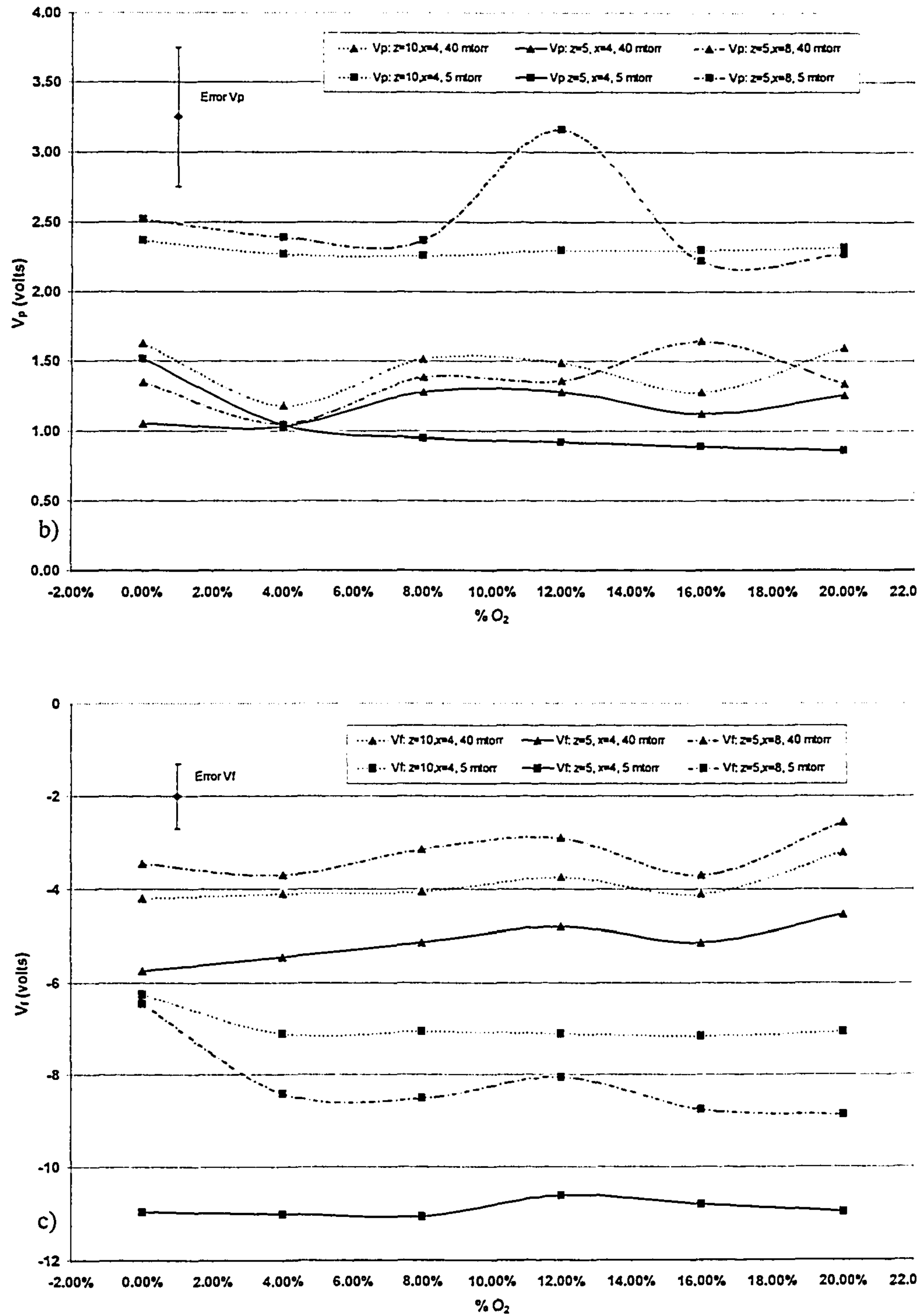

Figure 3.7: LP plasma parameters for oxygen surveys. b) plasma potential (V_p), c) floating potential (V_f). Typical error bars are indicated on each graph.

Reproduced with permission of the copyright owner. Further reproduction prohibited without permission.

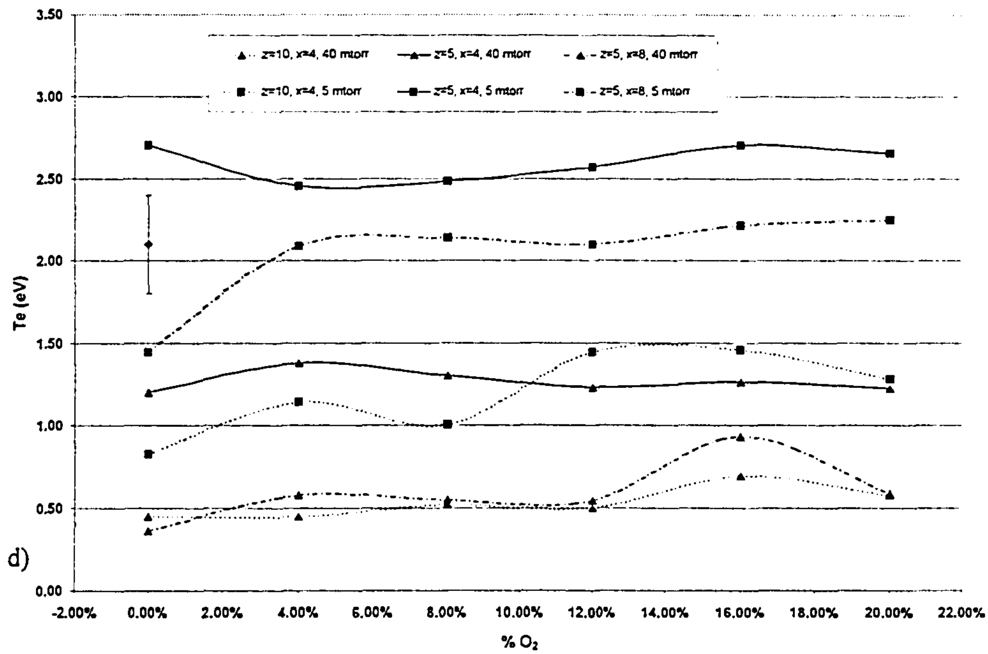

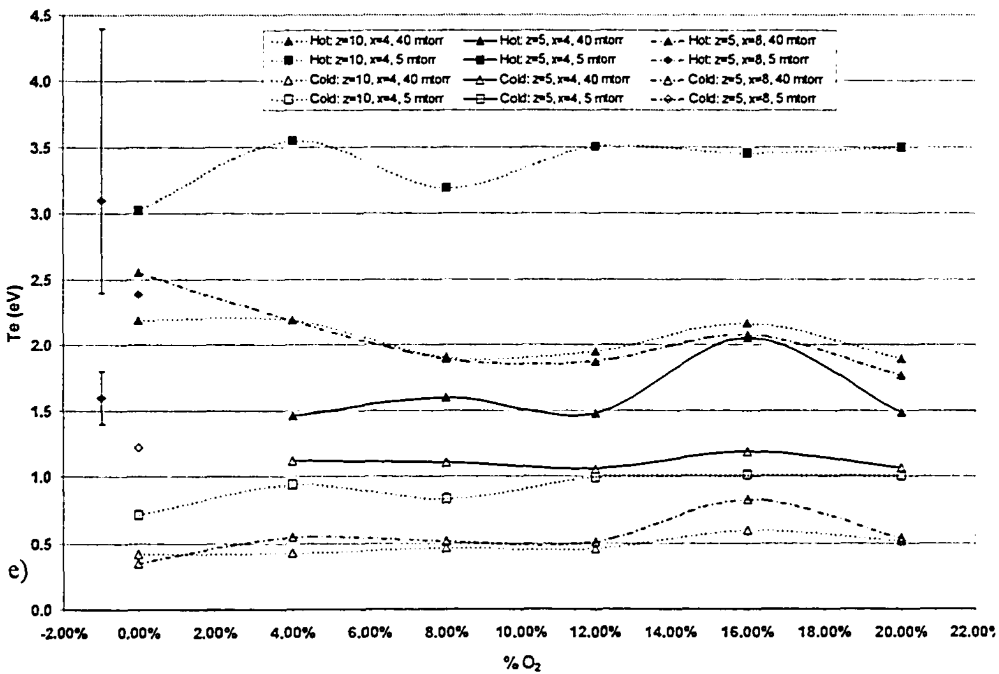

Figure 3.7: d) electron temperatures (T_{eff} where bi-Maxwellian distributions exist), e) hot and cold electron group temperatures where bi-Maxwellian groups exist. Typical error bars are indicated on each graph.

Reproduced with permission of the copyright owner. Further reproduction prohibited without permission.

In general, the trends observed for lateral surveys with oxygen seem to be preserved, though the responses to oxygen appear more subtly than they did previously. The weakened response could be due to some shorter term systemic hysteresis that is more dominant when oxygen levels are frequently adjusted. This could include target poisoning due to the oxygen within the reactor. As the oxygen level is adjusted for consecutive data points, the system does not reach equilibrium (in terms of target poisoning vs. ambient oxygen level) for some time beyond when the next probe trace was taken. This effect would be minimized for the spatial surveys since there was a long period of time between adjustment to the oxygen level.

Figure 3.7a shows the response of n_e to oxygen. Higher densities are observed for 40 mTorr over 5 mTorr and for the location closest to the plasma source, as before. As the oxygen level increases from 0% to 20% the electron density drops, regardless of pressure or location. This remains consistent with the trends observed in the previous section.

As with the n_e, the response of T_e (fig 3.7d) to oxygen level appears dampened for these surveys compared to the spatial surveys. In some cases there does appear to be a very subtle trend whereby the T_e increases with oxygen. However, the response is so weak it is questionable the trend exists. If there is no response, then this is consistent with the previously observed lack of change to V_f versus oxygen - a trend observed here as well. As mentioned before, this may result from more energy being used to dissociate O_2, requiring a higher cathode voltage leading to higher T_e. Also, as previously, the presence of negative ions may be a factor and obscure the trends with respect to n_e and T_e. In general higher electron temperatures are observed for 5 mTorr versus 40 mTorr and for locations closer to the plasma source. These responses have been observed for the inert gas (Ar) case. It is unclear if T_e changes with oxygen level, and it appears the LP technique may not be ideally suited for plasmas with oxygen components.

The V_f and V_p in figure 3.7c and 3.7b do not indicate any trend with respect to oxygen level. The responses are quite flat and deviations appear random and within estimated error. The V_f is lower (more negative) for 5 mTorr vs. 40 mTorr which mirrors the higher T_e for 5 mTorr. For these oxygen surveys and with respect to

Reproduced with permission of the copyright owner. Further reproduction prohibited without permission.

location and pressure, the V_f does respond, as expected, to the observed T_e in figure 3.7d. This response does not appear with respect to oxygen level, nor did it appear for the lateral surveys with various oxygen levels previously. V_p, as before, appears to have little to no response to oxygen level, although it is noted that lower pressures seem to have slightly higher V_p. This was also observed between the two pressures used for lateral surveys in pure argon. Thus, V_p seems to respond to pressure. This will be further discussed in the section that deals with pressure surveys (§3.3.4).

The hot and cold electron temperatures in figure 3.7e show no noteworthy trends. Where bi-Maxwellian distributions exist, they do not seem to respond to oxygen level. Figure 3.7e is therefore included only for completeness.

The responses to oxygen level are weak and therefore, inconclusive. As such, alternative experimental techniques should be used in conjunction with simulation to determine the effect of oxygen on plasma parameters and specifically on electron dynamics.

3.3.4 Pressure Surveys for Three Select Locations within the Reactor

Langmuir probe surveys were conducted versus pressure at the same three locations used for the oxygen surveys. This was done for 3 different oxygen levels: 0%, 4% and 16% O_2. Cathode voltage and the response to process conditions is shown in appendix 1. These surveys showed some distinctive trends for n_e, T_e, V_f and even V_p.

In figure 3.8a, n_e showed a definite increase with pressure, this being most obvious above the etch region at z = 5 cm, x = 4 cm. Here, at 0% O_2, the n_e increases approximately by a factor of two for a factor of ten increase in pressure. For higher oxygen levels, lower n_e is again observed and the increase in n_e with pressure is lesser than for pure argon. At the other two locations, densities also increase with pressure though by varying degrees. This data appears to support the existence of a trend in n_e with respect to oxygen level and reinforces the contention that the data taken in §3.3.3 was obscured by some sort of short term system hysteresis, a factor that should be limited here as in §3.3.2. At the well region (z = 5 cm, x = 8 cm), the trend first

Reproduced with permission of the copyright owner. Further reproduction prohibited without permission.

observed for lateral surveys with oxygen (§3.3.2) can be seen where higher oxygen levels lead to lower n_e. This is consistent for all three oxygen levels and all pressures. Far from the cathode, at z = 10 cm, x = 4 cm, the highest oxygen level of 16% always has the lowest n_e, however, the 0% and 4% levels appear not to indicate a consistent difference. The difference in n_e between all these oxygen levels is admittedly small and the deviations from a 'smooth' trend line for 0% and 4% are more apparent than for other surveys. It appears the previously observed trend with respect to oxygen levels exists here, especially for the z = 5, x = 4 location. This is another situation where detailed simulation will be of use in determining the likelihood of subtle trends.

The trend whereby higher n_e is observed at higher pressures has been observed (see Bell *et al*[92] and Spatenka *et al*[12] for typical examples). It is not altogether apparent as to why this would necessarily be the case. One perspective is to view the plasma density as a balance between creation and loss of the charged plasma species. Creation predominantly taking place through ionizing collisions and loss predominantly through collisions with walls. Recombination of charged species is a low probability event and regarded negligible[16] except for plasmas with negative ions[114,116]. At higher pressures, the collision frequency for energetic electrons increases as the mean free path decreases. This effectively increases the ionization rate (or ion creation rate), a factor not necessarily matched by the loss rate to the chamber walls. This would result in a higher plasma density at higher pressures.

In figure 3.8d, the T_e shows some interesting results, particularly at the low end of the pressure range. In general, higher pressures lead to lower T_e under all conditions. Closest to the etch region (z = 5 cm, x = 4 cm), the T_e is approximately 2.5 eV at 5 mTorr. This drops rapidly to less than 2 eV at 10 mTorr after which T_e drops less aggressively with pressure. This is also observed at the other locations and under all conditions. This suggests that between 5 and 10 mTorr there may be a change in the dominant electron cooling or transport mechanisms and may be further indication that the λ_m/L_r ratio is of some relevance as discussed in §3.3.1

Reproduced with permission of the copyright owner. Further reproduction prohibited without permission.

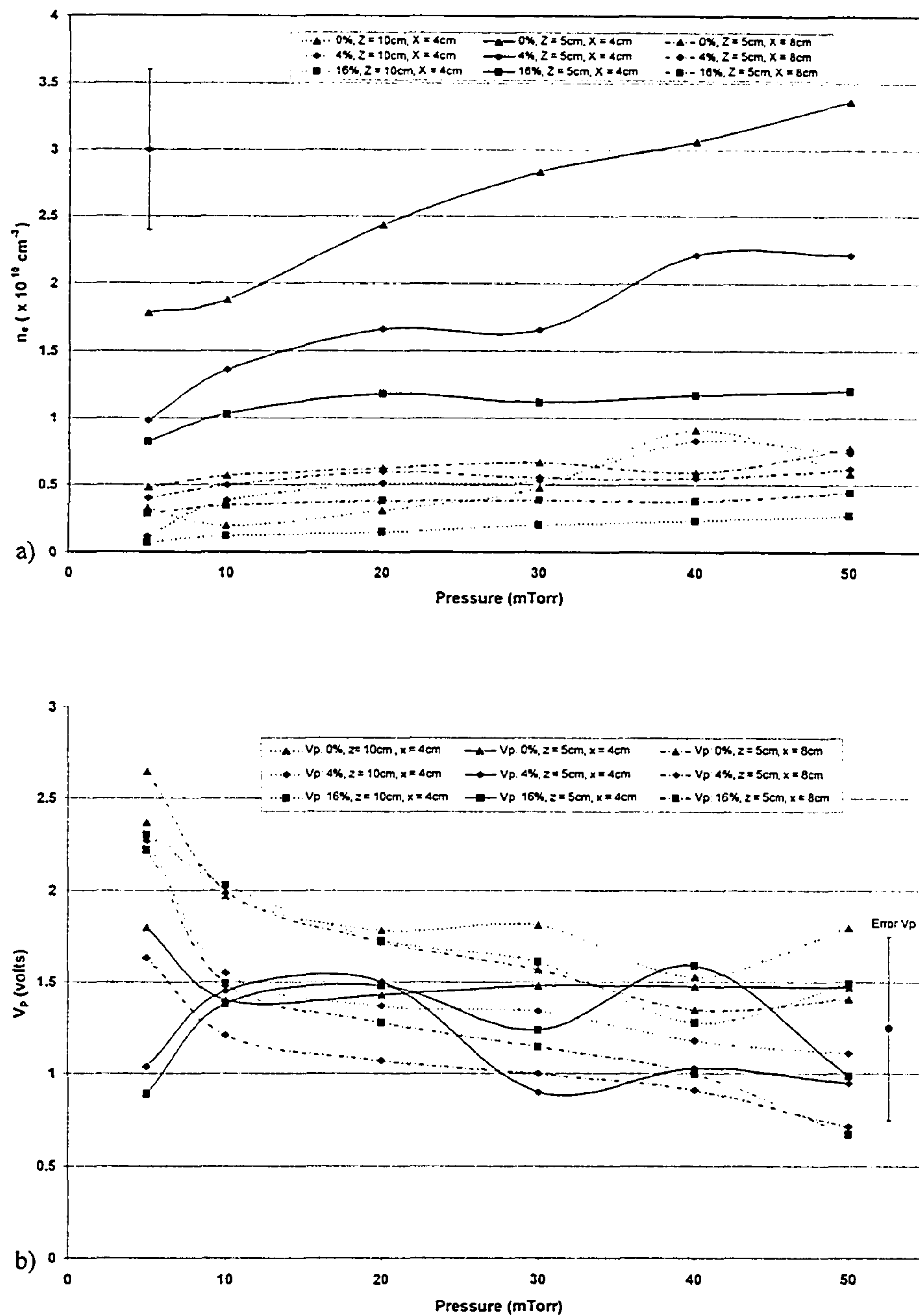

Figure 3.8: a) Electron density for the survey in pressure for three locations within the reactor, b) Plasma potential (V_p) for the pressure surveys. Typical error bars are indicated on each graph.

Reproduced with permission of the copyright owner. Further reproduction prohibited without permission.

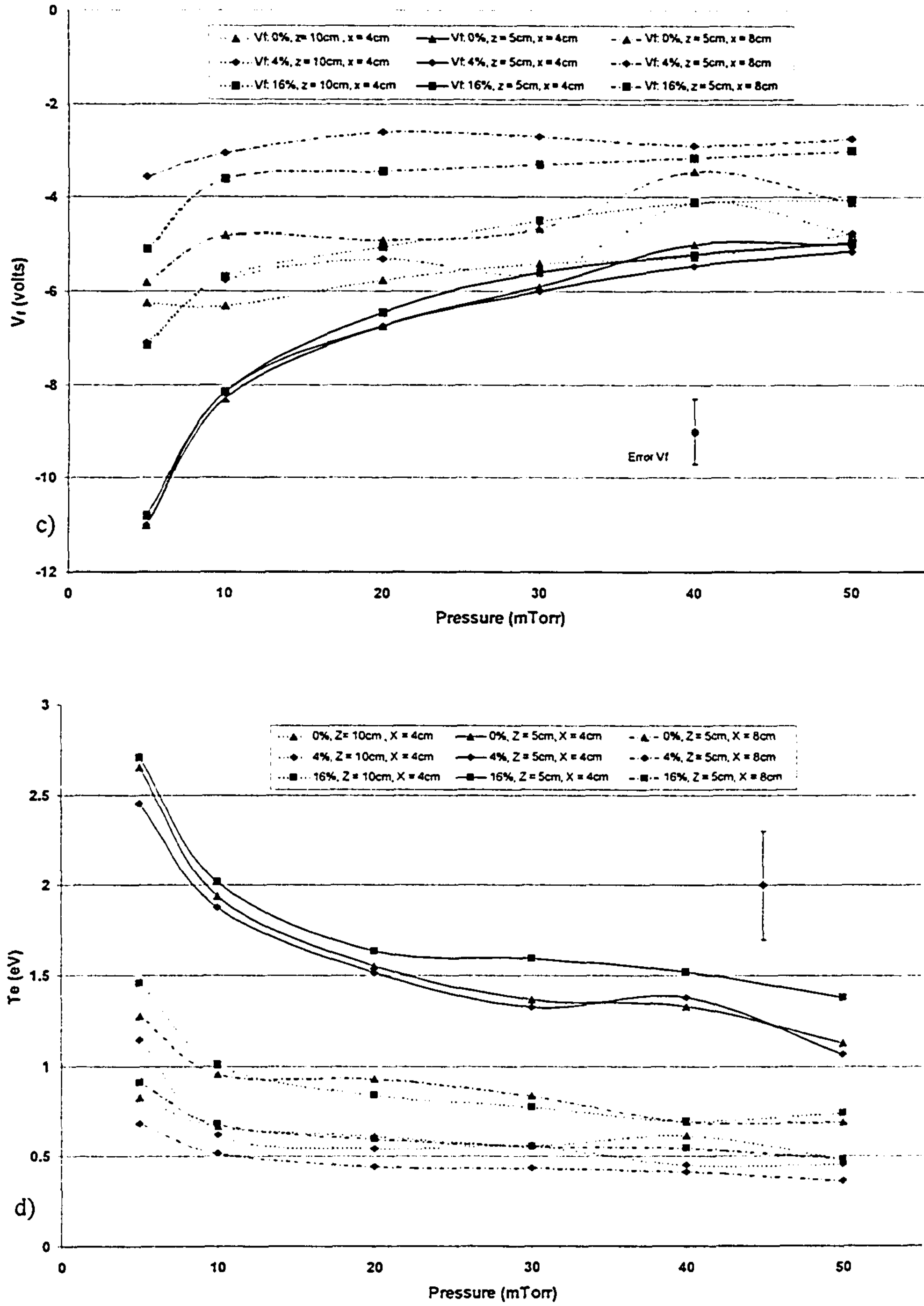

Figure 3.8: c) floating potential (V_f), d) electron temperatures (T_{eff} where bi-Maxwellian distributions exist). Typical error bars are indicated on each graph.

Reproduced with permission of the copyright owner. Further reproduction prohibited without permission.

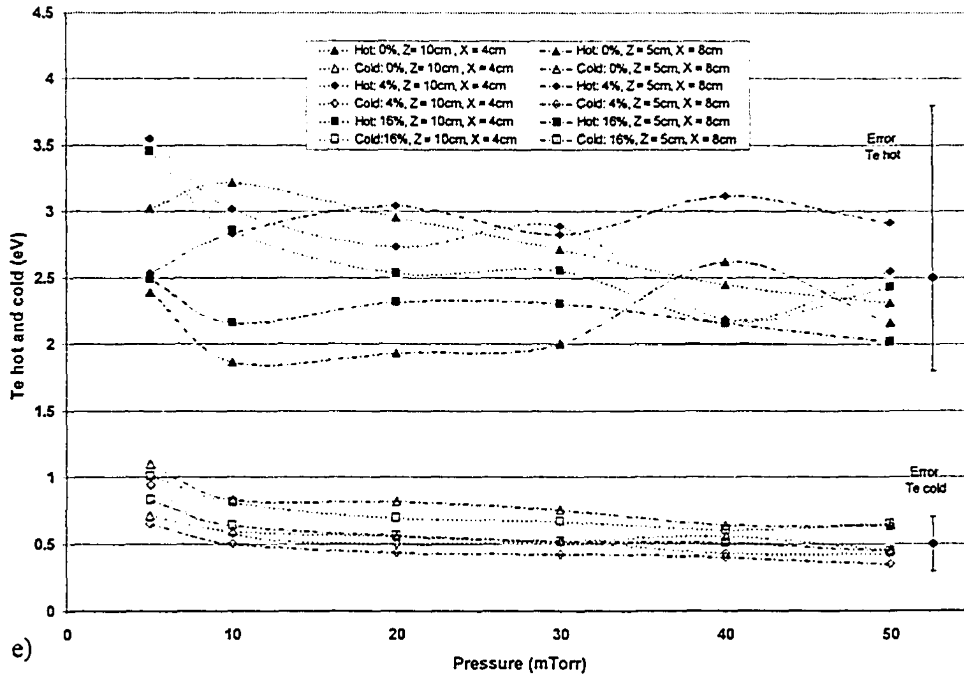

Figure 3.8 e) Hot and cold electron group temperatures where bi-Maxwellian groups exist for the pressure surveys. Typical error bars are indicated on each graph.

Bi-Maxwellian distributions do not appear just above the etch region at any pressure. However, elsewhere, it appears that the cold electron group temperature decreases with higher pressures mirroring the T_{eff} response. The hot electrons at z = 10, x = 4 cm also showed a decrease with higher pressures, though at z = 5, x = 8 cm no trend was obvious possibly due to less consistent data there.

For pressure surveys, the V_f (figure 3.8c) does correlate well with the T_e such that V_f is more negative where T_e is higher. The most dominant changes in V_f, as with T_e, take place between 5 mTorr and 10 mTorr with smaller changes taking place at higher pressures.

V_p (fig. 3.8b), which previously showed some small changes spatially, now also appears to show some dependence on the test parameter pressure. The exception here is immediately above the etch region where it appears V_p does not respond significantly. This is contrasted by the other two locations, which have V_p range from approximately 1.6 to 2.6 volts at 5 mTorr but drop to a range of 0.67 to 1.8 volts at 50 mTorr. Rossnagel and Kaufman[5] obtained V_p for two normal surveys (5 and 30 mTorr) above the etch region of a similar device. They found that at greater distances

Reproduced with permission of the copyright owner. Further reproduction prohibited without permission.

from the cathode, V_p was higher at 5 mTorr compared to 30 mTorr but close to the cathode the values were closer or had a very slightly higher V_p for 30 mTorr. This is the same type of response as observed here, though Rossnagel and Kaufman did not obtain data for other pressures or for other laterally positioned regions. It is unclear if V_p responds to oxygen level here. The greatest discrepancy with respect to oxygen is in the well region (z = 5, x = 8 cm) where pure argon appears to have a V_p that is about 0.5 volts above that for other oxygen levels. This is the approximate level of error in such measurements.

The trends observed here, possibly with the exception of V_p, suggests the plasma structure is sensitive to change in pressure.

3.3.5 Cathode Current Surveys for Three Select Locations within the Reactor

As with oxygen level and chamber pressure, surveys were completed by varying cathode current (I_c) and using the LP at the same three locations within the reactor. This was done in absence of oxygen but for two different pressures, 5 mTorr and 40 mTorr. The cathode voltages under these conditions are shown in appendix 1.

The n_e (figure 3.9a) increases with cathode current for both pressures where higher pressure correlates with greater density. For an increased cathode current to be realized there must be an increased flux of ions to the cathode sheath edge. Transport to the sheath edge is generally thermal in nature due to the lack of significant electric field in the plasma bulk. Thus, the ion flux will only increase if the ion density or ion temperature increases. For a 5-fold increase in cathode current there will have to be an approximate 5-fold increase in ion flux to the sheath edge. From figure 3.9a, one sees about a 5-fold increase in plasma density suggesting that the ion temperature has not increased significantly, if at all. It appears that it is much easier for the system to create ions than it is to heat the gas and ions. Naturally, as the ion flux to the cathode increases by 5-fold, the electron emission from the cathode should increase likewise. More energetic electrons will create more ions, and the trend is approximately correct. With an increase in I_c from 0.2 to 1.0 A the voltage increases from 350 V to 435 V at 40 mTorr and from 449 V to 632 V at 5 mTorr. This means each primary

Reproduced with permission of the copyright owner. Further reproduction prohibited without permission.

electron will be capable of ionizing more neutral gas atoms than if the voltage remained constant (about 25% more at 40 mTorr and 40% more at 5 mTorr). This is observed in fig. 3.9a where the increases in density are greater than 5 fold for each pressure. This is particularly obvious at x = 4, z = 5 cm.

The data obtained for T_e with respect to cathode current (fig. 3.9d) shows a rather interesting result. As the cathode current increases, the voltage increases to sustain the current. Primary electrons then enter the plasma from the cathode with higher energy so it might be expected that the average electron energy or T_e would increase with cathode current (I_c). However, the opposite occurs. As the cathode current increases from 0.2 amps to 1.0 amps (current density of 15.3 A/m^2 to 76.6 A/m^2), the electron temperature drops by as much as half. This effect is more substantial at 5 mTorr than at 40 mTorr, although it is present for all cases. This trend is reflected in the data for V_f (fig. 3.9c) where lower cathode currents reflect more negative floating potentials. It has been suggested[103,117] that the reduction in T_e may be due to the increasing density of metallic atoms in the vapor state. If the metal vapor constitutes a significant portion of the gas vapor then there is another energy loss 'channel' for the energetic electrons. Any electron with energy above the ionization (or excitation) threshold for Ag should cool more rapidly as there are more energy sinks available down to lower energies. This is in contrast to the energy lost for electrons in elastic collisions (the only channel available to electron below ionization and excitation threshold for argon) which takes thousands of collisions to lose a comparable amount of energy (poor energy transfer in high mass discrepancy collisions). Thus, if very little metal (Ag) vapor is available, this effect should not be seen and the T_e should rise with I_c (and cathode voltage). If, however, there is sufficient silver vapor present, then a reduction in T_e should be observed as the vapor level increases. Since the sputter rate depends on ion flux, and thus I_c, the metal vapor density should scale with I_c. Fang and Marcus[109] found for diode discharges with their typical low currents (12 and 15 mA), the T_e increased with I_c. This is consistent with a very low metal vapor concentration, typical of such systems. Rossnagel and Kaufman[91] used a magnetron system with a copper cathode (Cu has an ~ 7.7 eV

Reproduced with permission of the copyright owner. Further reproduction prohibited without permission.

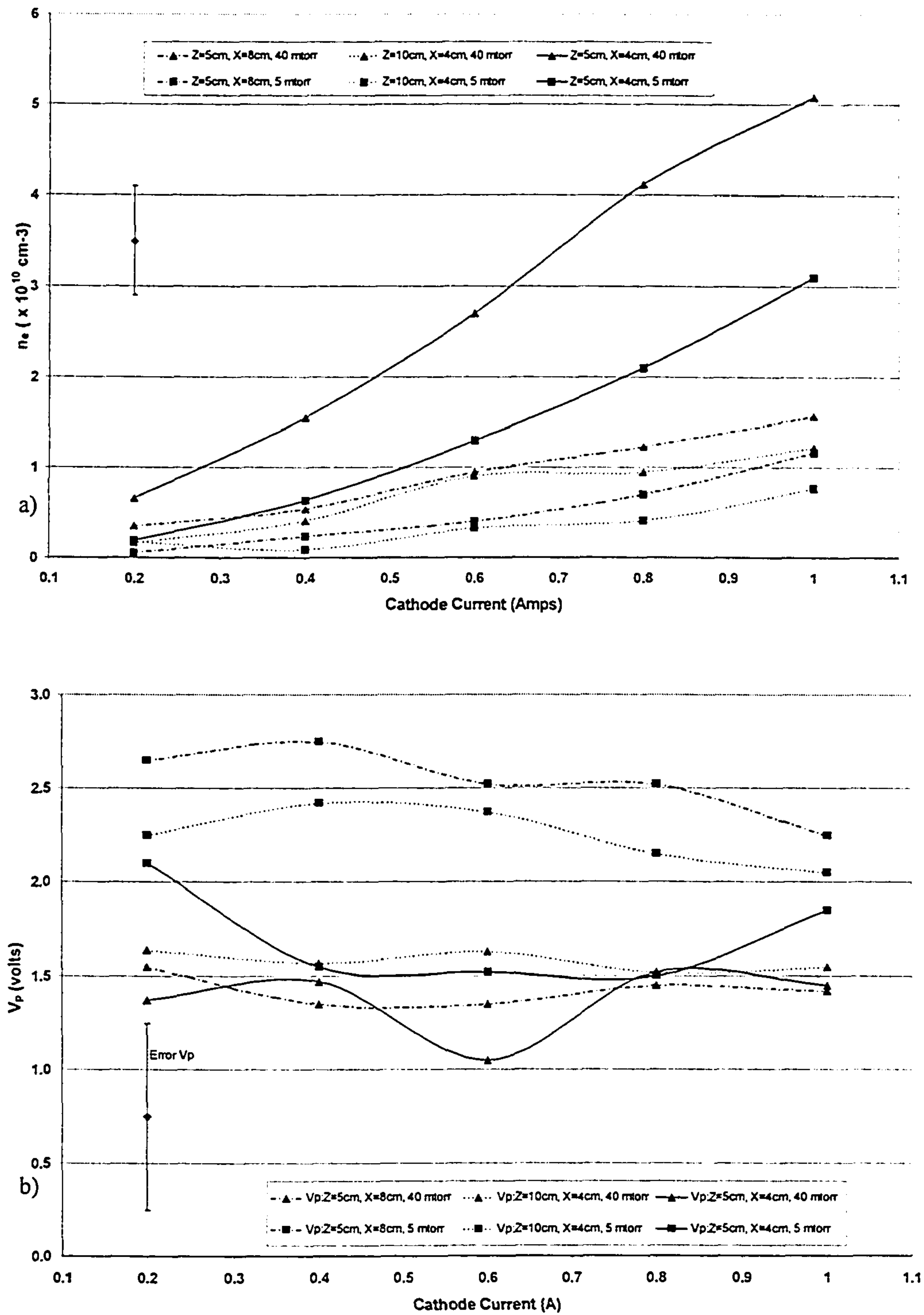

Figure 3.9: LP plasma parameters for the cathode current surveys. a) electron density b) plasma potential (V_p). Typical error bars are indicated on each graph.

Reproduced with permission of the copyright owner. Further reproduction prohibited without permission.

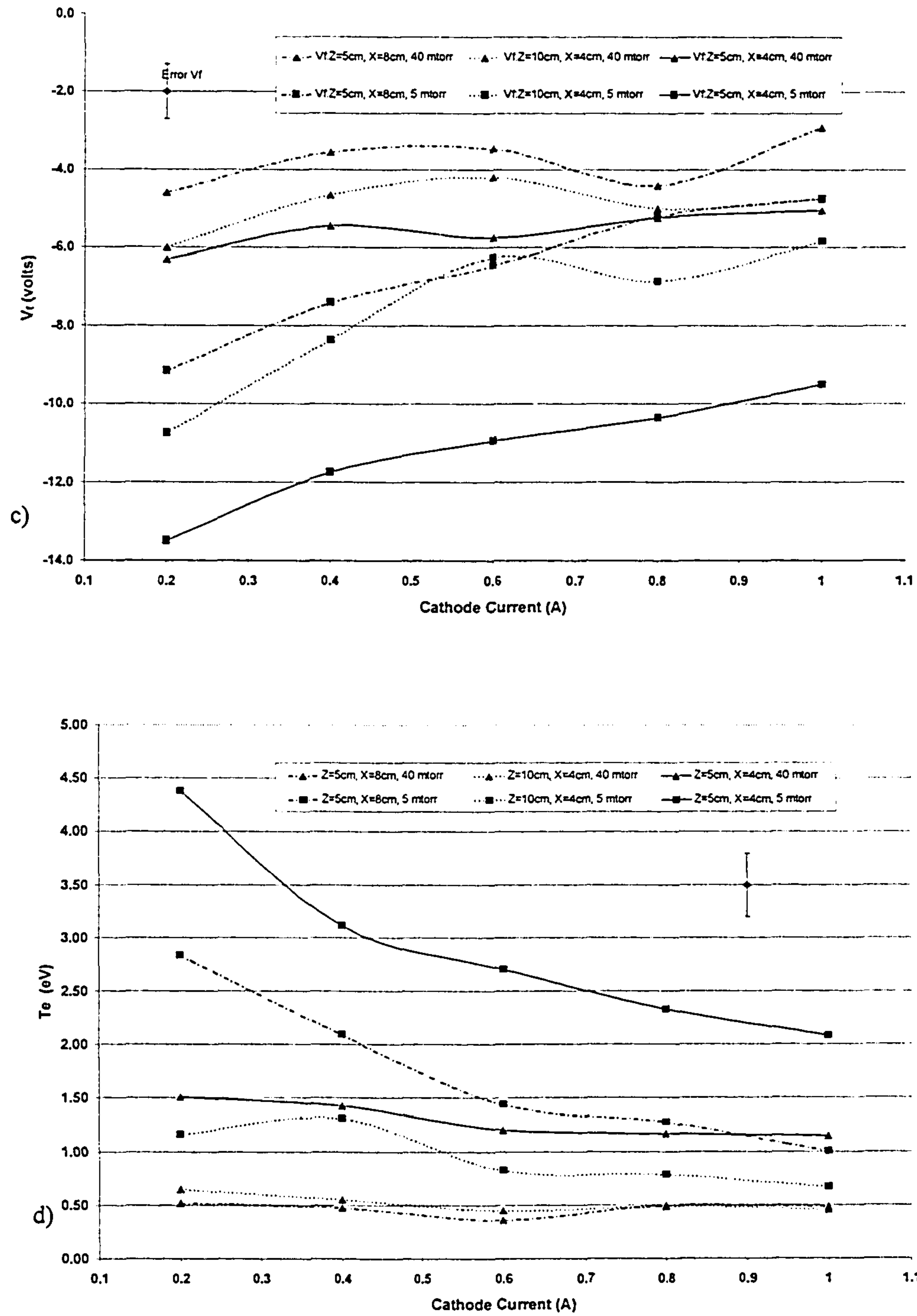

Figure 3.9: LP plasma parameters for the cathode current surveys. c) floating potential (V_f), d) electron temperatures (T_{eff} where bi-Maxwellian distributions exist). Typical error bars are indicated on each graph.

Reproduced with permission of the copyright owner. Further reproduction prohibited without permission.

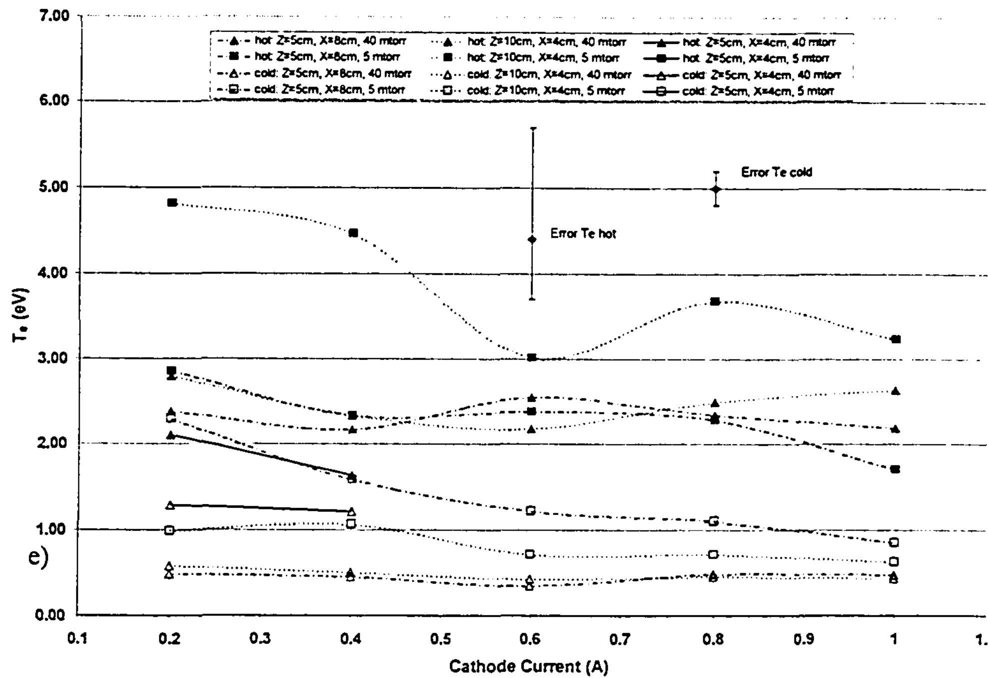

Figure 3.9 e) Hot and cold electron group temperatures where bi-Maxwellian groups exists for the cathode current surveys. Typical error bars are indicated on each graph.

ionization potential, comparable to the ~ 7.6 eV potential of Ag[118]) and noted the T_e did not change as I_c increased. They did not, however, include data. Posadowski[117] used a very high power density cathode (Cu) where the I_c reached up to 18 amps for a similar sized cathode. At these power densities a very large portion of the vapor is sputtered cathode material and led to lower T_e with higher metal vapor concentrations (power densities). It appears that the level of metal vapor in such a system can play a major role in determining T_e. If the concentration of metal vapor is low, such as with Fang and Marcus, T_e increases with I_c, Extremely high metal vapor concentrations, such as with Posadowski, lead to decreased T_e with increased I_c. Somewhere in between must lie a transition region. The data taken here suggests that magnetrons such as these lie somewhat above this transition, however, the comments of Rossnagel and Kaufman suggest these systems may be very near the transition regime. Obviously, if the sputtered material had a ionization energy above that of argon or near to that of argon the effect would be quite different. Thus, it should be considered that the effect here is dependent on the species of sputtered material and the relative ionization energy with respect to the working gas. Additionally, all inelastic events with all species may be important dependent on their propensity to

Reproduced with permission of the copyright owner. Further reproduction prohibited without permission.

occur and the relative density of the parent species for the various processes. It simply means the effect here described will depend on the various cooling pathways available to the electrons.

There did not appear to be any trend in V_p except for the previously detailed spatial and pressure responses.

As for the hot and cold electron temperatures, essentially everything cooled as I_c increased. The possible exception being the high pressure (40 mTorr) hot electrons in the well region which appear to hold the same temperature regardless of I_c. For data taken at 40 mTorr and at z = 5 cm, x = 4 cm and at low current levels (0.2A and 0.4A), there were observed bi-Maxwellian distributions. At the higher currents, only a normal Maxwellian distribution is observed. It does appear the difference between hot and cold electron temperatures is greatest at the lowest current of 0.2 A and decreases at 0.4 A. A likely explanation for this is that at lower current levels where plasma density is low, the plasma 'source' above the etch track will be spatially smaller. The point at which the EEDF is observably bifurcated will then move closer to the cathode. This suggests that the point of bifurcation is at 5 cm when the current is somewhere between 0.4 and 0.6 amps. Ideally, many more LP traces would be obtained with much finer resolution to confirm this. It is conceivable that a bi-Maxwellian distribution exists for all current levels at 40 mTorr but that at higher currents the low population of electrons in the hot electron group are not discernible through the strong signal of the cold electron group.

Reproduced with permission of the copyright owner. Further reproduction prohibited without permission.

3.4 Summary and Conclusions

This section will summarize the main discoveries presented in this chapter and will review the major issues raised from those results. Remarks will be made on recommended future research with respect to those issues.

Magnetron plasmas are highly structured entities although most of the salient dynamic processes are far from being well understood. It was found that, in general, n_e increased with higher pressures and in regions generally considered closer (in the sense of electron transport) to the plasma source. Also, the maximum in n_e moves from above the etch region near the cathode to above the well region far from the cathode. This is clearly depicted in figure 3.10 where the spatial surveys at 5 and 40 mTorr of pure argon gas are summarized as contour maps. Figure 3.11 depicts the spatial response of T_e at those pressures. Linear interpolation of the available data (denoted by dots on the left side of Figure 3.10, but applicable to all graphs) is used to fill out these graphs. The increase of n_e with pressure is regarded as an increase in ionization rate without a commensurate increase in ion loss rate. With higher I_c, n_e increased (hence ion density increased to maintain plasma quasineutrality) so that the flux of ions to the sheath edge increased to supply the current. Since the flux of ions to the sheath edge is dependant on ion density and temperature, and since the n_e increased approximately 1:1 relative to I_c this suggests that there is not a significant increase in ion temperature in the plasma bulk, though this remains to be confirmed.

The 2-D spatial profile of T_e in pure argon (fig. 3.11) shows decreased T_e at higher pressures. This was previously regarded as due to increased collision rates as electrons are transported out of the magnetic trap region. However, it appears such a simple model may not be sufficient. The mechanisms for electron transport across magnetic field lines in such plasmas need to be investigated much more closely. In the spatial sense, T_e increased in regions with higher n_e for any given pressure, likely due to a closer proximity to the plasma source. Electrons also appeared to be colder in the well region, close to the cathode, than farther out. I.e. there is a region of cold electrons bounded by regions of hot electrons found above the etch tracks and further

Reproduced with permission of the copyright owner. Further reproduction prohibited without permission.

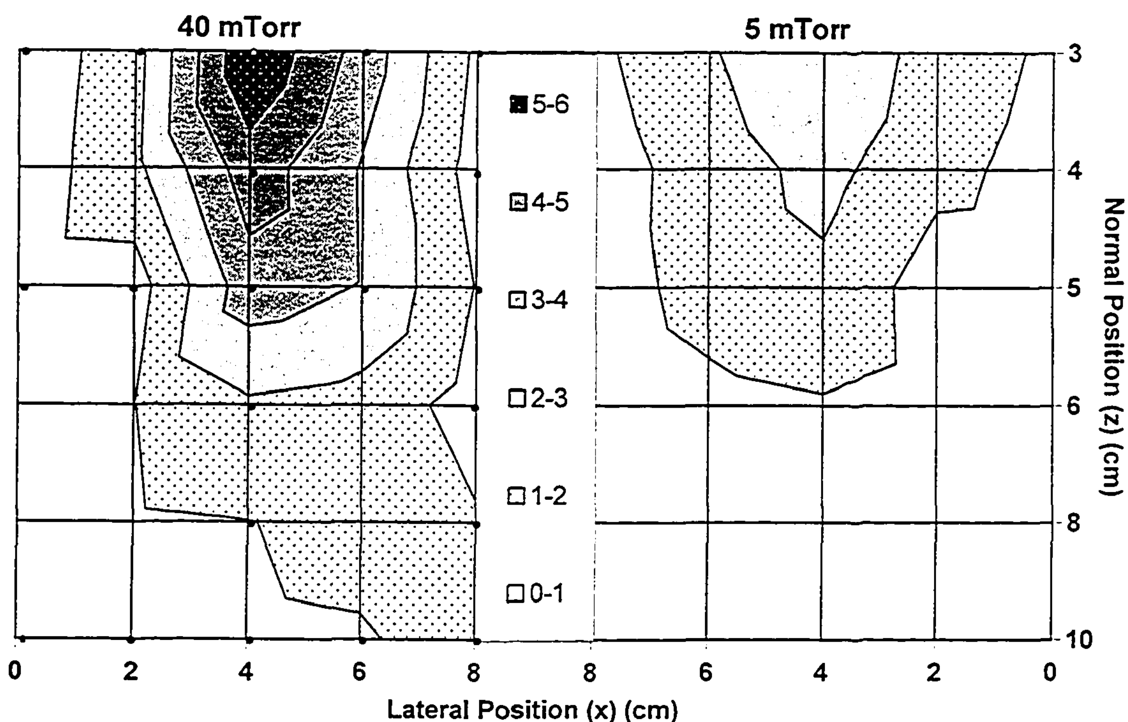

Figure 3.10: 2-D spatial map of electron density (x 10^{10} cm^{-3}) for 40 and 5 mTorr of pure argon gas. Note lateral positions are mirror imaged around central axis of magnetron at 8 cm. Dots indicate positions, under all conditions, at which experimental data was obtained and from which other point values are interpolated.

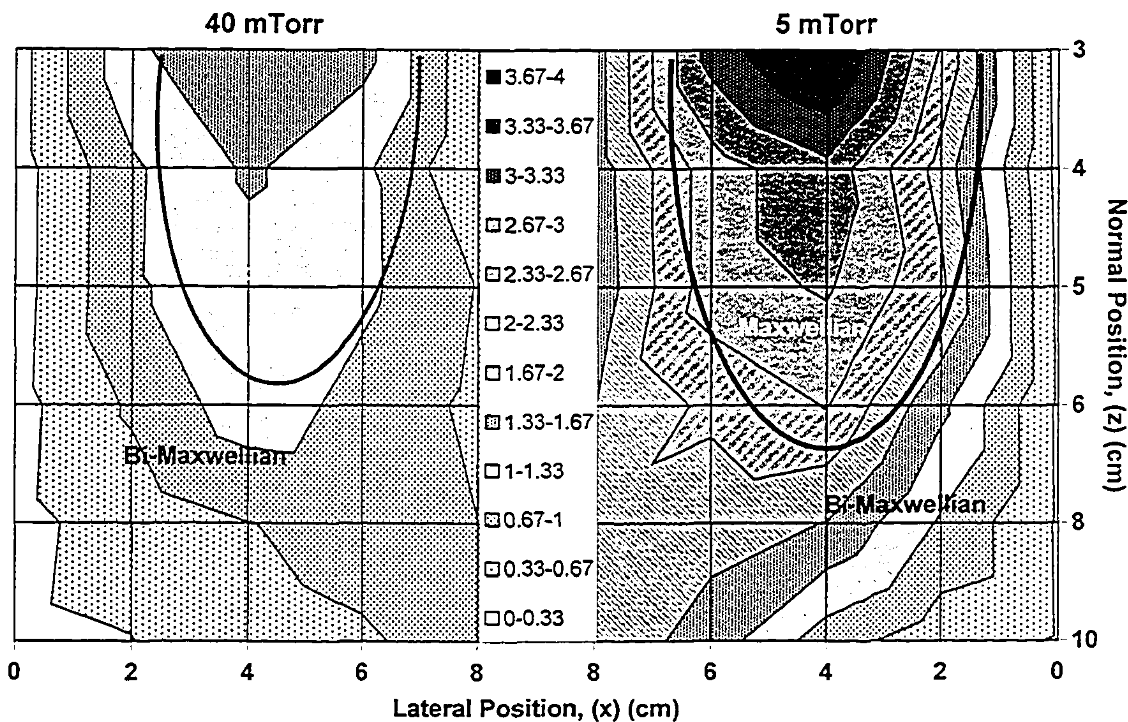

Figure 3.11: 2-D spatial map of electron temperature (eV) for 40 and 5 mTorr of pure argon gas. Approximate boundary outside of which bi-Maxwellian EEDF's are observed, is indicated. Note lateral positions are mirror imaged around central axis of magnetron at 8 cm.

Reproduced with permission of the copyright owner. Further reproduction prohibited without permission.

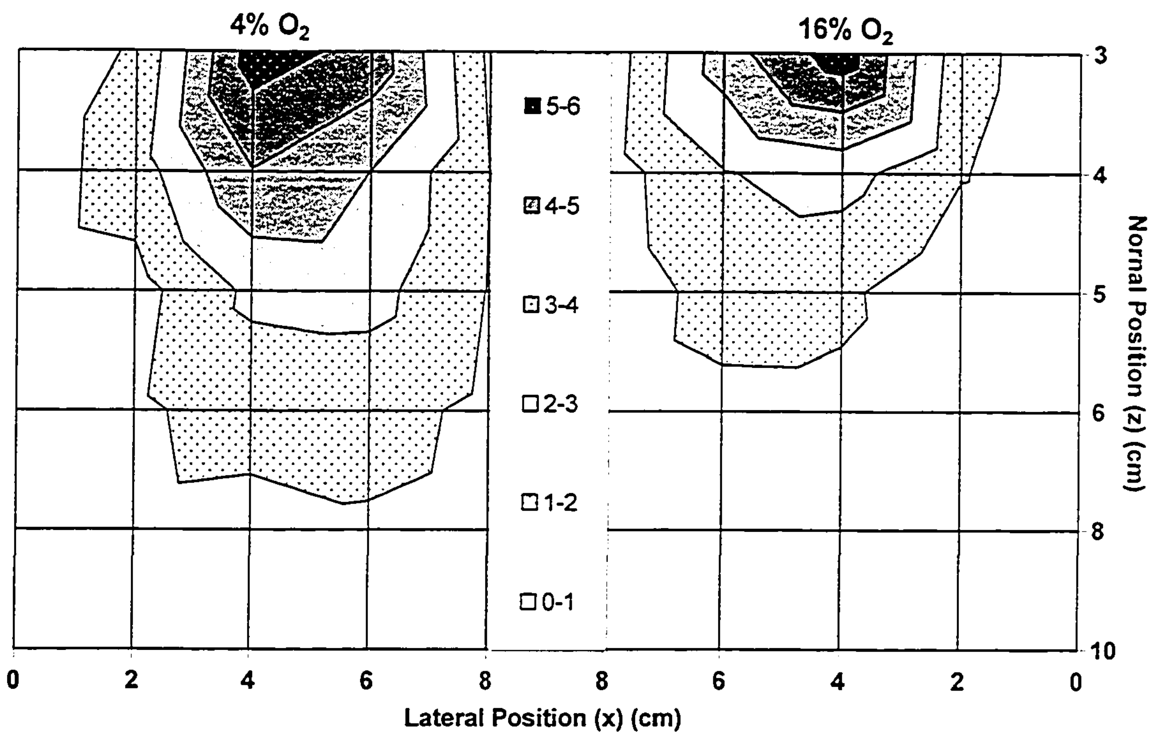

Figure 3.12: 2-D spatial map of electron density (x 10^{10} cm^{-3}) for 4% and 16% O_2 at 40 mTorr. Note lateral positions are mirror imaged around central axis of magnetron at 8 cm.

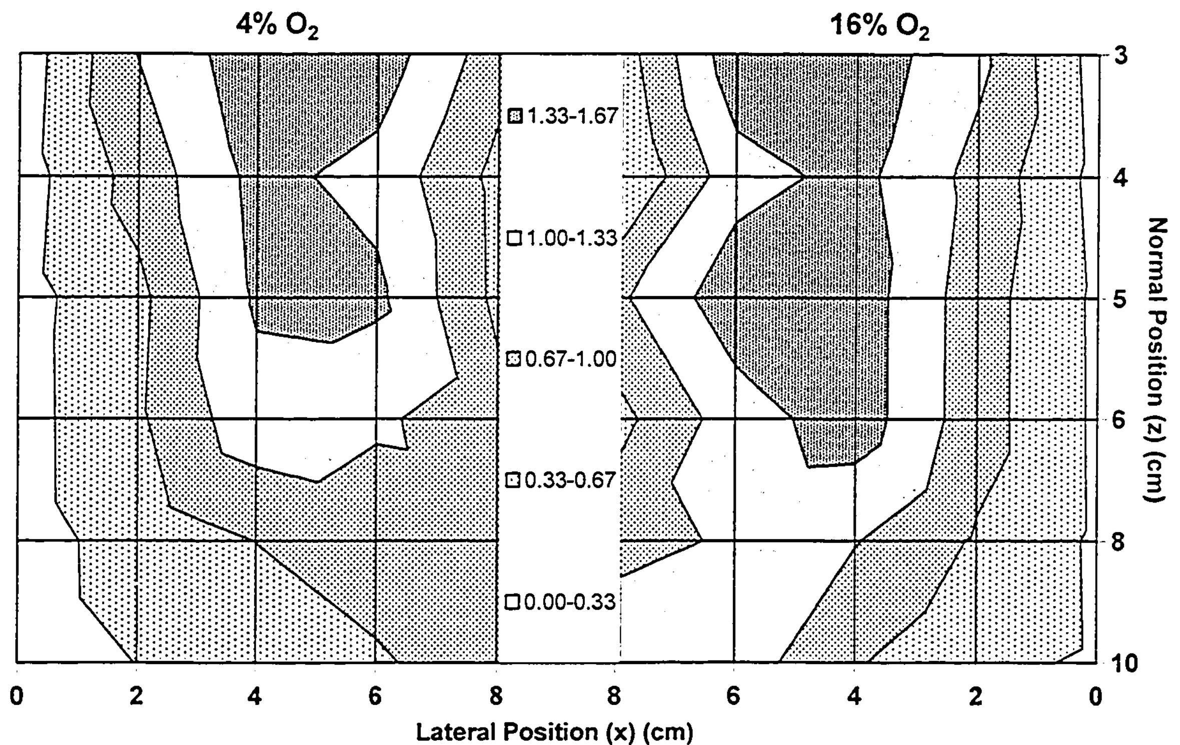

Figure 3.13: 2-D spatial map of electron temperature (eV) for 4% and 16% O_2 at 40 mTorr. Approximate boundary outside of which bi-Maxwellian EEDF's are observed, are indicated. Note lateral positions are mirror imaged around central axis of magnetron at 8 cm.

Reproduced with permission of the copyright owner. Further reproduction prohibited without permission.

out above the well region. Indicated on fig. 3.11 is the approximate boundary outside of which bi-Maxwellian EEDF's were observed. This boundary was found to contract at higher pressures and lower cathode currents. This result cannot be correlated directly to changes in either n_e or T_e since n_e increases at higher pressures but decreases at lower currents. T_e generally increases at lower currents but decreases at higher pressures. As I_c increases, T_e drops, potentially due to the increase in sputtered metal vapor and subsequent changes in the relative predominance of the various cooling pathways for electrons. This needs to be confirmed; best with a mass spectrometer or simulation.

It is not clear how much of a factor the addition of oxygen is with respect to n_e, though it appears higher oxygen levels (up to 20% of the sputter gas) are correlated with lower n_e, possibly due to gas heating effects or additional inelastic processes introduced by the oxygen. Figure 3.12 shows 2-D maps of n_e data taken from spatial surveys for cases with 4% and 16% O_2 at 40 mTorr. Compared to figure 3.10 these maps show the reduction in n_e with higher levels of oxygen (at 40 mTorr) and a significant contraction of the region having n_e greater than 10^{10} cm^{-3}. The oxygen surveys, themselves, did not provide the accuracy desired to determine how, exactly, such plasmas respond to oxygen levels. This is likely due to the increased complexity of such systems, the increased complexity in analyzing the LP data and the potential difficulty in eliminating hysteresis due to contamination and 'poisoning' in such systems. To understand these plasmas, with oxygen as a constituent part, better, alternative techniques, such as mass spectroscopy, optical spectroscopy and extremely detailed simulations, should all be utilized.

The response of T_e to oxygen levels is an opaque issue. Spatial surveys indicated T_e is hotter for higher oxygen levels but only in regions more remote from the cathode such as at 5 and 10 cm away (see spatial maps in figure 3.13). Closer to the cathode, it is difficult to discern a difference in T_e versus oxygen level. Surveys in oxygen seemed to mirror this response as well, with changes to T_e most obvious at $z = 10$, although changes in these surveys were subtle. This is again reflected in pressure surveys where 3 levels of oxygen were used. The $z = 10$, $x = 4$ cm surveys showed higher T_e at higher oxygen levels. For the oxygen and pressure surveys, it

Reproduced with permission of the copyright owner. Further reproduction prohibited without permission.

was not obvious there was any response to T_e versus oxygen for locations nearer than 10 cm.

For all surveys that included oxygen, there appeared very little response in V_f versus oxygen. This is not an expected result since V_f typically responds concurrently with T_e. If T_e is increasing, then the relative flux of electrons should increase to the probe forcing V_f lower. If V_f does not go lower, it is possible that an increasing portion of the negative charge collected by the probe is due to heavier, and thus slower, negative ions. The change in electron-negative ion ratio would have to be sufficient to balance any changes in T_e to prevent V_f changing significantly. The result of the oxygen surveys is that many more questions arise than have been answered. Aside from the oxygen surveys, V_f responded to T_e as one would expect with lower V_f correlating with higher T_e. This was generally consistent.

Spatially, bi-Maxwellian distributions are observed in regions remote from the plasma 'source' (within the magnetic trap) and also are only slightly more prevalent at higher pressures. Hotter electron temperatures at lower pressures may not be derived exclusively from fewer collisions. Additionally, the bi-Maxwellian electron temperatures observed are not well accounted for by the collision cross section minimum nor by the proposed model due to Sheridan *et* al[13]. Super-elastic collisions should be investigated as a potential cause for such EEDF's.

An interesting feature of the data presented for bi-Maxwellian cases was how the difference in hot and cold temperatures was smallest in regions where densities were higher. As the cold electron temperature dropped in value, the hot electron temperature rose in value, and the density of electrons decreased.

V_p appeared to be relatively insensitive. There did appear some spatial and pressure dependence, though the response was weak. As a better understanding of magnetrons emerges, it will be easier to hypothesize on and investigate the response of V_p.

Figures 3.14 and 3.15 show n_e, T_e, T_e^{hot}, and T_e^{cold} for surveys in pressure. These trend lines are average values taken from the three tested locations (i) z = 5 cm, x = 4 cm, ii) z = 5 cm, x = 8 cm, and iii) z = 10 cm, x = 4 cm) in the pressure

Reproduced with permission of the copyright owner. Further reproduction prohibited without permission.

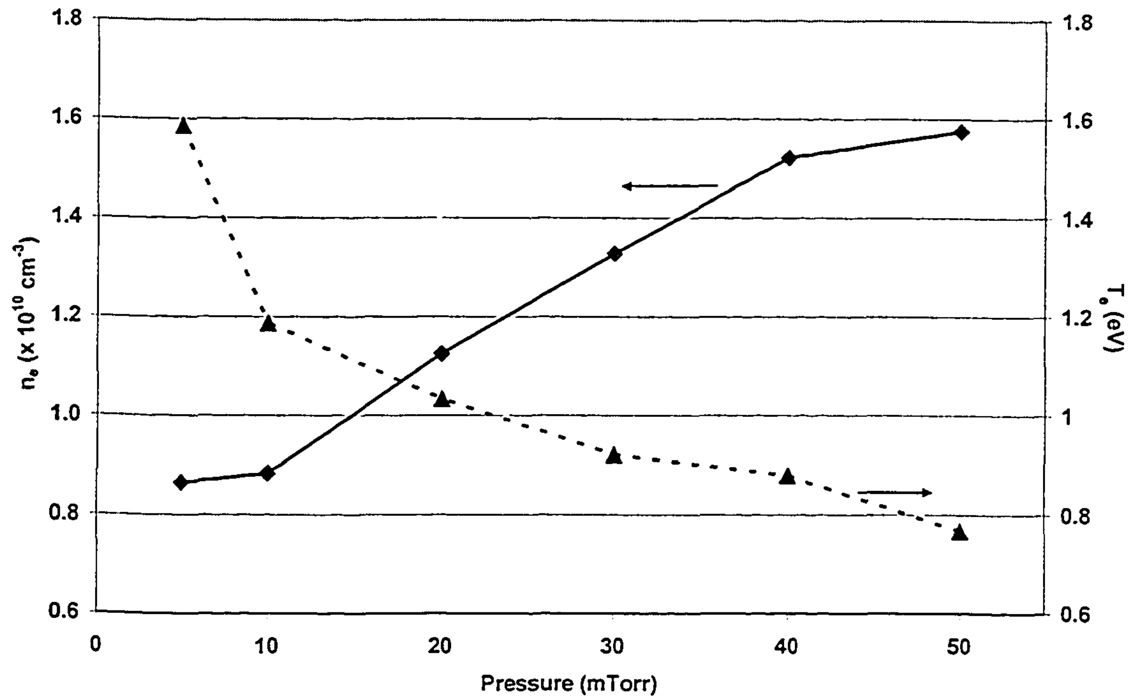

Figure 3.14: Average electron density (n_e) and temperature (T_e) versus pressure. Average of 3 spatial locations within reactor. Note that the trends and features from those locations (see fig.3.8 a) and d)) are preserved in the average value.

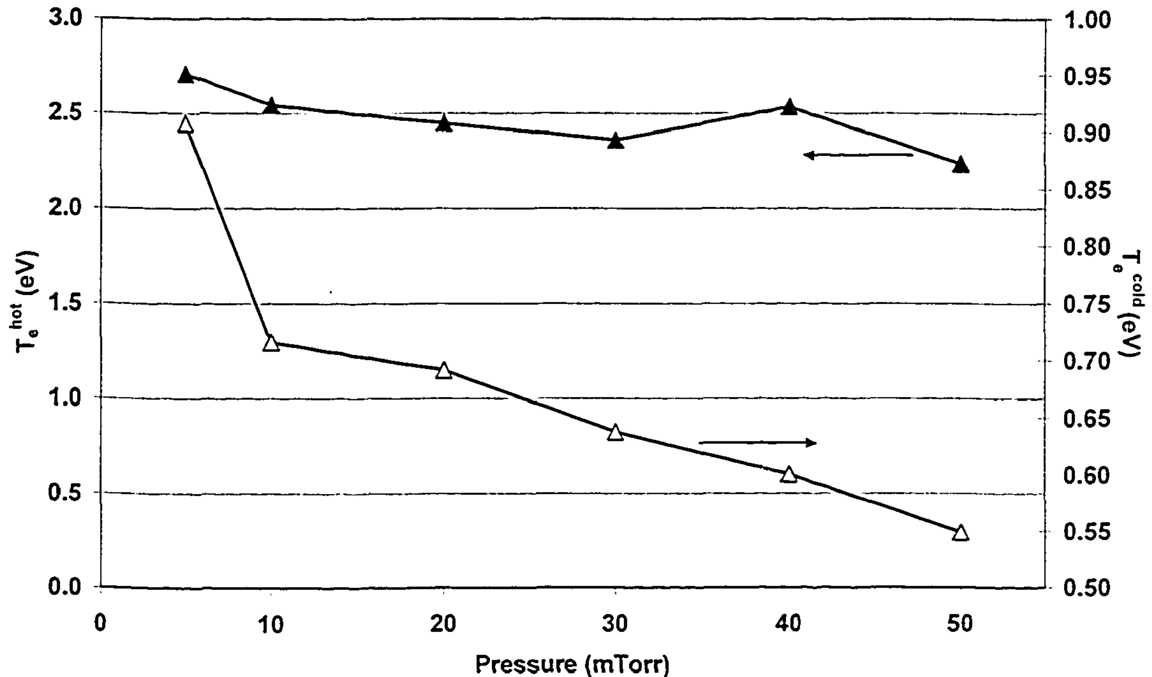

Figure 3.15: Average hot and cold electron temperatures (T_e^{hot} and T_e^{cold}) versus pressure. Average of spatial locations within reactor where bi-Maxwellian distributions exist. Note that the trends and features from those locations (see fig.3.8 e)) are preserved in the average value.

Reproduced with permission of the copyright owner. Further reproduction prohibited without permission.

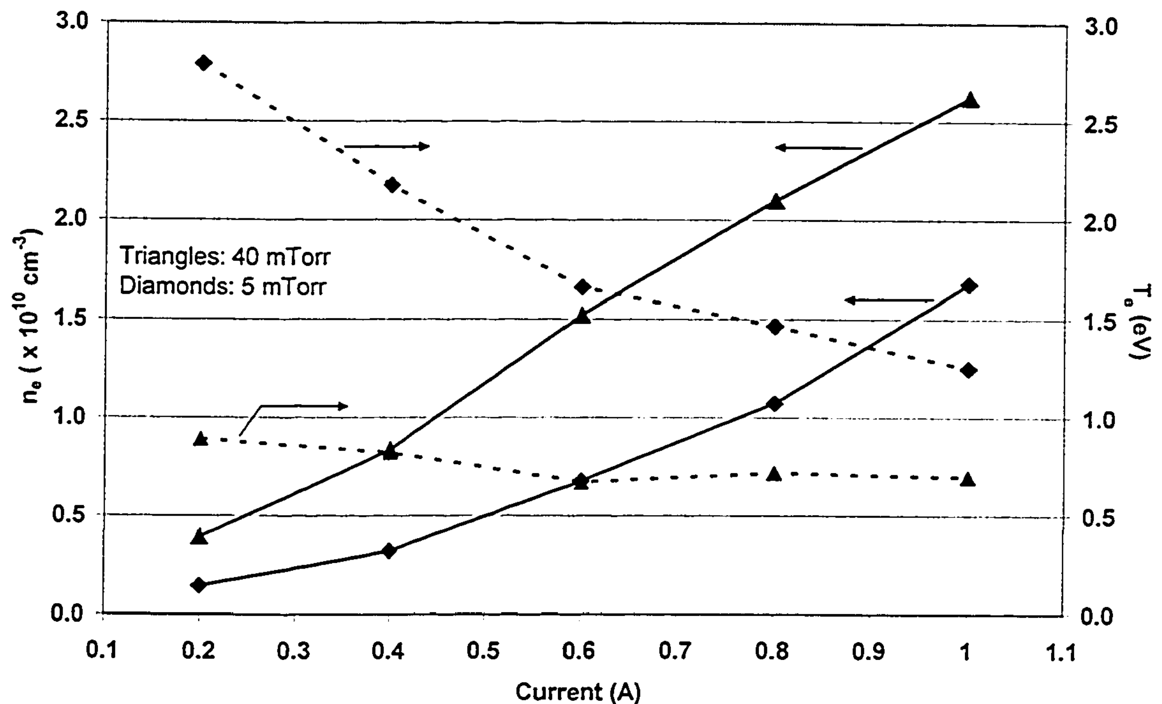

Figure 3.16: Average electron density (n_e) and temperature (T_e) versus cathode current for 5 and 40 mTorr. Average of 3 spatial locations within reactor. Note that the trends and features from those locations (see fig.3.9 a) and d)) are preserved in the average value.

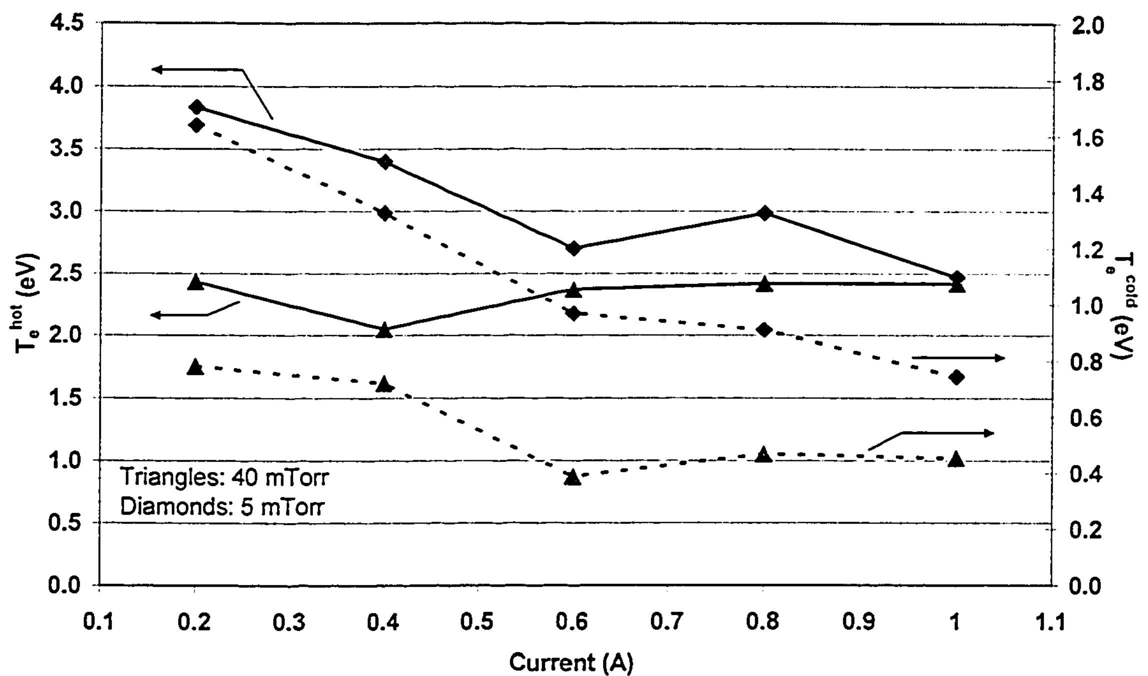

Figure 3.17: Average hot and cold electron temperatures (T_e^{hot} and T_e^{cold}) versus current. Average of spatial locations within reactor where bi-Maxwellian distributions exist. Note that the trends and features from those locations (see fig.3.9 e)) are preserved in the average value.

Reproduced with permission of the copyright owner. Further reproduction prohibited without permission.

surveys. These average trend lines do preserve the features of each individual data set and thus general trends may be obtained. Figure 3.16 and 3.17 show the same type of data for surveys in cathode current.

The salient features of these surveys indicate that, in general, higher operating pressures and cathode currents both result in higher electron densities and lower overall electron temperatures. Even in the case of bi-Maxwellian EEDF's, both electron groups cool under those conditions. This is contrasted by the location of the approximate boundary where EEDF's bifurcate. This region contracts at higher pressures but expands at higher currents. Between 5 and 10 mTorr there appears to be an abrupt change in cooling rate for electrons, which may be due to a change in the dominant cooling mechanism. This may be related to changes in electron transport mechanisms.

Finally, for additional insight, the 2-D spatial maps of n_e and T_e could be analyzed with respect to the particle pressure - magnetic pressure ratio (known as β). The value of β may be indicative of the general dynamics involved in such systems. However, since the magnetic field strength varies along the magnetic field (see Chen[19]) this analysis is beyond the scope of the present study and so is recommended for future work.

Reproduced with permission of the copyright owner. Further reproduction prohibited without permission.

Chapter 4: Simulation

The complex dynamics within bulk plasmas makes them difficult to investigate theoretically and experimentally. Experimental investigation of a plasma is rife with difficulties, resulting from the varied analytical methods and the invasive nature of the experimental techniques. Any probe or sensing element immersed into the plasma will perturb it, locally changing its characteristics forming a sheath region. Theoretical assumptions are required to extract meaningful information in spite of the perturbation. Whatever experimental technique is employed, whether it be Langmuir Probe, Optical Emission Spectrometry, Laser Induced Fluorescence, etc., there are often several explanations for the observed behavior, or worse, no explanations at all. Further, as theoretical models are developed, experimental confirmation can be extremely difficult. For example, no experimental investigation has provided any indication of the dominant mechanisms that lead to the bi-Maxwellian EEDF's observed in some magnetrons. Simulations may prove to be the ultimate investigative tool in this regard since mechanisms (such as ionizing or elastic collisions) suspected of being an important factor for an observed behavior can be included or excluded from simulation runs. Differences between the runs will indicate the influence of that mechanism.

As mentioned in the first chapter, the focus here will be on the development and use of a Monte Carlo (MC) simulation module for energetic electrons in magnetron plasmas. The specific MC method implemented as Plaspud1 is described below.

4.1 Plaspud1: General Operational Details, Boundary Conditions, and Initial Conditions.

The simulation takes place in a simulation space that represents the physical ARGO chamber. Since the plasma has been shown to be symmetrical across the width (lateral or x-direction) of the magnet assembly, only half the system need be

Reproduced with permission of the copyright owner. Further reproduction prohibited without permission.

simulated, reducing simulation time but not accuracy. Likewise, the simulation space is reduced to a central plane in the direction down the length (y direction) of the magnet assembly since all LP data was taken in this plane or 'slab'. Plaspud1 (and Plaspud2, the plasma fluid model for thermalized plasma species) is designed to be a full 3-D simulator. Operation in the 'slab' mode is accomplished by only considering source particles on this plane and by ensuring that all simulated particles are restricted to this plane even though their trajectories are determined by a 3-D motion algorithm.

To facilitate collection and calculation of the sought after data, as well as to store local conditions, a spatial grid is superimposed on the simulation space. Each cell within the grid contains information including local electric potential, electric field, magnetic field, and particle densities for all species of interest. Each cell also collects run time information, such as number of ionization events accumulated in each cell while Plaspud1 runs. When Plaspud1 is finished, this information can be scaled (see §4.3) to provide real values such as ionization rates or fast electron densities. The grid cells are nominally set at 2.5 x 2.5 mm, however, near the cathode, where there is strong electric field over only ~1 mm, the grid is refined and the cells may be as small as 0.15625 x 0.15625 mm.

Before presenting the general operational algorithm for Plaspud1 specific operational details, boundary conditions and initial conditions are discussed.

4.1.1 Numerical solution to the equations of motion for charged particles in electric and magnetic fields.

Charged particles move in electric and magnetic fields according to the Lorentz force equation:

$$m\frac{d\mathbf{v}}{dt} = q(\mathbf{E} + \mathbf{v} \times \mathbf{B}) \tag{1}$$

Reproduced with permission of the copyright owner. Further reproduction prohibited without permission.

where m is the mass of the particle, **v** is the particle's velocity, q is the particle's charge, and **E** and **B** are the localized electric and magnetic fields. Equation (1) is numerically solved by first breaking it into its spatial components yielding:

$$m\frac{d\mathbf{v}_x}{dt} = q(\mathbf{E}_x + \mathbf{v}_y\mathbf{B}_z - \mathbf{v}_z\mathbf{B}_y) \tag{2}$$

$$m\frac{d\mathbf{v}_y}{dt} = q(\mathbf{E}_y + \mathbf{v}_z\mathbf{B}_x - \mathbf{v}_x\mathbf{B}_z) \tag{3}$$

$$m\frac{d\mathbf{v}_z}{dt} = q(\mathbf{E}_z + \mathbf{v}_x\mathbf{B}_y - \mathbf{v}_y\mathbf{B}_x) \tag{4}$$

These equations are simultaneously solved using a fourth order Runge-Kutta integration method with a discrete time step[119]. The particle is moved one time step after another using a dynamic time stepping procedure where accuracy determines the maximum allowable time step and efficiency considerations attempt to increase the time step. Thus the algorithm is constantly seeking a balance between efficiency and accuracy as determined by local conditions. This time step must also be small compared to the particle's gyroperiod and the inverse collision frequency.

4.1.2 Collision with obstructions such as walls and targets.

When charged particles collide with ground potential walls they are considered neutralized and therefore 'lost'. When charged particles collide with the cathode, however, different events can take place. When an electron is incident on the cathode, an important consideration is the finite probability the electron will be reflected[120] and returned to the system. The reflection coefficient depends on the target material (and crystallite orientation) and electron energy and can range from 0.15 to 0.6 for an energy range of 5 eV to 0.5 eV, respectively (for Cu(100)). Since

Reproduced with permission of the copyright owner. Further reproduction prohibited without permission.

precise information for the various crystallographic orientations of Ag was not available and since the ARGO target crystalline properties were not known, it will suffice to assume a value of 0.2, although the effect of this variable can be tested using simulation. Electrons are emitted from the cathode with approximately 4 eV and so should have about 4 eV remaining at the cathode, should they return there without suffering a collision after initial ejection by ion bombardment.

When an ion approaches the cathode, electrons are emitted as a result of the potential emission model[121]. Electron emission becomes[122]:

$$\gamma_p = 0.2(0.8E_i - 2\phi)/E_f \qquad (5)$$

where γ_p is the secondary electron emission probability, E_i is the ionization energy of the ion (15.76 eV for Argon), E_f is the Fermi energy of the target (5.49 eV for Ag)[123,124], and ϕ is the work function of the target (4.26 eV for Ag)[123]. It is noted that the secondary electron emission does not depend on the ion's kinetic energy. It is noted that equation 5 is for a target at ground potential, differing from the case here where the cathode is at several hundred volts negative. In such a case, it may be that the simple potential emission model does not account for all electrons emitted. Field emission effects may contribute[125], or the Fermi energy may change due to the excess charge carriers[126]. In such cases, increasing γ_p by more than a factor of two may be appropriate[127]. The effects of this, too, can be tested by simulation.

The kinetic emission model, due to electron excitation as an ion traverses the interior of a target, does have a dependence on the electron's kinetic energy and angle of incidence. However, this model is only appropriate for ion energies higher than the ~0.5 keV ion energies used here. For energies under about 1 keV, the potential emission model (eqn. (5)) is regarded as more appropriate[124,128].

For every impinging ion, a random number can be generated and compared to the γ_p. If the random number is less than γ_p, a secondary electron is emitted. Otherwise no electron is emitted.

Also, the ion energy, angle of incidence, ion type, and target type are used to determine if a sputtering event and the ejection of a neutral target atom may occur.

Reproduced with permission of the copyright owner. Further reproduction prohibited without permission.

This is used as a source term for Themspud1 module, which simulates sputtered and other energetic neutral particles.

4.1.3 Gas phase collisions.

After each time step is taken for a particle in free flight, the probability of a collision is used to determine if an actual collision takes place. The distance the particle has moved, δd, in the last time step determines the probability of a collision by[129]:

$$P = 1 - e^{\left(-\delta d \sum_{i=1}^{m} n_i \sigma_i(E)\right)} \tag{6}$$

where n_i is the local density for particle species i, $\sigma_i(E)$ is the energy dependent total collision cross section of the primary particle with species i, and Σ accounts for all the various species with which the primary particle may collide. A uniformly distributed random number [0,1) is generated and compared to P. Only if the random number is smaller than P does a collision take place.

If a collision has taken place, then the type of collision is to be determined by a second random number. First, each process type for each species is weighted by the respective species local density and normalized to the cumulative probability for all species and processes to generate a fractional probability for each specific process. Similar to Nanbu[129], for m species (for example argon and silver) and $\tilde{m}$ processes for each species i (for example, excitation, ionization, metastable excitation, elastic collisions, etc.), the fractional probability for a specific process becomes:

$$P_{i,j} = \frac{n_i \sigma_{i,j}}{\sum_{i=1}^{m} n_i \sum_{j=1}^{\tilde{m}} \sigma_{i,j}} \tag{7}$$

Reproduced with permission of the copyright owner. Further reproduction prohibited without permission.

where:

$$\sum_{i=1}^{m}\sum_{j=1}^{\tilde{m}} P_{i,j} = 1$$

Generation of a single random number and comparison to the various fractional probabilities will determine which process occurred. For example, if there are only two processes in the system with process A having a probability 3 times larger than process B, selection of a random number between 0 and 0.75 will mean process A occurred while selection of a random number between 0.75 and 1.0 will mean process B occurred. This method is general for an arbitrary number of particle species and processes.

Once a collision type has been determined, the energy loss and the scattering angle of the primary particle must be determined. The scattering angle is determined by an anisotropic scattering model, where forward scattering is more predominant at higher energies[55], but large angle scattering is significant at lower energies. To accommodate this effect, the model used by Surendra, Graves, and Jellum is used[55]:

$$rnd = 2\pi \int_{0}^{\psi} \sigma(E_o, \psi') \sin\psi' d\psi' \quad (8)$$

where E_o is the initial particle energy. Equation (8) is integrated up through ψ' until the integral equals the random number. $\sigma(E_o, \psi')$ is given by:

$$\sigma(E_o, \psi') = \frac{E_o}{4\pi[1 + E_o \sin^2(\psi'/2)]\ln(1 + E_o)}$$

This analytic expression, though borrowed from coulomb scattering, captures the main features of electron-neutral collisions, particularly with respect to scattering angle[55]. The resulting normalized scattering angle probability for various energies is given in figure 4.1.

Reproduced with permission of the copyright owner. Further reproduction prohibited without permission.

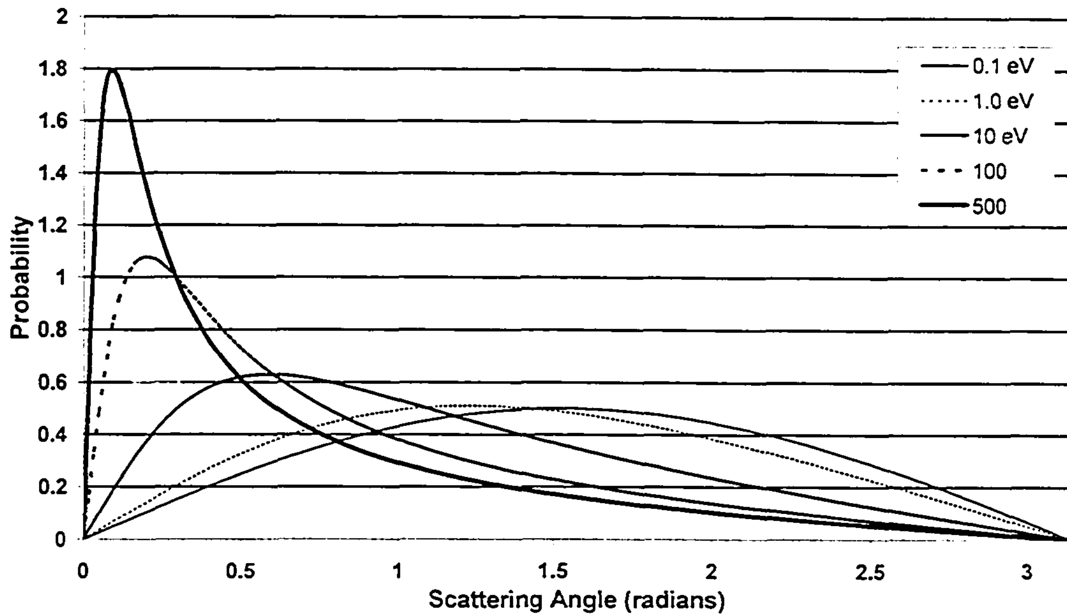

Figure 4.1 Normalized Scattering Angle Probability for Electron-Argon Collisions for Various Electron Energies.

The azimuthal angle is given by:

$$\phi = 2\pi(rnd) \tag{9}$$

The energy lost by the primary particle depends on the process type. For inelastic processes, the energy of the primary particle is reduced by the inelastic energy specific to that process. For example, the electron-argon ionization energy is 15.76 eV, so an electron would lose 15.76 eV in this instance. Technically, in the case of an ionizing event, the liberated electron should also be given some kinetic energy at the expense of the primary particle. Carman[33] provided some cross sections showing relatively few ejected electrons had energies above 4 or 5 eV, but a nearly uniform distribution of energies below 4 or 5 eV. In Plaspud, where an ionizing event takes place, the liberated electron is given from 0 to 5 eV of energy, as determined by a uniform random number. This energy is taken from the primary electron along with the inelastic energy of the collision type.

For elastic collisions, the kinetic energy of a primary particle is given by[37]:

Reproduced with permission of the copyright owner. Further reproduction prohibited without permission.

$$E = E_o[1 - 2\frac{m_a}{m_b}(1 - \cos\psi)] \qquad (10)$$

where m_a is the primary particle mass and m_b is the struck particle's mass.

Collision cross-sections for all species and processes used here are shown in figure 4.2. Table 4.1 list the various processes and gives the associated inelastic energy used for those processes.

Table 4.1: Processes and Inelastic Energy of Process

PROCESS		**Inelastic Energy (eV)[123]**
$e^- + Ar \rightarrow e^- + Ar$	elastic collision	0
$e^- + Ar \rightarrow 2e^- + Ar^+$	argon ionization	15.76
$e^- + Ar \rightarrow e^- + Ar^{*1}$	argon excitation 1	11.79
$e^- + Ar \rightarrow e^- + Ar^{*2}$	argon excitation 2	14.25
$e^- + Ar \rightarrow e^- + Ar^{*3}$	argon excitation 3	14.79
$e^- + Ar \rightarrow e^- + Ar^{*4}$	argon excitation 4	15.48
$e^- + Ar \rightarrow e^- + Ar^m$	argon metastable excitation	11.60
$e^- + Ar^m \rightarrow 2e^- + Ar^+$	argon step ionization	4.14
$e^- + Ag \rightarrow 2e^- + Ag^+$	silver ionization	7.57
$e^- + Ar^m \rightarrow Ar + e^-(fast)$	super elastic collision	-11.60

Reproduced with permission of the copyright owner. Further reproduction prohibited without permission.

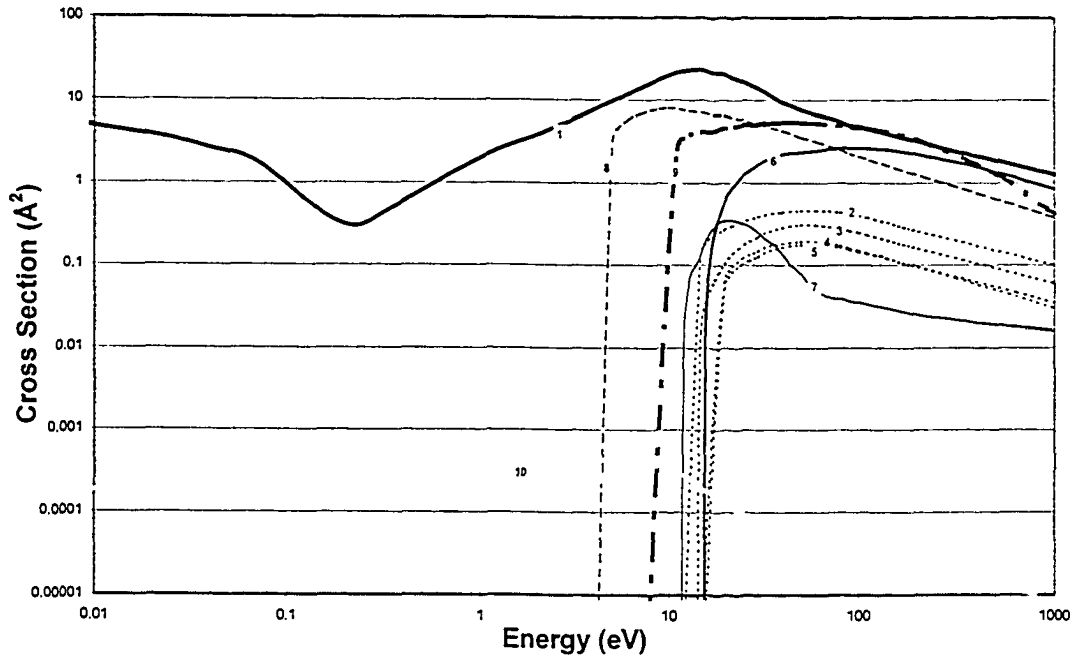

Figure 4.2: Energy Dependant Collision Cross Sections: 1) e⁻ - Ar elastic[50], 2) e⁻ - Ar excitation #1[50], 3) e⁻ - Ar excitation #2[50], 4) e⁻ - Ar excitation #3[50], 5) e⁻ - Ar excitation #4[50], 6) e⁻ - Ar ionization[130], 7) e⁻ - Ar excitation to metastable , 8) e⁻ - Ar metastable step ionization, 9) e⁻ - Ag ionization[118], 10) e⁻ - Ar metastable super elastic (de-excitation)[131].

4.1.4 Boundary Conditions

Boundary conditions for the simulations are the physical walls and target, the voltage on the walls (ground potential) and target, and, in the case of 2-D simulations, the restriction of particles to the slab. Also, where the simulation space is cut in half laterally, a barrier is in place to reflect all particles incident upon it. Since the system is symmetrical about this barrier, any particle crossing this barrier and out of the simulation space will be matched by one coming into the simulation space. Therefore, reflection is an appropriate mechanism there. This implies the simulation will capture effects from the adjacent etch region portion of the cathode that is not part of the restricted simulation space. The cathode current is set as a scaling factor. The ratio of this value over the number of charged particles simulated will be used to calculate simulation results.

Reproduced with permission of the copyright owner. Further reproduction prohibited without permission.

4.1.5 Initial Conditions

The initial conditions for these simulations are several and include: pressures of all neutral gas phase species, cathode sheath thickness, secondary electron emission characteristics of the target, electron reflection coefficient of the target, total flux density distribution of ions to the cathode, electrical potential and electrical field everywhere and the magnetic field. These initial conditions do involve some estimations, although are less important when Plaspud 1 and 2 run iteratively resulting in a self-consistent solution. In cases where Plaspud1 is run by itself, such as here, more careful attention must be paid to the initial conditions. Each initial condition is thus discussed here.

4.1.5.a Pressure or neutral gas density.

For Plaspud1 to run properly, a map of local gas density is required for the gas phase collision aspect of the algorithm. The simplest way to do this is to specify at run time a uniform partial pressure for all the various gas species. However, there are some complexities preventing the ubiquitous application of such a model.

If there is significant rarefaction of the argon working gas due to the sputtered particle flux, there could be a significant departure from a uniform density distribution, having a commensurate effect on simulation results. This is known to be more of a factor at higher pressures, such as 40 mTorr, and much less a factor at lower pressures, such as 5 mTorr[132]. Thus, where appropriate, various non-uniform density profiles are used as part of the overall investigation. The profiles are based on only a few measurements taken by Rossnagel[132]. The exact nature of these profiles will be presented as appropriate to the discussion.

Also present is a non-uniform density distribution of sputtered atoms, with a higher density nearest the etch tracks and lower densities further away. Unfortunately, there is not an abundance of information on sputtered atom density distributions (there is much more available on sputtered atom flux density profiles) so the profiles

Reproduced with permission of the copyright owner. Further reproduction prohibited without permission.

selected here are intended to compare qualitatively with some of the limited data available[133,134].

Once the entire SpudII simulation package is in place, the Thermspud1 and Thermspud2 portions will be able to accurately provide density profiles of the rarefied working gas, the sputtered atoms, and other all other neutral particles such as metastables. This is interesting in itself, but also eliminates the need to use estimated neutral density profiles in Plaspud1, greatly enhancing its accuracy and enabling the extraction of much more meaningful information The neutral particle density is held by the Thermpsud2 grid.

4.1.5.b Plasma Density.

The plasma density is relevant for iterative execution of Plaspud1 and Plaspud2, where Plaspud2 will use plasma density to calculate more accurate electrical potential and field profiles. It would also be relevant if Plaspud1 was considering collisions with ionic or electronic species. However, as plasma densities are approximately 1/10,000 that of the neutral species, inclusion of these processes would likely add little to the simulation results at the expense of computation time and so is not considered here. The plasma density profile is held by Plaspud2's grid.

4.1.5.c Sheath Thickness.

Typical values for the plasma sheath width are on the order of 1 mm and decrease with higher working pressures, lower cathode voltages, higher magnetic field strengths, and higher ion currents to the cathode[28]. Within the Plaspud simulation, the sheath thickness cannot be set to any arbitrary value due to the discretized nature of the spatial grid. Within the grid, the electric field value in a given cell is a constant. As such, if any part of a cell is within the sheath, then the whole cell is also considered within the sheath. For examples of this effect, refer to figure 4.3 where the predefined sheath thickness is less than the actual thickness, as

Reproduced with permission of the copyright owner. Further reproduction prohibited without permission.

defined by the simulation's calculation. The variability of electric sheath thickness then has some practical dependence on the local grid spacing.

Choosing an appropriate value for the sheath thickness is another matter. Gu and Lieberman[99] found the sheath edge was consistent with the region of highest intensity light emission from the plasma directly above the cathode. Using optical emission spectrometry they determined this ranged from 1.5 to 3.5 mm at 5 mTorr under a variety of magnetic fields and cathode voltages. From this data they developed :

$$d_s = C\frac{V_c^{7/8}}{I^{1/2}B_o^{1/4}}$$

which is a scaled version of Child's law for the sheath thickness. It is noted this is dependant on a constant factor, C, which, among other things, is intended to characterize the magnetic field's curvature. V_c is the cathode voltage, I is the cathode ion current and B_o is the magnetic field strength at a given reference point. This law was found by Nanbu[28] to be quite consistent with simulated results at 5 mTorr. However, without a method to determine the constant, C, and thereby account for magnetic field curvature, there is no practical way to apply such a formula. After Gu and Lieberman, the sheath thickness here is determined by optical, or rather, visual means. The ARGO system was fitted with a series of flat mirrors, which allowed the user a line-of-sight directly across the surface of the cathode. By visual inspection, the distance from cathode surface to the region of most intense glow was estimated to be 1.0 to 1.25 mm (±0.25). By predefining a thickness of 1.0 mm the simulation, due to the discretized grid, produces a sheath electric field extending out 1.27 mm. This value will be used for all simulations unless noted by exception.

Some simulation efforts, particularly those of Nanbu *et al*[28,51] and Shidoji *et al*[57,58], indicate that the sheath width is not uniform. It is thinnest above the etch region where the plasma density is highest. Recalling that Gu and Lieberman's model depends on the ion current to the cathode and that the ion flux density varies across the width of the etch track (it is likely the magnetic field curvature was really

Reproduced with permission of the copyright owner. Further reproduction prohibited without permission.

accounting for the variability in ion current), it is sensible to expect a wider sheath further from the center of the etch track. At the center of the etch track, the electric field is restricted to a region very near the cathode. Above the well region and in the region outside the etch track the electric field can extend out from the cathode considerably[28,51,57,58]. If this is an important factor, then an accurate sheath thickness and electric field profile are required which can only be provided by iterative execution of Plaspud1 and Plaspud2. To guess at a sheath thickness distribution would be very speculative and likely obfuscate the results derived therein. As such, the work undertaken here assumes an initial uniform sheath thickness across the entire surface of the cathode.

4.1.5.d Potential and Electric Field

The Plaspud2 grid is initialized with an electric potential set to be plasma potential (estimated as a uniform 10 volts) everywhere in the simulation space except within cathode and anode sheaths. Within a sheath, the potential is set to a value intermediary between the plasma potential and the potential of the nearest obstruction. Within a sheath, the potential is set to:

$$\phi = \phi_{c,a} + \frac{d_{c,a}}{d_s}\left(\phi_p - \phi_{c,a}\right) \qquad (11)$$

where d_s is the sheath width, ϕ_p is the plasma potential, $\phi_{c,a}$ is the potential on the local cathode or anode, as appropriate, and $d_{c,a}$ is the distance to the local cathode or anode, as appropriate.

Using this electrical potential distribution, Plaspud2 solves for the initial electric field in cell ijk using:

$$E_x^{i,j,k} = \frac{1}{2}\left(\frac{\phi^{i,j,k} - \phi^{i-1,j,k}}{dx^{i\leftrightarrow i-1}} + \frac{\phi^{i+1,j,k} - \phi^{i,j,k}}{dx^{i+1\leftrightarrow i}}\right) \qquad (12a)$$

$$E_y^{i,j,k} = \frac{1}{2}\left(\frac{\phi^{i,j,k} - \phi^{i,j-1,k}}{dy^{j\leftrightarrow j-1}} + \frac{\phi^{i,j+1,k} - \phi^{i,j,k}}{dy^{j+1\leftrightarrow j}}\right) \qquad (12b)$$

Reproduced with permission of the copyright owner. Further reproduction prohibited without permission.

$$E_z^{i,j,k} = \frac{1}{2}\left(\frac{\phi^{i,j,k} - \phi^{i,j,k-1}}{dz^{k \leftrightarrow k-1}} + \frac{\phi^{i,j,k+1} - \phi^{i,j,k}}{dz^{k+1 \leftrightarrow k}} \right) \quad (12c)$$

where $d\alpha^{\varepsilon<->\varepsilon+1}$ is the spatial separation of cells ε and ε+1 in the α direction.

Since these solutions are taking place on a discretized grid, the solution has a piecewise continuous nature, although the resulting piecewise electric field integrated from cathode to plasma is always within a few volts of the correct cathode-plasma potential difference. Voltage profile examples taken above the center of the cathode through the sheath are shown in figure 4.3 for a –565 volt cathode, a 10 volt plasma, and various sheath widths. When operating SpudII in 2-D slab mode, it is assumed there are no gradients (electric field or potential) normal to the slab.

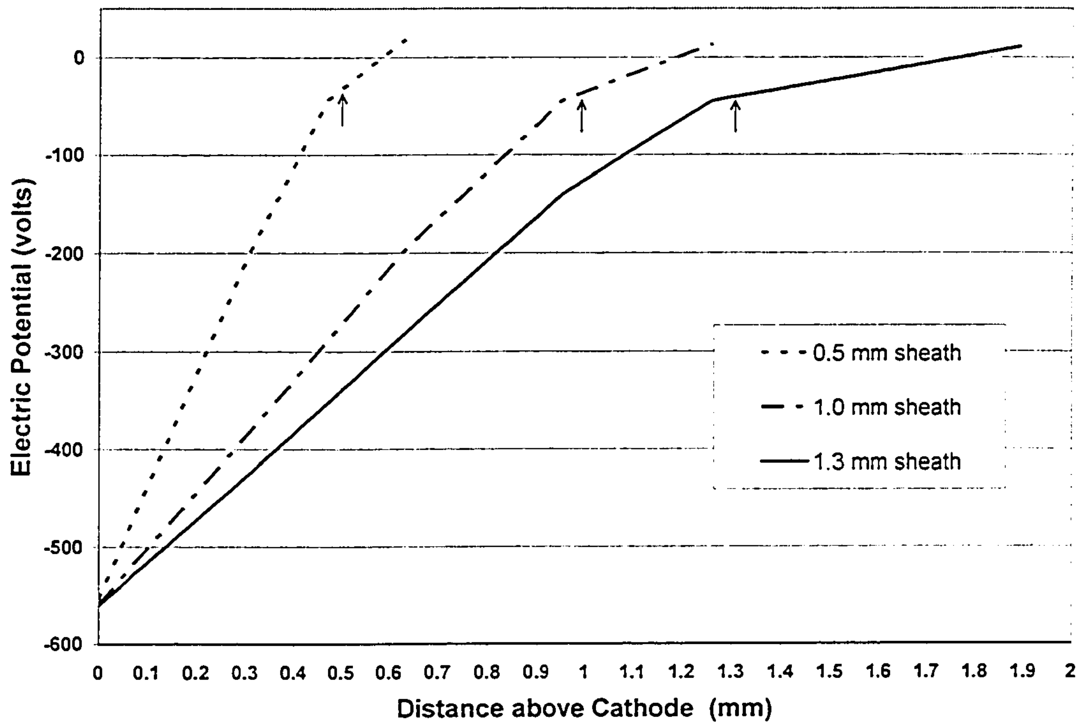

Figure 4.3: Examples of electric potential within cathode sheath. Sheath thicknesses specified are 0.5 mm, 1.0 mm and 1.3 mm resulting in actual sheaths that are 0.63, 1.27, and 1.90 mm, respectively. Note the arrows indicate sheath edge location as defined prior to simulation execution. Profiles are due to discretization of electric field on a finite grid.

Reproduced with permission of the copyright owner. Further reproduction prohibited without permission.

4.1.5.e Secondary Electron Emission Coefficient

The secondary electron emission coefficient (γ_p) (see eqn. (5)) is used to determine the average number of electrons emitted per ion incident on the cathode. This method is due to Krishinevsky[122] and is for a metal target at ground potential. In the case of silver, equation (5) becomes:

$$\gamma_p = 0.2(0.8E_i - 2\phi)/E_f = 0.2(0.8 \times 15.76 - 2 \times 4.26)/5.49 = 0.15 \qquad (13)$$

However, since the target is at several hundred volts negative, changing this coefficient to a higher value is appropriate[127] (see §4.1.2). While it is not entirely clear what value should be used, it will be seen, in §4.1.6.5, that this coefficient's only influence is as an approximate 1:1 scaling factor on absolute creation rates and n_e. It has no influence on the EEDF's or qualitative shape of spatial profiles for creation rates or n_e. Since, in this case, precise values are not known for γ_p, it must be recognized that absolute densities and creation rates may be in error by the same factor by which γ_p is in error. Values of 0.36 are mostly used here with the intent of accounting for effects arising from the voltage on the cathode[127] (see §4.1.2). Since higher γ_p values lead to more electrons ejected per incident ion, the simulation will also run faster without qualitatively influencing results. Simulations are performed to test the effect of this variable by using values of 0.27 and 0.18. Notes will be made for all simulations where the γ_p deviates from 0.36.

All emitted electrons are given a nominal energy of 4 eV[33,120]. It is important that the electron energy not be 0 eV on emission, since this can prevent the electron from future interactions with the cathode, which normally would take place and would in effect artificially eliminate the ability of the cathode to recapture emitted electrons. Since the reflection coefficient is finite this could lead to significant inaccuracies in the simulation's results[120].

Reproduced with permission of the copyright owner. Further reproduction prohibited without permission.

4.1.5.f Electron Reflection Coefficient

The Electron Reflection Coefficient (ERC) is set to a value of 0.2 (see §4.1.2). Any electron impinging on the cathode has this probability (determined by a random number) of being reflected and thus returned to the simulation. All electrons and ions colliding with anodes or other non-cathode obstruction have a reflection coefficient of 0.0, i.e. they are all lost.

4.1.5.g Cathode Ion Flux

The initial ion flux distribution obtained by Plaspud1 is based on the target erosion profile. Goeckner *et al*[27] showed the target erosion profile matches very closely to the ion flux distribution at the cathode. Shidoji *et al*[59] found the cathode ion flux is predominantly directed normal to the cathode, so here, ions obtained by the simulation at the sheath edge can be based on the erosion profile found experimentally on the target. The erosion profile used to obtain an initial ion flux distribution is given in figure 4.4.

This erosion profile could not be taken from the ARGO system since the motion of the magnet assembly results in even erosion of the cathode. Here, the erosion profile was taken from a cathode with a motionless magnet assembly using a near identical configuration with the exception that it was approximately two times longer than the ARGO magnet assembly. It is assumed this does not significantly affect the erosion profile across the width near the center lengthwise. Figure 4.4 shows the ARGO magnetic field above the erosion profile. It appears the deepest erosion regions align well with the locations where the magnetic field is predominantly parallel to the cathode contributing to the confidence that erosion profile used is appropriate.

The ion flux distribution is normalized and multiplied by the actual cathode current taken from experiment. It is then further multiplied by $(1-\gamma_p)$ to isolate the ion

Reproduced with permission of the copyright owner. Further reproduction prohibited without permission.

component of the total cathode current from the electron component. The initial ion flux distribution is managed by Plaspud2.

For 2-D simulations, the cathode current is divided by half the erosion track length (in 2-D simulation there are two sides of the erosion track being simulated) to give a line current density in units of ions/sec/meter, effectively eliminating one spatial dimension.

4.1.5.h Magnetic field

The magnetic field used for all simulations is the same as shown in chapter 3 and figure 4.4. The Gemini software (see §2.1 in Chapter 2) was used to generate sets of data with a resolution down to a 2.5 x 2.5 mm grid spacing. This data is loaded at run-time by a magnetic field manager called Magspud.

In general, Plaspud1 operates by tracking energetic particles through their life history and recording events associated with that history to form a statistical picture of the magnetron plasma. Once the boundary and initial conditions are established, Plaspud1 can begin operation.

Reproduced with permission of the copyright owner. Further reproduction prohibited without permission.

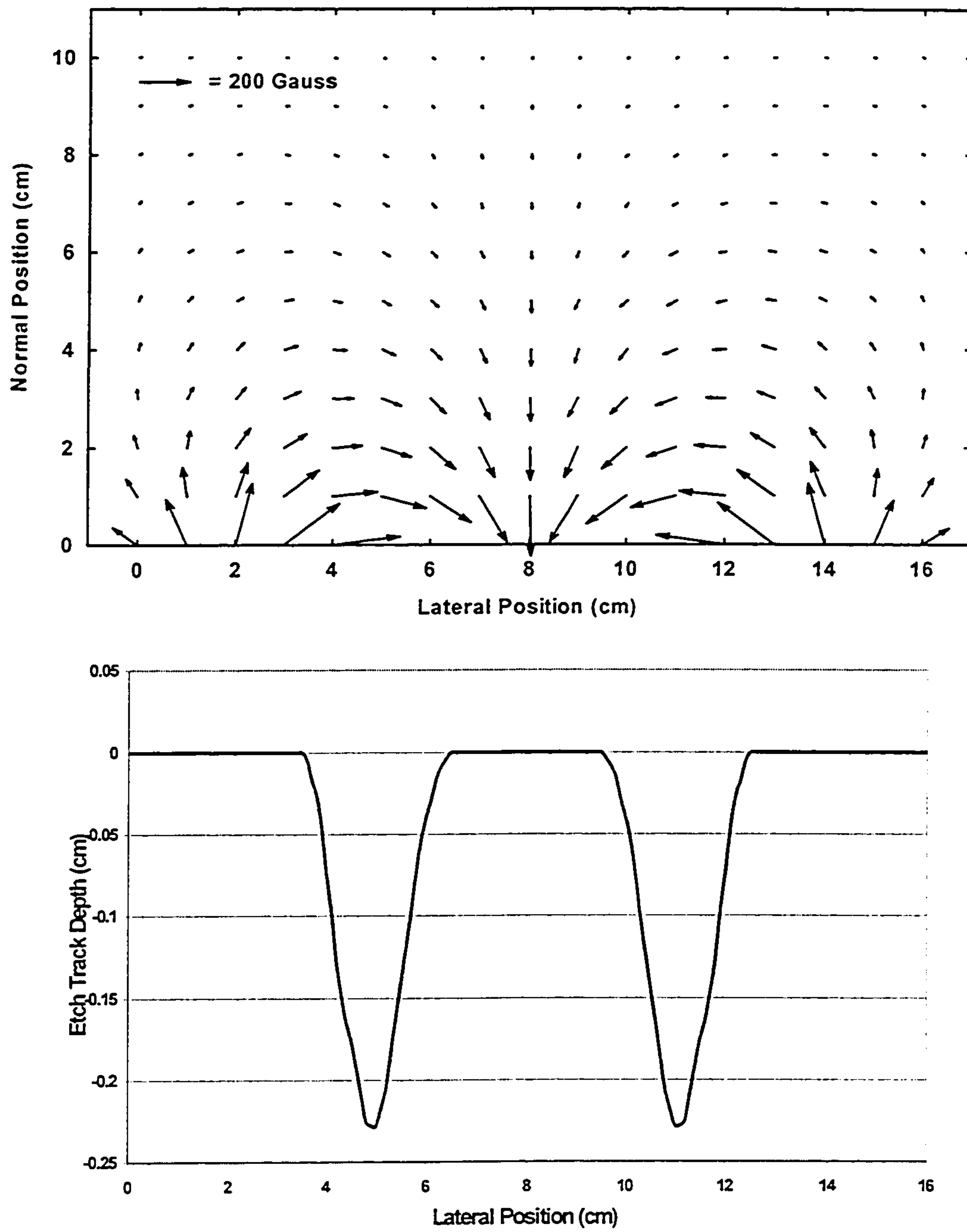

Figure 4.4: Target erosion profile (bottom) and magnetic field profile (top).

Reproduced with permission of the copyright owner. Further reproduction prohibited without permission.

4.2 Plaspud1 Functional Algorithm

4.2.1 General Description of Algorithm

The PS1 algorithm begins by obtaining a single initial ion from the edge of the sheath above the cathode. This ion is located on the sheath boundary at a position determined by random selection based on the initial ion flux density distribution.

Every time a particle is created in Plaspud1 local information is collected from Plaspud2 (electric field), Magspud (magnetic field), Thermspud (gas densities) and the spatial extent of the cell in which this information is obtained. Any time a particle (ion or electron) leaves a cell, new local information is obtained.

The ion, moving by Runge-Kutta integration steps, will be attracted to the cathode due to the high electric field present in the sheath. Upon colliding with the cathode, the ion is lost and a secondary electron may be ejected as determined by γ_p (§4.1.4.e). If no secondary electron is generated another initial ion is obtained from the sheath boundary and tracked similarly. At this point, the software will also generate sputtered neutral particles based on the ion type, target type, and ion energy and angle of incidence. These particles can be routed to Thermspud1 for Monte-Carlo simulation of neutral particles.

On generation of a secondary electron it is tracked until it is lost to an obstruction (cathode or anode) or until it is outside the sheath (within which it could still gain energy) and its kinetic energy drops (due to gas phase collisions) below a specified value, hereafter referred to as the thermalization threshold. After each time step, a check is first made to determine if a collision with an obstruction has occurred and if the electron has been lost (section 4.1.2). If the electron has not been lost to an obstruction, then a check is made to determine if the electron has undergone a gas phase collision. If so, the energy and direction of the electron is changed according to the collision dynamics. Also, if an excitation, ionization or other inelastic event occurs, the location of this event is recorded by Plaspud2 for use in calculating the absolute rates of these events, including local thermalized ion and electron creation rates. If the electron energy falls below the thermalization threshold, then it is deemed

Reproduced with permission of the copyright owner. Further reproduction prohibited without permission.

lost. If an electron is lost due to a gas phase collision, then the location of this is recorded by Plaspud2 and used by the fluid model as part of the source term to calculate the local thermalized electron creation rate.

Each time an electron crosses the physical boundary out of the cell it is in, the amount of time the particle spent in the cell is recorded. Section 4.3.1 shows how this can be used to calculate fast electron densities, which are interesting in themselves, but are also necessary to compute electric fields in Plaspud2.

If new charged particles are created, such as in an ionization event, then one of two things will happen to those particles. If the particles are created outside of the sheath, then the species type and location are recorded for later use in Plaspud2 for calculating creation rates of such species (see §4.3.2). If new charged particles are created within the sheath region, where they can gain a significant amount of energy from the electric field, they will be stored (location, type and energy) and processed sequentially in Plaspud1 after the current particle reaches the end of its life.

If no charged species are created in the collision but new neutral species are (excitation event, etc.), then the location and type of species created can be saved and passed along to Thermspud1 for later processing.

Within Plaspud1, when charged particles are created inside the sheath or at the cathode through a collision event, the new particles are placed in a 'bucket' to store them for future use. Once the current simulation particle has been expended, a new particle is obtained from the bucket. This continues until the bucket is empty whereupon a new sheath ion is obtained.

The thermalization threshold (TT), where the electron is deemed 'cold' enough to be no longer of interest as an energetic electron, can be set at any desired value. This is commonly set as the lowest energy inelastic collision included in the simulation[30,60,135]. For example, if the only inelastic process included in the simulation is argon ionization (15.76 eV), then any electron with energy below 15.76 eV is dropped. If metastable excitation (11.60 eV) is included, then electrons are tracked until they fall below that value. Sometimes, the thermalization threshold is set at an arbitrary value that lies below the lowest inelastic energy in the system[57]. Calculation of fast electron densities in Plaspud1 is only pertinent to electrons with

Reproduced with permission of the copyright owner. Further reproduction prohibited without permission.

energy higher than this arbitrarily set threshold. Here, electrons are tracked down to 6 eV in order to extract information on the EEDF in an interesting energy range. While it is desirable to extend this energy range to lower values, going to very low levels is a massive tax on computation time. This is because the only energy loss mechanism is elastic collisions of the light electrons with massive ions and atoms. In such cases, the energy loss rate of electrons is poor (see eqn.(10)). Consequently, it takes much longer to simulate progressive lower increments in energy.

Plaspud1 properly halts execution under any of three potential conditions: 1) a specified number of sheath ions has been simulated, 2) Plaspud2 indicates it has enough samples for convergence, or, 3) the simulation operator inspects periodically output run time data and deems the simulation to be converged, signaling it to cease operation. A flow chart for Plaspud1 is included as figure 4.5 to enhance clarity.

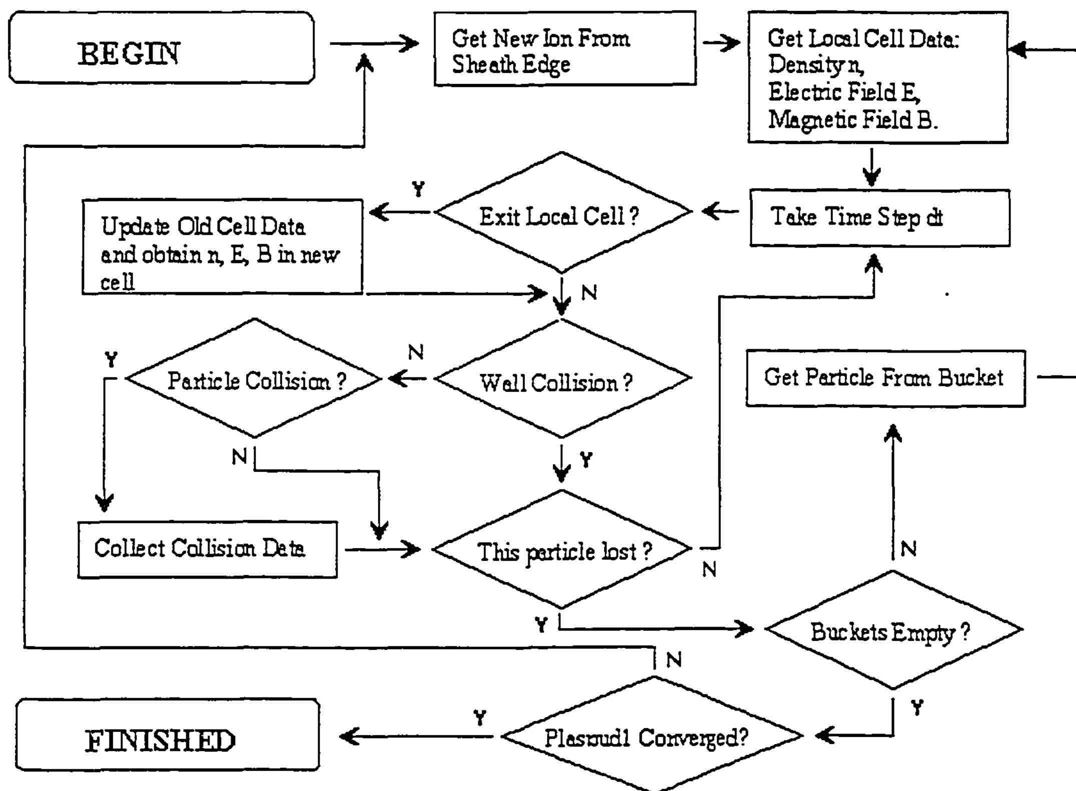

Figure 4.5: Flow chart for the operation of Plaspud1 module.

Reproduced with permission of the copyright owner. Further reproduction prohibited without permission.

4.3 Extracting meaningful data from the simulation

4.3.1 Fast electron density

Densities are calculated as discrete values within cells and are stored in the grid owned by Plaspud2. This 3-D grid is composed of many cells of varying volumes since localized grid refinements are permitted. Each cell has its own values for B, E, n_n, n_e, and n_i.

For the purposes of obtaining the densities of fast electrons, the following scheme is used:

Plaspud2 will provide the absolute flux of ions to the target which is denoted as $\mathbf{I}_{i,t}$ (in units of #ions/sec.). Given the average number of secondary electrons ejected from the target per incident ion, $<e_s>$ (electrons/ion), the absolute number of secondary electrons ejected from the target can be determined as:

$$\eta_e = \mathbf{I}_{i,t}<e_s> \tag{14}$$

(in units of # e^- ejected per second).

Plaspud1 will simulate N secondary electrons ejected from the target, which implies we have simulated (assuming N is large enough to be statistically meaningful) $N/\eta_e = T$ seconds of absolute time.

Now consider a specific cell in the density grid (cell ijk), within which the fast electron density is to be computed. Of the N simulated fast electrons, n_{ijk} of them will pass through cell ijk. Therefore n_{ijk}/T = the number of electrons through cell ijk in T (absolute) seconds. Consider $<\Delta t_{ijk}>$ as the average time a fast electron spends in cell ijk so that the density per cell is $\rho_c = (n_{ijk}/T) < \Delta t_{ijk} >$ (units of # per cell), where

$$n_{ijk} \cdot < \Delta t_{ijk} >= \sum_{m=1}^{n_{ijk}} (\Delta t_{ijk})_m$$

The absolute spatial density is just this value divided by cell ijk's volume:

Reproduced with permission of the copyright owner. Further reproduction prohibited without permission.

$$\rho_{ijk} = \frac{n_{ijk} \cdot < \Delta t_{ijk} >}{T \cdot V_{ijk}} \tag{15}$$

After substituting into (15) we get:

$$\rho_{ijk} = \beta_{ijk} \sum_{m=1}^{n_{ijk}} (\Delta t_{ijk})_m \quad \left(m^{-3}\right) \tag{16}$$

where

$$\beta_{ijk} = \frac{\mathbf{I}_{i,t} \cdot < e_s >}{N \cdot V_{ijk}} \quad (\sec^{-1} m^{-3}) \tag{17}$$

and is a constant for each cell, needing to be calculated only once at the end of the iteration. Thus the fast electron density can be determined by using the constant β_{ijk} and by maintaining a running sum of all the time spent in cell ijk by fast electrons.

Since $<e_s>/N$ is equal to $1/N_i$, where N_i is the number of ions incident on the cathode, β_{ijk} becomes:

$$\beta_{ijk} = \frac{\mathbf{I}_{i,t}}{N_i \cdot V_{ijk}} \quad (\sec^{-1} m^{-3}) \tag{18}$$

In this case, one must be wary that N_i is not solely due to primary ions originating at the sheath edge. It now also includes ions impacting the cathode that were created in the sheath due to electron-ion collisions there.

For implementation of the 2-D slab mode, $\mathbf{I}_{i,t}$ has units of ions/sec./meter (see section 4.1.4.g) to account for the lost spatial dimension. V_{ijk} in (17) or (18) is then replaced by $A_{\alpha\gamma}$ the area of the cell normal to the lost dimension (α and γ represent the two remaining spatial dimensions of i, j, or k).

4.3.2 Ion and electron creation rates

Cold (or thermalized) electron creation rates are found by monitoring a fast electron's energy when it exits the sheath region. The energy will drop due to collisions and eventually fall below an arbitrary thermalization threshold value. The

Reproduced with permission of the copyright owner. Further reproduction prohibited without permission.

Plaspud2 cell in which this occurs records the event. Additionally, any electrons created (due to ionizing events) outside the sheath are assumed thermalized, and thus also recorded in the Plaspud2 cell. The number of 'thermalizing' events in any cell is scaled using (17) or (18) by a similar argument as before. Thus the slow electron creation rate becomes:

$$R_{ijk}^{e,slow} = R_{ijk}^{e,fast\rightarrow slow} + R_{ijk}^{e,ionize} = \beta_{ijk}\Gamma_{ijk}^{e} \tag{19}$$

where Γ^{e}_{ijk} is the number of electrons thermalized or created in cell ijk throughout the Plaspud1 invocation, $R_{ijk}^{e,fast\rightarrow slow}$ is the creation rate of slow electrons due to thermalization of hot electrons and $R_{ijk}^{e,ionize}$ is the creation rate of slow electrons due to ionizing events. The slow electron creation rate can be used by Plaspud2 as a source term in its fluid model algorithm but also is interesting in itself.

The creation rate of ions is done similarly, although, in this case the creation rate is due solely to ionization events. Following a similar convention:

$$R_{ijk}^{ion} = R_{ijk}^{ion,ionize} = \beta_{ijk}\Gamma_{ijk}^{ion} \tag{20}$$

This is generic to multiple ions species should they be present in the simulation.

Electron attachment, such as with highly electronegative gases such as oxygen, can be a factor in the cold electron creation rate since it is an effective sink for such electrons. This is accounted for in the simulation code though not a factor here since such processes are not deemed relevant.

For 2-D slab implementation, the same procedure is performed as in section 4.3.1.

4.3.3 EEDF's

Creation of EEDF's is simply a matter of calculating electron densities as a function of energy. When an electron leaves a cell and the amount of time it spent in that cell is recorded, the energy of that electron dictates into what energy bin that time

Reproduced with permission of the copyright owner. Further reproduction prohibited without permission.

goes. When the Plaspud1 iteration ends and densities are calculated, they are calculated for each energy bin. The sum of densities over all energy bins will equal the total fast electron density. If an electron has a collision in a cell and its energy drops, the time spent at the higher energy is sent to the higher energy bin, and the time spent at the lower energy is sent to the lower energy bin.

Since this algorithm is an additional tax on run time, a limited number of cells are tagged to collect EEDF information. These cells are chosen to reflect some of the locations where Langmuir probe data was collected.

Since electrons are only tracked down to 6 eV, the EEDF's below this value cannot be obtained. Use of the portion above 6 eV appears to be sufficient to fit Maxwellian or other theoretical distribution curves. To confirm this was appropriate, some few simulations were completed with a thermalization threshold down to 5 eV and the extra data point still followed the theoretical curve where a good fit had been obtained to data calculated using a 6 eV thermalization threshold.

4.4 Practical Details

SpudII is programmed in C++ using a simulation framework previously developed[136]. Linux or Solaris operating systems are used. For these runs, convergence is determined by monitoring the EEDF's every few thousand simulated primary ions. As the simulation progresses and changes to the EEDF's become negligible, the simulation can be considered converged. EEDF's are used as the determining factor since they will take the longest to converge due to much lower sampling than for other parameters.

The error in EEDF's is also calculated and recorded along with the number of samples per bin (i.e. the number of electrons that contributed a Δt to each bin). For a function of several independent variables $f(x_1,x_2,x_3,...,x_n)$ the uncertainty (δf) can be determined using the general formula for uncertainty[137]:

Reproduced with permission of the copyright owner. Further reproduction prohibited without permission.

$$\delta f = \sqrt{\left(\frac{\partial f}{\partial x_1}\right)^2 (\delta x_1)^2 + \left(\frac{\partial f}{\partial x_2}\right)^2 (\delta x_2)^2 + \left(\frac{\partial f}{\partial x_3}\right)^2 (\delta x_3)^2 + \ldots + \left(\frac{\partial f}{\partial x_n}\right)^2 (\delta x_n)^2} \quad (21)$$

In the case of fast electron density, application of (21) to (16) using (18) for β_{ijk} gives:

$$\delta \rho_{ijk} = \sqrt{\left(\frac{\partial \rho_{ijk}}{\partial \mathbf{J}_{i,t}}\right)^2 (\delta \mathbf{J}_{i,t})^2 + \left(\frac{\partial \rho_{ijk}}{\partial N_i}\right)^2 (\delta N_i)^2 + \left(\frac{\partial \rho_{ijk}}{\partial V_{ijk}}\right)^2 (\delta V_{ijk})^2 + \left(\frac{\partial \rho_{ijk}}{\partial \sum_{m=1}^{n_{ijk}} (\Delta t_{ijk})_m}\right)^2 \left(\delta \sum_{m=1}^{n_{ijk}} (\Delta t_{ijk})_m\right)^2} \quad (22)$$

The errors $\mathbf{J}_{i,t}$, N_i, and V_{ijk} are taken to be zero. The sum in the fourth term can be considered the number of samples times the average Δt for cell ijk:

$$\sum_{m=1}^{n_{ijk}} (\Delta t_{ijk})_m = n_{ijk} \left(\frac{\sum_{m=1}^{n_{ijk}} (\Delta t_{ijk})_m}{n_{ijk}} \right) \quad (23)$$

and the error is due to the error in the number of samples. I.e. $\delta n_{ijk} = \sqrt{n_{ijk}}$. Simple manipulation of (22) using (23) leaves:

$$\delta \rho_{ijk} = \frac{\rho_{ijk}}{\sqrt{n_{ijk}}} \quad (24)$$

Both (24) and n_{ijk} are recorded as simulations are run. Since EEDF's converge the slowest, only their error is monitored.

Reproduced with permission of the copyright owner. Further reproduction prohibited without permission.

4.5 Results and Discussion

Simulations were performed to investigate effects from a variety of physical and model parameters. The main focus is at a pressure of 5 mTorr where effects on electron and ion creation rates, fast electron densities and EEDF's due to cathode voltage, sheath thickness, gas phase silver and metastable argon atom density, cathode electron reflection coefficient, and gas rarefaction are investigated. Subsequently, simulations are run at 40 mTorr.

4.5.1 Simulations at 5 mTorr.

4.5.1.1 Uniform Argon Pressure

The baseline run at 5 mTorr is done with the following conditions:

Pressure:	5 mTorr argon, uniform everywhere.	
Gas phase silver concentration:	0.0	
Argon metastable concentration:	0.0	
Cathode current:	0.6 A.	
Cathode voltage*:	-575 V	
γ_p:	0.36	(see §4.1.4.e).
ERC:	0.2	(see §4.1.4.f).
Electron thermalization threshold:	6 eV.	
Inelastic Collision processes:	Argon ionization	
	Argon excitation (4 processes)	
	Argon metastable excitation	

* Note that the cathode voltage was taken from the experimental value obtained for this current and pressure. See Chapter 3, Appendix 1.

Periodic simulation results were output and monitored until convergence at which point the simulation was halted. In this case, 20,000 primary ions were simulated. Some runs were allowed to run past convergence - up to 30,000 primary ions - without noteworthy improvements or changes.

Figure 4.6 shows the thermalized electron and ion creation rate (ECR and ICR) results. Qualitatively, it is an expected result as the majority of such particles are

Reproduced with permission of the copyright owner. Further reproduction prohibited without permission.

created at the site of argon ionization by energetic electrons. Since the energetic electrons are effectively trapped by the magnetic field, the magnetic field lines largely delineate the creation rate profiles. Naturally, the sheath region is completely devoid of creation rates since all charged species there are subject to energy gain from the electric field and thus cannot be considered thermalized, even with low kinetic energy. The thermalized electron creation rate is slightly higher (figure 4.6 c) than the ion creation rate since it includes thermalization of primary electrons as well as electrons resultant from ionization events. Here, ion creation rates depend exclusively on ionization events.

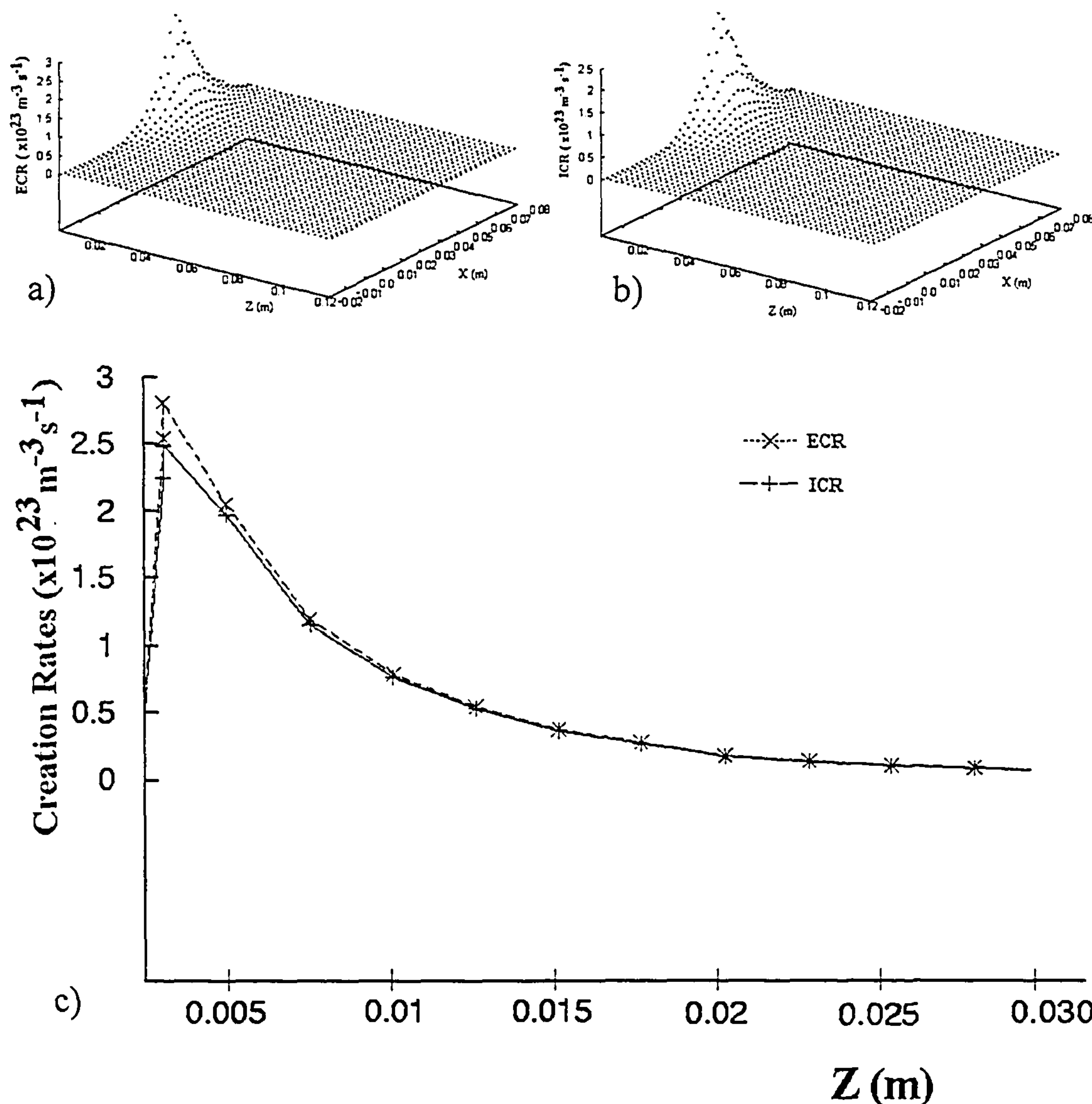

Figure 4.6: Electron and Ion Creation Rates. A) Electron creation rate in x-z plane. B) Ion Creation Rate in x-z plane. C) Electron and Ion creation rates taken along chord above center of etch track (~ x = 4 cm) normal to cathode.

Reproduced with permission of the copyright owner. Further reproduction prohibited without permission.

Figure 4.7 shows the fast electron density profile, which is all electrons with energy above the thermalization threshold of 6 eV. The profile is generally consistent with the region delineated by the magnetic field. However, directly above the etch track (where the magnetic field is parallel to the cathode) and immediately adjacent to the sheath edge, there is an abrupt and major peak in the profile.

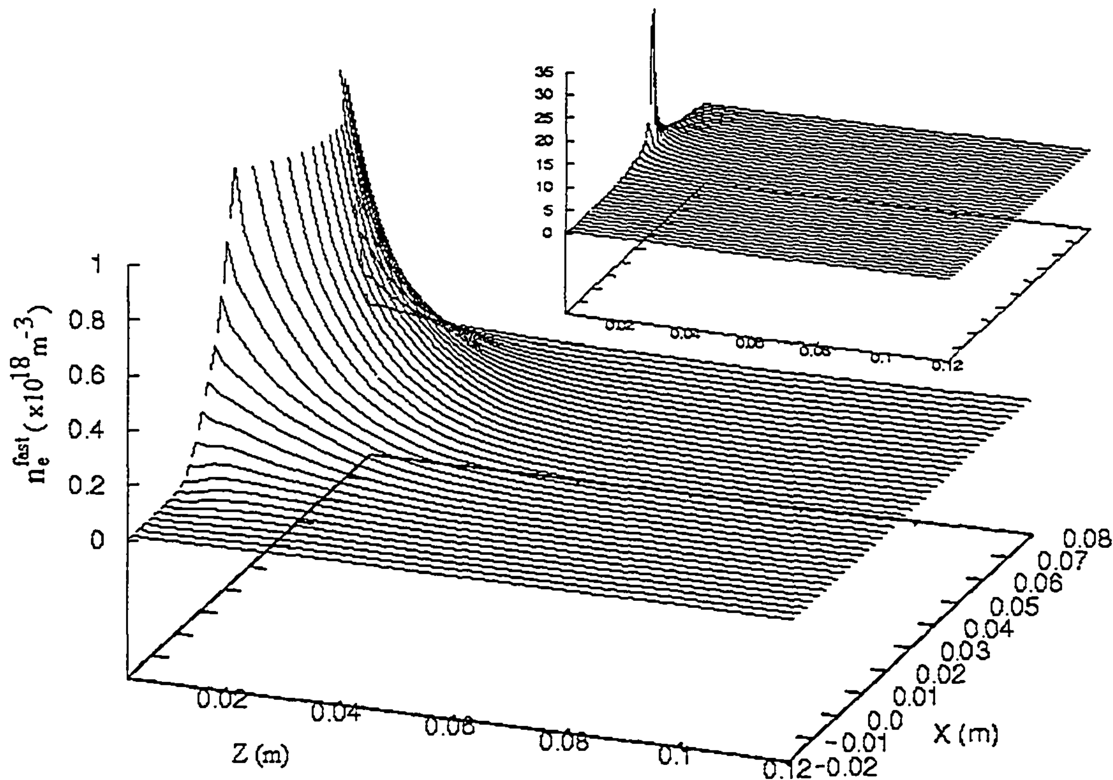

Figure 4.7: Fast electron density detail. Inset shows abrupt peak in full scale fast electron density. Note scale difference. X scale is same for both graphs.

This abrupt peak has been observed in simulations by other researchers[58,49] but not by all. It appears this peak likely results from the relatively low energy electrons confined to an extremely small area by the magnetic and electric field. The local magnetic field is shaped so as to abruptly return the electron to the sheath edge since the electron will tend to spiral around and along the magnetic field line (See figure 4.8). At the sheath edge, the electron is reflected by the electric field because its energy is too low to significantly penetrate the sheath. As a result, low energy electrons traverse this region many times before a collision scatters them away. Higher energy electrons will have a longer path between reflections at the electric

Reproduced with permission of the copyright owner. Further reproduction prohibited without permission.

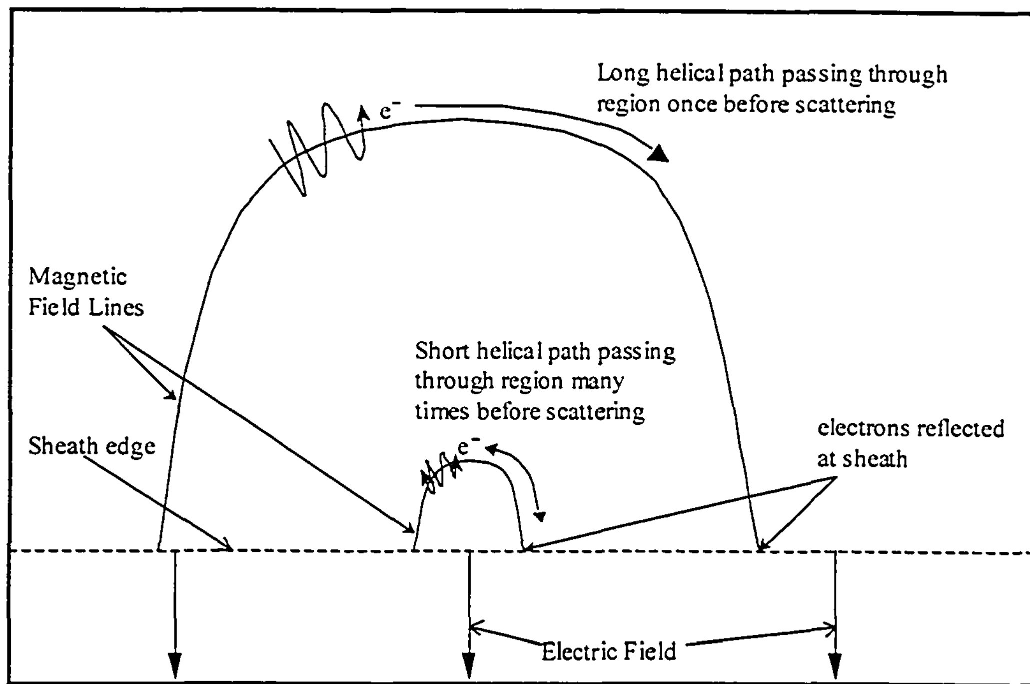

Figure 4.8 Demonstration of how low energy electrons near center of the magnetic trap can promote high densities compared to higher energy electrons or regions far from this region. Low energy electrons will travel back and forth several times between reflections at the electric sheath due to the short path length between reflections relative to the mean free path. High energy electrons will have a larger Larmor radius and thus a longer path between reflections. Low and high energy electrons following a magnetic field line that is relatively long will also traverse the area fewer times before scattering.

field due to the increase in Larmor radius and thus will traverse the region fewer times before scattering away. Thus, the observed abrupt peak should be extremely sensitive to the thermalization threshold set within the simulation.

Simulations were performed with higher thermalization thresholds (8.5 and 11 eV). The fast electron density profile for these runs is shown in figure 4.9 along the chord normal to the cathode and above the etch region, where the densities are highest. A dramatic effect is seen within the high magnetic field trap region, confirming the hypothesis. The area between the trend lines in figure 4.9 can be attributed to the electrons within the energy bands 6 to 8.5 eV and 8.5 to 11 eV. The greatest contribution to fast electron density in the sharply peaked region is predominantly due to electrons with less than 8.5 eV of energy. Also noted is an increase in density just inside the sheath edge, which can be attributed to minor penetration into the sheath of the low energy electron groups. Deeper in the sheath,

Reproduced with permission of the copyright owner. Further reproduction prohibited without permission.

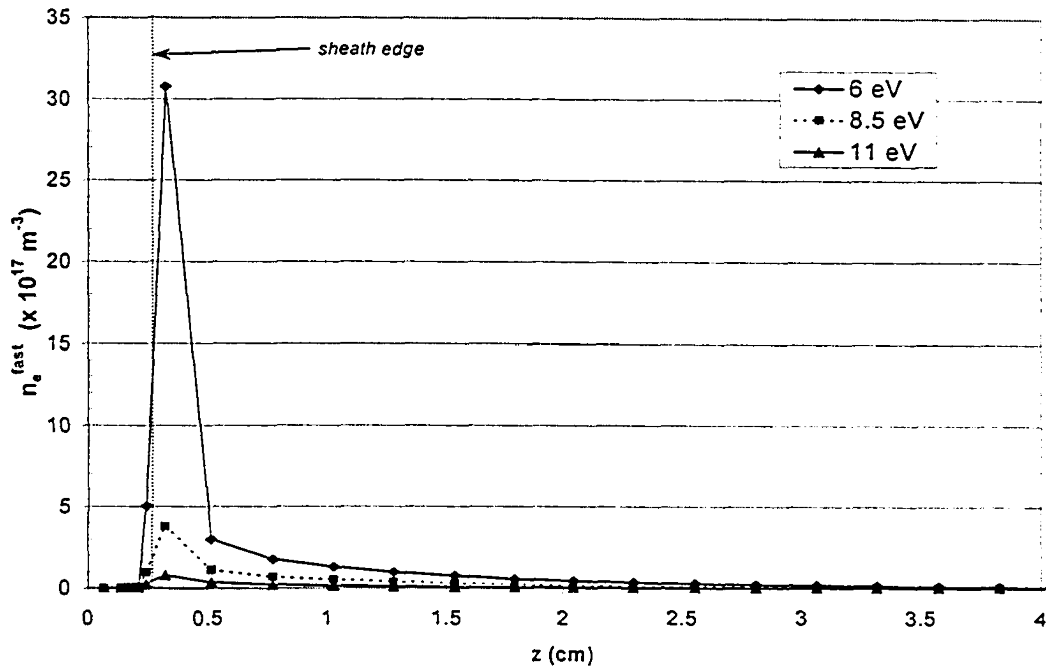

Figure 4.9 Electron density profile along a chord normal to the cathode and above the etch region where density is highest. Each trend line represents total density of electrons above the given energy threshold. Note the area between the curves represents the density due to electrons between 6 and 8.5 eV and 8.5 and 11 eV respectively. (see text for discussion)

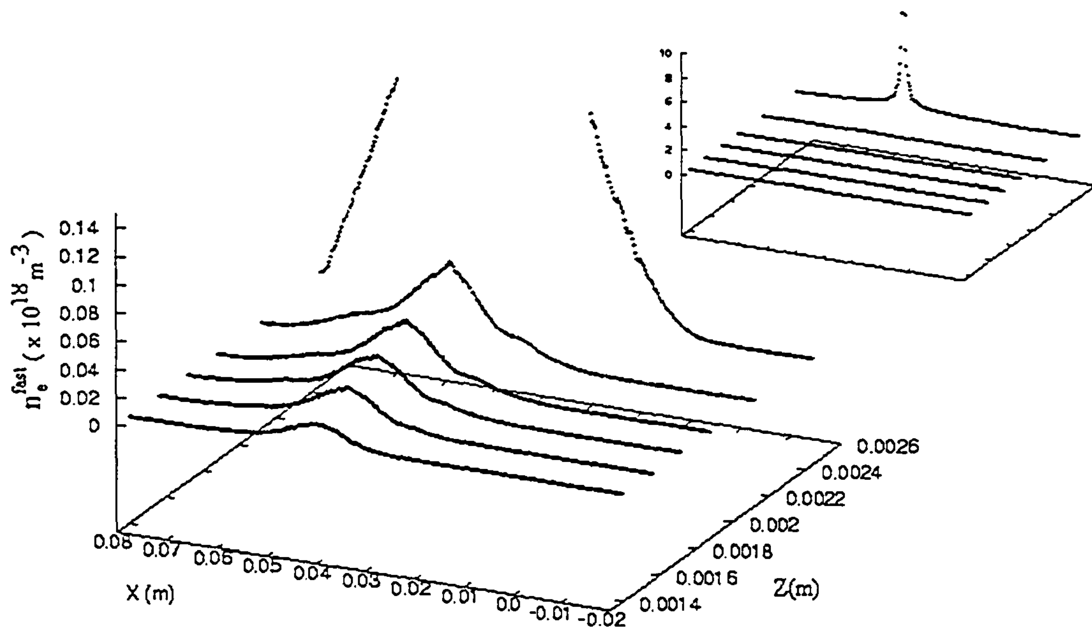

Figure 4.10: Detail of the fast electron density within the electric sheath region. Note that Figure 4.7 shows only fast electron density outside sheath region. Inset shows abrupt peak near sheath edge. Note scale difference. Scales for x and y are same for inset.

Reproduced with permission of the copyright owner. Further reproduction prohibited without permission.

the density does not change since none of the electrons under 11 eV can penetrate that far into the sheath. When these higher thermalization thresholds are used, no differences are observed in the EEDF's with the exception of missing data at lower energies. Figure 4.10 shows the fast electron density within the sheath, also indicating the abrupt peak near the sheath edge.

Figure 4.11 shows an EEDF result 4 cm (z) directly above the etch region (x = 4 cm). The simulation produced a series of energy dependant densities at this location, which are overlaid with various theoretical energy distributions. Figure 4.11a shows Maxwellian energy distributions, which describe a group of particles in thermal equilibrium with each other:

$$f(E) = \frac{2n_e^M \pi}{(\pi T_e)^{3/2}} \sqrt{E} e^{-E/T_e} \qquad (25)$$

Here n_e^M is the density (m^{-3}) of the Maxwellian group, E is energy (eV), and T is temperature (eV). The temperature and density are adjusted to provide the closest fit to the simulated data. In this case, the temperature matches quite well with that found from the experimental data: 2.9 eV. The density (~6.3 x 10^{16} m^{-3}) does not match that from the experimental section (~ 2.0 x 10^{16} m^{-3} ±0.6 x 10^{16}). The other distributions in 4.11a are also Maxwellian but using temperatures of 3.4 and 2.4 eV and densities of 5.2 and 8.8 x 10^{16} m^{-3}, respectively. These are qualitatively poorer fits to the simulated data. Note, also, that an extra data point has been added to the 5 to 6 eV bin. This data point was obtained from an additional, unconverged, run with a 5 eV thermalization threshold (error bars are indicated). This point also lends support that the 2.9 eV Maxwellian fit is the most accurate. It should be re-iterated that the method to fit the distribution is to adjust n_e^M and T_e to get the best qualitative fit, not to use the correct T_e and adjust n_e^M, although it may appear this was the case. As an important note, the n_e^M obtained by this method is an n_e taken to represent the entire analytical distribution, assuming the electrons below 5 eV follow the same

Reproduced with permission of the copyright owner. Further reproduction prohibited without permission.

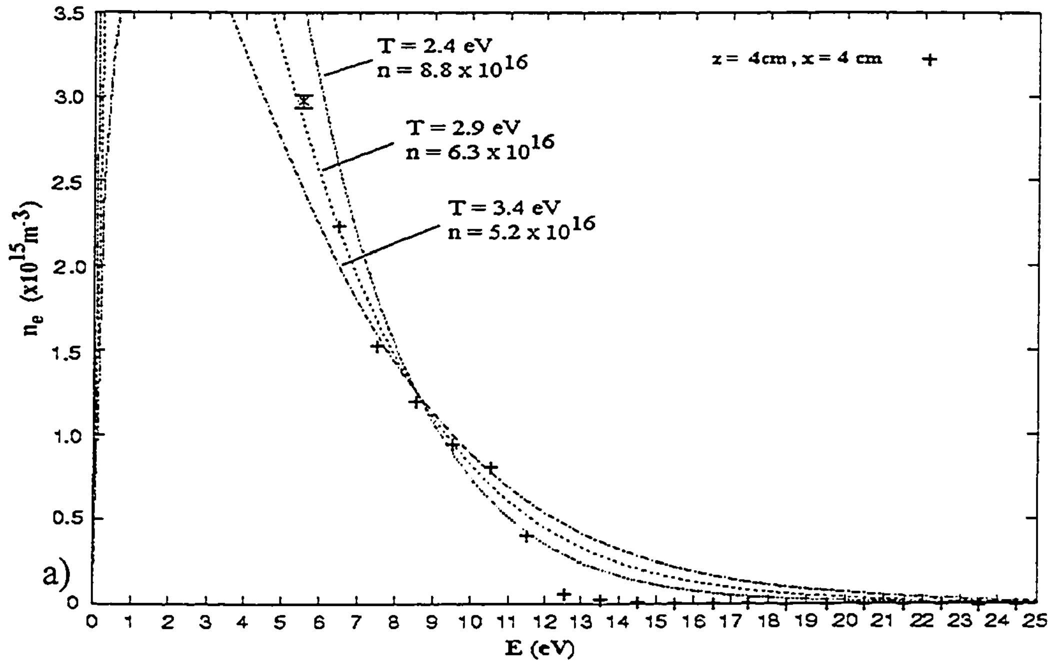

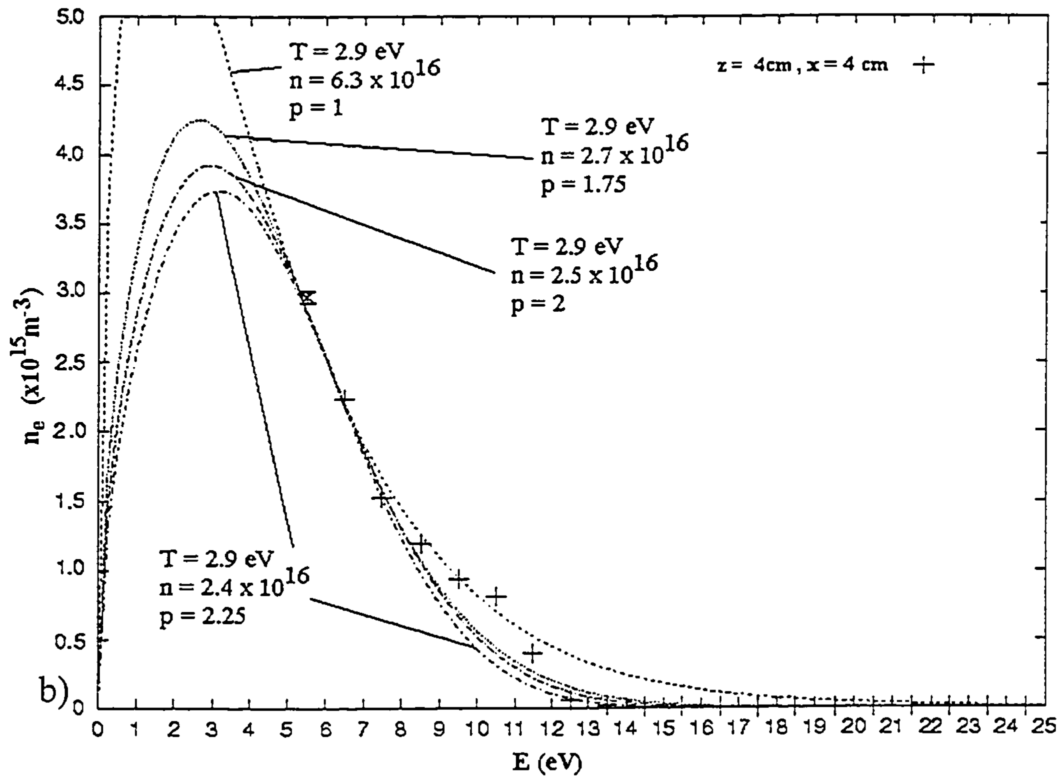

Figure 4.11: a) Maxwellian distributions (a 'best' fit and two bracketing fits) with simulated data, b) three Rundle group (one Dreyvestyn) and a 'best' fit Maxwellian distribution (p=1) with the simulated data. Included, with error bars, is one simulated data point at 5 eV from an unconverged solution.

Reproduced with permission of the copyright owner. Further reproduction prohibited without permission.

distribution. The fast electron density (sometimes called FED), as in figures 4.7, 4.9 and 4.10 represents only the portion of electrons above 6 eV in energy and is only a portion of the n_e^M from the analytical distribution. It must be recognized that the extraction of n_e^M from the simulated EEDF's assumes that the EEDF's continue to follow the Maxwellian distribution type to lower energies. There is no evidence to support this other than the Maxwellian nature of all EEDF's found in Chapter 3. While using n_e^M values, taken from extrapolating EEDF's generated by simulation, allows comparison to experimental data, caution must be exercised in interpreting values and trends in this variable. T_e, on the other hand, will represent the temperature of electrons within the energy range for which simulation data is generated, and so is more meaningfull, particularly for higher energy electrons. Once again, care must be taken in comparing T_e to low energy, or 'cold' electrons in experimental data sets, as these values of T_e may not be representative.

n_e^M is not a good match to the experimental data. However, as shall be seen, n_e^M (and FED) is more sensitive to, and can be influenced by, a wider variety of factors including boundary and initial conditions, whereas the T_e*'s* (EEDF's) are not sensitive to many of those factors. Changes in inaccurate boundary conditions may change density but are not likely to change temperature.

For all simulated EEDF's, it is noted there is a significant deviation from the Maxwellian distributions above approximately 12 eV. This can be attributed to the greater number of energy loss channels available to the electrons above the inelastic thresholds of argon. There, the energy loss of electrons due to a single inelastic collision is great compared to many elastic collisions, and electrons do not spend as much time within a particular energy bin. This results in depletion of electrons above the inelastic threshold since they have more efficient energy loss channels than do electrons below the threshold. Such distribution may be characterized by what are known as Rundle distributions[138]:

Reproduced with permission of the copyright owner. Further reproduction prohibited without permission.

$$f(E) = \frac{p}{<E>_e^{3/2}} \frac{[\Gamma(5/2p)]^{3/2}}{[\Gamma(3/2p)]^{5/2}} \exp\left[-\left[\frac{2[\Gamma(5/2p)]}{3[\Gamma(3/2p)]}\right]^p \left(\frac{E}{\left(\frac{2}{3}\right)<E>_e}\right)^p \right] \quad (26)$$

where p is an arbitrary factor (p ≥ 1), $<E>_e$ is the mean kinetic energy (most researchers substitute with $(3/2)T_e$ from the Maxwellian distribution as is done here)[138], E is the energy, and Γ(s) is the well known gamma function:

$$\Gamma(s) \equiv \int_0^\infty x^{s-1} e^{-x} dx$$

Rundle distributions reduce to Maxwellian when p = 1 and to Druyvesteyn distributions when p = 2. Druyvesteyn distributions were originally developed by considering electrons in a weak electric field[16] and predicted fewer electrons with energies greater than a few times average. Rundle distributions consider the effects of inelastic collisions in the derivation. Figure 4.11b shows the experimental data with three Rundle group distributions (including the Druyvesteyn) and the Maxwellian 'best fit' from 4.11a. The 2.9 eV electron temperature from the Maxwellian distribution is used in (26) for $<E>_e = (3/2)T_e$. All the Rundle distributions appear to account for the severely depressed density above 12 eV, particularly the distribution with p = 2.25. Additionally, these distributions appear to have a density much closer to the density taken from Langmuir probe data. However, all of these distributions do not correctly follow the trend between 8 and 12 eV, a trend which is much more closely followed by the Maxwellian distribution. Attempts at fitting other Rundle distributions were not more successful. The experimental data did not indicate such deviations from a Maxwellian-type distribution. However, the signal to noise ratio in this energy region would have been very low and such differences may have been missed. The abrupt features in the simulated EEDF between 10 to 13 eV are likely smoothed somewhat by electrostatic collisions[131] which have not been accounted for. However, Capetelli *et al*[131] showed such effects are more subtle, potentially bringing the 10 to 12 eV data closer to the Maxwellian fit but unlikely to move the 8 to 12 eV

Reproduced with permission of the copyright owner. Further reproduction prohibited without permission.

data closer to the Rundle group distributions. While it is recognized there may be elements of Rundle distributions in magnetron systems, there is not evidence to suggest they are any better fits than the Maxwellian distribution. Since the LP data was all analyzed as Maxwellian-like, use of a Maxwellian fit to the simulated results makes it more comparable to experimental data. As such, Maxwellian distributions are used here.

Figure 4.12 (a-c) shows simulated EEDF's for 6 locations above the etch region and the best fit Maxwellian distribution curves. Temperatures and densities (n_e^M) derived from 4.12 are plotted in figures 4.13 and 4.14, respectively. Also on these plots is the experimental data from chapter 3 (§3.3.1) including T_e (in the case of Maxwellian distributions) or T_{eff}, T_{cold} and T_{hot} (in the case of bi-Maxwellian distributions) and n_e and n_e^{hot} (in the case of bi-Maxwellian distributions).

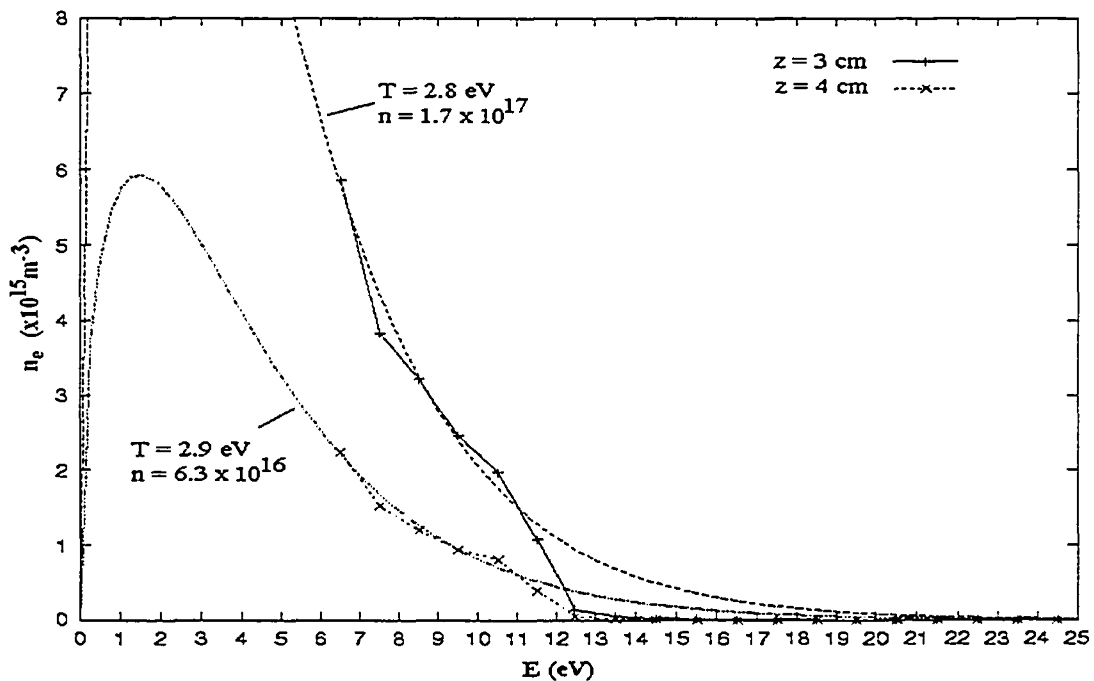

Figure 4.12 a: Simulated EEDF's with best fit Maxwellian distributions at 3 and 4 cm above the etch regions.

Reproduced with permission of the copyright owner. Further reproduction prohibited without permission.

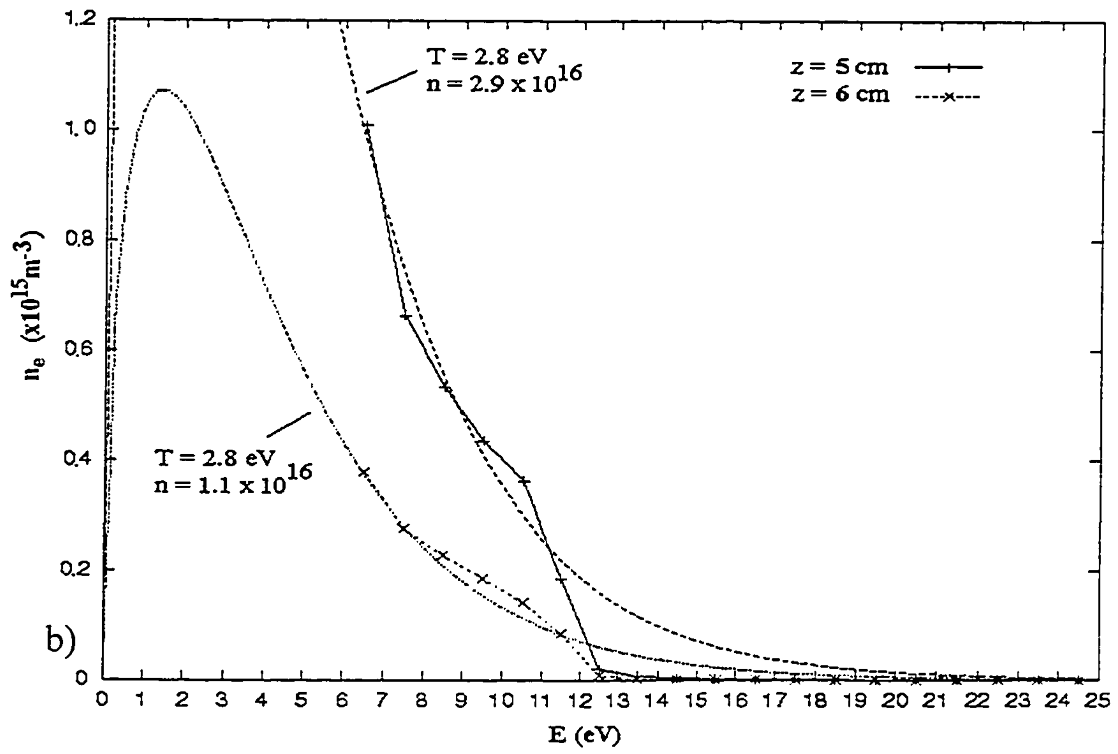

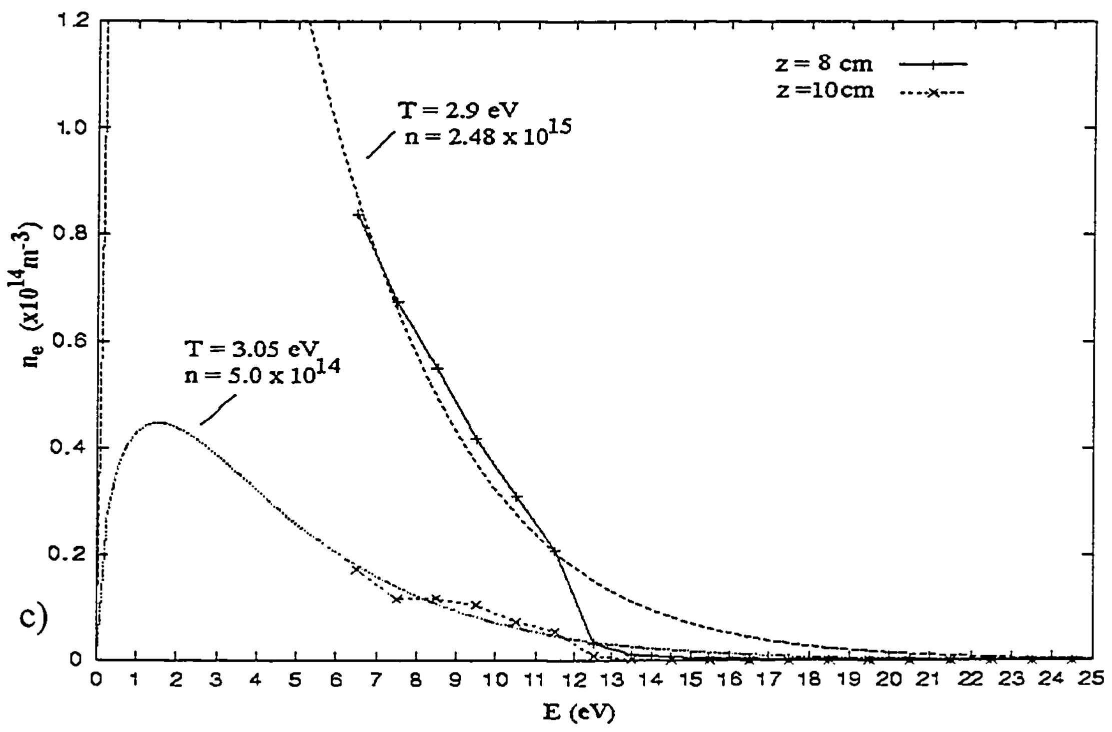

Figure 4.12 b and c: Simulated EEDF's with best fit Maxwellian distributions at 5, 6, 8 and 10 cm above the etch regions.

Reproduced with permission of the copyright owner. Further reproduction prohibited without permission.

In fig. 4.13, T_e does not agree with experimental data at all locations, and so can not be regarded as an ideal result. However, at 8 and 10 cm, the only locations where bi-Maxwellian distributions were experimentally found, the agreement with the actual hot electron temperatures (from §3.3.1) is excellent. This suggests the simulated electrons, which are those that have in some fashion gained energy from the cathode sheath, are representative of the hot electron portion of bi-Maxwellian electron distributions. If this is, in fact, the case, it is a positive and insightful result. At 3, 4, 5, and 6 cm locations the experimental signal due to hot electrons was too weak or was overshadowed by the signal due to colder, thermalized electrons. Thus hot electron temperatures were not found and agreement with the results here can not be confirmed. Potentially, optical emission spectroscopy may be able to experimentally detect the hot electron group and determine its temperature in that region and confirm the simulation result. T_e derived from simulated EEDF's do correlate with temperatures of Maxwellian group electrons at 4 and 5 cm, but not at other locations. This may suggest that the bulk of electrons observed in these regions is due to the hot electron group, though this is speculative.

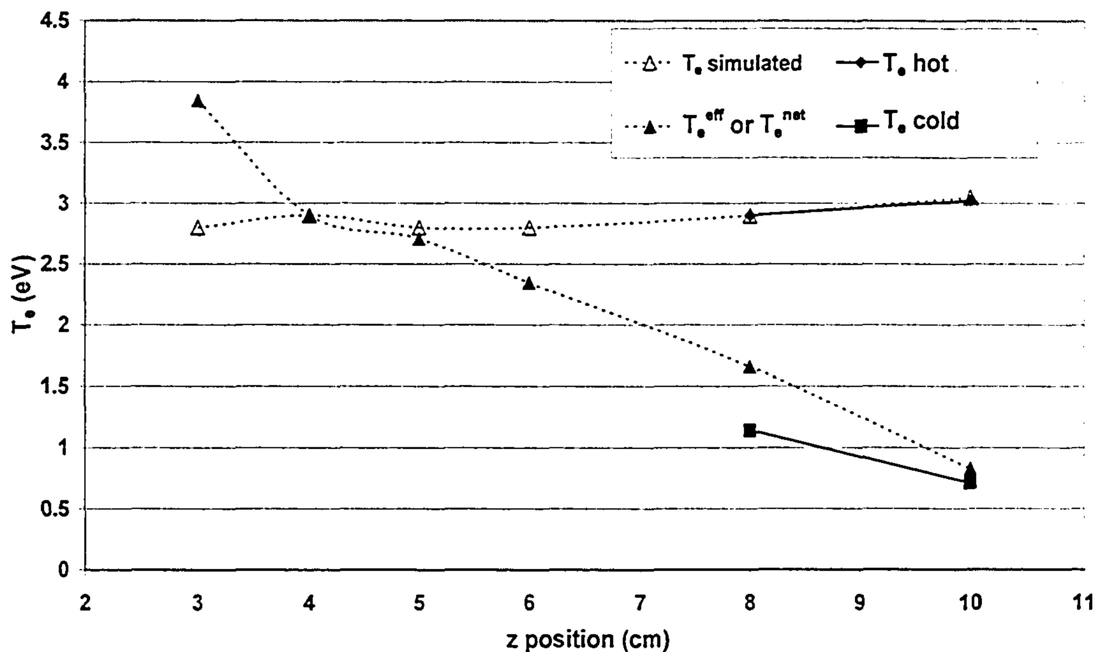

Figure 4.13: Simulated Electron Temperature and Experimental data along a chord normal to the cathode and above the etch track. Solid symbols are experimental data, open are simulated data.

Reproduced with permission of the copyright owner. Further reproduction prohibited without permission.

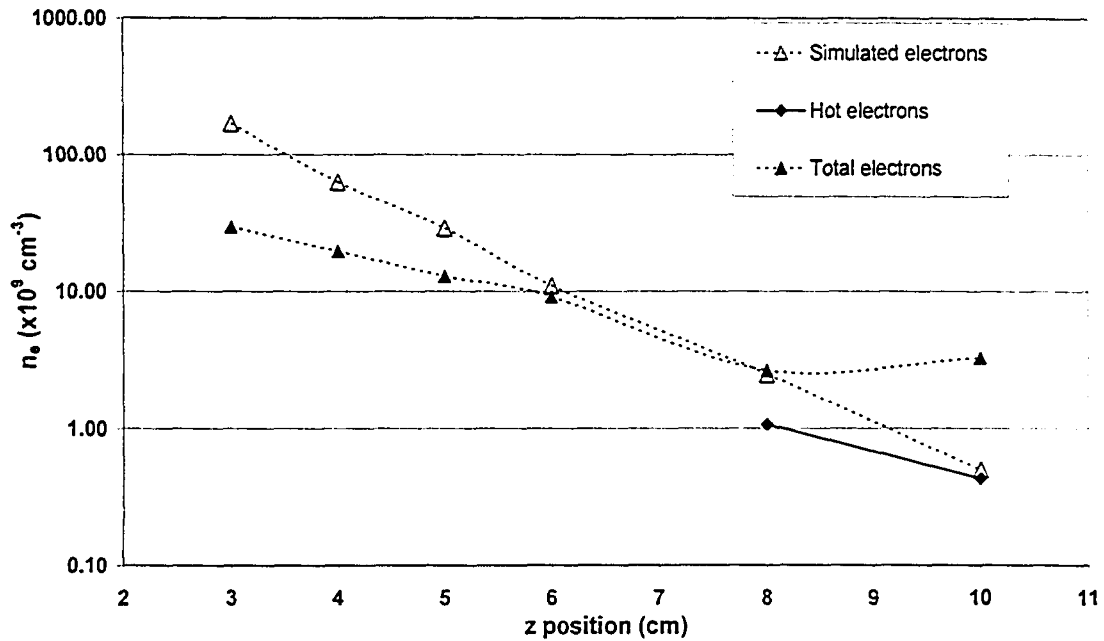

Figure 4.14: Simulated electron density (n_e^M) and experimental data along chord normal to cathode and above etch track. Solid symbols are experimental data, open are simulated data. Note log scale.

The simulated electron densities shown in figure 4.14 are values taken from Maxwellian fits to the simulated EEDF data (i.e. n_e^M). In general, the density values are not close to experimental values, either in magnitude or in gradient. However, the general trend in 4.14 is similar to that observed in 4.13 where the simulated electron density more closely follows the hot electron density where bi-Maxwellian distributions exist. Since n_e^M makes assumptions about low energy electrons that may not be true, errors may be introduced and the magnitude of the densities affected. Additionally densities may be affected by γ_p, ERC, neutral gas heating and rarefaction above the etch track, ionization and superelastic collisions with metastable argon, cathode sheath thickness, and cathode voltage. The gradient in n_e^M observed in fig. 4.1.4 may also be sensitive to similar variables. Given the poor results in figure 4.1.4, n_e^M can not be used to gain direct insight into experimental data. However, it can still be used as a metric by which to compare various simulation efforts and the influence of simulation variables on densities and distributions.

Reproduced with permission of the copyright owner. Further reproduction prohibited without permission.

Above the center of the cathode (well region), EEDF's are also accumulated in the simulation space. The results are presented in figure 4.15. The results are far from Maxwellian or Rundle with a pronounced peak near 11 eV for all cases. It is not entirely clear as to why this would be the case, although it supports the contention in Chapter 3 (§3.3.1) that there may be some unique or unusual transport mechanisms taking place in that region. The profiles obtained here suggest that those unique mechanisms are related specifically to the local shape of the magnetic field, the proximity to the magnetic trap region, and the gas density since those are the only factors in this simulation that could affect electron transport. This can be said since this simulation did not include electric fields outside the sheath, neutral gas rarefaction, transient effects, or any inelastic collision processes beyond the most basic ones.

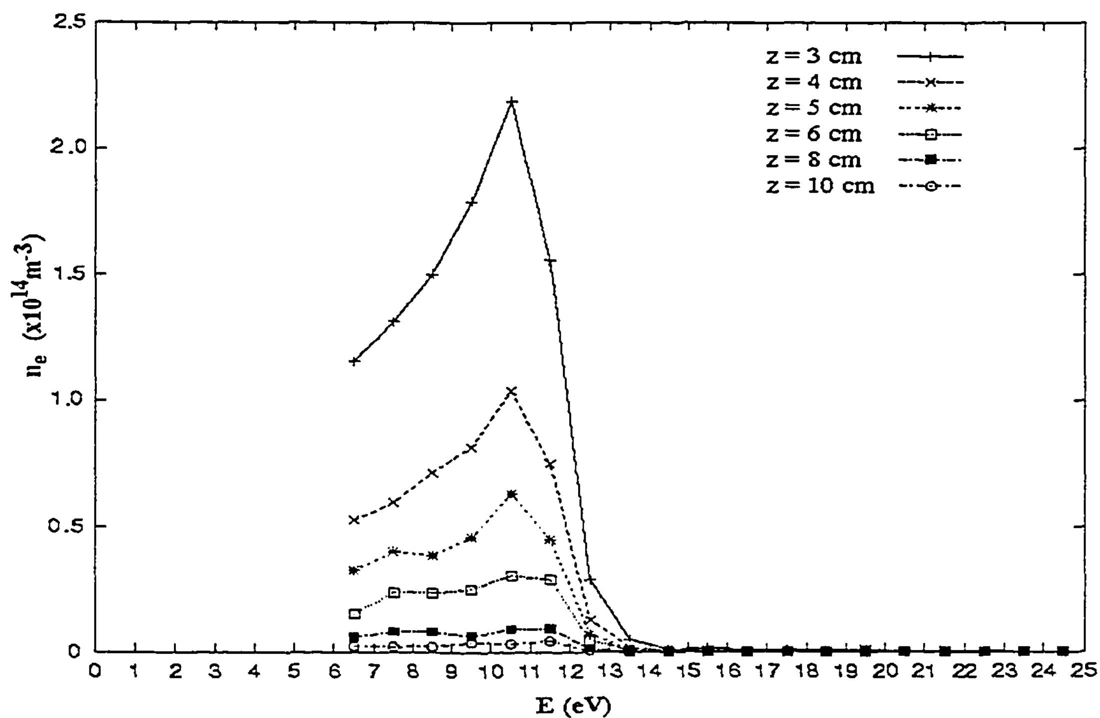

Figure 4.15: EEDF's obtained above the centre of the cathode along a chord normal to the cathode.

The well region is the only region in the magnetron system where a magnetic mirror (where magnetic field lines symmetrically converge) exists. This would make it more difficult for lower energy electrons to penetrate into the mirror (toward the cathode) from regions further out, and since at the very center the magnetic field lines

Reproduced with permission of the copyright owner. Further reproduction prohibited without permission.

are directed straight out from the cathode, any electrons within this region would be expelled rapidly. It is conceivable that the distributions in 4.15 are the result of an subtle algorithmic error in the simulations, however, EEDF's obtained laterally across the width of the cathode at 5 cm distance (see figure 4.16) indicate the unusual features in 4.15 are restricted to the region directly above the center of the cathode. Everywhere else are EEDF's that appear Maxwellian-like. To determine more precisely what is happening in this region, a more sophisticated simulation should be constructed that monitors the flux of electrons into and out of the well region and resolved for energy dependence. This could conceivably be achieved by summing the velocity vectors of electrons within the individual cells throughout the simulation space.

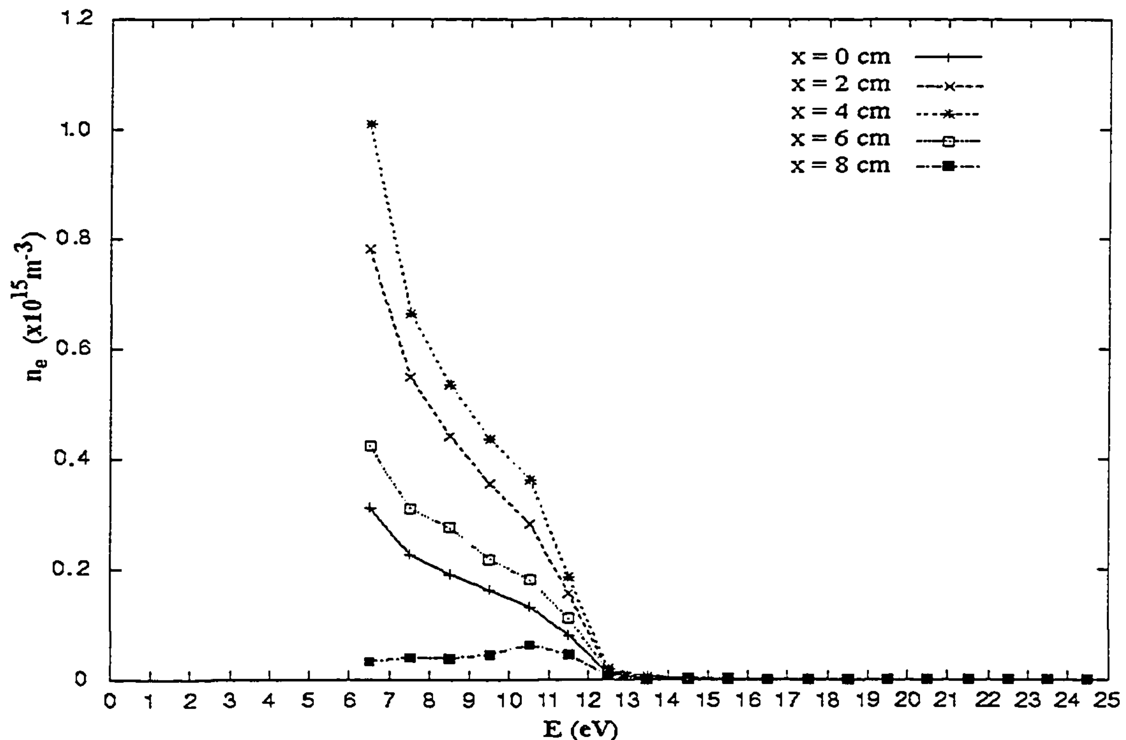

Figure 4.16: EEDF's obtained laterally across the width of the cathode at z = 5 cm distance from the cathode. Note: x = 4 cm is above etch track and x = 8 cm is above the well region.

One of the most appealing aspects of simulation is the ease in which data can be obtained. In this case, simply flagging a cell just outside the sheath region allowed the collection of an EEDF 3.5 mm above the cathode (~2 mm outside the sheath) and

Reproduced with permission of the copyright owner. Further reproduction prohibited without permission.

directly above the etch region. The low energy portion of this EEDF is shown in figure 4.17 where a high density (n_e^M = 3.05 x 10^{18} m^{-3}) of electrons is present with a fairly low temperature, only 2.4 eV. This is a lower T_e than found further out of the magnetic trap and suggests these electrons are not arriving from the cathode, but from crossing magnetic field lines to move *into* the trap region where they are held by the trap to support the much higher density.

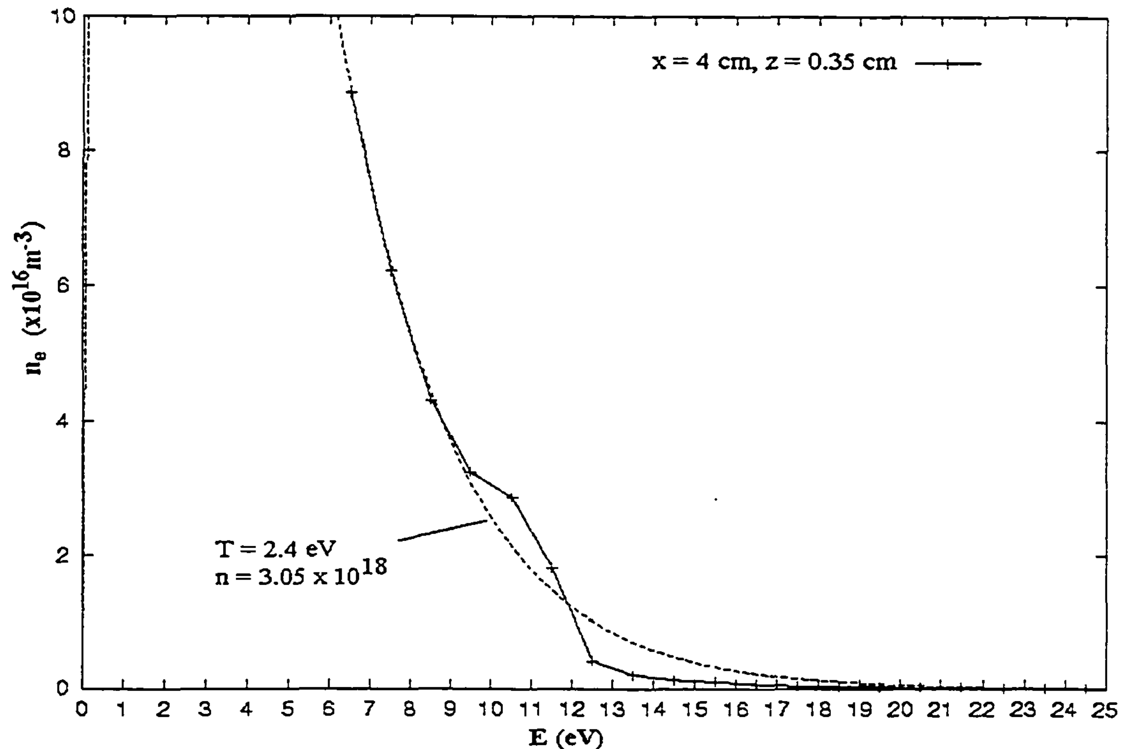

Figure 4.17: Simulated EEDF 2 mm outside sheath above etch region.

At the high energy end of the EEDF (figure 4.18) is observed a rather unique distribution. There are several peaks separated by approximately 15.8 eV with the largest peak at approximately 575 eV and the peaks decaying to almost nothing by 490 eV. While unusual in nature, there is a simple explanation for such features. Electrons ejected from the cathode cross the sheath gaining an energy of approximately 575 eV. The magnetic field causes the electron to return to near the cathode due to its resultant cyclical motion. Along the way they have a few elastic collisions giving them an energy distribution slightly spread out around 575 eV.

Reproduced with permission of the copyright owner. Further reproduction prohibited without permission.

These electrons show up as the major peak at the end of the distribution. Each time the electron has an ionizing collision, it drops in energy to a lower peak. Since the electrons undergo more and more elastic collisions as they also undergo more and more ionizing collisions, the peaks become more spread out, lower, and less resolved at lower energies. The resolution of the peaks in 4.18 is only apparent because the high energy electrons have experienced few collisions in this region. While such features have not yet been experimentally observed in such systems, this may well represent a real phenomenon.

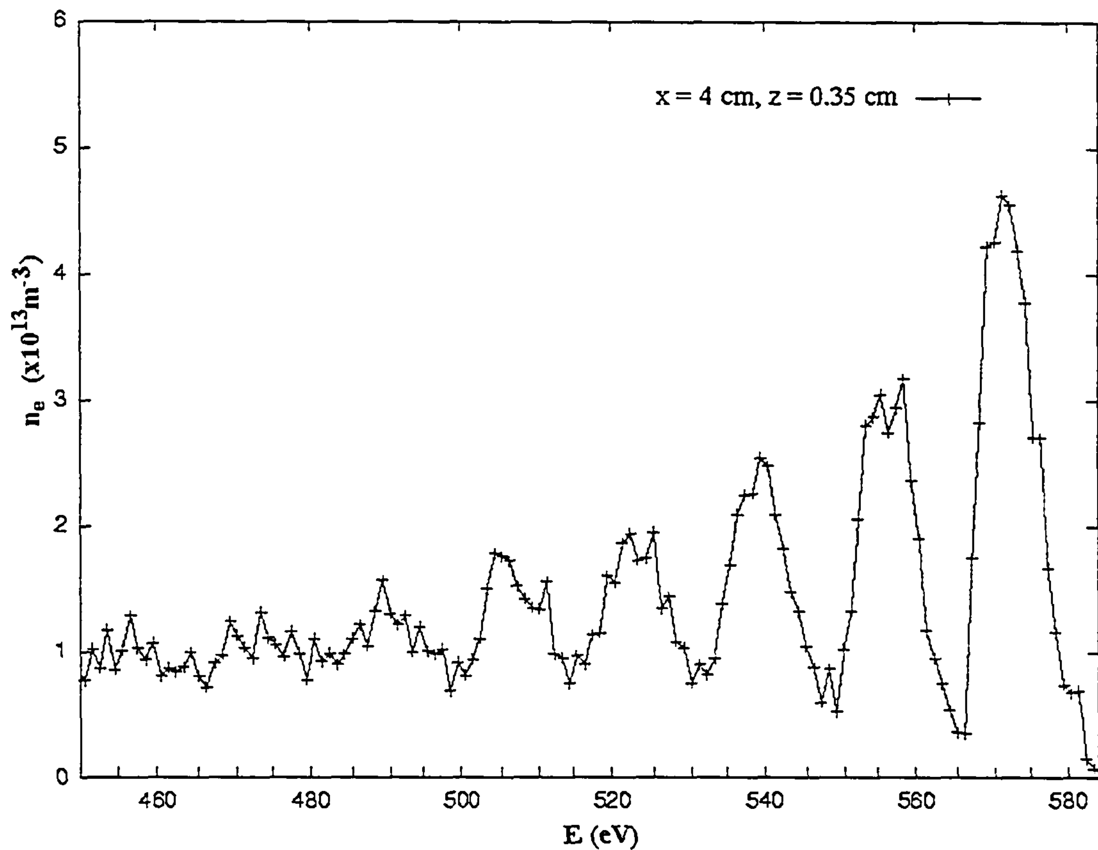

Figure 4.18: High energy portion of the EEDF ~2 mm outside sheath above etch region. Note that the peaks are separated by roughly 15.76 eV, the ionization energy of argon.

Reproduced with permission of the copyright owner. Further reproduction prohibited without permission.

4.5.1.2 Effect of Various Levels of Sputtered Ag in Gas Phase

The simulation conditions used in this section are identical to that of the previous section except here gas phase silver atoms and the silver ionization processes are included.

To evaluate the effect of sputtered silver atoms in the gas phase on electron densities and EEDF's, two runs with different levels of Ag were conducted. Since it is incorrect that the Ag density is uniform everywhere, a mathematical profile was chosen so as to be qualitatively similar to published results on sputtered particle densities[133,134]. Until a fully integrated and self-consistent SPUDII sputtering model is operating and providing precise sputtered particle density profiles, such qualitative measures will have to suffice. The normalized density profile used is shown in figure 4.19.

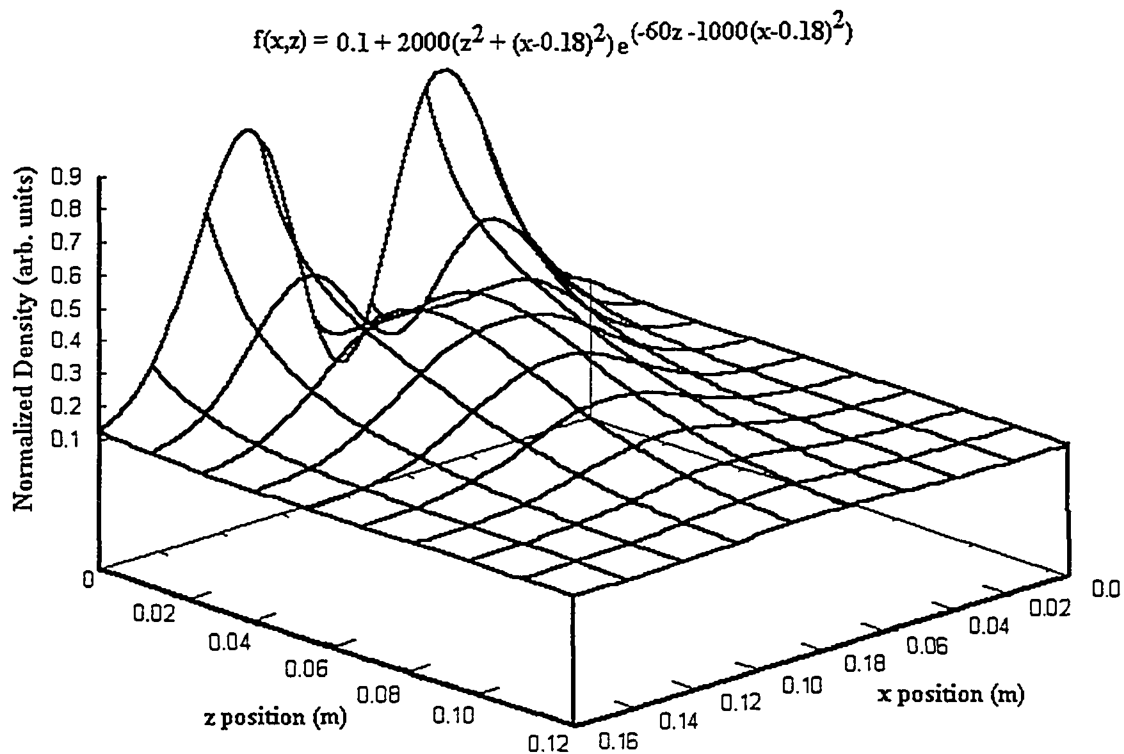

Figure 4.19: Normalized density profile used in runs incorporating gas phase Ag atoms.

Reproduced with permission of the copyright owner. Further reproduction prohibited without permission.

In one run, the profile was multiplied by 10^{17} atoms/m^3 (low Ag density), and in the second, it was multiplied by 10^{18} atoms/m^3 (high Ag density). In the latter case, the density at 10 cm from the cathode was approximately sufficient to provide a (thermal) silver flux to the substrate of 0.6 mono-layers per second. While this is a low value, it is sufficient to provide the qualitative results sought.

For the electron and ion creation rates there was no significant change due to the Ag atoms presence, either qualitatively or quantitatively. This cannot be regarded as remarkable since the relatively low density of silver implies few silver ions will be created, relative to argon, and so the overall creation rates will not significantly differ. Additionally, when a silver ion is created, the energy expended in doing so will not be available to ionize argon. Given the relative ionization energies of the two species one can estimate that the creation of two silver ions (7.57 eV) uses enough energy to prevent the creation of one argon ion (15.76 eV).

Higher levels of silver did appear to contribute to a subtle drop in fast electron density. This is consistent with an extra electron energy loss channel available through the Ag ionization path reducing each electron's lifetime and thus the overall density. Given the relatively low levels of Ag atoms, the effect is not significant. Figure 4.20 shows the fast electron density along the chord normal to the cathode above the etch region.

In Chapter 3 (§3.3.5), it was suggested that gas phase silver atoms may be responsible for cooling electrons at higher cathode currents. The theory reasoned that as the cathode current increased, so did the gas phase silver density which provided an increasingly important extra energy loss channel to the energetic electrons. Figure 4.21 shows the result for an EEDF taken at 5 cm above the etch region. The high silver density has cooled the electron distribution significantly and appears to bring it closer to a Maxwellian distribution by reducing the abrupt features in the EEDF between 10 and 13 eV. The high silver level appears to reduce the electron temperature by ~25%. The low silver level also had a minor effect, again 'softening' the abrupt features in the EEDF.

Reproduced with permission of the copyright owner. Further reproduction prohibited without permission.

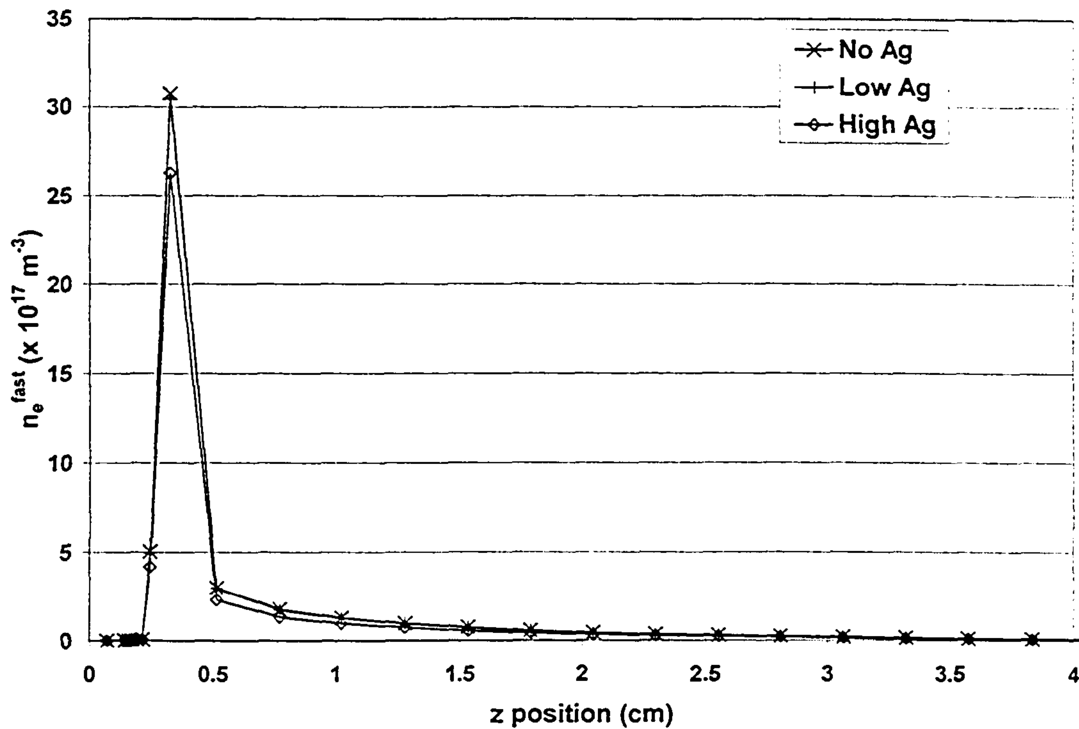

Figure 4.20: Fast electron density along the chord normal to the cathode and above the etch region for various levels of gas phase silver atoms.

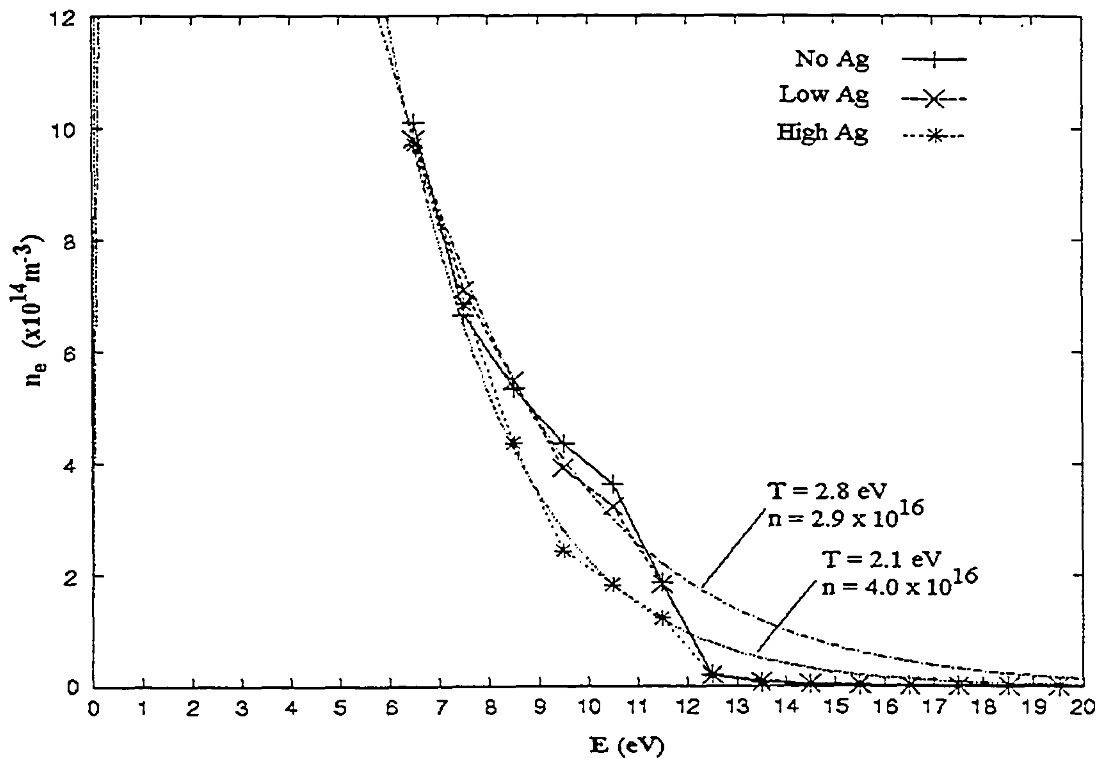

Figure 4.21: EEDF's produced by simulation at 5 cm above the etch region for three levels of silver: no silver, low silver and high silver. Maxwellian fits are included (see text).

Reproduced with permission of the copyright owner. Further reproduction prohibited without permission.

Figure 4.22 and 4.23 show the T_e and n_e^M for these simulations. Figure 4.22 shows a consistent drop in T_e by ~0.8 eV indicating the cooling effect is universal. In figure 4.23, there is an increase in n_e^M as extrapolated from the obtained EEDF's. Both of these effects are consistent with the observed higher n_e and lower T_e at increasing cathode currents. This confirms that Ag density can be an important factor in the response of both T_e and n_e to cathode current. However, the addition of Ag does not significantly correct for the overestimation of n_e close to the cathode. Also the T_e shown in fig. 4.22 is a poorer match to the experimental hot electron temperature at 8 and 10 cm. This is in absence of an accurate Ag density profile that also correlates with the simulations cathode current (0.6 amps). Thus, this discrepancy is not meaningful. The addition of Ag to the simulation also does not improve results for n_e^M (already subject to suspicion) in figure 4.23. Therefore, the results obtained here are qualitative and confirm that higher levels of gas phase silver atoms lower T_e significantly and can increase n_e.

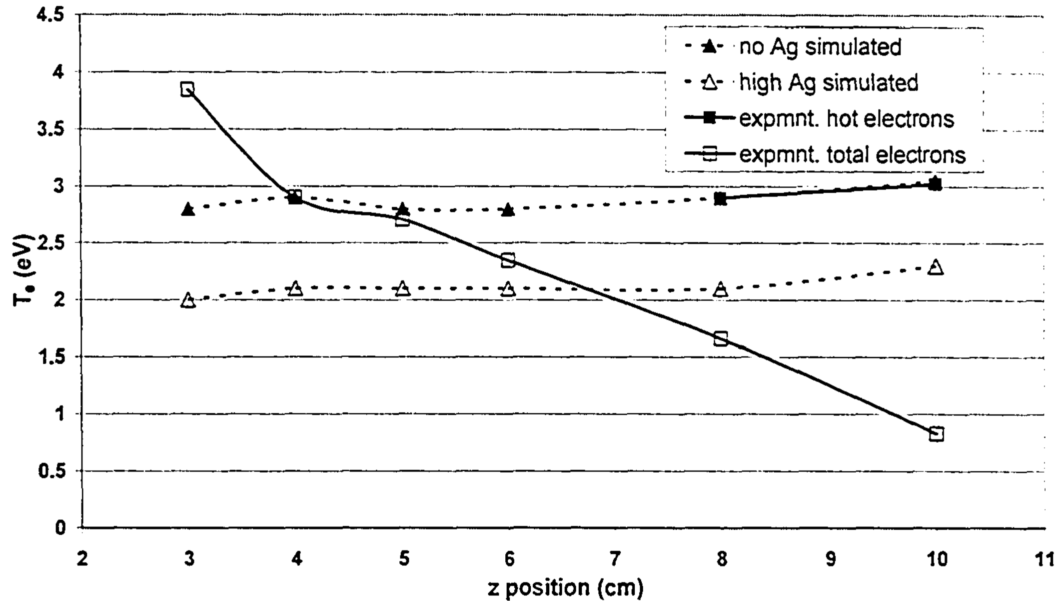

Figure 4.22: Electron temperature taken from Maxwellian fits to simulated EEDF's with no silver and high silver at various distances from the cathode above the etch region. Experimental values are included for comparison.

Reproduced with permission of the copyright owner. Further reproduction prohibited without permission.

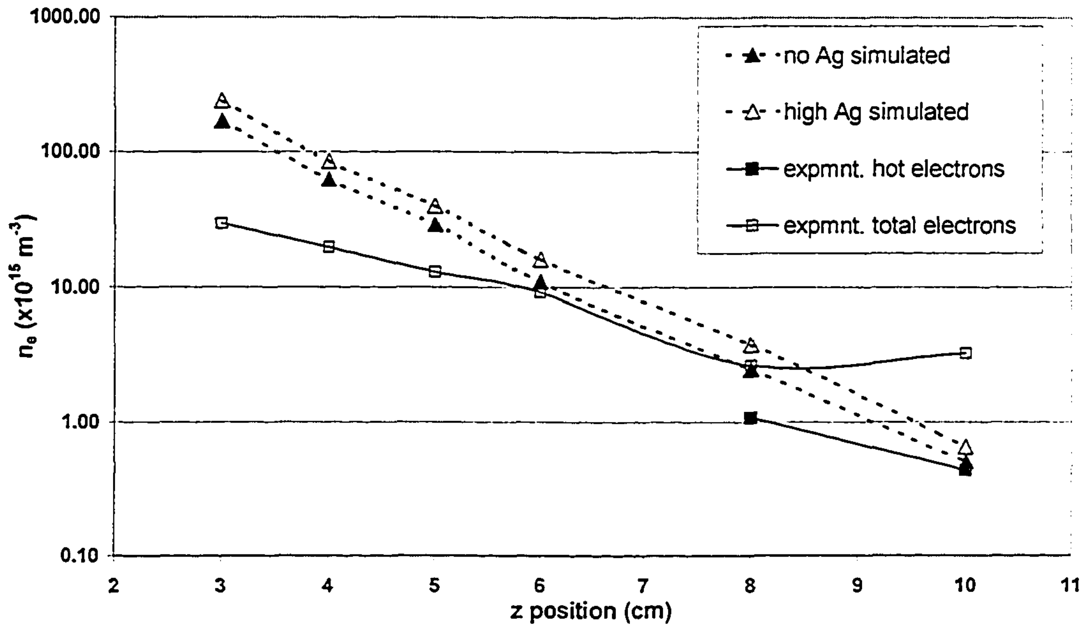

Figure 4.23: Electron density (n_e^M) taken from Maxwellian fits to simulated EEDF's with no silver and high silver at various distances from the cathode above the etch region. Experimental values are included for comparison.

4.5.1.3 Effect of Cathode Voltage

The conditions used for these simulations was identical to the first run except the cathode voltage is set to –400 volts instead of the experimentally obtained –575 volts so as to investigate the influence cathode voltage has on electron temperatures and densities. Figure 4.24 shows EEDF's at 4 cm above the etch region for both cathode voltages. There appeared only a minor difference in the EEDF structure. Curiously, the EEDF using –400 volts matched the previously fit Maxwellian curve marginally better than –575 volts. This results in no discernable influence on the T_e or n_e^M as extracted from the Maxwellian fit. So, while it can be said that cathode voltage has limited influence on T_e, the qualitative improvement of the data with respect to Maxwellian distributions is interesting. Figure 4.24 is typical of EEDF's obtained at all other locations.

Reproduced with permission of the copyright owner. Further reproduction prohibited without permission.

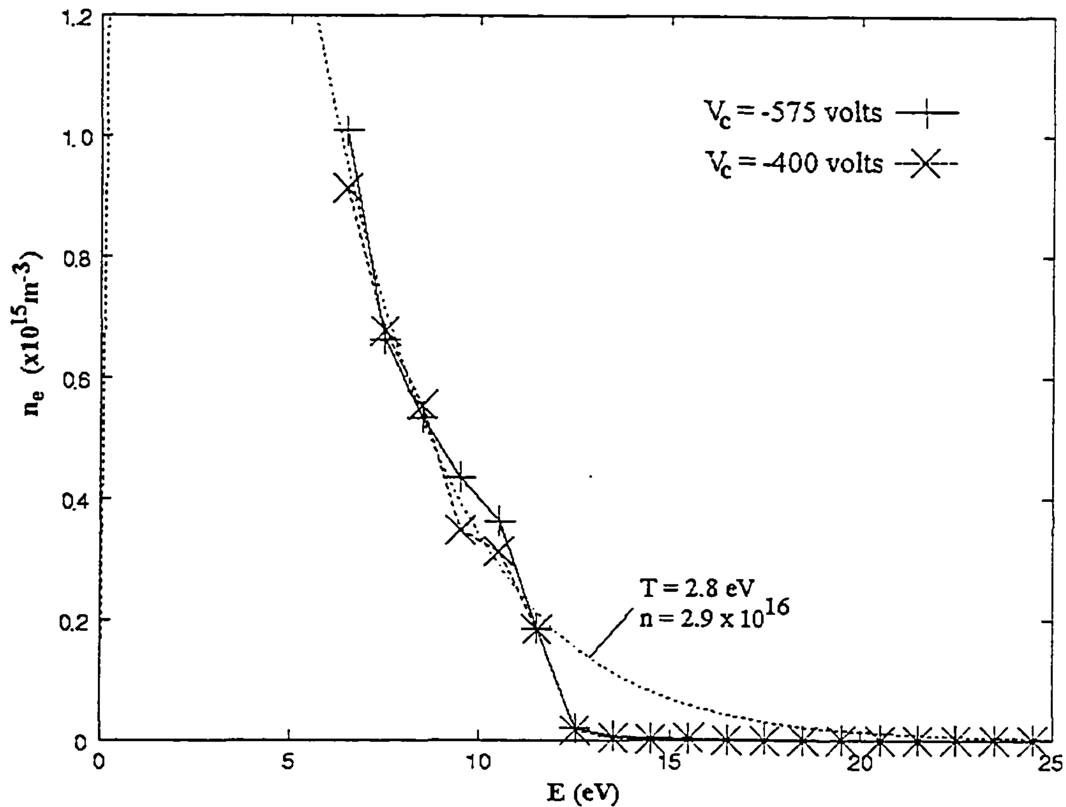

Figure 4.24: EEDF's generated at 4 cm above etch region for two different cathode voltages. The Maxwellian distribution fit to the original EEDF (-575 volt) is shown and appears even better represented by the EEDF generated by the -400 volts cathode, though only subtly so.

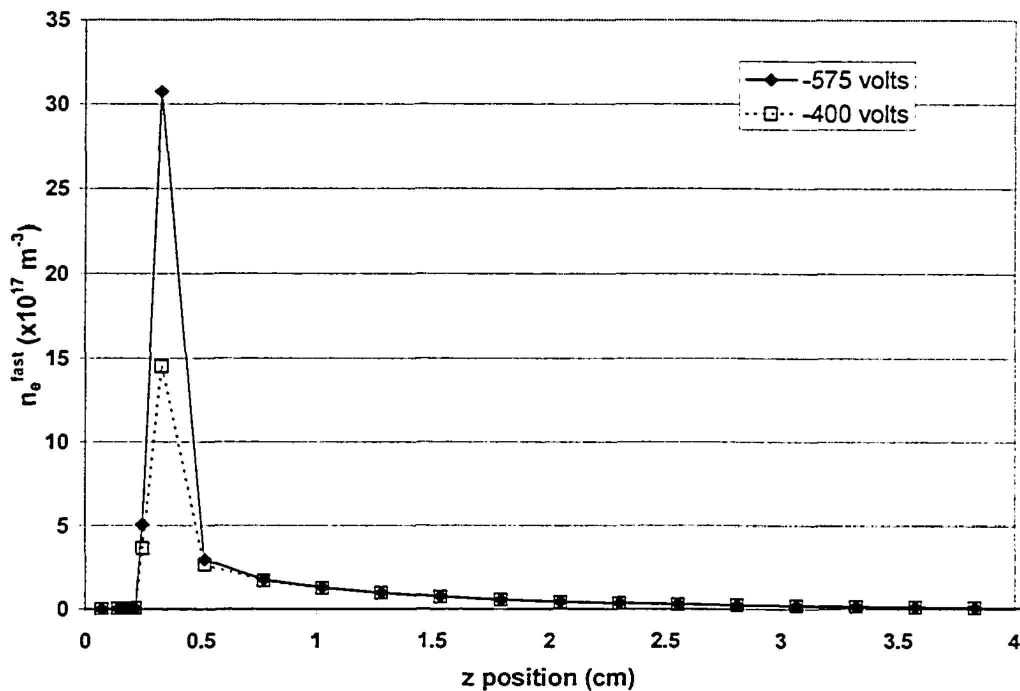

Figure 4.25: Fast electron density for two cathode voltages at varying distance from cathode the above etch region.

Reproduced with permission of the copyright owner. Further reproduction prohibited without permission.

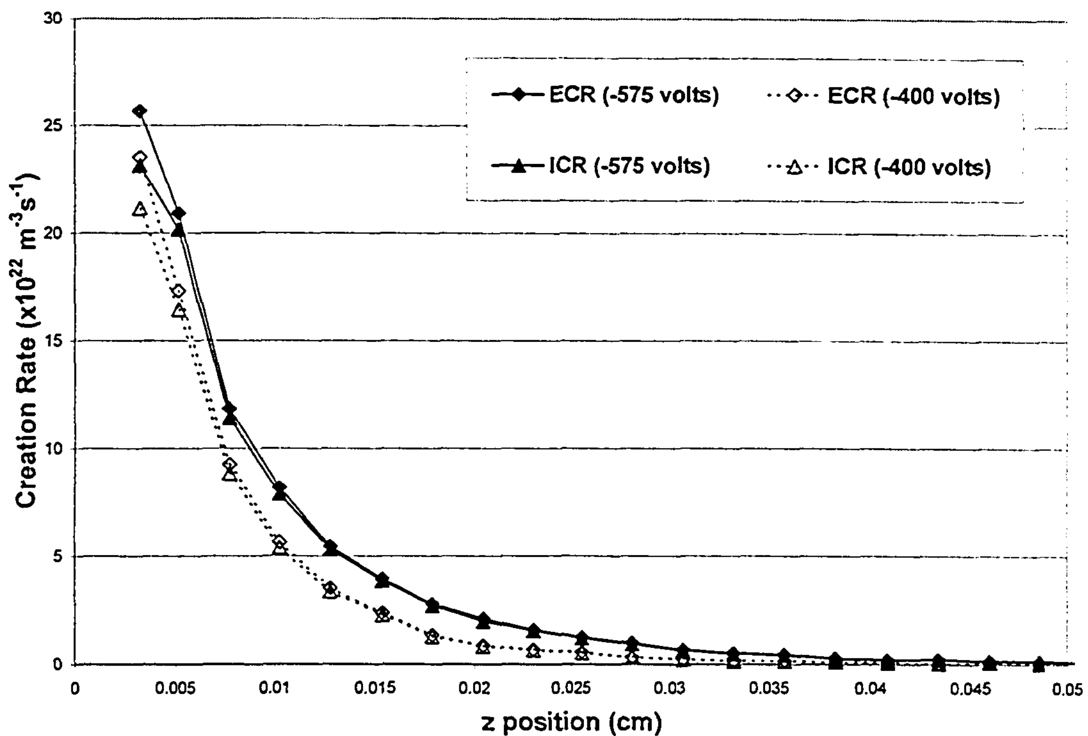

Figure 4.26: Electron and ion creation rates for two cathode voltages at varying distances above the etch region.

Figure 4.25 and 4.26 show data for the fast electron density and the electron and ion creation rates respectively. Figure 4.25 shows a reduction in fast electron density for the lower magnitude cathode voltage case. This can be explained easily as the lower voltage produces lower energy primary electrons exiting the sheath, which have a shorter lifetime. Figure 4.26 shows a reduction in the ECR and ICR values for the lower voltage case. This is simply a result of primary electrons having less energy with which to cause ionization events. i.e. every primary electron creates fewer ions and secondary electrons. Thus, it appears cathode voltage influences fast electron density and creation rates but has only subtle influences on T_e.

Reproduced with permission of the copyright owner. Further reproduction prohibited without permission.

4.5.1.4 Effect of Metastable Argon Gas

This set of simulations was conducted identically to runs performed using silver, except instead of a silver gas density the profile in figure 4.19 is used to represent metastable (MS) argon atoms (see table 4.1). Four runs are conducted. Two where the normalized distribution is multiplied by densities of 10^{17} m^{-3} (low MS) and two where it is multiplied by 10^{18} m^{-3} (high MS). For each density, one simulation is conducted where only ionization of metastable argon is allowed and a second run where super-elastic collisions (where the metastable can surrender its inelastic energy to an electron thereby increasing the electron's energy) are also allowed.

Qualitatively, the 2-D results were not different from those presented for previous runs and so only 1-D results are required here. Figure 4.27 and 4.28 show the ECR and ICR data taken above the etch region. For runs where superelastic collisions are forbidden, but metastable ionization is allowed ('high MS no SE' and 'low MS no SE' in figures), near the cathode the creation rates increase at progressively higher levels of metastable species (over the original run where the metastable density was zero). This is easily understood when considering the metastables represent an additional neutral source species for ionization and that this is a process type that requires little energy (only ~ 4 eV), such that low energy electrons, which previously could not produce ions, now can. The increase in creation rates is more pronounced near the cathode where the electron density is highest but becomes negligible at only 2 cm above the cathode.

A further similar increase in creation rates is observed when superelastic collisions are allowed ('high MS w SE' and 'low MS w SE' in figures). This is because electrons which are below the ionization threshold of argon can now gain energy via the superelastic collision and end up with sufficient energy to ionize argon. This is yet another ionization pathway added to the system and so creation rates increase.

Figure 4.29 shows the fast electron density above the etch region, data which is consistent with the ECR and ICR results. For increasingly high levels of metastable species, the number of energy loss channels via ionization pathways increases such

Reproduced with permission of the copyright owner. Further reproduction prohibited without permission.

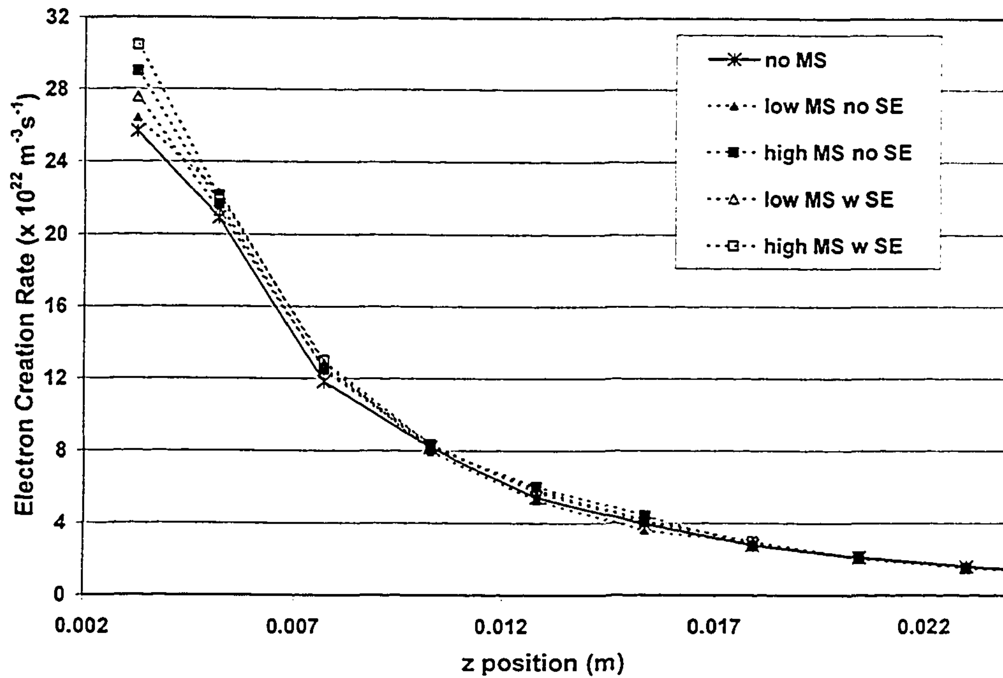

Figure 4.27: Thermalized electron creation rates versus normal position (z) above etch region for five different run conditions. 1. no metastable density (no MS), 2. low metastable density with no superelastic collisions (low MS no SE), 3. high metastable density with no superelastic collisions (high MS no SE), 4. high metastable density with superelastic collisions (high MS w SE), 5. low metastable density with superelastic collisions (low MS w SE).

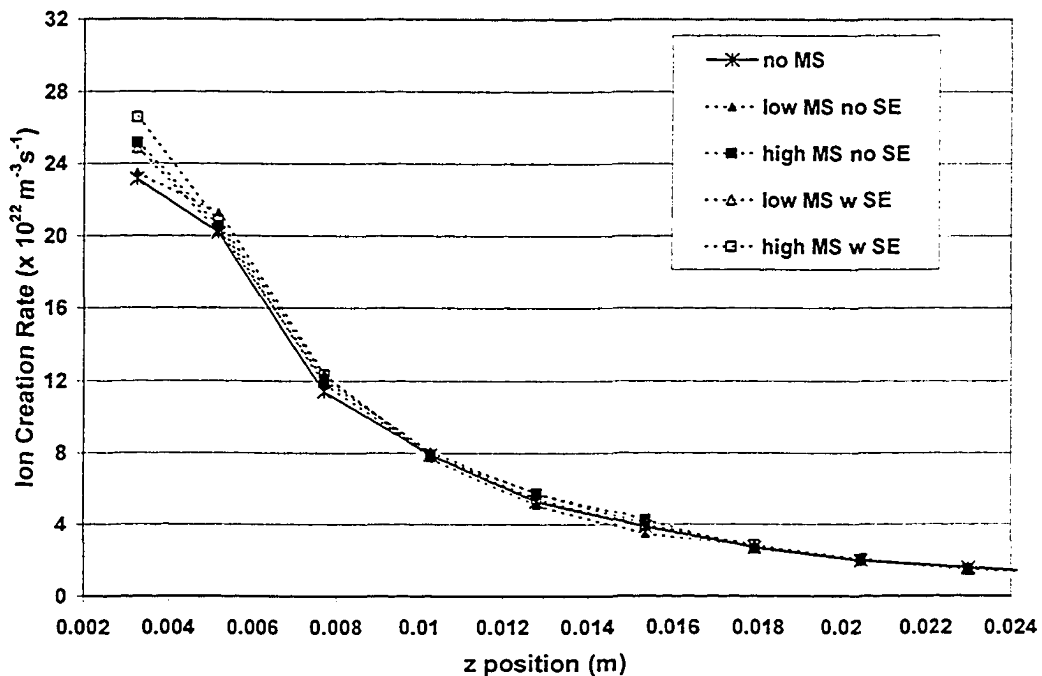

Figure 4.28: Thermalized ion creation rates versus normal position (z) above etch region for five different run conditions. 1. no metastable density (no MS), 2. low metastable density with no superelastic collisions (low MS no SE), 3. high metastable density with no superelastic collisions (high MS no SE), 4. high metastable density with superelastic collisions (high MS w SE), 5. low metastable density with superelastic collisions (low MS w SE).

Reproduced with permission of the copyright owner. Further reproduction prohibited without permission.

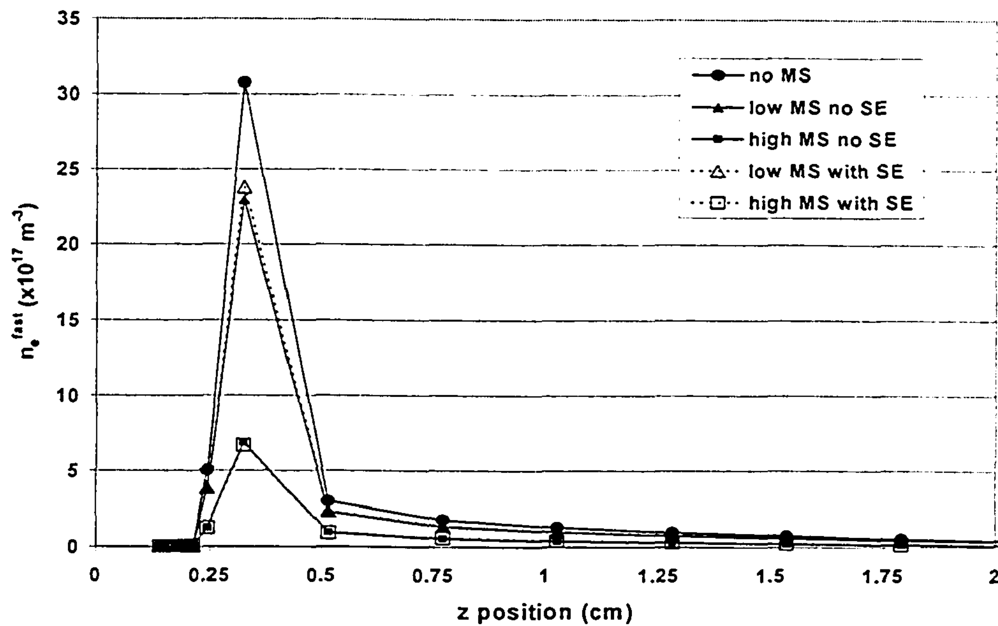

Figure 4.29: Fast electron densities versus normal position (z) above the etch region for five different run conditions. 1. no MS, 2. low MS no SE, 3. high MS no SE, 4. high MS w SE, 5. low MS w SE. (see figure 4.27 and 4.28)

that the electrons undergo shorter lifespans. Thus at high metastable densities, a significant decrease in electron density is observed. However, in the cases where superelastic collisions are allowed, no further decrease is observed. This is because the superelastic collisions increase the electron energy thereby prolonging the electron's lifetime. While some of these electrons may rapidly become thermalized through an ionizing collision (much faster than if they had to be thermalized through a long series of elastic collision) many of these electrons may yet still be thermalized through a prolonged series of elastic collisional events. As a result, there is not necessarily expected a significant effect, and none is seen. Where the metastable density is low, a minute increase in fast electron density is observed, whereas for higher metastable densities, no effect is observed.

The metastable density did influence the EEDF's by reducing the density of the electrons, n_e^M (as extracted from a Maxwellian fit to the data – see figure 4.30) and by cooling the electrons (figure 4.31). Maxwellian distributions fit to the EEDF data showed a decrease in electron density, n_e^M, in qualitative agreement with the fast

Reproduced with permission of the copyright owner. Further reproduction prohibited without permission.

electron density data in figure 4.29. The densities here follow the same trend as for simulations where metastables were not present and so do not improve agreement with experimental data. The electron temperature (from Maxwellian fits to EEDF's) was affected by the presence of metastables. The general trend was that this tended to cool the electrons. Little effect was observed for low metastable densities but a more significant effect was observed for higher densities. This cooling effect arises from preferential depletion of electrons in the higher energy region of the sub-11 eV range (below the threshold for all other inelastic processes). This is due to the shape of the metastable ionization cross-section (see figure 4.2), which rises abruptly from 4 to 11 eV. It increases the probability of inelastic energy loss to electrons in that energy range. Higher densities of argon metastable species would amplify this effect. Curiously, the opposite effect appeared to take place out at the 10 cm location where hotter electrons were observed. This may be a function of the speculatively applied metastable density distribution and so the results here are only qualitative. A fully integrated self-consistent simulation where accurate metastable density distributions can be determined is necessary to illuminate this further.

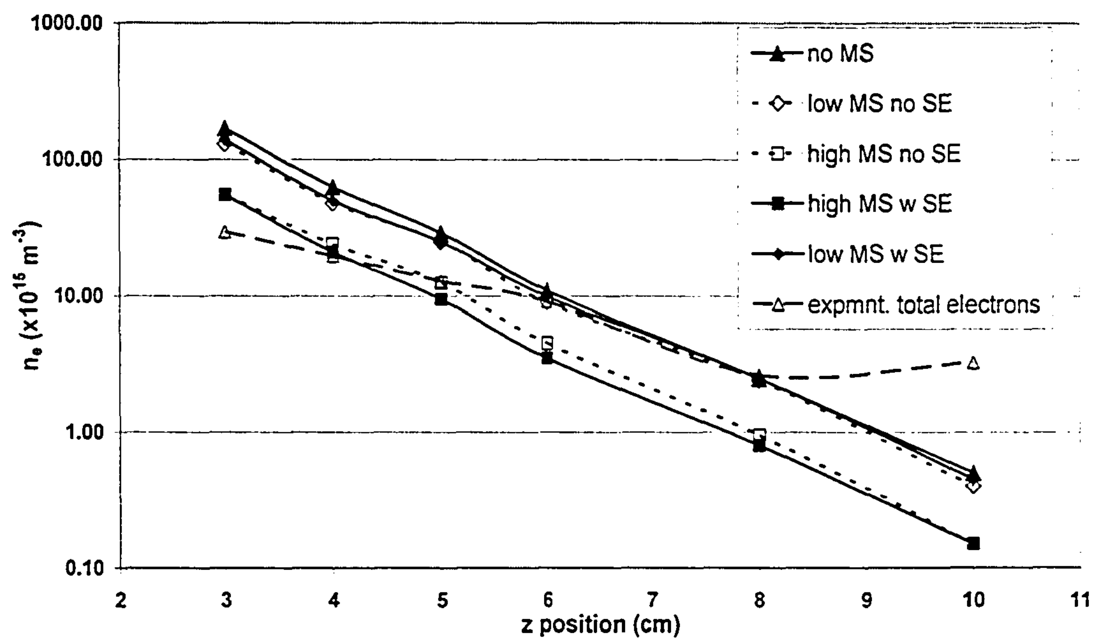

Figure 4.30: Electron density (n_e^M) as extracted from a Maxwellian fit to EEDF data versus position (z) above etch track. Key is as given in figure 4.27. 'Total electrons' are taken from Langmuir probe data (see figure 4.14).

Reproduced with permission of the copyright owner. Further reproduction prohibited without permission.

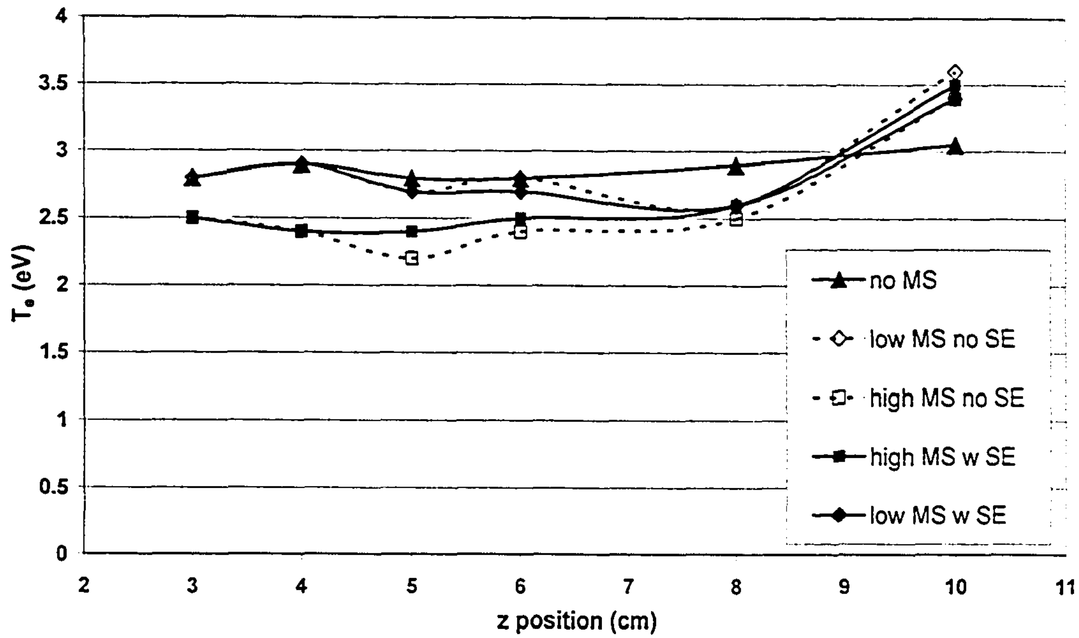

Figure 4.31: Electron temperature as extracted from a Maxwellian fit to EEDF data versus position (z) above etch track. Key is as given in figure 4.27. Can be compared to experimental results as shown in figure 4.13.

4.5.1.5 Effect of Secondary Electron Emission Coefficient (γ_p) and Electron Reflection Coefficient (ERC)

The conditions used for these simulations was identical to those used in the first run except in each run the γ_p and ERC were set as follows:

Original Run:	$\gamma_p = 0.36$	ERC = 0.2
Run A:	$\gamma_p = 0.18$	ERC = 0.2
Run B:	$\gamma_p = 0.27$	ERC = 0.2
Run C:	$\gamma_p = 0.36$	ERC = 0.15
Run D:	$\gamma_p = 0.36$	ERC = 0.25

Figures 4.32, 4.33, and 4.34 show the electron creation rates, ion creation rates, and fast electron densities taken above the etch region for various values of γ_p and ERC. A decrease in γ_p shows a linear, 1:1 decrease in the creation rates and in the fast electron densities. This is a decrease in the number of electrons per ion and is therefore a decrease in the number of electrons per given cathode current. Then the

Reproduced with permission of the copyright owner. Further reproduction prohibited without permission.

number of statistical samples taken by a given cell will decrease in a like ratio, assuming convergence, and these values will be sensitive to variations in γ_p.

As the ERC is decreased (more electrons recaptured by the cathode) or increased (fewer electrons recaptured by the cathode) there is a respective decrease or increase in the creation rates, although not on a 1:1 ratio. This is because the ERC only affects those electrons that do not have a scattering collision prior to returning to the cathode along its **E** x **B** path. Thus the creation rates are not as sensitive to the ERC as they are to γ_p.

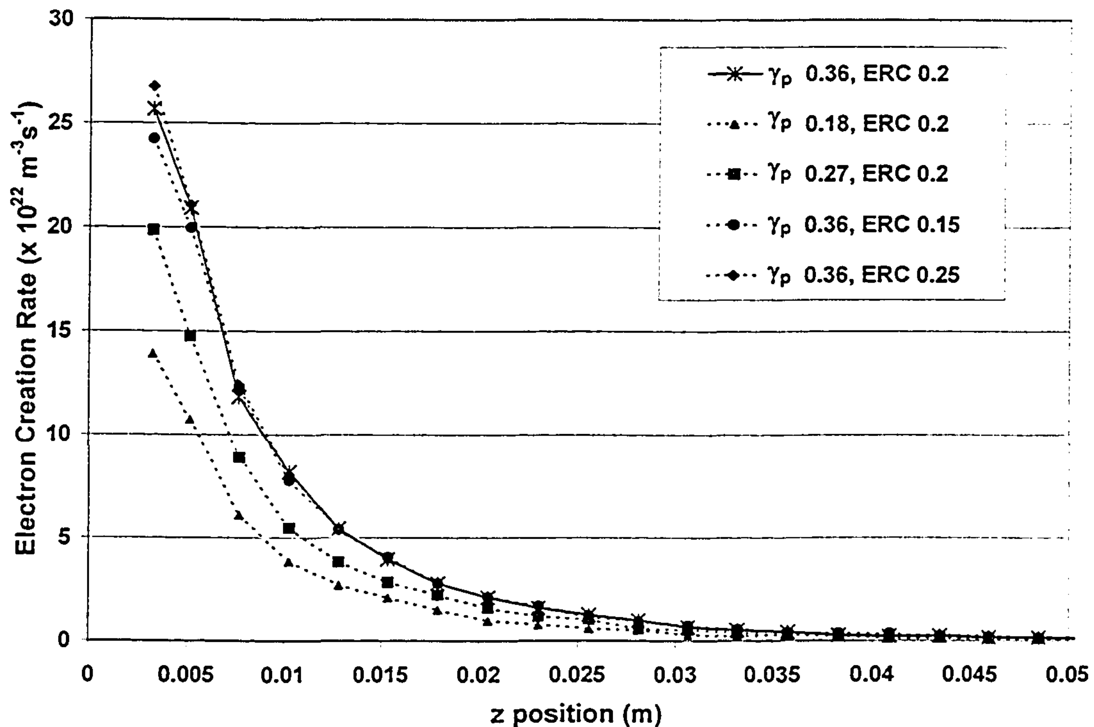

Figure 4.32: Electron creation rates above the etch region for various values of the secondary electron emission coefficient and the electron reflection coefficient. The series with the solid line is indicative of values used for all other simulations.

The fast electron density appeared even less sensitive to the ERC than the creation rates, with a minute decrease in fast electron density for both the higher and lower value of ERC. There were no noteworthy changes observed, either qualitatively or quantitatively to the electron temperature profiles. All EEDF's were unchanged in shape with the exception of overall density, n_e^M, which changed in like fashion to that of the fast electron density. Temperatures derived from these EEDF's were unchanged.

Reproduced with permission of the copyright owner. Further reproduction prohibited without permission.

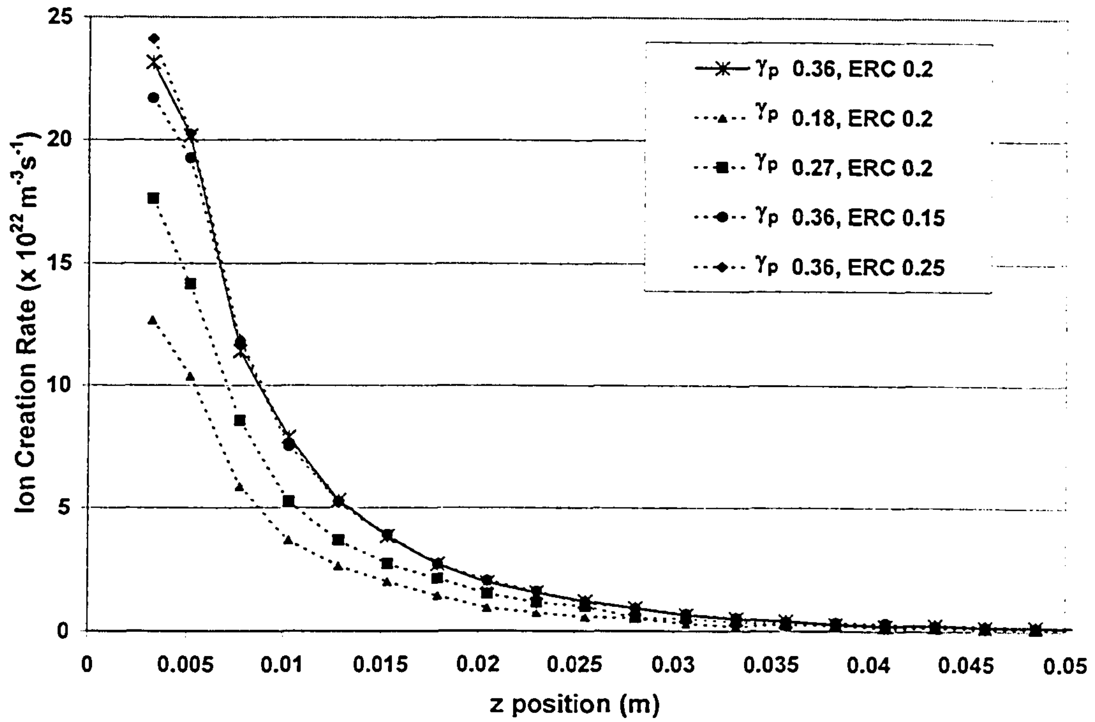

Figure 4.33: Ion creation rates above the etch region for various values of the secondary electron emission coefficient and the electron reflection coefficient. The series with the solid line is indicative of values used for all other simulations.

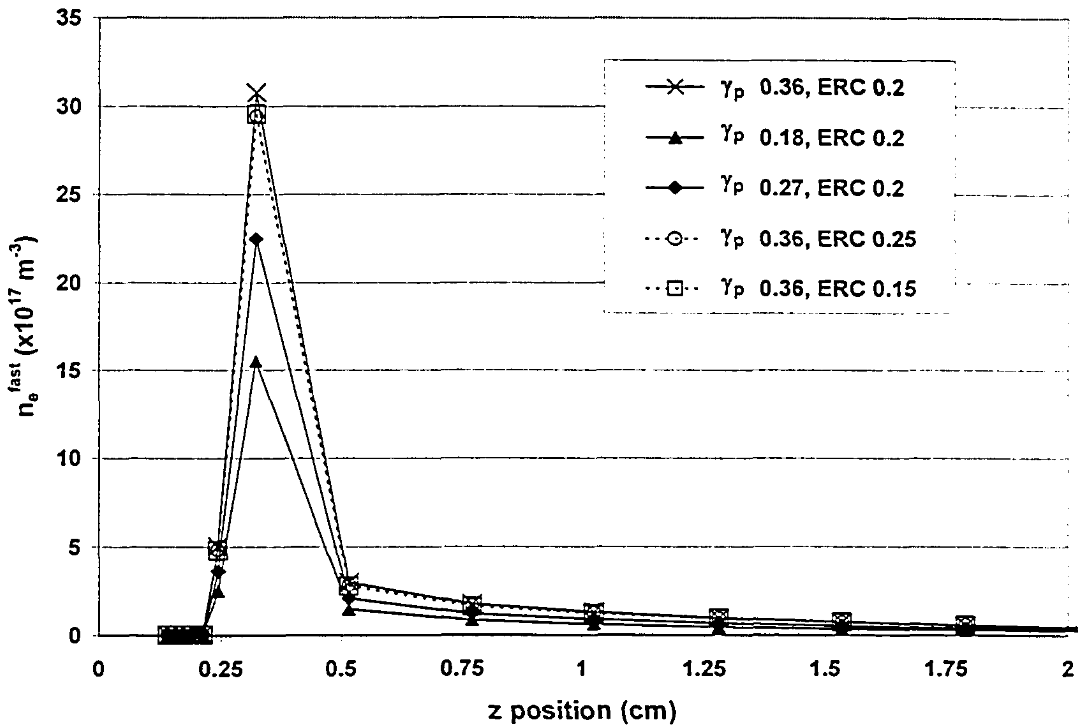

Figure 4.34: Fast electron density above the etch region for various values of the secondary electron emission coefficient and electron reflection coefficient. The series with the solid line show values used for all other simulations.

Reproduced with permission of the copyright owner. Further reproduction prohibited without permission.

4.5.1.6 Effect of Gas Rarefaction at 5 mTorr

Gas densities in magnetron sputter devices are known to be rarefied in regions near the etch tracks due to energy input from sputtered particles[132]. To accurately determine the precise nature of the 2 or 3-D gas density profile would require the completion of a fully integrated and self-consistent simulation. In the absence of such a tool, one can attempt to use an approximate gas density profile and obtain a qualitative idea as to how gas rarefaction will affect the simulated electron population. The gas density profile used for this simulation is shown in figure 4.35. It is a scaled inverse of the profile used earlier for silver and argon metastable densities.

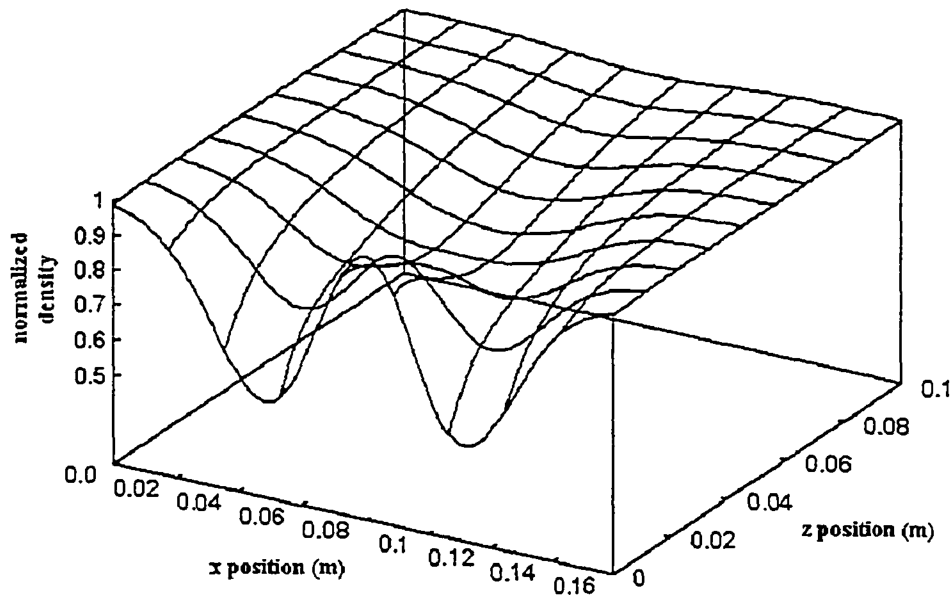

Figure 4.35: Normalized gas density profile used in 5 mTorr rarefied gas simulation. Note the maximum rarefaction is to 50% of original gas density.

Figure 4.36 shows the 2-D electron creation rates for this rarefied gas simulation compared to that for the un-rarefied case. The spatial distribution has become less peaked in the magnetic trap region to reflect the lower collision rate and thus lower ionization rate there. As a result, there is an overall attenuation in the electron creation rate and the profile has become generally flatter. The ion creation

Reproduced with permission of the copyright owner. Further reproduction prohibited without permission.

rate profiles did not show any qualitative difference with the exception of being at slightly lower values.

The fast electron density (figure 4.37) has changed significantly. At the very center of the magnetic trap, the FED becomes much more peaked since there are fewer collisions within this region to promote scattering of energetic electrons across the magnetic field line. At this pressure, the fast electrons experience greater

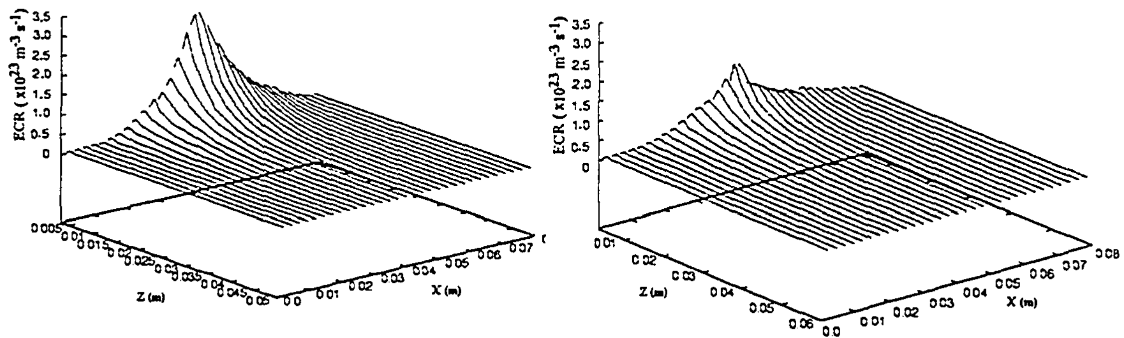

Figure 4.36: Electron creation rates for rarefied argon gas (right) and unrarefied case (left).

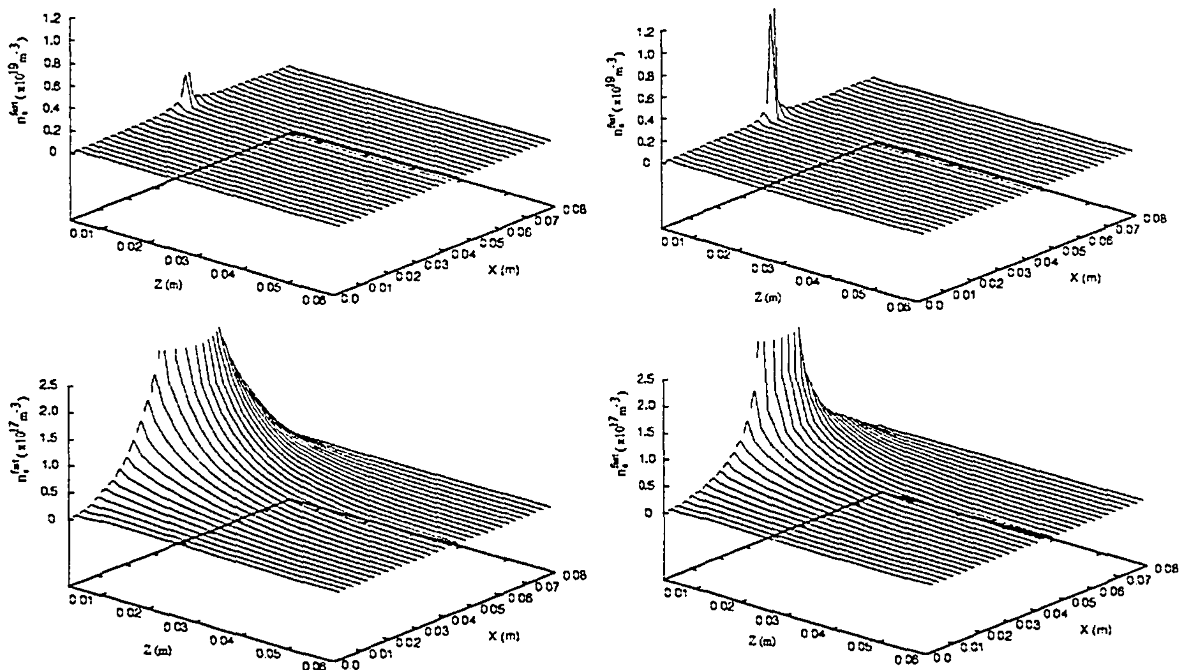

Figure 4.37: Fast electron density for rarefied argon gas case (right) and unrarefied case (left). Top graphs show full-scale density profiles and bottom graphs shows detail of the lower density range.

Reproduced with permission of the copyright owner. Further reproduction prohibited without permission.

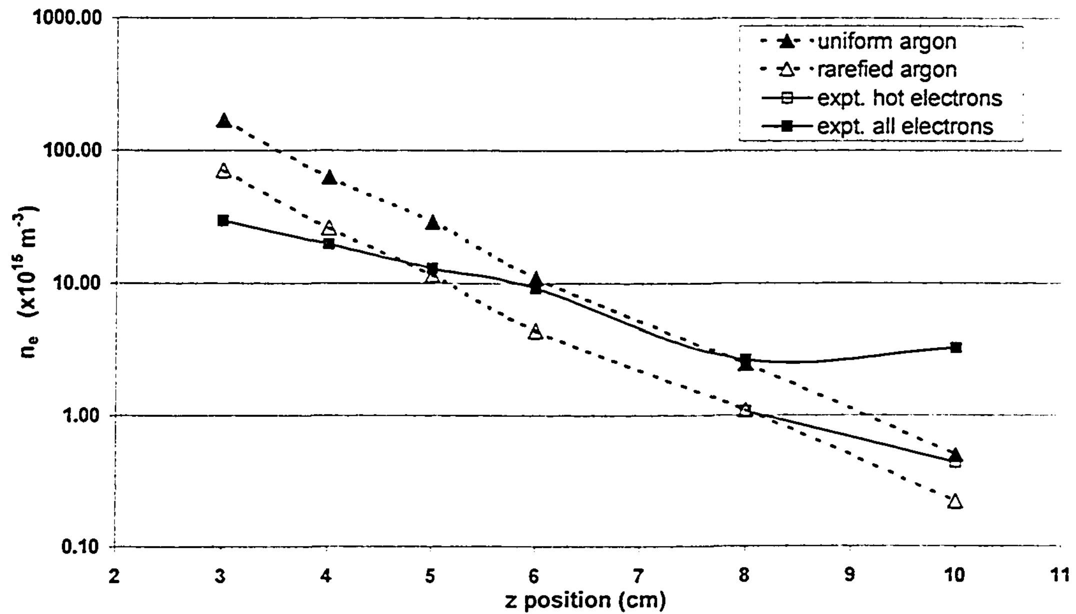

Figure 4.38: Electron density for uniform gas density and rarefied gas density taken from Maxwellian fits to EEDF data for various positions over the etch region.

confinement within the trap whereas, when no rarefaction was considered, the FED was more spatially spread out.

Figure 4.38 shows the electron density, n_e^M, taken from the Maxwellian fit to EEDF data for the two cases. The difference in densities decreases further from the cathode (note the log scale), where the difference in neutral gas density decreases. There is no qualitative improvement in the match to experimental data, suggesting gas rarefaction may not be responsible for this discrepancy.

Figure 4.39 shows the electron temperature taken from the Maxwellian fit to EEDF data for the two cases. The results are for the region above the etch track only. Clearly, the electron temperature has increased as a result of the reduction in argon density near the cathode. It suggests that lower pressures (i.e. lower densities) are consistent with higher electron temperatures; a result observed experimentally in Chapter 3 (see figure 3.2). It is also strongly implying the collision frequency and dynamics are extremely important in determining the electron temperature for these electrons.

Figure 3.2 d showed that above the etch region, the T_e decreased at greater distances from the cathode, which is not the trend observed in fig. 4.39 for rarefied

Reproduced with permission of the copyright owner. Further reproduction prohibited without permission.

argon. However, figure 3.2 e shows there is a hot electron component to the overall electron population in those regions, and that that component appeared to increase in temperature at greater distances from the cathode. Although, there were insufficient data points at 5 mTorr in fig. 3.2 e to be conclusive, it was a trend observed consistently for other conditions. This again suggests that electrons created within the sheath, or at the target surface, evolve into the hot electron portion of bi-Maxwellian EEDF's. It is not clear, that 'mono-Maxwellian' distributions, observed closer to the cathode, are dominated by this same electron group, or by 'cold' electrons created through ionizing events, or by some balance of the two groups. Figure 4.39 signifies that gradients and spatial profiles of argon gas have a considerable influence on the evolution of EEDF's. There is not an improvement in correlation to experimental data, with the exception of the point at 3 cm where the simulated T_e is close to the experimental T_e, indicating that the gas rarefaction profile may be reasonably accurate in the region closer to the cathode.

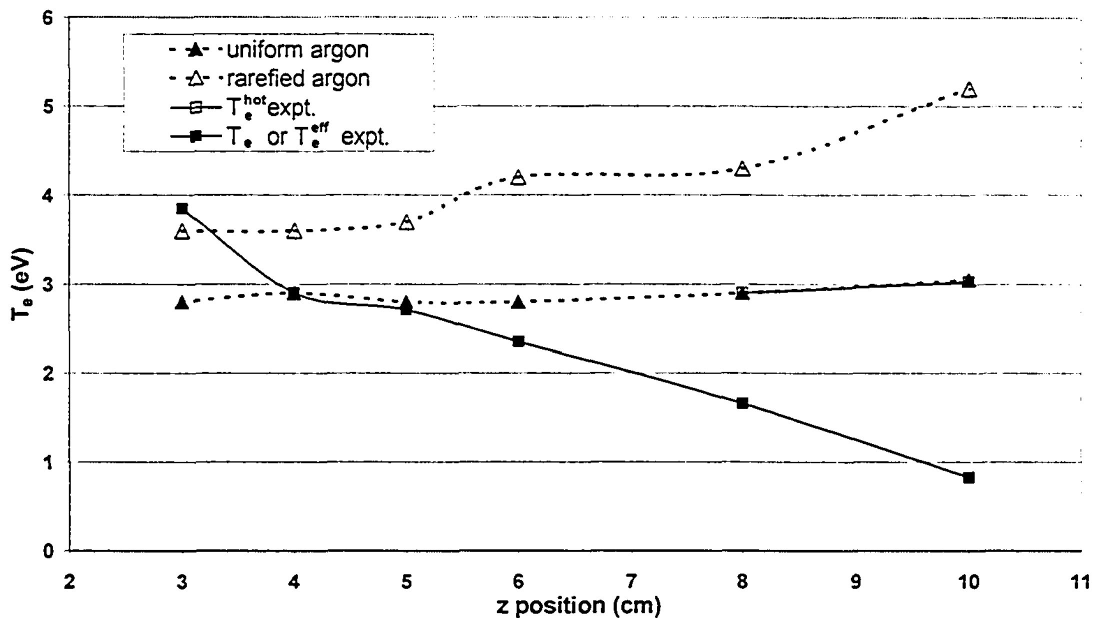

Figure 4.39: Electron temperature for uniform gas density and rarefied gas density taken from Maxwellian fit to EEDF data for various positions over etch region.

Reproduced with permission of the copyright owner. Further reproduction prohibited without permission.

4.5.1.7 Effect of Cathode Sheath Thickness

A simulation was conducted with the cathode sheath thickness set at 1.9 mm (see figure 4.3) compared to the normally used 1.27 mm to ascertain any effect arising there from. In doing this, some obvious changes take place. The sheath edge will be located further from the cathode where the magnetic field is subtly weaker and of nominally different shape. Electrons ejected from the cathode will spend more time within the sheath region and have slightly different shaped trajectories due to the more spread out electric field. Finally, the wider sheath will provide greater space within which *ionizing collisions* may occur and which can be measured by simply monitoring the number of ionizing collisions within the sheath for each simulation. With the 1.27 mm sheath, there were 384 ionizing collisions within the sheath per 1000 primary ions sourced from the sheath edge. With an γ_p coefficient of 0.36, this is approximately one ionizing collision per electron ejected from the cathode. For the 1.9 mm sheath case the number of ionizing collisions in the sheath rose to 1222 per 1000 primary ions, or 3.4 ionizing collisions per ejected secondary electron. This is approximately a 3.4 fold increase in ionizing collisions in the sheath. Ionizing collisions in the sheath will have two major effects. First, more ions sourced from these ionization events will strike the cathode per ion sourced from the sheath, lowering the number of sheath ions needed to maintain a cathode current. Second, greater numbers of energetic electrons will enter the plasma from the sheath region but with less energy than those in the thin sheath case due to greater energy loss from ionizing collisions.

Figure 4.40 and 4.41 show the thermalized electron creation rates outside of the sheath region for the two cases. In figure 4.40, there appears very little qualitative difference with a slightly more peaked shape for the thick sheath case. There is a significantly higher overall creation rate as shown in 4.41 for the ECR's at various distances above the etch region.. However, the thick sheath case data has been scaled down by a factor of 5.5 to show the qualitative similarity between the two profiles. It does appear that the thick sheath case gives rise to a slightly more peaked shape with

Reproduced with permission of the copyright owner. Further reproduction prohibited without permission.

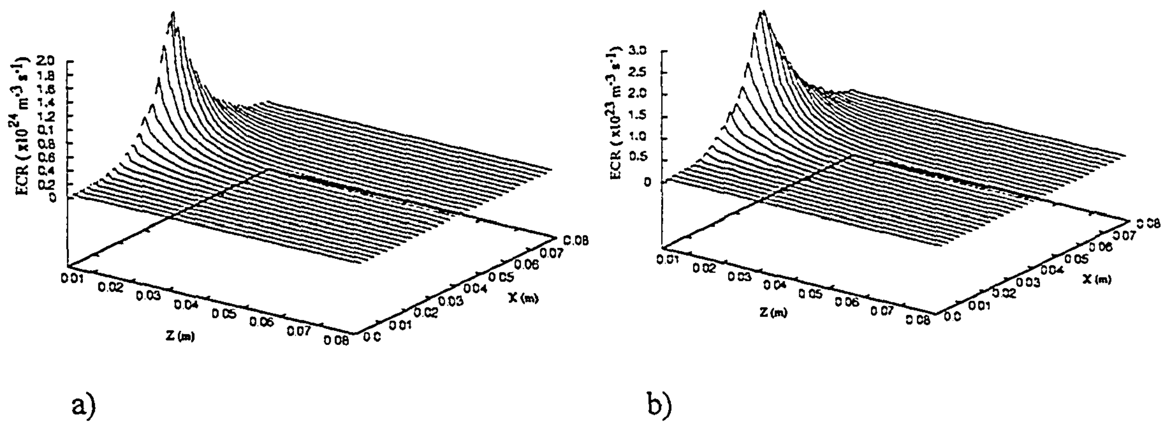

Figure 4.40: 2-D depictions of thermalized electron creation rates for a) thick sheath (1.9mm) case, and, b) thin sheath case (1.3 mm). All other simulation have used the 1.3 mm sheath.

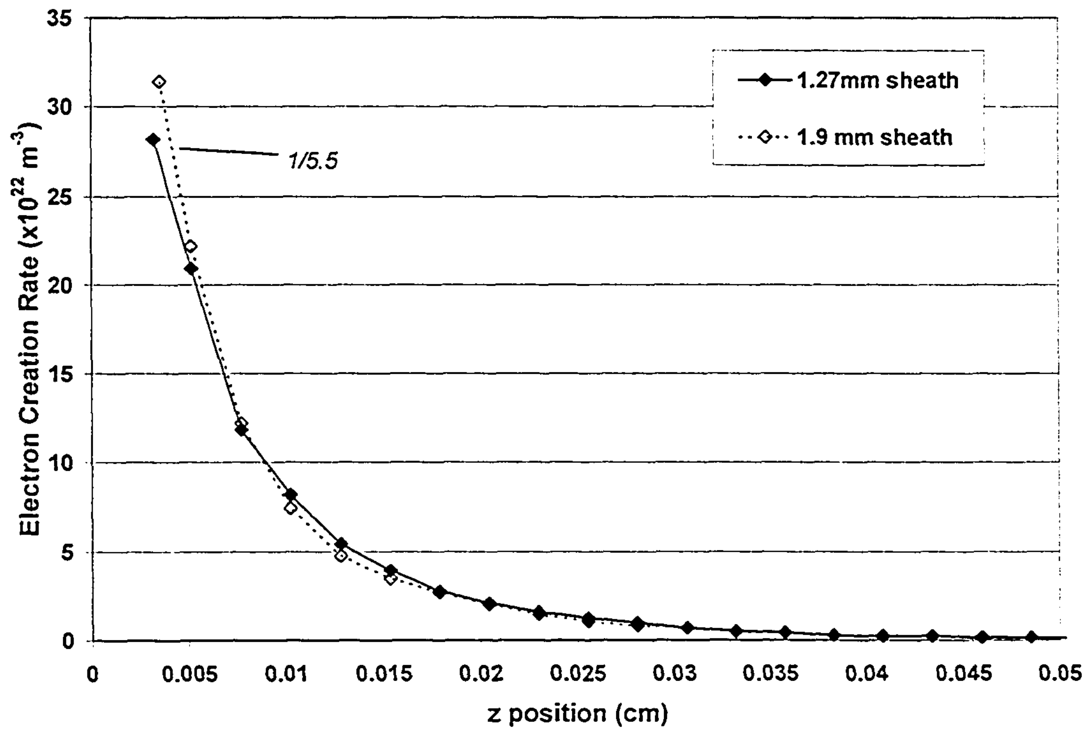

Figure 4.41: Thermalized electron creation rates at various distances above etch region for thick (1.9mm) and thin (1.3 mm) cases. Note that data for the thick sheath case has been divided by a factor of 5.5 for better illustrative purposes.

Reproduced with permission of the copyright owner. Further reproduction prohibited without permission.

a relatively higher creation rate near the sheath than farther out, though the factor of 5.5 is generally a good scaling factor throughout. The factor of 5.5 is reflective of the increase due to both the increased number of energetic electrons and the average energy gained from the sheath, dependant on where in the sheath the ionization event took place, for these additional electrons. Electrons born near the sheath edge would not gain much energy in the sheath and be able to ionize only a few atoms outside the sheath, whereas electrons born near the cathode would gain a lot of energy and be able to ionize many atoms. Ion creation rates were not found to be any different with the exception of being slightly lower in both cases as has been observed before.

The 2-D fast electron density profiles are shown in figures 4.42 and 4.43. Both show the abrupt peak near the center of the magnetic trap region due to the very low energy electrons. The thick sheath case (fig 4.42) shows that the magnitude of the abrupt peak has only increased by a factor of about 2 over the thin sheath case (fig. 4.43), whereas elsewhere there is a more dramatic increase. This may be due to the slightly weaker magnetic field just outside the sheath for the thick sheath case. At 3 cm and further from the cathode, where EEDF's are monitored, the electron density, n_e^M , was obtained from Maxwellian fits to the EEDF data. This showed a consistent increase by a factor of between 7.25 and 8.0 everywhere, with no apparent trend with respect to position. This suggests that while there is some differences in density profile shape near the cathode, at 3 cm and beyond there is only a scale factor difference. The electron temperatures as taken from the EEDF's did not change at all. They gave exactly the same temperatures obtained for the thin sheath case. There were no qualitative changes to the EEDF's above the well region.

Reproduced with permission of the copyright owner. Further reproduction prohibited without permission.

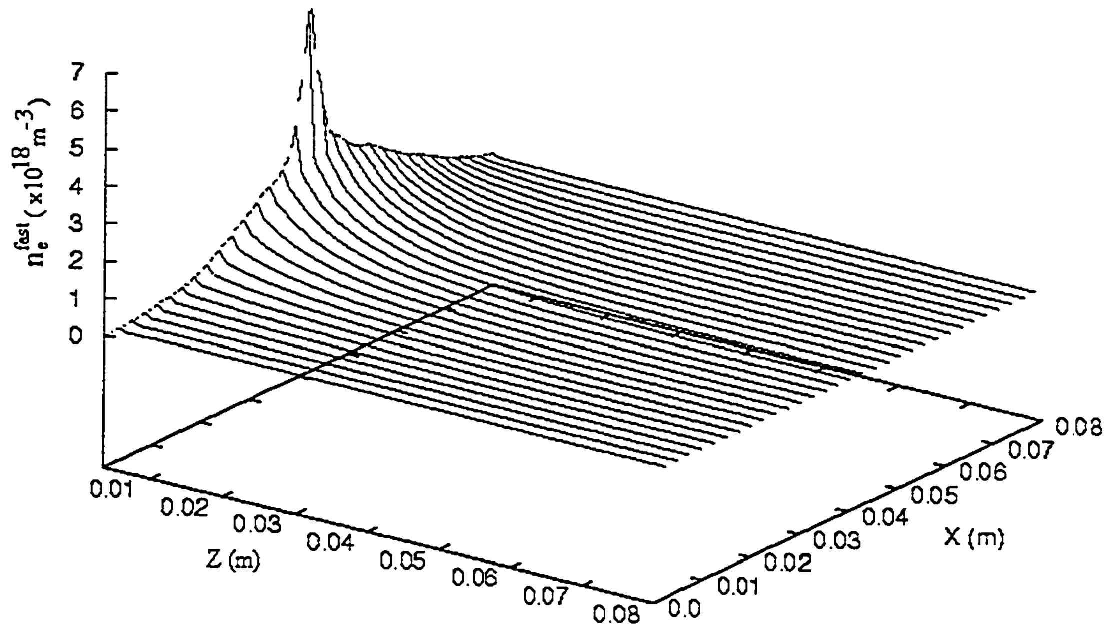

Figure 4.42: Fast electron density outside of the sheath for the thick sheath (1.9 mm) case.

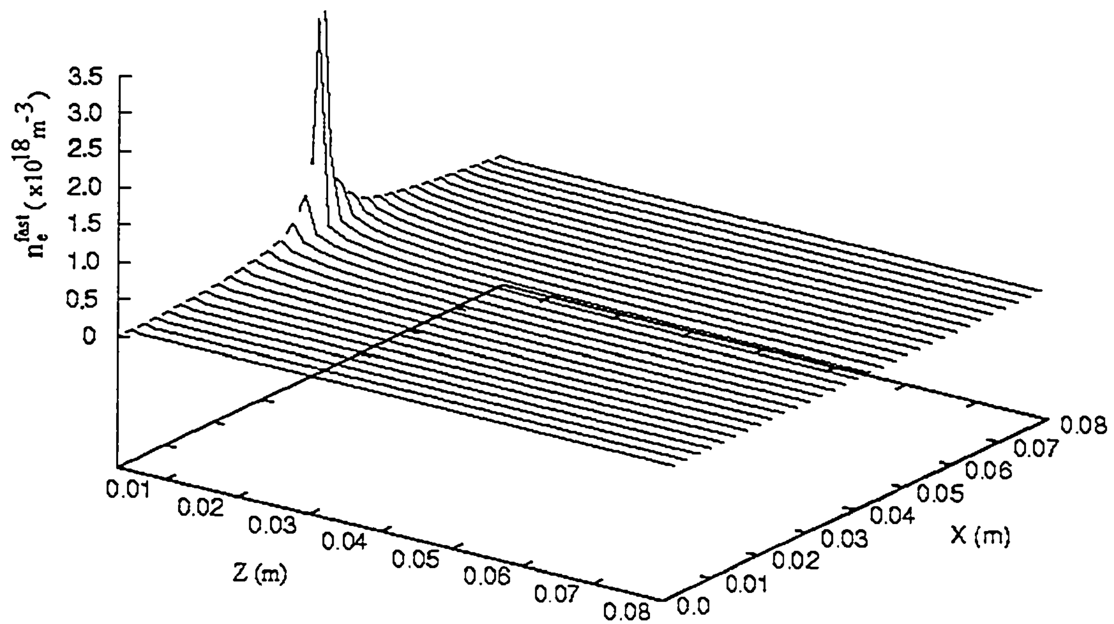

Figure 4.43: Fast electron density outside of the sheath for the thin sheath (1.3 mm) case.

Reproduced with permission of the copyright owner. Further reproduction prohibited without permission.

4.5.2 Simulations at 40 mTorr

Simulations were conducted with an argon sputtering gas pressure of 40 mTorr. One simulation with a uniform argon gas pressure and four with various rarefied gas density profiles as shown in figure 4.44. Note that the first profile is identical to one used for gas rarefaction at 5 mTorr. The other profiles, of course, were to investigate the impact of shape.

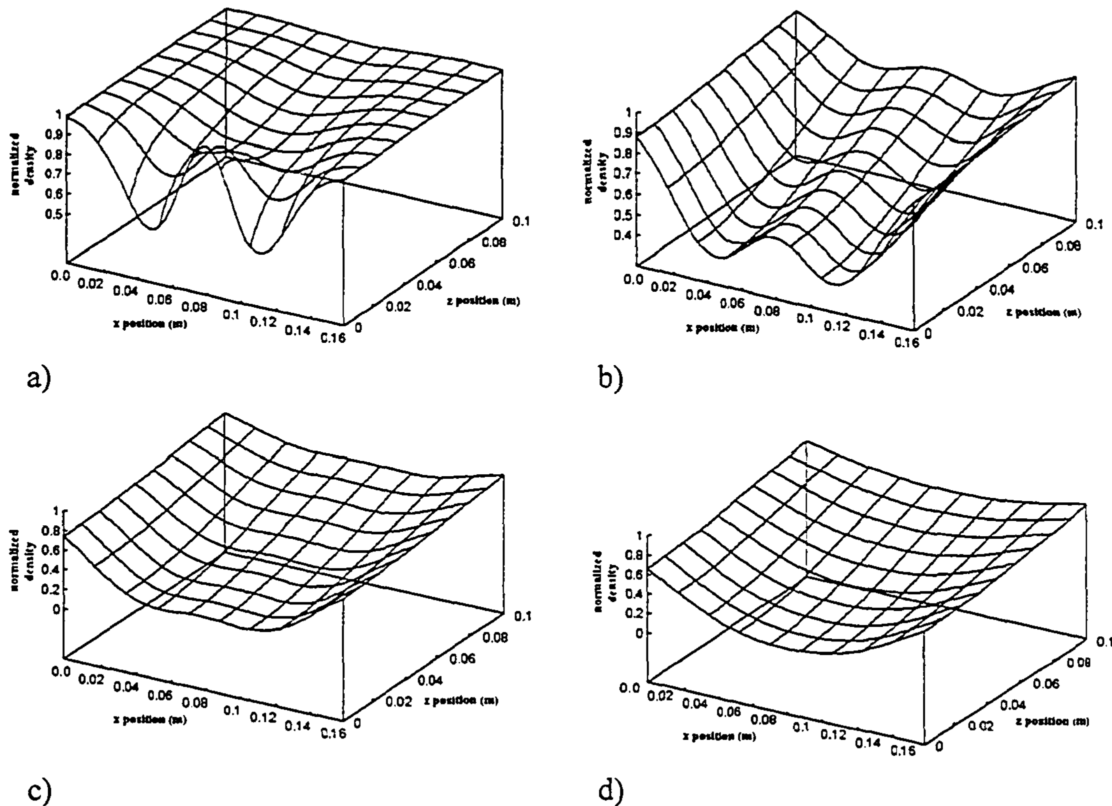

Figure 4.44: Various rarefied gas denisty profiles used in simulations at 40 mTorr. Profiles are designated a, b, c, and d.

Figure 4.45 and 4.46 show the hot T_e and n_e^M (taken from EEDF's) at various distances above the etch region for all five simulations and for the hot electron and total electron groups taken from the LP data (see §3.3.1). The simulation, using 40 mTorr and a uniform gas density, consistently showed a higher n_e^M and lower T_e than the experimental data indicated. Beyond 6 cm distance from the cathode, the hot

Reproduced with permission of the copyright owner. Further reproduction prohibited without permission.

electron density dropped rapidly leaving an unconverged EEDF. Therefore, a reasonable Maxwellian fit could not be made to the data. The low T_e and high n_e^M are consistent with a neutral species density that is artificially high, leading to excessive collisions near the cathode cooling the electrons. At this pressure, it appears to also limit the rate at which electrons diffuse away from the cathode, increasing the density there. The simulations that used various rarefied gas profiles did vary enough to span the temperatures and densities of hot electrons found by experimental means. Furthermore, the general trend was qualitatively the same. However, at this pressure it appears that T_e and n_e^M are quite sensitive to changes in the neutral gas density profiles, so that, without more accurate profiles, it is difficult to make quantitative interpretations. It does appear that for cases b, c, and d, the T_e follows the same general trend as the total electron group LP data. It is not clear that, with a more accurate density profile, the T_e wouldn't follow the hot electron group's temperature trend beyond 6 cm where the electrons bifurcate into two groups, as appeared to be

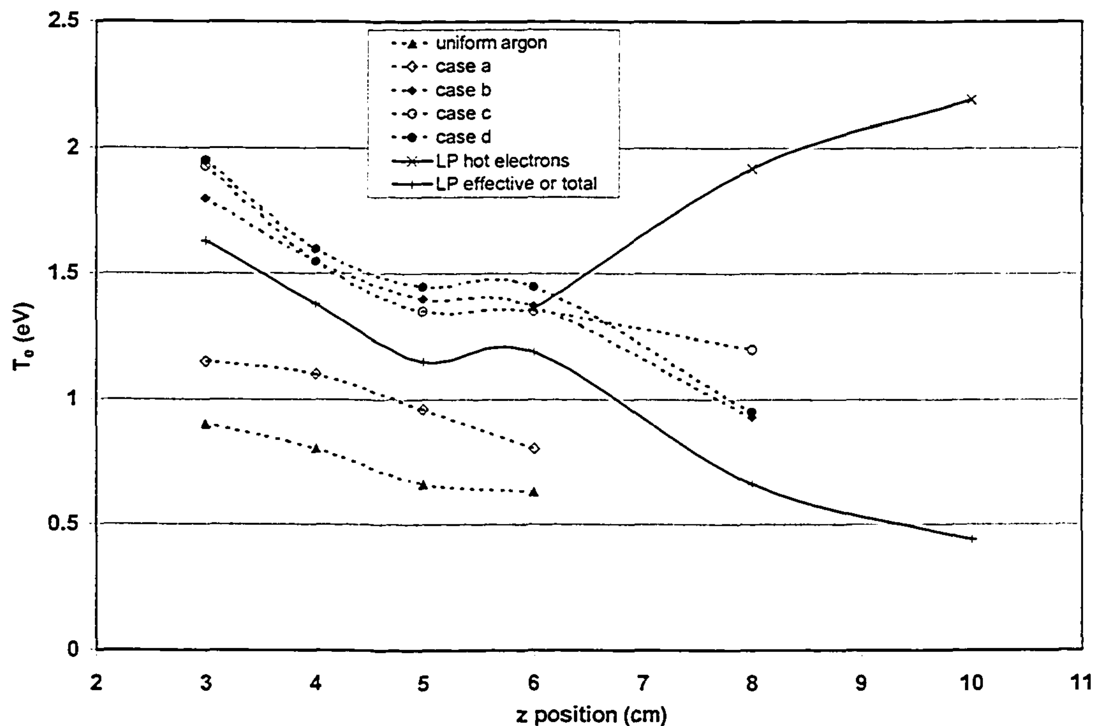

Figure 4.45: Electron temperature (from Maxwellian fit to EEDF's) taken at various positions above the etch region at 40 mTorr for various rarefied gas profiles. Experimental (LP) data for the total and hot electron groups is also included.

Reproduced with permission of the copyright owner. Further reproduction prohibited without permission.

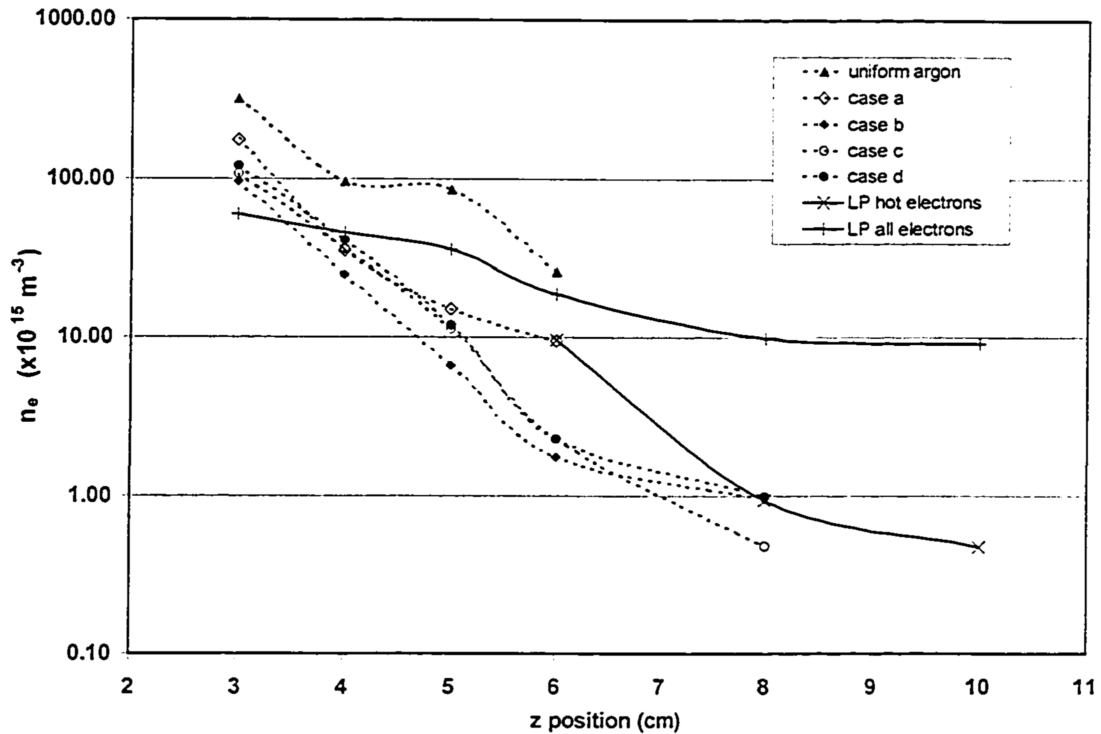

Figure 4.46: Electron density, (n_e^M) (from Maxwellian fit to EEDF's) taken at various positions above the etch region at 40 mTorr for various rarefied gas profiles. Experimental (LP) data for the total and hot electron groups is also included.

the case for 5 mTorr simulations. It is also unclear that the n_e^M are following the trend established by the LP hot electrons, although that generally appears to be the case (fig 4.46).

One notable difference for the simulation at 40 mTorr was that the shape of the EEDF's above the well region was not abnormally peaked at 11 eV (see figure 4.15) but appeared Maxwellian, like those found elsewhere. This enabled fitting of a Maxwellian function to extract temperatures and densities. The results are shown in figures 4.47 and 4.48. In this case, the LP data was at the upper end of the ranges in T_e and n_e^M established by the various rarefied gas profiles. Beyond 6 cm above the cathode, the sampling was again too low to obtain reasonable results (i.e. it was not converged). The change in shape of the EEDF's above the well region at higher densities strongly suggests that the local gas density is a major factor in determining

Reproduced with permission of the copyright owner. Further reproduction prohibited without permission.

not just the energy dependant transport dynamics into and out of the well region, but, in general, all EEDF's.

Since the simulation results for T_e and n_e^M at 40 mTorr do not agree with experimental results as well as the simulations at 5 mTorr, and since the values obtained at 40 mTorr appear much more sensitive to the rarefaction and gas density profile, it can be concluded that gas rarefaction is a considerably more important factor at this pressure for electron transport dynamics and development of EEDF's. Until self-consistent simulations are available, this avenue of exploration will have limited benefit.

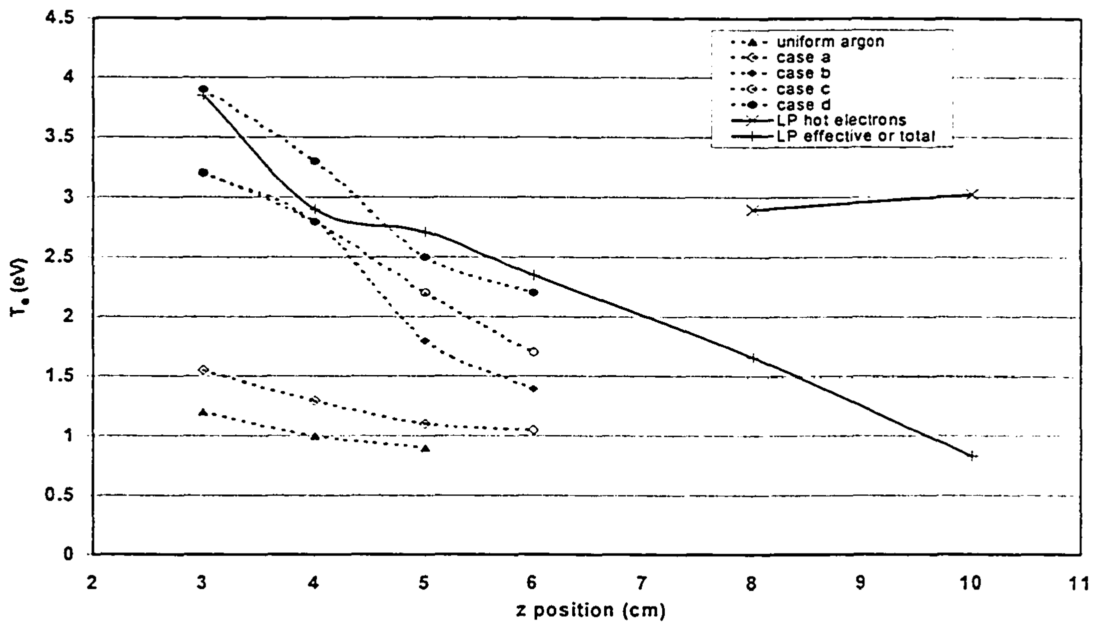

Figure 4.47: Electron temperature (from Maxwellian fit to EEDF's) taken at various positions above the well region at 40 mTorr for various rarefied gas profiles. Experimental (LP) data for the total and hot electron groups is also included.

Reproduced with permission of the copyright owner. Further reproduction prohibited without permission.

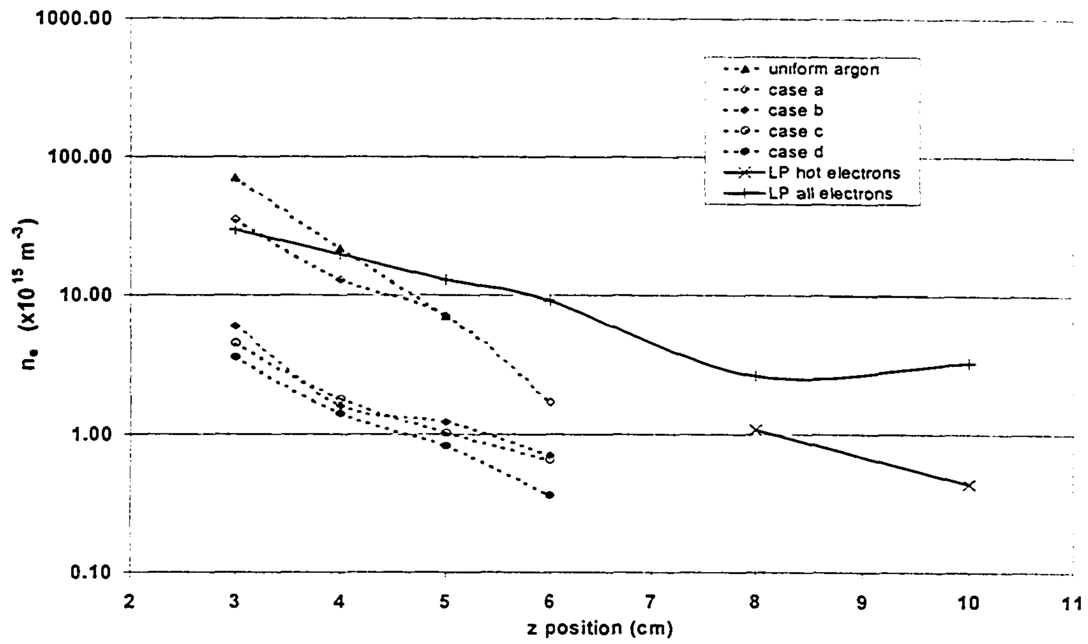

Figure 4.48: Electron density, (n_e^M) (from Maxwellian fit to EEDF's) taken at various positions above the well region at 40 mTorr for various rarefied gas profiles. Experimental (LP) data for the total and hot electron groups is also included.

Reproduced with permission of the copyright owner. Further reproduction prohibited without permission.

4.6 Simulation Summary and Conclusion

The simulations completed in this investigation were intended to elucidate some of the dominant processes within magnetron plasma systems that lead to the experimentally observed electron densities, temperatures, and more generally, EEDF's. As a byproduct the simulations are also capable of providing creation rate data, which also provides insight into these processes. This investigation was to illuminate general concepts and provide understanding into how these systems operate. In future investigations, more specific simulations may be performed as specialized information is sought. Such work can be extended into attempts to develop analytical models, a penultimate goal.

Here the simulations gave strong indications as to the fate of primary electrons ejected from the cathode in a sputtering event. The density and temperature, or EEDF of these electrons, while in their non-equilibrium state, was found to depend on various factors, some more important than others.

The creation rates of thermalized species depends on many factors. While the addition of Ag atoms to the simulation did not indicate any change to the creation rates, the addition of metastable argon did. Higher creation rates were found with higher levels of metastable argon, an effect that was enhanced even further when super-elastic collisions were allowed, even though the corresponding collision cross-section is very small. These creation rates were, obviously, decreased when the argon neutral density was decreased due to rarefaction. Changes in the target voltage also had an effect, where lower voltages lead to lower energy primary electrons, which were able to ionize fewer argon atoms. Changes to boundary conditions such as γ_p and ERC coefficients also had effects, where changes to γ_p had like changes to the creation rates on a 1:1 ratio. The ERC also was an influence, albeit a lesser one, since it did not directly involve every simulated electron, only those that had sufficient energy to return to the cathode. Changes in the sheath thickness also influenced the creation rate since wider sheaths provided more space within which ionizing events would produce low energy electrons that subsequently gained energy from the sheath

Reproduced with permission of the copyright owner. Further reproduction prohibited without permission.

electric field and were able to produce yet more ions outside the sheath. This was found to be a major factor in creation rates where a 1.5 times increase in sheath width produced an approximate 5.5 times increase in creation rates.

The fast electron density, or FED, which considers only the electrons above the thermalization threshold, was also influenced by a wide variety of factors. It was definitely sensitive to the value used as a thermalization threshold, which strongly implies interpretation of the results must be done carefully. The extent to which this variable is a factor, where great increases in the FED occurred directly above and near to the etch track when using lower thresholds, should definitely be considered when reviewing published results of this type. The FED generally decreased when more energy loss paths were present such as when Ag and metastable argon were introduced into the simulation. Superelastic collisions did not appear to significantly affect the FED. The initial energy of the primary electron was found to be important, such that lower cathode voltages lead to lower primary electron energies, which became thermalized faster. The reduced lifetime of such species was realized as a reduced density. As with the creation rates, reductions to the γ_p coefficient showed reductions in the FED. Argon gas rarefaction was one of the greatest factors in changing the qualitative shape of the FED profile. Fewer collisions directly above the etch track, where the rarefaction was most extreme, reduced the number of electron-argon collisions there, increasing the residence time and thus density of those electrons. Further from this region, there was an apparent reduction of fast electrons since they were much slower in moving out from the trap region. Increasing the sheath width influenced the fast electron density profile shape and increased the density of such species. However, there was no influence whatsoever on the electron temperatures, at least in the regions tested here. At higher pressures, such as at 40 mTorr, electron density was extremely sensitive to argon rarefaction profiles, although it appeared to follow the general trend obtained experimentally by LP for the hot electron group.

While electron densities (both those of the fast electrons above the thermalization threshold and those as extracted from fitting Maxwellian functions to simulated EEDF's, n_e^M) were affected by a wide variety of factors, the T_e was much

Reproduced with permission of the copyright owner. Further reproduction prohibited without permission.

less sensitive. The electron temperature experienced a significant decrease at higher levels of gas phase Ag and metastable argon species. This results from the ability of these species to deplete energy from the higher energy portion of the EEDF – those energies lying above the inelastic threshold for the Ag ionization and metastable ionization processes but below the inelastic threshold for ground state argon. Both of these species would be expected to increase in density at higher cathode currents and so are likely the best explanation for the experimentally observed lower T_e at higher cathode currents. Interestingly, superelastic collisions did not influence T_e. T_e also was not sensitive to the cathode voltage with only very minor changes in the EEDF. Argon rarefaction tended in increase T_e as there was less impetus for energy loss for the higher energy electrons. Boundary conditions such as γ_p and ERC had no influence whatsoever on T_e. At 40 mTorr, T_e was, as with the electron densities, quite sensitive to the argon rarefaction profile, although it appeared to follow the same general trends. In this case it was not clear if the simulated T_e would follow the trend established experimentally by hot electrons or the bulk electrons. An interesting note is that at 40 mTorr, the EEDF's in the well region appeared very Maxwellian-like as opposed to the 5 mTorr case where they displayed an unusual distribution, peaked at 11 eV. This strongly suggested both, that the local magnetic field shape in the well region and the local and overall gas density are the major factors in the electron's transport into and out of the well region. This seems to be generally applicable everywhere, as T_e is most susceptible to changes in gaseous species densities and is not sensitive to changes in boundary conditions. The EEDF's obtained in the well region also suggested it is unique in terms of electron transport.

Generally, the Maxwellian fits to EEDF's were not ideal. It remains possible that Maxwellian distributions are not the most appropriate given the abrupt drop in the EEDF's at the lowest inelastic threshold energy of argon. It was not conclusive that Rundle or Dreyvestyn distributions were more appropriate. Minor deviations from Maxwellian distributions may be smoothed in real systems by electrostatic collisions, a factor not considered here, though worthy of further investigation. It did not appear immediately meaningful to extract densities, n_e^M, from Maxwellian fits to EEDF's, though with self-consistent algorithms, which can provide more accurate

Reproduced with permission of the copyright owner. Further reproduction prohibited without permission.

rarefaction profiles, and potentially weak electric fields within the plasma, it may be that more far-reaching results can be obtained. It is also noted that values such as n_e^M give no consideration to electrons created as by-products of ionization events which may constitute a significant portion of the total electron population.

Just outside of the sheath (~2 mm), the electron group still appeared to be of similar temperature to those groups elsewhere, though slightly cooler. This suggested the dominant electrons even this near the cathode were of generally low energy. At the very high end of the EEDF was found a sinusoidal distribution reflective of the 'inexperienced' primary electron's life history.

In general, at 5 mTorr the T_e values matched quite well with the experimentally obtained data and were sensitive to gas phase and magnetic field conditions. The electron densities did not match well but were sensitive to almost everything and thus are prone to greater error. A self-consistent simulation is needed to reveal the finer nuances of such reactors.

Table 4.2 reviews that response of creation rates, fast electron density, n_e^M, and T_e to the various tested simulation parameters.

Reproduced with permission of the copyright owner. Further reproduction prohibited without permission.

Table 4.2: Response of creation rates, fast electron density, n_e^M, and T_e to various tested simulation parameters.

Parameter tested	Electron and Ion creation Rates	Fast Electron Density	n_e^M	T_e
Higher electron Thermalization Threshold	NC	↓	NC	NC
Higher Levels of Ag	NC	↓	↑ Increase is greater close to cathode (see fig. 4.23)	↓
Higher Cathode Voltage	↑	↑	↑	NC
Higher levels of metastable argon	↑ Slight profile change (see fig. 4.27 and 4.28)	↓	↓ Greater drop close to cathode (see fig. 4.30)	↓
Higher γ_p	↑	↑	↑	NC
Higher ERC	↑	NC	NC	NC
Include rarefied argon profile (lower gas density in some areas)	↓	Distinct profile change (see fig. 4.37)	↑ more peaked in magnetic trap (see fig. 4.38)	↑ rises more further from cathode
Increase sheath thickness	↑ change to 2-D profile shape (see fig. 4.40)	↑ change to 2-D profile shape (see fig. 4.42 and 4.43)	n/a	NC
Higher gas pressure	↑	↑	↑	↓

NC = no change
n/a = data not collected

Reproduced with permission of the copyright owner. Further reproduction prohibited without permission.

Chapter 5: Summary

5.1 Summary and Conclusions

The results presented in chapters 3 and 4 provide spatial information on the structure of a magnetron sputtering plasma. When the experimental work of Chapter 3 is brought together with the simulation work of Chapter 4 deeper insights can be obtained into the important factors within such a complex process.

Langmuir probe data provided a significant amount of data, including V_f, V_p, n_e, and T_e or T_{eff}, T_e^{cold} and T_e^{hot}. The simulation work provided thermalized electron creation rates, thermalized ion creation rates, fast electron densities (those above 6 eV), several EEDF's, as well as T_e and n_e extracted from Maxwellian fits to the EEDF's.

A primary issue raised by the LP data was that of transport mechanisms across magnetic field lines for electrons. The processes and boundary conditions that were responsible for the observed densities and temperatures or EEDF's of the electrons were not clear. The simulation work determined that boundary conditions such as target emission and reflection coefficients, and particularly target voltage were either insignificant, or very minor factors, in determining spatial distributions of electron densities and temperatures. Sheath thickness had some influence on the qualitative shape of the electron density distribution, although that may have been related to a change in the magnetic field near the sheath edge. Of crucial importance was the magnetic field, local and global density of all various gas species, and the variety of inelastic processes allowed within the system. This is to say that n_e and T_e are strong functions of pressure, gaseous species type and magnetic field. The dependence on pressure suggests that collision rate is extremely important to the dynamics of this system. The dependence found here on pressure, gas species, and magnetic field further implies that the energy of the electron is important since that energy couples with pressure to determine mean free path, with magnetic field to determine Larmor Radius, and with various gas species to determine inelastic event probabilities. This means specific transport mechanisms are energy dependent.

Reproduced with permission of the copyright owner. Further reproduction prohibited without permission.

Previous conceptual models used to describe bi-Maxwellian plasmas within magnetrons all require improvement. Speaking to the general motion of the more energetic group is insufficient as transport mechanisms will differ for each energy range and generalizations are not likely reliable, at least for the electron energy regime considered here. Fluid models may be appropriate for electron groups with energies significantly below all the inelastic process energies in the system.

It was not clear exactly what portion of the system was represented by the simulated electrons, although it appeared they correlated fairly well with the hot electron group from LP data. This was most apparent when simulating at 5 mTorr, though was not clear when simulating at 40 mTorr. Conceptually the correlation to hot electrons is sensible, since the group of electrons simulated were only those born at the cathode or within the sheath, both of which would gain high levels of energy from the sheath electric field. These are the energetic electrons of the system as opposed to the cold electrons supplied by as byproducts from ionizing collisions outside the sheath. These electrons, which never have a high energy, were not simulated here since they were of too low an energy to be of interest.

The EEDF's found in the simulation studies showed significantly more structure than those found experimentally, a result that can be regarded in two ways. First, the LP method, which only found Maxwellian and bi-Maxwellian distributions may not have been sensitive enough to pick up the more subtle features of non-Maxwellian distributions. Secondly, the simulation did not consider all possible processes within the reactor. Specifically, it did not consider electrostatic collisions, a factor known to smooth abrupt features in distribution functions, bringing them closer to Maxwellian states. The features in simulated EEDF's that deviated from Maxwellian were related to the available inelastic process energy thresholds, such that, above those thresholds there was an abrupt drop in electron density. These features did not appear to be any better described by Rundle group distributions. Interestingly, one potential model for bi-Maxwellian EEDF formation, that of superelastic collisions, did not appear to be a factor, at least at the metastable densities used here.

Reproduced with permission of the copyright owner. Further reproduction prohibited without permission.

Electron densities and temperatures in the well region, experimentally obtained at 5 and 40 mTorr, suggested some subtle and unobvious mechanisms were responsible for transport of electrons into and out of that area. Simulations showed that at 5 mTorr there was an unusual effect where EEDF's departed drastically from Maxwellian with the EEDF's rising with energy to a peak at about 11 eV. After that there was a severe drop in density attributed to electron depletion due to inelastic processes. This suggests that higher energy electrons move into this region much more easily than do low energy electrons. At that pressure it appeared the magnetic field, which was loosely shaped like a magnetic mirror, was the dominant factor in determining electron transport. This was because it was the only region with both the unusual EEDF shape and the symmetrical configuration. Above the outer row of magnets, where the gas density and magnetic field strength were equivalent, the EEDF was Maxwellian-like. However, the magnetic field, though similar to that in the well region, was not symmetrical and thus was a poor magnetic mirror. At 40 mTorr, where the gas density was much higher, the EEDF's became Maxwellian, suggesting collisions phenomenon had replaced magnetic field shape in dominating electron transport.

LP data taken for increasing cathode currents showed a definitive increase in n_e but a decrease in T_e. At that point it was speculated that this may be due to increased levels of Ag atoms in gas phase, which could further cool the electrons due to the lower ionization threshold compared to argon. Simulations showed both higher densities (from Maxwellian fits to EEDF's) and lower temperatures were possible with even low, albeit speculative, Ag density profiles. Furthermore, simulations revealed that the presence of metastable argon would also contribute to this effect and that gas rarefaction, which is likely more significant at higher cathode currents, would act to increase T_e. Thus all of these factors likely contribute to the final densities and temperatures.

While gas rarefaction was found to have an effect at 5 mTorr, the results obtained at 40 mTorr showed even more sensitivity to the degree and shape of the (postulated) spatial rarefied gas profiles. This suggests that gas phase collisions are of greater importance at higher pressures.

Reproduced with permission of the copyright owner. Further reproduction prohibited without permission.

The addition of oxygen to the system created difficulties in experimentally obtaining consistent data, due to a variety of potential reasons including system hysteresis and deficiencies in analytical techniques. The primary effects expected in the plasma are likely to revolve around the multiple additional inelastic processes that oxygen brings with its presence. This can be said now that the insensitivity of the plasma, and electron transport appear to be quite independent of boundary conditions such as γ_p, target voltage, etc.

The simulations also provided significant amount of ECR and ICR data. ECR results were always higher than ICR results which implies that, left unchecked, the electron population would overwhelm the ion population. This coupled with the fact that ions are lost to the cathode much more extensively than electrons, implies electrons must leave the plasma by other means and at a higher rate than ions. Creation rates increased with higher gas densities (more frequent ionizing collisions), addition of species with lower ionization thresholds such as metastable argon (able to ionize species with lower energy electrons), increases in cathode voltage (primary electrons end up with more energy and can ionize more atoms) and increases in target coefficients (γ_p and ERC which increased the number of primary electrons which could produce ions).

The magnetic field was found to be particularly adept at trapping low energy electrons directly above the etch region. The shape of the magnetic field coupled with the bounding cathode sheath electric field formed an effective trap. Low energy electrons were found to dominate the electron density found there, an affect attributed to the subsequent smaller Larmor radius. This decreased the low energy electron path length between reflections at the sheath electric field causing them to traverse the region several times before escaping due to collisional scattering. Even the collisional scattering would have been less effective for low energy electrons since a scattering event would only move them, at most, one Larmor radius out of the trap per collision. For higher energy electron the Larmor radius is larger and so requires fewer collisions to escape the region.

Reproduced with permission of the copyright owner. Further reproduction prohibited without permission.

5.2 Recommended Future Studies

Understanding more about the transport of electrons, which are likely the most complex component of the system given their low mass and resultant susceptibility to influence by magnetic fields, is an important step in obtaining an overall understanding of magnetron plasma systems. Even with this intent there is still a significant amount of work that can be done. Finer resolution LP surveys may be helpful in revealing more detail about electron transport in the various plasma regions. Unidirectional Langmuir probes, where electrons are sampled on only one side, may be helpful in revealing total electron fluxes through the various regions. This can be correlated with more advanced simulations that can monitor energy dependant electron fluxes. This combined with the LP data may enable the development of analytical functions describing electron transport. Additionally, a completed self-consistent simulation package will undoubtedly contribute to more accurate results and a better understanding of the system. Such a package should treat all ionic and electronic species by either a fluid or MC model and incorporate effects such as gas rarefaction, target poisoning, and chamber wall heating. All of these factors can then be tested as factors in the system. Also, experimental and simulation investigations should definitely be conducted into the influence of the magnetic field strength and shape as this is one of the least understood influences on process operation.

Use of other experimental techniques such as Mass Spectrometers would be very useful in ascertaining the spatial distribution and energies of the various positive ions, negative ions, and neutral atomic and molecular species. Simulation should also be able to produce maps of like kind, once they incorporate sufficient detail. This would include an extensive library of collision and chemical process types so that simulations with reactive species such as oxygen can be performed. Other experimental techniques may include the use of optical emission spectrometers and laser induced fluorescence.

While it is a major goal to understand how these systems operate generally, it is an important goal to eventually develop a simulation, and ideally, analytical

Reproduced with permission of the copyright owner. Further reproduction prohibited without permission.

models, for investigating the influence of process conditions on depositing film structure and chemistry. The penultimate achievement would be to apply those models to better engineer advanced materials. This is a desirable goal since magnetron sputtering appears capable of producing nanocrystalline materials with highly unique properties that other processes have yet to produce. However, to achieve this noble goal an explicit understanding of how process conditions influence the variety and energies of all the plasma species bombarding the growing film must be obtained.

Reproduced with permission of the copyright owner. Further reproduction prohibited without permission.

Appendix 1:
List of Experimental Run Conditions and Cathode Voltage

Section	Pressure (mTorr) (0% O2)	Cathode Current (Amps)	Normal Position (z) (cm)	Lateral Position (x) (cm)	Cathode Voltage (volts) ± error *
3.3.1	40	0.6	3	0 -16	-412 ± 7
	5	0.6	3	0 -16	-579 ± 15
	40	0.6	5	0 -16	-408 ± 5
	5	0.6	5	0 -16	-572 ± 7
	40	0.6	10	0 -16	-408 ± 6
	5	0.6	10	0 -16	-566 ±10
	40	0.6	3 -10	4	-403 ± 1
	5	0.6	3 -10	4	-561 ± 5
	40	0.6	3 -10	8	-407 ± 3
	5	0.6	3 -10	8	-564 ±4

Section	Pressure (mTorr)	% O2	Cathode Current (Amps)	Normal Position (z) (cm)	Lateral Position (x) (cm)	Cathode Voltage (volts) ± error *
3.3.2	40	4	0.6	3,5,10	0 - 8	-441 ± 5
	40	4	0.6	3 - 10	4,8	-443 ± 3
	40	16	0.6	3,5,10	0 - 8	-506 ± 6
	40	16	0.6	3 -10	4,8	-505 ± 5

Section	Pressure (mTorr)	% O2	Cathode Current (Amps)	Normal Position (z) (cm)	Lateral Position (x) (cm)	Cathode Voltage (volts) ± error *
3.3.3	40	0	0.6	5,10	4,8	-406 ± 2
	40	4	0.6	5,10	4,8	-438 ± 1
	40	8	0.6	5,10	4,8	-467 ± 5
	40	12	0.6	5,10	4,8	-486 ± 6
	40	16	0.6	5,10	4,8	-508 ± 2
	40	20	0.6	5,10	4,8	-518 ± 4
	5	0	0.6	5,10	4,8	-562 ± 6
	5	4	0.6	5,10	4,8	-582 ± 5
	5	8	0.6	5,10	4,8	-604 ± 9
	5	12	0.6	5,10	4,8	-618 ± 18
	5	16	0.6	5,10	4,8	-640 ± 17
	5	20	0.6	5,10	4.8	-645 ± 14

Reproduced with permission of the copyright owner. Further reproduction prohibited without permission.

Section	Pressure (mTorr)	% O2	Cathode Current (Amps)	Normal Position (z) (cm)	Lateral Position (x) (cm)	Cathode Voltage (volts) ± error *
3.3.4	50	0	0.6	5,10	4,8	-392 ± 1
	40	0	0.6	5,10	4,8	-406 ±2
	30	0	0.6	5,10	4,8	-418 ± 1
	20	0	0.6	5,10	4,8	-443 ± 2
	10	0	0.6	5,10	4,8	-485 ± 3
	5	0	0.6	5,10	4,8	-562 ± 6
	50	4	0.6	5,10	4,8	-432 ± 3
	40	4	0.6	5,10	4,8	-438 ± 1
	30	4	0.6	5,10	4,8	-452 ± 1
	20	4	0.6	5,10	4,8	-470 ± 1
	10	4	0.6	5,10	4,8	-520 ± 1
	5	4	0.6	5,10	4,8	-595 ± 11
	50	16	0.6	5,10	4,8	-498 ± 6
	40	16	0.6	5,10	4,8	-508 ± 2
	30	16	0.6	5,10	4,8	-524 ± 2
	20	16	0.6	5,10	4,8	-548 ± 3
	10	16	0.6	5,10	4,8	-592 ± 4
	5	16	0.6	5,10	4,8	-647 ± 14

Section	Pressure (mTorr) (0% O2)	Cathode Current (Amps)	Normal Position (z) (cm)	Lateral Position (x) (cm)	Cathode Voltage (volts) ± error *
3.3.5	40	0.2	5,10	4,8	-349 ± 5
	40	0.4	5,10	4,8	-381 ± 1
	40	0.6	5,10	4,8	-407 ± 2
	40	0.8	5,10	4,8	-419 ± 2
	40	1.0	5,10	4,8	-435 ± 3
	5	0.2	5,10	4,8	-449 ± 6
	5	0.4	5,10	4,8	-515 ± 2
	5	0.6	5,10	4,8	-562 ± 6
	5	0.8	5,10	4,8	-592 ± 5
	5	1.0	5,10	4,8	-632 ± 12

Reproduced with permission of the copyright owner. Further reproduction prohibited without permission.

Appendix 2: Spatial map of locations where Langmuir Probe data has been obtained.

Lines indicate positions where lateral and normal spatial survey where conducted. Circles indicate three positions where oxygen, pressure, and current surveys were conducted.

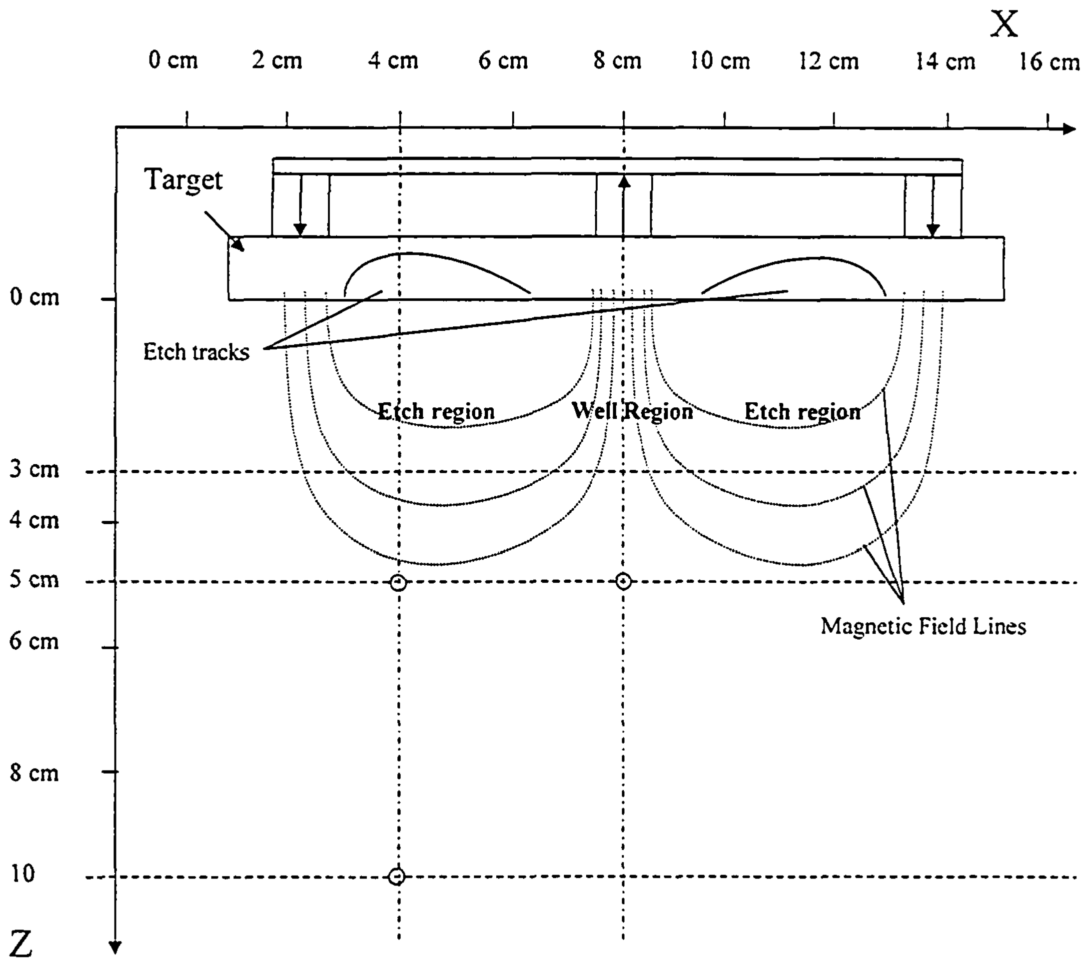

Reproduced with permission of the copyright owner. Further reproduction prohibited without permission.

1 J.A. Thornton, J. Vac. Sci. Technol. A, 4(6), 3059, 1986.

2 R.N. Tait, Thin Film Microstructure Effects in VLSI Metallization, Ph.D. thesis, Department of Electrical Engineering, University of Alberta, Edmonton, 1992.

3 C. Suryanarayana, *High Temperature High Performance Materials for Rocket Engines and Space Applications*, Edited by K. Upadhya. The Minerals, Metals & Materials Society, 1995.

4 J. Musil, D. Hovorka, M. Misina, A.J. Bell, V. Studnicka, Czeck. J. Phys. 48(8), 963, 1997.

5 J. Musil, J. Vlcek, Mater. Chem. Phys., 54, 116, 1998.

6 J. Musil, I. Leipner, M. Kolega, Surf. Coat. Technol., 115, 32, 1999.

7 D. J. Field, S. Djokic, N. Le, R.E. Burrell, J. Electrochem. Soc., 148(3), 191, 2001.

8 J. Musil, J. Vlcek, V. Jezek, M. Benda, M. Kolega, R. Boomsma, Surf. Coat. Technol. 76-77, 274, 1995.

9 D. Mattox, J. Vac. Sci. Technol. A, 7(3), 1105, 1989.

10 I. Ivanov, Sv. Statev, V. Orlinov, R. Shkevov, Vacuum, 43(8), 837, 1992.

11 J. Vlcek, P. Spatenka, J. Musil, L. Forejt , Surf. Coat. Technol., 98, 1557, 1998.

12 J. Vlcek, P. Spatenka, J. Blazek, Vacuum, 55, 165, 1999.

13 T. E. Sheridan, M.J. Goeckner, J. Goree, J. Vac. Sci. & Technol. A 9, 688 1991.

14 A. Bogearts, R. Gijbels, J. Anal. At. Spectrom., 12, 751, 1997.

15 E. Nasser, *Fundamentals of Gaseous Ionization and Plasma Electronics*, Wiley InterScience, New York and London, 1971.

16 B.N. Chapman, *Glow Discharge Processes*, John Wiley and Sons, 1980.

17 D.M. Manos and D.L. Flamm editors, *Plasma Etching*, Academic Press, 1989.

18 Cuomo and Rossnagel editors, *Handbook of Plasma Processing Technology*, Noyes Publications, 1992.

Reproduced with permission of the copyright owner. Further reproduction prohibited without permission.

19 F.F. Chen, *Introduction to Plasma Physics and Controlled Fusion*, Plenum Press, 1984.

20 D. Mattox, *Handbook of Physical Vapor Deposition (PVD) Processing*, Noyes Publications, 1998.

21 F.F. Chen, 'Electric Probes' in *Plasma Diagnostic Techniques*, edited by Huddlestone and Leonard, Academic, New York, 1965.

22 J.G. Laframboise, UTIAS Rep. No. 100, Institute for Aerospace Studies, Univ. of Toronto, 1966.

23 J.D. Swift and M.J.R. Schwarr, *Electrical Probes for Plasma Diagnostics*, American Elsevier, New Tork, 1969.

24 N. Hershkowitz, in *Plasma DiagnosticTechniques*, edited by O. Auciello and D.L. Flamm, Academic, New York, 1989.

25 A. Bogearts, R. Gijbels, Anal. Chem. News & Features, 719 A, December 1, 1997.

26 T.E. Sheridan, M.J. Goeckner, J. Goree, Jpn. J. Appl. Phys., 34 Part 1 No. 9A, 4977, 1995.

27 M.J. Goeckner, J.A. Goree, T.E. Sheridan, IEEE Trans. Plasma Sci., 19(2), 301, 1991.

28 K. Nanbu, S. Kondo, Jpn. J. Appl. Phys., 36, 4808, 1997.

29 T. E. Sheridan, M.J. Goeckner, J. Goree, , J. Vac. Sci. Technol. A, 8(1), 30, 1990.

30 T. E. Sheridan, J. E. Miranda, M.J. Goeckner, J. Goree, , J. Vac. Sci. Technol. A, 8(3), 1627, 1990.

31 K. Nanbu, I. Warabioka, p. 428, *Rarefied Gas Dynamics-Space Science and Engineering*, eds. B.D. Shizgal, and D.P. Weaver (AIAA, New York, 1992).

32 S. Ido, K. Nakamura, Vacuum, 47(6-8), 1035, 1996.

33 R.J. Carman, J. Phys. D: Appl. Phys., 22(55), 1989.

34 Li, Chen, Li, J. Phys. D: Appl. Phys. 28, 681, 1995.

35 Li, Chen, Li, J. Phys. D: Appl. Phys. 28, 1121, 1995.

36 R. Razdan, C.E. Capjack, H.J.J. Seguin, J. Appl. Phys. 57(11), 4954, 1985.

Reproduced with permission of the copyright owner. Further reproduction prohibited without permission.

37 A. Bogaerts, M. van Straaten, R. Gijbels, Spectrochimica Acta. 50B(2), 179, 1995.

38 J.P. Boeuf, E. Marode, J. Phys. D: Appl. Phys. 15, 2169, 1982.

39 J. Sun, Y. Gong, D. Wang, J. Phys. D: Appl. Phys. 26, 436, 1993.

40 C. H. Shon, J.S. Park, B.K. Kang, J.K. Lee, Jpn. J. Appl. Phys. 38, 4440, 1999.

41 C.H. Shon, J.K. Lee, Y. Yang, T.H. Chung, IEEE Trans. Plasma. Sci. 26(6), 1635, 1998.

42 C.H. Shon, J.K. Lee, Appl. Surf. Sci. 192, 258, 2002.

43 T. A. van der Straaten, N.F. Cramer, I.S. Falconer, B. W. James, J. Phys. D: Appl. Phys. 31, 191, 1998.

44 T. A. van der Straaten, N.F. Cramer, I.S. Falconer, B. W. James, J. Phys. D: Appl. Phys. 31, 177, 1998.

45 K. Nanbu, J. Kagayama, Vacuum, 47(6-8), 1031, 1996.

46 K. Nanbu, V.V. Serikov, J. Appl. Phys., 82(12), 5948, 1997.

47 K. Nanbu, S. Kondo, J. Phys D: Appl. Phys., 32, 1142, 1999.

48 K. Nanbu, V. V. Serikov, S. Kawamoto, IEEE Trans. Plasma Sci., 27(5), 1999.

49 K. Nanbu, S. Kondo, J. Vac. Sci. Technol., 19(3), 838, 2001.

50 K. Nanbu, K. Mitsui, S. Kondo, J. Phys. D: Appl. Phys. 33, 2274, 2000.

51 K. Nanbu, S. Kondo, J. Vac. Sci. Technol., 19(3), 830, 2001.

52 M. van Straaten, R. Gijbels, A Vertes, Anal Chem. 64, 1855, 1992.

53 J. D. Bukowski, D.B. Graves, P. Vitello, J. Appl. Phys. 80(5), 2614, 1996.

54 C. Costin, G. Gousset, L. Marques. G. Popa, Preprint Copy, 2003.

55 M. Surendra, D.B. Graves, G.M. Jellum, Phys. Rev. A, 41,1112, 1990.

56 J.P. Boeuf, A. Fiala, L.C. Pitchford, Phys. Rev. E, 49(6), 5607, 1994.

57 E. Shidoji, N. Nakano, T. Makabe, Thin Solid Films, 351, 37, 1999.

Reproduced with permission of the copyright owner. Further reproduction prohibited without permission.

58 E. Shidoji, T. Makabe, Thin Solid Films, 442, 27, 2003.

59 E. Shidoji, H. Ohtake, N.Nakano, T. Makabe, Jpn. J. Appl. Phys., 38, 2131, 1999.

60 E. Shidoji, M. Nemoto, T. Nomura, Y, Yoshikawa, Jpn. J. Appl. Phys., 33, 4281, 1994.

61 E. Shidoji, E. Ando, T. Makabe, Plasma Sources Sci. Technol., 8, 621, 2001.

62 A. Bogaerts, R. Gijbels, W.J. Goedheer, J. Appl. Phys., 78(4), 2233, 1995.

63 A. Bogaerts, R. Gijbels, J. Appl. Phys., 78(11), 6427, 1995.

64 A. Bogaerts, R. Gijbels, W.J. Goedheer, Anal. Chem., 68, 2296, 1996.

65 A. Bogaerts, R. Gijbels, Anal. Chem., 68, 2676, 1996.

66 A. Bogaerts, R. Gijbels, J. Anal. At. Spectrom., 13, 945, 1998.

67 A. Bogaerts, R. Gijbels, J. Vlcek, J. Appl. Phys., 84(1), 121, 1998.

68 A. Bogaerts, R. Gijbels, J. Anal. At. Spectrom., 15, 1191, 2000.

69 A. Bogaerts, R. Gijbels, V.V. Serikov, J. Appl. Phys., 87(12), 8334, 2000.

70 T. Motohiro, Y. Taga, Thin Solid Films, 112, 161, 1984.

71 G.M.Turner, I.S. Falconer, B.W. James, D.R. McKenzie, J. Appl. Phys., 65(9), 3761, 1989.

72 S. Dew, T. Smy, M. Brett, Jap. J. Appl. Phys., 33 (Pt. 1), 1140, 1994.

73 S. Kadlec, C. Quaeyhaegens, G. Knuyt, L.M. Stals, Surf. & Coat. Technol. 97, 633, 1997.

74 H. Urbassek, D. Sibbold, J. Vac. Sci. Technol. A, 11(3), 676, 1993.

75 A. Kersch, W. Morokoff, Chr. Werner, J. Appl. Phys., 75(4), 2278, 1994.

76 G. M. Turner, J. Vac. Sci. Technol. A, 13(4), 2161, 1995.

77 S.K. Dew, NSERC Application 103557, 1998.

78 Y. Yamamura, M. Ishida, J. Vac. Sci. Technol. A, 13(1), 101, 1995.

Reproduced with permission of the copyright owner. Further reproduction prohibited without permission.

79 L. Friedrich, S.K. Dew, M.J. Brett, T. Smy, Thin Solid Films, 266, 83, 1995.

80 L.J. Friedrich, D.S. Gardner, S.K. Dew, M.J. Brett, T.J. Smy, J. Vac. Sci. Technol. B, 15(5), 1790, 1997.

81 D. Vick, L.J. Friedrich, S.K. Dew, M.J. Brett, K. Robbie, M. Seto, T. Smy, Thin Solid Films, 339, 88, 1999.

82 D.G. Cornell, D.E. Hansen, A.F. Voter, C. Lui, J.D. Kress, Appl. Phys. Let., 73(26), 3860, 1998.

83 I. D. Sudit, R. C. Woods, Rev. Sci. Instrum. 64(9), 2440, 1993.

84 J.H. Rogers, J.S. De Groot, D.Q. Hwang, Rev. Sci. Instrum. 63(1), 31, 1992.

85 A. Brockhaus, C. Borchardt, J. Engmann, Plas. Sources Sci. Technol. 3, 539, 1994.

86 D. Fang, R.R. Williams, R.K. Marcus, J. Anal. Atom. Spec. 5 569, 1990.

87 A. Savitzky, M.J.E. Golay, Anal. Chem., 36(8), 1964.

88 M. Benda, J. Musil, Vacuum 55, 171, 1999.

89 J. Kong, H Shen, B. Chen, Z. Li, W. Shi, W. Yao, Zh. Qi, Thin Solid Films 207, 51, 1991.

90 J. Musil, A.J. Bell, M. Cepera, J. Zeman, Surf. Coat. Technol. 96, 359, 1997.

91 S.M. Rossnagel, H.R. Kaufman, J. Vac. Sci. & Technol. A 4, 1822, 1986.

92 B.C. Bell, D.A. Glocker, J. Vac. Sci. & Technol. A 6, 2047, 1988.

93 T. E. Sheridan, J. Goree, J. Vac. Sci. & Technol. A 7, 1014, 1989.

94 I. Petrov, I. Ivanov, V, Orlinov, J. Kourtev, Contrib. Plasma Phys. 30, 223, 1990.

95 I. Ivanov, Sv Statev, V. Orlinov, R. Shkevov, Vacuum 43, 837, 1992.

96 T. E. Sheridan, J. Goree, Phys. Rev. E 50, 2991, 1994.

97 E. Passoth, P. Kudrna, C. Csambal, J.F. Behnke, M. Tichy, V. Helbig, J. Phys. D 30, 1763, 1997.

98 T. E. Sheridan, M.J. Goeckner, J. Goree, J. Vac. Sci. & Technol. A 16, 2173, 1998.

Reproduced with permission of the copyright owner. Further reproduction prohibited without permission.

99 L. Gu, M.A. Lieberman, J. Vac. Sci. & Technol. A 6, 2960, 1988.

100 S. Miyake, N. Shimura, T. Makabe, A. Itoh, J. Vac. Sci. & Technol. A 10, 1135, 1992.

101 M.J. Goeckner, J. Goree, T. E. Sheridan, J. Vac. Sci. & Technol. A 8, 3920, 1990.

102 Y.W. Choi, M. Bowden, K. Muraoka, Jpn. J. Appl. Phys. 35, 5858, 1996.

103 J.E. Foster, A.E. Wendt, W.W. Wang, J.H. Booske, J. Vac. Sci. & Technol. A, 16(4), 2198, 1998.

104 S.Y. Kim, J.S. Lee, J. Mat. Sci. Let., 16, 547, 1997.

105 J. Vlcek, P. Spatenka, J. Musil, L. Forejt, Surf. Coat. Technol., 98, 1557, 1998.

106 S.M. Rossnagel, H.R. Kaufman, J. Vac. Sci. & Technol. A 5, 88, 1987.

107 D.M. Chambers, J. Poehlman, P. Yang, G.M. Hieftje, Spectrochim. Acta 46, 741, 1991.

108 BW. Koo, N. Hershkowitz, M. Sarfaty, J. Appl. Phys. 86, 1213, 1999.

109 D. Fang, R.K. Marcus, Spectrochim. Acta 45B, 1053, 1990.

110 R.L.F. Boyd and J.B. Thompson, Proc. Royal Soc. London A 1959.

111 C. Lee, M.A. Lieberman, J. Vac. Sci. & Technol. A, 13(2), 368, 1995.

112 T.K. Popov, S.V. Gateva, Plasma Sources Sci. Technol. 10, 614, 2001.

113 M. Bacal, H.J. Doucet, Vacuum, 24(11/12), 595, 1973.

114 A.J. Lichtenberg, M.A. Lieberman, I.G. Kouznetsov, T.H. Chung, Plasma Source Sci. Technol. 9, 45, 2000.

115 G. M. Rao, S. Mohan, Vacuum, 42, 8/9. 515, 1991.

116 J.S. Kim, G.H. Kim, T.H. Chung, G.Y. Yeom, K.H. Kwan, J. Kor. Phys. Soc. 38, 3, 259, 2001.

117 W.M. Posadowski, Thin Solid Films, 392, 201, 2001.

Reproduced with permission of the copyright owner. Further reproduction prohibited without permission.

118 R.S. Freund, T.C. Wetzel, R.J. Shul, T.R> Hayes, Phys. Rev. A, 41(7), 3575, 1990.

119 W.H. Press, S.A. Teukolsky, W.T. Vetterling, B.T. Flannery, *Numerical Recipes in C, the Art of Scientific Computing*, Second Edition, pages 710-722.

120 G. Buyle, D. Depla, K. Eufinger, J. Haemers, R. De Gryse, W. De Bosscher, *Society of Vacuum Coaters* 45th *Annual Technical Conference Proceedings,* 2002.

121 H. Hagstrum, Physical Review 96, 336, 1954.

122 L.M. Kishinevsky, Radiation Effects 23, 1973.

123 *CRC Handbook of Chemistry and Physics*, CRC Press, Boca Raton, 1990.

124 M. Stepanova, *Unpublished Review of Secondary Electron Emission From Solids,* 2003.

125 R.A. Serway, C.J. Moses, C.A. Moyer, *Modern Physics*, page 175, Saunders College Publishing, 1989.

126 B. Streetman, *Solid State Electronic Devices*, Prentice Hall, Chapter 4, page 110, 1995.

127 M. Stepanova, Private Communication, 2003.

128 D.B. Medved, P. Mahadevan, J.K. Layton, Phys. Rev. 129(5), 1963.

129 K. Nanbu, Jpn. J. Appl. Phys., Vol. 33, 4752, 1994.

130 P.L. Bartlett, A.T. Stelbovics, Phys. Rev. A, 66(012707), 2002.

131 M. Capitelli, G. Colona, A. Giequel, K. Hassouni, S. Longo, Physical Review E, 554(2), 1843, 1996.

132 S.M. Rossnagel, H.R. Kaufman, J. Vac. Sci.Technol. A, 6(2), 223, 1988.

133 Y. Matsuda, M. Muta, H. Fujiyama, Thin Solid Films, 345, 167, 1999.

134 H.M. Urbassek, D. Sibbold, J. Vac. Sci. Technol. A 11,676, 1993.

135 E. Shidoji, K. Ness, T. Makabe, Vacuum, 60, 299, 2001.

136 S. Leonard. M.Sc. Thesis, University of Alberta, 2002.

Reproduced with permission of the copyright owner. Further reproduction prohibited without permission.

137 J. R. Taylor, *An Introduction to Error Analysis: A study in the uncertainties in physical measurements.*,University Science Books, 1982.

138 M. Li, S.K. Dew, M.J. Brett, J. Phys. D: Appl. Phys. 32, 2056, 1999.

Reproduced with permission of the copyright owner. Further reproduction prohibited without permission.